NASA CR179455
RI/RD86-168

NASA

FINAL REPORT

SSME LONG-LIFE BEARINGS

July 1986

Myles F. Butner
Brian T. Murphy

ROCKWELL INTERNATIONAL
ROCKETDYNE DIVISION

Prepared For
NATIONAL AERONAUTICS AND SPACE ADMINISTRATION
NASA-Lewis Research Center
Contract NAS3-23263

ERRATA SHEET, NASA CR179455

PAGE	ERROR IN: TABLE	TEXT	LINE	AS ISSUED	CORRECT TO:
40	FIG. 17		4	L/D RANGE = 1.2 TO 1.0	0.2
	FIG. 17		5	PRESSURE DROP units = Pa/m^2	Pa OR N/m^2
41	FIG. 18		1	LD RANGE = 1.58...	1.38
	FIG. 18		6	PRESSURE DROP units = Pa/m^2	Pa OR N/m^2
53	FIG. 29		6	LD = $1.39X10^{-3}$ TO $7.9X10^{-9}m^2$	10^{-3}
54	FIG. 30		1	LD = $3.05X10^{-4}$ TO $8.78X10^{-5}m^2$	$1.39X10^{-3}$ TO $7.9X10^{-3}$
	FIG. 30		3,5	N = 418.9 rad/s	4189
	FIG. 30		4	ECCENTRICITY RATIO = 0 TO 0.09	0.9
62	Table		6	Internally Fed Bearing Working Fluid = LH_2	LN_2
137		Last Para	8 From Bottom	test points becomes $2.27X10^8$ N/m	$3.06X10^8$
		Last Para	6 From Bottom	stiffness becomes $3.06X10^8$ N/m	$2.27X10^8$

1. Report No.	2. Government Accession No.	3. Recipient's Catalog No.
CR179455		

4. Title and Subtitle	5. Report Date
SSME Long-Life Bearings	July 1986
	6. Performing Organization Code 506-42-11

7. Author(s)	8. Performing Organization Report No.
Myles F. Butner, Brian T. Murphy	RI/RD86-168
	10. Work Unit No. YOS 1370

9. Performing Organization Name and Address	11. Contract or Grant No.
Rockwell International Rocketdyne Division 6633 Canoga Avenue Canoga Park, CA 91304	NAS3-23263
	13. Type of Report and Period Covered Final (1-82/7-86)

12. Sponsoring Agency Name and Address	14. Sponsoring Agency Code
National Aeronautics and Space Administration NASA-Lewis Research Center 21000 Brookpark Road Cleveland, OH 44135	

15. Supplementary Notes

Project Manager: Paul W. Spica
NASA-Lewis Research Center
Cleveland, Ohio 44135

16. Abstract

Hybrid hydrostatic/ball bearings for LH_2 and LO_2 service in turbopumps were studied as means of improving speed and life capabilities. Four hybrid bearing configurations were designed with emphasis on achieving maximum stiffness and damping. Parallel load bearings were tested at steady-state and transient conditions with LH_2 (externally fed) and LN_2 (internally fed). The hydrostatic elements were tested with Freon 113 for empirical determination of dynamic characteristics. Tests using an eccentric journal for loading showed the externally and internally fed hydrostatic bearings to have significant separated coefficients of direct stiffness and damping. For the internally fed bearing, the strongly speed-dependent cross-coupling stiffness arising from fluid swirl, along with significant cross-coupling damping, resulted in low net effective stiffness and damping. The test method used can produce separated coefficients with a sufficiently elliptic journal orbit; otherwise, only net effective coefficients combining direct and cross-coupling terms can be determined. Testing with nonsynchronous excitation is recommended to avoid this restriction. Investigation of hard materials, including ceramics, is recommended as a means of eliminating the need for the rolling bearing for startup and shutdown support. The testing was performed in 1984 (LH_2), 1985 (LN_2), and 1985-86 (Freon).

17. Key Words (Suggested by Author(s))	18. Distribution Statement
Hydrostatic Bearings Damping Turbopump Cryogenic	

19. Security Classif. (of this report)	20. Security Classif. (of this page)	21. No. of Pages	22. Price*
Unclassified	Unclassified	162	

* For sale by the National Technical Information Service, Springfield, Virginia 22161

CONTENTS

ILLUSTRATIONS

TABLES

SUMMARY

The SSME Long-Life Bearing Program was conducted to extend the radial load and speed capabilities of turbopump bearings for high-performance Oxygen/Hydrogen rocket engines. Hybrid combinations of ball bearings with hydrostatic bearings were analyzed and designed for operating conditions typical of high-pressure turbomachinery, using the SSME high-pressure turbopumps as bases. Four types of hybrid bearings were designed, including two parallel load and two parallel speed configurations, each with an externally and internally fed hydrostatic element. Prediction of the operation and performance of the four types of hybrid bearings was made, including the effects on ball bearing life, and the effect on damping and stiffness arising from the hydrostatic element. Parametric treatments were used to define the effects of geometric features of the hydrostatic elements on the stiffness and damping characteristics obtained, and also to define methods for identifying the optimum magnitude of damping for a rotor system, and the optimum bearing geometry to obtain the desired results.

Three configurations of hybrid bearings based on a 45 mm bore ball bearing were fabricated: PLEX (Parallel Load Externally fed) PLIN (Parallel Load Internally fed), and PSIN (Parallel Speed Internally fed). The first two of these were tested with LH2 and LN2, respectively. The hydrostatic elements were also tested to determine dynamic characteristics.

A test method was defined to measure empirically the dynamic stiffness and damping coefficients of hydrostatic bearings. Damping tests with LH2 as the working fluid were not successful in producing coefficients because of interference by casing vibration. After modification of the tester mount, coefficients were successfully determined for both externally fed and internally fed bearings using Freon 113 as the working fluid. Separate direct and cross-coupling stiffness and damping coefficients as well as effective coefficients (direct stiffness combined with cross-coupled damping, and direct damping combined with cross-coupled stiffness) were determined for the 75 mm diameter externally fed hydrostatic bearing and for the 55 mm diameter internally fed bearing. Requisites for separated coefficient determination were found to be a journal orbit ellipticity of at least 1.175, and a high degree of journal roundness. Accurate centering of the journal is also considered necessary. The externally fed hydrostatic bearing's measured direct stiffness and damping coefficients were found to agree fairly well with analytic predictions. Cross-coupled stiffness was negative rather than positive as predicted. Cross-coupled damping was significantly larger than predicted and speed dependent. For the net effective coefficients, the stiffness was 30% lower and damping 150% higher than predicted. Stiffness and damping were approximately proportional to supply pressure.

The internally fed bearing's coefficients of direct and cross-coupled stiffness and direct damping were more speed dependent, but coincide with predictions at 200 to 250 Hz. Net effective stiffness was 35% of that predicted; net effective damping was larger than predicted, although only about 10% of that for the externally fed bearing.

In steady-state testing of the externally fed bearing with LH2, the stiffness was greater and fluid flow was less than predicted by approximately 20%. Transient tests simulating turbopump start and shutdown of the parallel load hybrid bearings (externally fed with LH2 and the internally fed bearing with LN2) were satisfactory. Accumulations of the silver plating from the internally fed bearing jammed the bearing on two occasions. The initiating cause was concluded to be particles in the working fluid.

These were the principal conclusions drawn from the analysis and testing:

- Hydrostatic bearings can be used in combination with ball bearings to improve turbopump radial bearing capabilities for load capacity, life, and dynamic characteristics of stiffness and damping.

- Externally fed hydrostatic bearings possess significant direct stiffness and damping, with a reasonable magnitude of cross-coupling stiffness.

- Internally fed hydrostatic bearings with journal surface recesses and smooth bearing surface have low effective stiffness and damping. This characteristic does not rule out this type of bearing for all applications. Since fluid swirl is considered to be the cause of low effective coefficients, means of attenuating fluid tangential velocity could modify the conclusions reached from this test series.

- Deriving separated coefficients from synchronous testing has inherent limitations of minimum orbit ellipticity, which are difficult to achieve with asymmetric stator stiffness.

Recommendations were made for continued development of hybrid and hydrostatic bearings including:

- Nonsynchronous excitation with a separately driven mass is recommended as a means of bypassing the minimum ellipticity requirement.

- Testing of the Parallel Speed Internally fed configuration should proceed, as this configuration has the greatest potential for improvement of speed and life capabilities of propellant-cooled ball bearings.

- Development of internally fed hydrostatic bearings with means of reducing fluid swirl to improve their stiffness and damping should proceed.

- Materials studies to improve the wear and seizure resistance of hydrostatic bearings should be conducted to consider the use of wrought or fusion-applied hard surfacing materials, ceramic inserts of materials like Silicon Carbide or other hard materials. The studies should include definition of mounting techniques that maintain compressive stress for brittle materials. If sufficient wear resistance can be obtained, the need for rolling bearings for start and shutdown may be eliminated.

INTRODUCTION

In the Space Shuttle Main Engine (SSME) turbopumps, the use of propellant-cooled ball bearings achieves reduced turbopump size and weight by eliminating the need for separate lubricants, and the attendant seals and heaters. Ball bearings are capable of functioning in the severe environments typical of turbopumps, where high speeds and loads are combined with large temperature excursions, negligible lubrication and particulate contamination. Ball bearings with 440-C balls and races and Teflon-fiberglass cages were entirely satisfactory for liquid hydrogen and liquid oxygen service in single-flight engines like the J-2 used in the Apollo Program.

With the advent of reusable vehicles, the SSME and other advanced engine requirements have placed progressively greater demands on turbopump bearings in terms of life, load capacity, speed capability, and rotor support characteristics, surpassing the capabilities of ball bearings. Speed capabilities exceeding 2×10^6 DN, with service lives of 10 h are required for advanced applications in the near future with further increases anticipated. Achieving these increased performance requirements is hindered by the often severe operating conditions encountered in turbopumps. Ball bearing lives will fall short of predictions based on fatigue ratings due to wear resulting from the lack of lubrication provided by the pumped propellants. In Fig. 1, the speed limit shown for a 10 h fatigue life is an optimistic prediction for lightly loaded LH_2 or LO_2 cooled bearings. The extent to which additional radial or axial load and propellant cooling will reduce speed and life limits will depend upon the magnitude of loads or misalignments imposed, and the adequacy of cooling supplied by the propellant.

As a means of improving the life and speed capabilities of ball bearings, hydrostatic bearings are attractive alternates, as they are theoretically speed limited only by the centrifugal shaft stress, and thus can operate at journal speeds up to approximately 5×10^6 DN, have increased load capacity (providing sufficient fluid pressure and flow are available), provide improved shaft support through greater stiffness and damping, and have essentially unlimited life if rubbing contact is avoided. However, since they require pressurization from an external source to develop significant load capacity, hydrostatic bearings need some means of avoiding wear and heat generation during start and shutdown. Various hybrid bearing configurations have been tested to combine the startup capability of rolling bearings with the speed, life, and damping advantages of film bearings, (Ref. 1 through 11). The type investigated for cryogenic turbopumps has been the parallel speed configuration for radial loads wherein the hydrostatic bearing is coplanar and concentric, surrounding the ball bearing outer races that are free to rotate with the shaft (Ref. 1, 2, 7, and 11). Other configurations have been proposed or tested with oil as the working fluid (Ref. 3, 4, 5, 6, 9, and 10). Parallel load, as well as thrust bearing configurations are described in Ref. 8.

Hydrostatic and hybrid bearings are adaptable to rocket engine turbomachinery, since typical liquid rocket propellant delivery systems can supply the high-pressure fluid required for hydrostatic bearings without significant performance penalty. Potential improvements in speed and life capability through use of

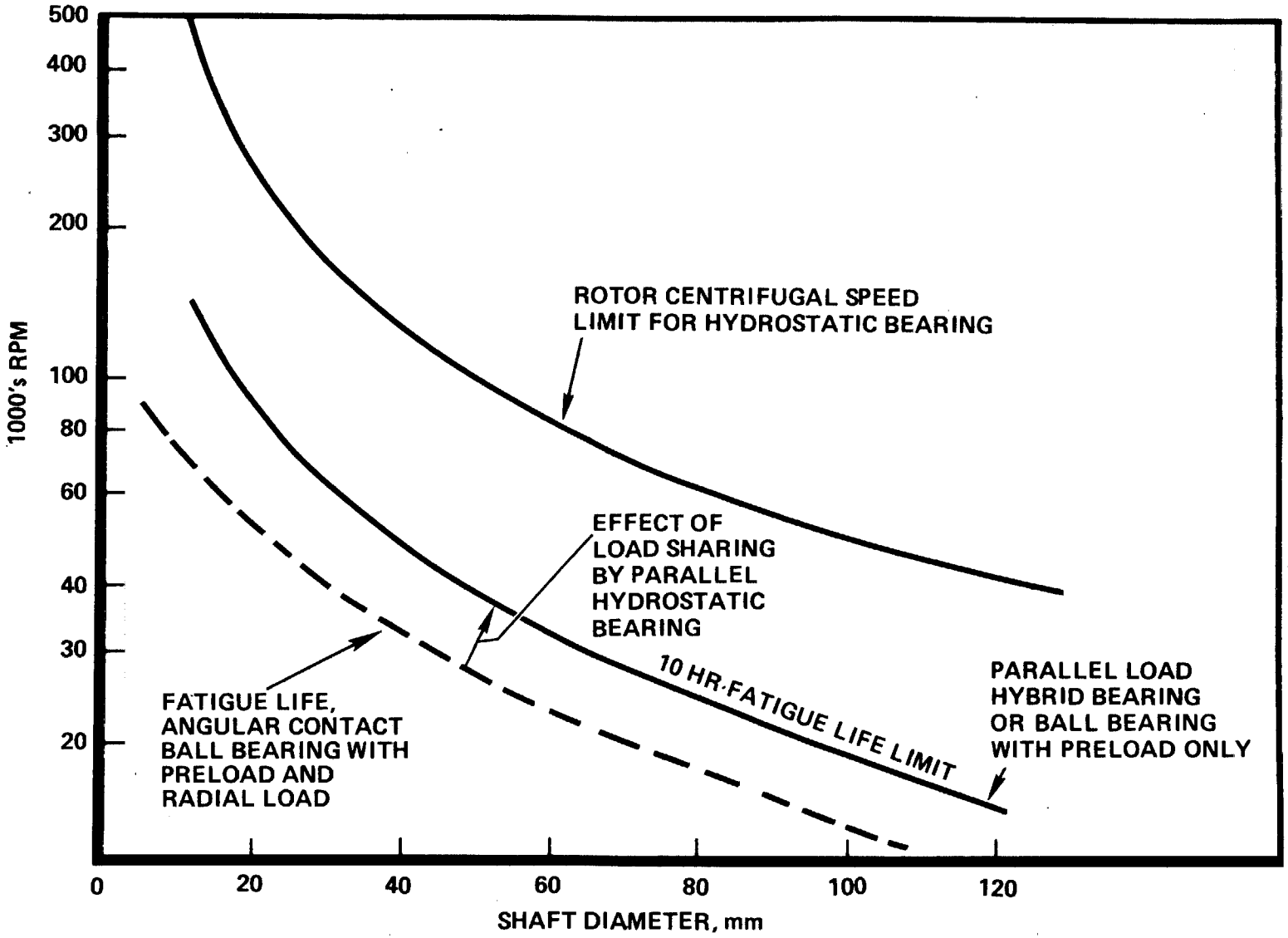

Figure 1. Speed, Load Sharing Effects, Hydrostatic and Hybrid Bearings

hydrostatic or hybrid bearings to share load are indicated in Fig. 1. Hybrid bearings have been tested and demonstrated to be feasible in turbopumps (Ref. 1, 7, and 11), and are being actively considered for incorporation into new turbopump designs.

NASA/Lewis Research Center (LeRC) initiated the SSME Long-Life Bearing Program under Contract NAS3-23263 with the goal of extending bearing capabilities by providing practical design information for improved radial bearings suitable for SSME (Space Shuttle Main Engine) and other advanced propulsion systems.

The program effort focused on hybrid bearings using cryogenic working fluids in rocket engine turbopumps. However, the results are pertinent to other classes of rotating machinery utilizing more conventional fluids. The damping measurement techniques developed can be used for fluid film bearings in general for confirmation of dynamic stiffness and damping characteristics.

The objectives of the program were to design and test hybrid ball/hydrostatic bearings and to provide empirical data with which to confirm or modify analytic methods and models used in hydrostatic bearing design. Comparative evaluation of the internally and externally fed hydrostatic bearings for use as parallel load elements was a specific goal of the testing.

Testing of hybrid bearings was conducted using LH_2 and LN_2 as working fluids, imposing speed, accelerations, pressure, flow, and temperature conditions simulating turbopump environments. Fixed radial loads were imposed to determine bearing stiffness. Tests to measure damping were conducted using LH_2 and Freon 113 as the working fluids. Journal eccentricity was the source of radial loading for the damping tests.

In the cryogenic tests, the test hardware was chilled prior to applying working fluid operating pressure and rotation. Transient tests were conducted by concurrently applying supply pressure and rotational power to simulate turbopump shaft acceleration and pressure schedules.

NOMENCLATURE

SYMBOL	DESCRIPTION
A_o	Orifice Area m^2 ($in.^2$)
A_r	Recess Area Ratio = $\bar{x}\ \bar{y}$
B_p	Recess Circumferential Length, m (in.)
B_{xx}	Direct Damping Ns/m (lbf•s/in.)
c	Clearance, m (in.)
C_D	Coefficient of Discharge ($\simeq$1.0)
D	Journal Diameter m (in.)
d_o	Orifice Diameter m (in.)
g	Gravitational Constant = 9.81 m/s^2 (386.4 $in./s^2$)
G_p, G_z, G_x	Turbulent Correction Factor for Viscosity
h	Film Height, m (in.)
h_r	Recess Depth
I	Mass Moment of Inertia of Cartridge, $kg•m^2$ ($lb•in.^2$)
$\vec{i}$	Unit Vector in Circumferential Direction
$\vec{j}$	Unit Vector in Axial Direction
K	Stiffness, N/m (lbf/in.)
K_{xx}	Direct Stiffness, N/m (lbf/in.)
$\bar{K}_{xx}$	Nondimensional Direct Stiffness, $c\bar{K}_{xx}/(Ps-Pa)LD$
K_{xy}	Cross-coupling Stiffness, N/m (lbf/in.)
K_e	Inertia Coefficient
L	Bearing Length, m (in.)
L_p	Recess Axial Length, m (in.)
L_p'	Recess Sill Width, m (in.)

m	Number of rows
n	Number of recesses
$\vec{n}$	Unit Normal Vector
N	Rotational Speed, rpm
P	Pressure, N/m^2 (psia)
P_a	Ambient Pressure, N/m^2 (psia)
P_r	Recess Pressure, N/m^2 (psia)
P_s	Supply Pressure, N/m^2 (psia)
$\bar{P}_R$	Pressure Ratio = $(P_r-P_a)/(P_s-P_a)$
Q	Flow rate, m^3/s ($in.^3/s$)
R	Journal Radius, (=D/2)
R_f	Film Resistance, $s^2/(N\cdot m^2)$ ($s^2/lb\cdot in.^2$)
R_o	Orifice Resistance, $s_2/(N\cdot m^2)$ ($s^2/lb\cdot in.^2$)
T	Temperature, K (R)
T_f	Friction Torque, N•m (lb_f.in.)
v	Fluid Velocity, m/sec (in./sec)
W	Bearing Load, N (lbf)
z	Axial Direction
η	Excitation frequency, rad/s
θ	Circumferential Direction
θ_{tilt}	Angular Tilt, radian
ϕ	Attitude Angle, degree
ω	Rotational Speed, rad/s
L/D	Bearing length to diameter ratio
c/R	Clearance to journal radius ratio

$\bar{x}$ Recess circumferential length ratio = $\frac{nB_p}{\pi mD}$

$\bar{y}$ Total recess axial length ratio = $\frac{mL_p}{L}$

$\bar{y}'$ Sill width ratio = $\frac{L'_p}{L}$

ϵ Eccentricity ratio = $\frac{e}{c}$

$\bar{P}_R$ Recess pressure ratio = $\frac{P_r - P_a}{P_s - P_a}$

R_e Couette Reynold's number = $\frac{c\omega R\rho}{\mu}$

R_e^* Poiseuille Reynold's number = $\frac{2\, c^3 \rho (P_s - P_a)\bar{P}_R}{\mu^2 (1 - \frac{\bar{y}}{m})\, L}$

$\bar{W}$ Nondimensional load = $\frac{W}{(P_s - P_a)LD}$

$\bar{Q}$ Nondimensional flow = $\frac{m(\frac{L}{D})\,(1 - \frac{\bar{y}}{m})\,Q}{G_p c^3 \bar{P}_R (P_s - P_a)}$

$\bar{K}_{xx}$ Nondimensional direct stiffness = $\frac{c\, K_{xx}}{(P_s - P_a)LD}$

$\bar{K}_{xy}$ Nondimensional cross-coupling stiffness = $\frac{c\, K_{xy}}{(P_s - P_a)LD}$

$\bar{B}_{xx}$ Nondimensional damping = $(\frac{c}{R})^3 B_{xx}/\mu L$

$\bar{T}_f$ Nondimensional friction torque = $\frac{T_f}{(P_s - P_a)LD_c}$

Λ Bearing number = $\frac{\mu\omega RL}{G_p c^2 (P_s - P_a)}$

Λ_r Orifice restrictor parameter = $\dfrac{\rho(P_s-P_a)\, c^6 R}{\mu(A_o C_D)^2}$

σ Squeeze Number = $\dfrac{\mu n \left(\frac{R}{c}\right)^2}{(P_s-P_a)}$

Λ_i Inertia Parameter = $\dfrac{(P_s - P_a)c^4}{288\,(\mu R)^2}\,\rho K_e$

$\bar{R}_o$ Nondimensional orifice resistance = $\dfrac{\rho g G_p c^3 \bar{P}_R^{\,2}}{\mu(\frac{L}{D})(1-\frac{\bar{v}}{m})}\,(P_s-P_a)R_o$

$\bar{R}_f$ Nondimensional film resistance = $\dfrac{\rho g G_p c^3 \bar{P}_R^{\,2}}{\mu(\frac{L}{D})(1-\frac{\bar{v}}{m})}\,(P_s-P_a)R_f$

BEARING ANALYSIS AND DESIGN

Four hybrid bearing configurations, Fig. 2, were designed for the operating conditions (Table 1) of the SSME, but which are representative conditions for high-pressure LH_2 (liquid hydrogen) and LO_2 (liquid oxygen) turbopumps. The configurations are:

PLEX - Parallel Load Externally Fed, Fig. 2a
PLIN - Parallel Load, Internally Fed, Fig. 2b
PSIN - Parallel Speed, Internally Fed, Fig. 2c
PSEX - Parallel Speed Externally Fed, Fig. 2d

The geometric features of the hydrostatic members of the hybrid bearings are listed in Tables 2 through 5. All hybrid bearings incorporated the 45 mm bore ball bearing described in Table 6. Factors that influenced the choice of internally fed bearings for LO_2 service were (1) the high-friction torque caused by the higher density and viscosity of LO_2, which favor small journal diameters and (2) a source of high-pressure LO_2 currently exists in the shaft interior of the SSME HPOTP, which would be readily adaptable to feed hydrostatic bearings.

In Fig. 2, schematics below each cross section represent the clearances (dead bands) and forces linking the shaft to the housing both prior to pressurization of the hydrostatic bearing and at steady-state operation with working fluid supplied under pressure.

The predicted bearing performance characteristics are listed in Table 7.

The computer program HBEAR (Ref. 12) was used to analyze the hydrostatic bearings. Modifications of the program results were made for the internally fed bearings to account for fluid swirl effects.

Ball bearing analysis was performed using the methods of A.B. Jones, (Ref. 13).

Parametric treatments of bearing geometric and performance variables were used to:

1. Define the effects of geometry on LH_2 - fed hydrostatic bearing characteristics

2. Determine a method to define the optimum damping for a rotor

3. Identify the geometric features that most strongly affect the damping obtained

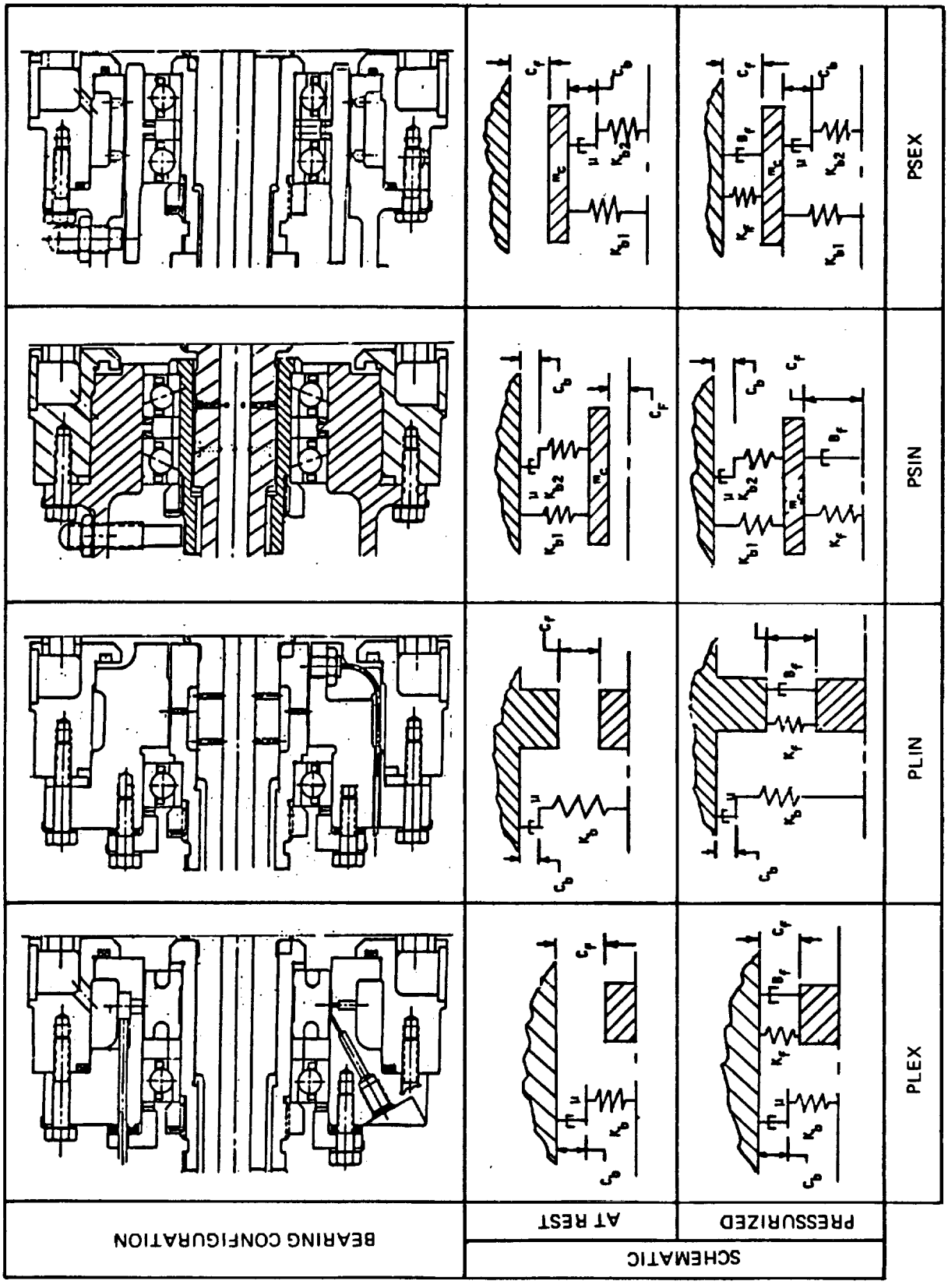

Figure 2. Hybrid Bearing Configurations

TABLE 1. SI AND ENGLISH UNITS BEARING OPERATING CONDITIONS

	ENGLISH UNITS					SI UNITS				
		OXIDIZER		FUEL			OXIDIZER		FUEL	
TURBOPUMP POSITION	UNITS	INLET	TURBINE	INLET	TURBINE	UNITS	INLET	TURBINE	INLET	TURBINE
COOLANT		LO_2	LO_2	LH_2	LH_2		LO_2	LO_2	LH_2	LH_2
SPEED	rpm	30,000	30,000	36,600	36,600	rad/s	3141	3141	3832	3832
DN	mm rpm	1.35	1.71	1.65	1.65	mm rpm	1.35	1.71	1.65	1.65
LOAD (PER BEARING)										
AXIAL TRANSIENT,	lb	SMALL	4000	NEGLIGIBLE	NEGLIGIBLE	N	SMALL	17792	NEGLIGIBLE	NEGLIGIBLE
AXIAL, STEADY STATE	lb	850	1000	700	700	N	3780	4448	3114	3114
RADIAL, FIXED	lb	500	500	SMALL	SMALL	N	2224	2224	SMALL	SMALL
RADIAL, SYNCHRONOUS	lb	600	600	400-900	400-900	N	2669	2669	1779-4003	1779-4003
FLUID PROPERTIES										
SUPPLY PRESSURE AVAILABLE	psia	2000	2000	2350	5600	MPa	13.8	13.8	16.2	38.6
SUMP PRESSURE	psia	400	400	350	3700	MPa	2.76	2.76	2.41	25.5
TEMPERATURE, INLET	R	196	196	45	90	K	109	109	25	50
DENSITY	lb/ft^3	70	70	5.0	4.9	kg/m^3	1123	1123	80.25	78.65
VISCOSITY	10^{-9} lb•sec/in.^{2}	20	20	1.12	1.86	10^{-4} N•s/m^2	1.379	1.379	0.0772	0.128

TABLE 2. DESIGN DESCRIPTION HYDROSTATIC BEARING ELEMENT
PARALLEL LOAD EXTERNALLY FED HYBRID BEARING

ITEM		MM	INCH
BEARING BORE, NOMINAL		75.04	2.9545
BEARING LENGTH, NOMINAL		25.4	1.00
RADIAL CLEARANCE	OPERATING	0.0381 + 0.0076 - 0.0000	0.0015 + 0.0003 - 0.0000
	AMBIENT	0.0431 + 0.0127 - 0.0000	0.0017 + 0.0005 - 0.0000
ORIFICE DIAMETER, d_o		1.27 ± 0.013	0.050 ± 0.0005
ORIFICE LENGTH, NOMINAL, l_o		1.80	0.071 (0.08 ± 0.020)
RECESS DESCRIPTION	WIDTH (CIRCUM)	11.405 ± 0.254	0.449 ± 0.010
	LENGTH (AXIAL)	8.890 ± 0.254	0.350 ± 0.010
	DEPTH, h_r	0.2286 ± 0.05	0.009 ± 0.002
	SURFACE RECESSED	BEARING	
	NUMBER OF RECESSES	6	
	NUMBER OF ROWS	1	
	AREA RATIO	0.10	

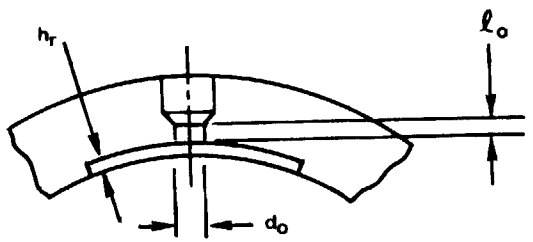

TABLE 3. DESIGN DESCRIPTION HYDROSTATIC BEARING ELEMENT
PARALLEL LOAD INTERNALLY FED HYBRID BEARING

ITEM		MM	INCH
BEARING BORE, NOMINAL		54.61	2.1500
BEARING LENGTH, NOMINAL		25.4	1.00
RADIAL CLEARANCE	OPERATING	0.0317 0.0457	0.00125 0.0018
	AMBIENT	0.0368 0.0508	0.00145 0.0020
ORIFICE DIAMETER, d_o		1.333 ± 0.0127	0.0525 ± 0.0005
ORIFICE LENGTH, NOMINAL, l_o		6.73	0.265
RECESS DESCRIPTION	WIDTH (CIRCUM)	8.18 ± 0.25	0.322 ± 0.010
	LENGTH (AXIAL)	8.90 ± 0.25	0.350 ± 0.010
	DEPTH, h_r	0.2032 ± 0.0508	0.008 ± 0.002
	SURFACE RECESSED	JOURNAL	
	NUMBER OF RECESSES	6	
	NUMBER OF ROWS	1	
	AREA RATIO	0.1	

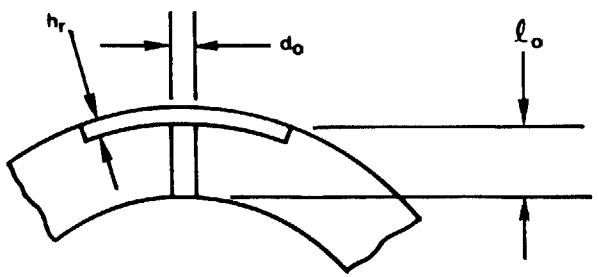

TABLE 4. DESIGN DESCRIPTION HYDROSTATIC BEARING ELEMENT
PARALLEL SPEED INTERNALLY FED HYBRID BEARING

ITEM		MM	INCH
BEARING BORE, NOMINAL		33.27	1.31
BEARING LENGTH, NOMINAL		43.18	1.70
RADIAL CLEARANCE	OPERATING	0.0228 0.6236	0.00057 0.00093
	AMBIENT	0.0086 0.0190	0.00035 + 0.0004 - 0.0000
ORIFICE DIAMETER, d_o		0.4267 ± 0.013	0.0168 ± 0.0005
ORIFICE LENGTH, NOMINAL, l_o		1.83	0.072
RECESS DESCRIPTION	WIDTH (CIRCUM)	6.908 ± 0.254	0.272 ± 0.010
	LENGTH (AXIAL)	8.636 ± 0.254	0.340 ± 0.010
	DEPTH, h_r	0.2286 ± 0.0254	0.009 ± 0.001
	SURFACE RECESSED	JOURNAL	
	NUMBER OF RECESSES	12	
	NUMBER OF ROWS	2	
	AREA RATIO	0.08	

TABLE 5. DESIGN DESCRIPTION HYDROSTATIC BEARING ELEMENT
PARALLEL SPEED EXTERNALLY FED HYBRID BEARING

ITEM		MM	INCH
BEARING BORE, NOMINAL		88.9	3.5
BEARING LENGTH, NOMINAL		38.1	1.5
RADIAL CLEARANCE	OPERATING	0.0444	0.00175
	AMBIENT	0.1193 + 0.0152 - 0.0000	0.0047 + 0.0006 - 0.0000
ORIFICE DIAMETER, d_o		1.219 ± 0.0127	0.0480 ± 0.0005
ORIFICE LENGTH, NOMINAL, l_o		2.87	0.113
RECESS DESCRIPTION	WIDTH (CIRCUM)	18.64 ± 0.254	0.734 ± 0.010
	LENGTH (AXIAL)	3.81 ± 0.254	0.150 ± 0.010
	DEPTH, h_r	0.305 ± 0.05	0.012 ± 0.002
	SURFACE RECESSED	BEARING	
	NUMBER OF RECESSES	12	
	NUMBER OF ROWS	2	
	AREA RATIO	0.08	

TABLE 6. BASELINE BALL BEARING DESIGN SUMMARY

TYPE - ANGULAR CONTACT	VALUE	UNITS
DIMENSIONS		
BORE	45	mm
PITCH DIAMETER	59	mm
OUTER DIAMETER	75	mm
WIDTH	16.51	mm
BALL DIAMETER	8.73	mm
NUMBER OF BALLS	14	-
INNER RACE CURVATURE, R/D	0.53	-
OUTER RACE CURVATURE, R/D	0.52	-
INNER RACE SHOULDER, H/D	0.23	-
OUTER RACE SHOULDER, H/D	0.19	-
INTERNAL DIAMETRAL CLEARANCE		
UNMOUNTED	0.101	mm
MOUNTED, AMBIENT	0.049	mm
MOUNTED, CHILLED	0.066	mm
CONTACT ANGLE, MOUNTED CHILLED	22.3	DEGREES
CAGE OD CLEARANCE	0.23	mm
CAPE POCKET CLEARANCE	0.616	mm
TOLERANCES		
DIMENSIONS	ABEC 7	-
BALL GRADE	AFBMA 10	-
MATERIALS		
BALLS	440C	-
RINGS	440C	-
CAGE	GFT*	-
STIFFNESS	8.0×10^7	N/m
(3874 rad/s, 3100 N preload)		

*GLASS FABRIC SUPPORTED PTFE

TABLE 7. HYDROSTATIC AND HYBRID BEARING DESIGN CHARACTERISTICS

CASE	CONFIGURATION FIGURE 2	CONFIGURATION HYBRID TYPE	SPEED Krad/s (krpm)	DIA., mm (inch)	LENGTH mm (inch)	FLUID	ΔP MPa (psi)	HYBRID STIFFNESS 10^6 N/m (10^6 lb/in.)	HYDROSTATIC ELEMENT FLOW 10^{-4} m^3/s (gpm)	HYDROSTATIC ELEMENT kg/s (lb/s)	HYDROSTATIC ELEMENT STIFFNESS 10^6 N/m (10^6 lb/in.)	HYDROSTATIC ELEMENT DAMPING 10^3 N-s/m (lb-s/in.)
1	a	PLEX	3.83 (36.6)	75 (2.95)	25.4 (1.0)	LH_2	13.1 (1900)	341 (1.95)	37.8 (60)	0.27 (0.6)	262 (1.5)	5.25 (30)(2)
2	a	PLEX	3.14 (30.0)	75.0 (2.95)	25.4 (1.0)	LO_2	11.0 (1600)	429 (2.45)	8.2 (13)	0.86 (1.9)	350 (2.0)	30.6 (175)(2)
3	b	PLIN	3.14 (30.0)	54.6 (2.15)	25.4 (1.0)	LO_2	11.0 (1600)	317 (1.8)	4.3 (6.8)	0.54 (1.0)	236 (1.35)	30.1(2) (172)
4	c	PSIN	3.14 (30.0)	33.3 (1.31)	43.2 (1.7)	LO_2	11.0 (1600)	107 (0.61)	1.8 (2.8)	0.18 (0.4)	318 (1.81)	114 (655)(1)
5	d	PSEX	3.83 (36.6)	88.9 (3.5)	38.1 (1.5)	LH_2	13.1 (1900)	127 (0.73)	61 (97)	0.45 (1.0)	611 (3.49)	26.2(1) (150)

(1) DAMPING FORCE APPLIED TO INTERMEDIATE MASS

(2) DAMPING DIRECTLY APPLIED

HYBRID BEARINGS

PLEX BEARING

The PLEX (Parallel Load, Externally Fed) hybrid bearing, (Fig. 2a), offers significant increases in stiffness and damping over that of the ball bearing alone. The life benefit in the presence of radial load is shown in Fig. 3. For the ball bearing alone, life declines with increased radial load from point 1 to point 2 . In the hybrid bearing, the radial load is shared between the hydrostatic and ball bearing elements so that the ball bearing life follows the path from 1 , 3 , 4 , and 5 . In the test bearing design with the ball bearing of Table 4 and the hydrostatic bearing, Case 1 of Table 7, from points 1 to 4 , the ball bearing radial load is limited to the friction force (product of preload and friction coefficient) required to move the outer race through the dead band. From 4 to 5 , the hydrostatic bearing supports most of the radial load by virtue of its high stiffness, 31.9 x 10^7 N/m as compared to 8 x 10^7 N/m for the ball bearing. Since the ball bearing runs at full rotor speed, there will be no life increase at low radial loads. However, benefits would be obtained from the added stiffness and damping.

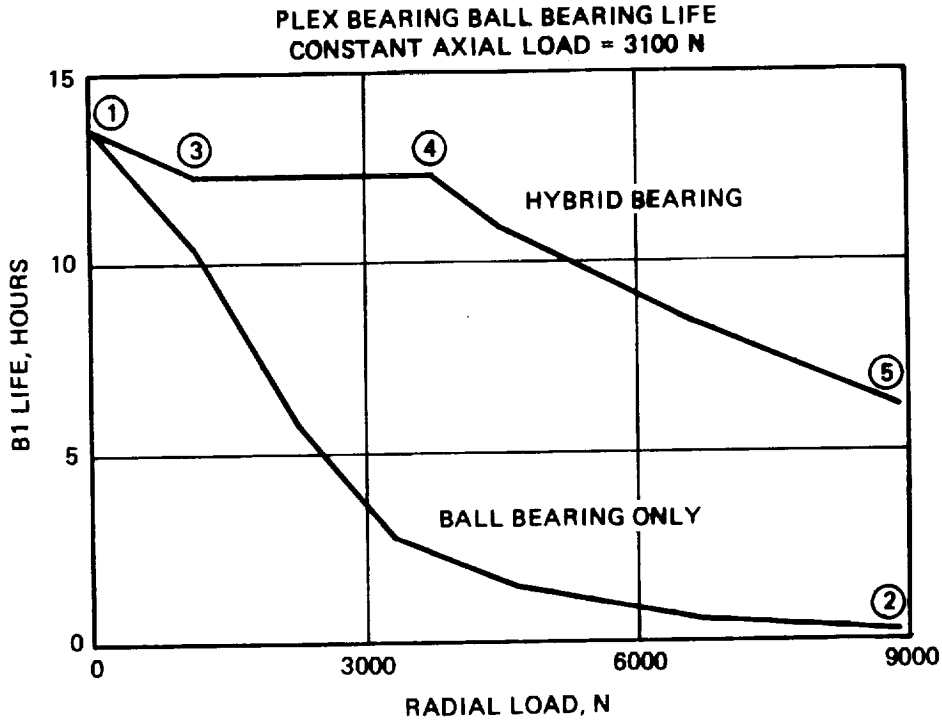

Figure 3. Life Effect, Plex Bearing

A desirable characteristic of the parallel load bearings is that the forces arising from the stiffness and damping of the film are transmitted directly to the housing rather than through the ball bearing as in the parallel speed bearings.

Avoidance of hydrostatic bearing contact during transients is an important advantage of the parallel load bearings, particularly in bearings operating in LO_2 or other reactive propellants where frictional heat might trigger ignition. An additional margin of 0.027 mm (0.001 in.) clearance exists at low speeds due to the allowance for centrifugal growth of the journal.

Since the hydrostatic bearing working fluid is supplied from the turbopump discharge, fluid pressure and properties will become functions of shaft speed as represented by Fig. 4. In a multistage pump, the bearing working fluid would be drawn from the lowest stage discharge which has sufficient pressure for bearing operation to minimize heating of the fluid. The predicted hydrostatic bearing performance characteristics including the speed effects, are presented in Fig. 5 for the bearing of Table 2. A similar determination of the speed dependent characteristics of the bearings should be included in rotordynamic analyses as part of the turbopump design process to define response during transient periods. For example, the possibility of a rotor resonant condition, which tracks rotor speed, may arise due to concurrent stiffness and speed variation (Ref. 11).

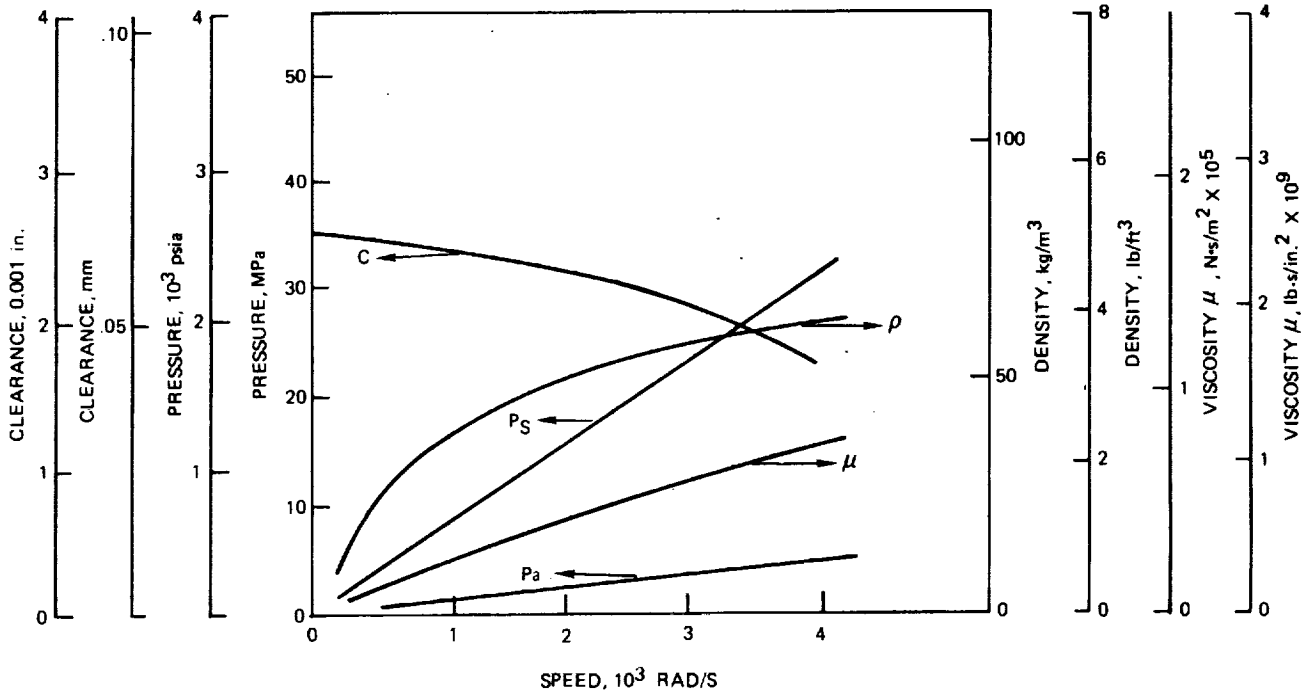

Figure 4. Speed Effects-LH_2 Bearing Conditions

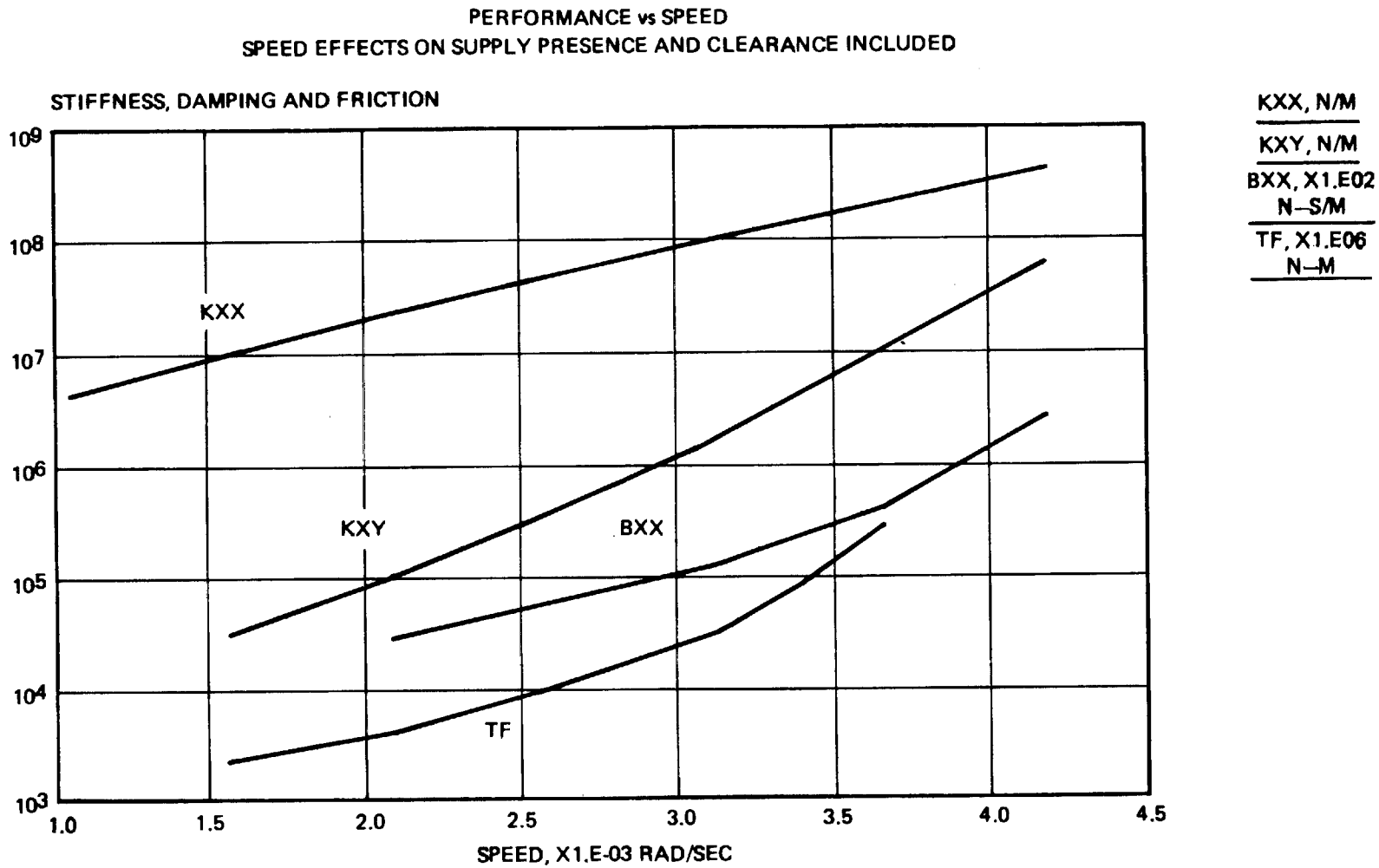

Figure 5. Calculated Performance, PLEX Bearing Hydrostatic Element, LH_2 Fed

PLIN BEARING

As with the PLEX bearing, the hydrostatic element of the PLIN (Parallel Load Internally fed) bearing, Fig. 2b, with a stiffness of 2.36 x 10^8 N/m supports part of the radial load, extending the fatigue life of the associated ball bearing (Fig. 6) with a 8 x 10^7 N/m stiffness, and also increases the combined stiffness and adds damping (Table 7). For the test bearing design, the journal diameter was selected to discharge the fluid (LO_2) between the inner race and cage of the ball bearing, providing cooling without impinging on race or cage. The bearing consists of a plain cylindrical inner diameter surface, while the orifices and recesses are incorporated into the journal outer diameter surface. The tangential velocity or swirl imparted to the fluid will theoretically increase the damping obtained, but will also significantly increase the cross-coupled stiffness. Fluid swirl effects were included in the predicted characteristics of the hydrostatic bearing using the approach developed for seals (Ref. 14).

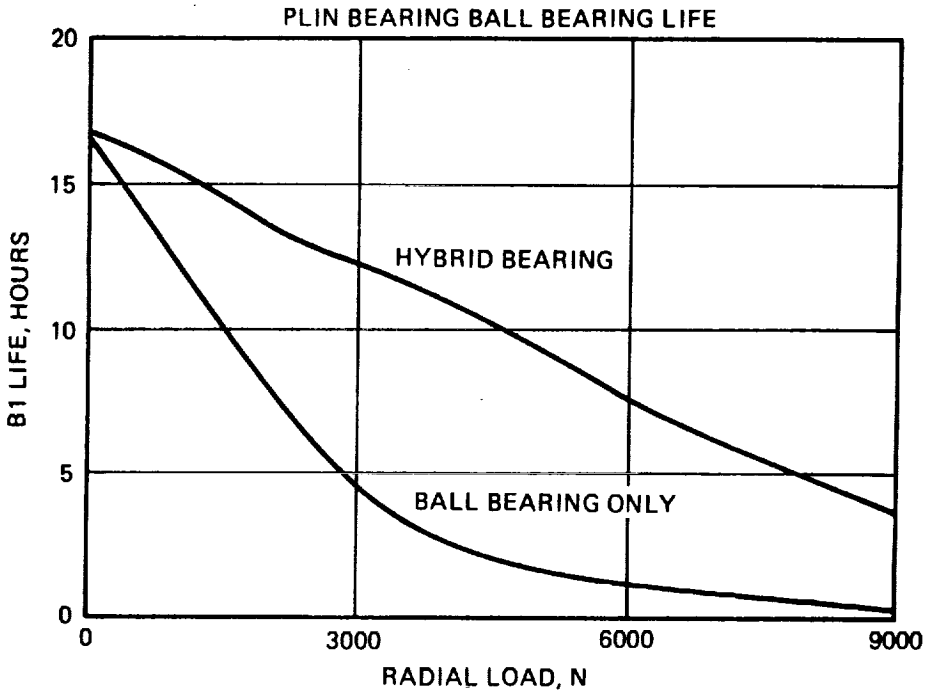

Figure 6. Life Effect, Plin Bearing

Figure 7 shows the speed dependence of fluid properties, pressures, and clearance used to analyze and predict the internally fed hydrostatic bearing characteristics that appear in Fig. 8.

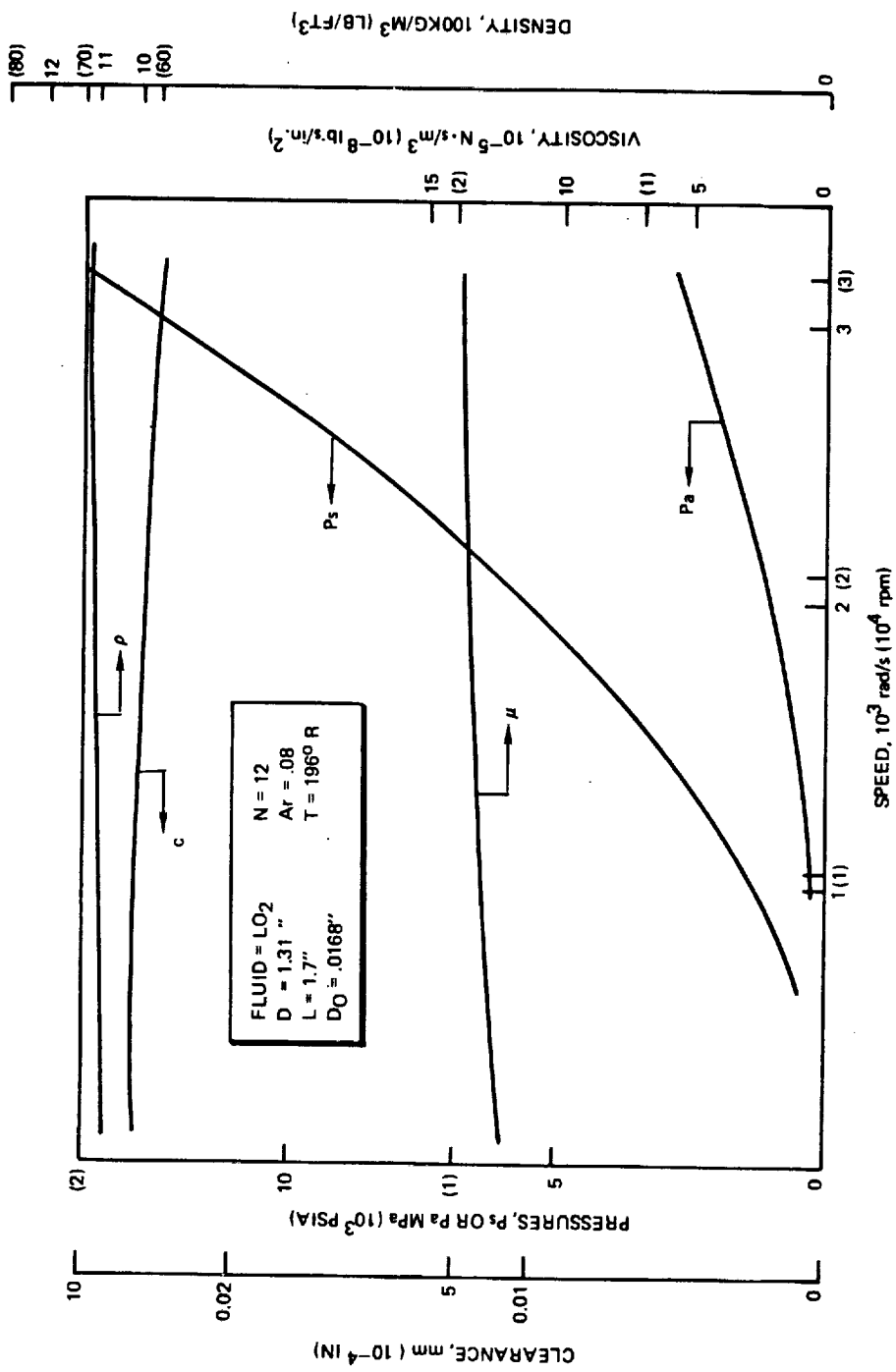

Figure 7. Speed Effects, LO_2 Bearing Conditions

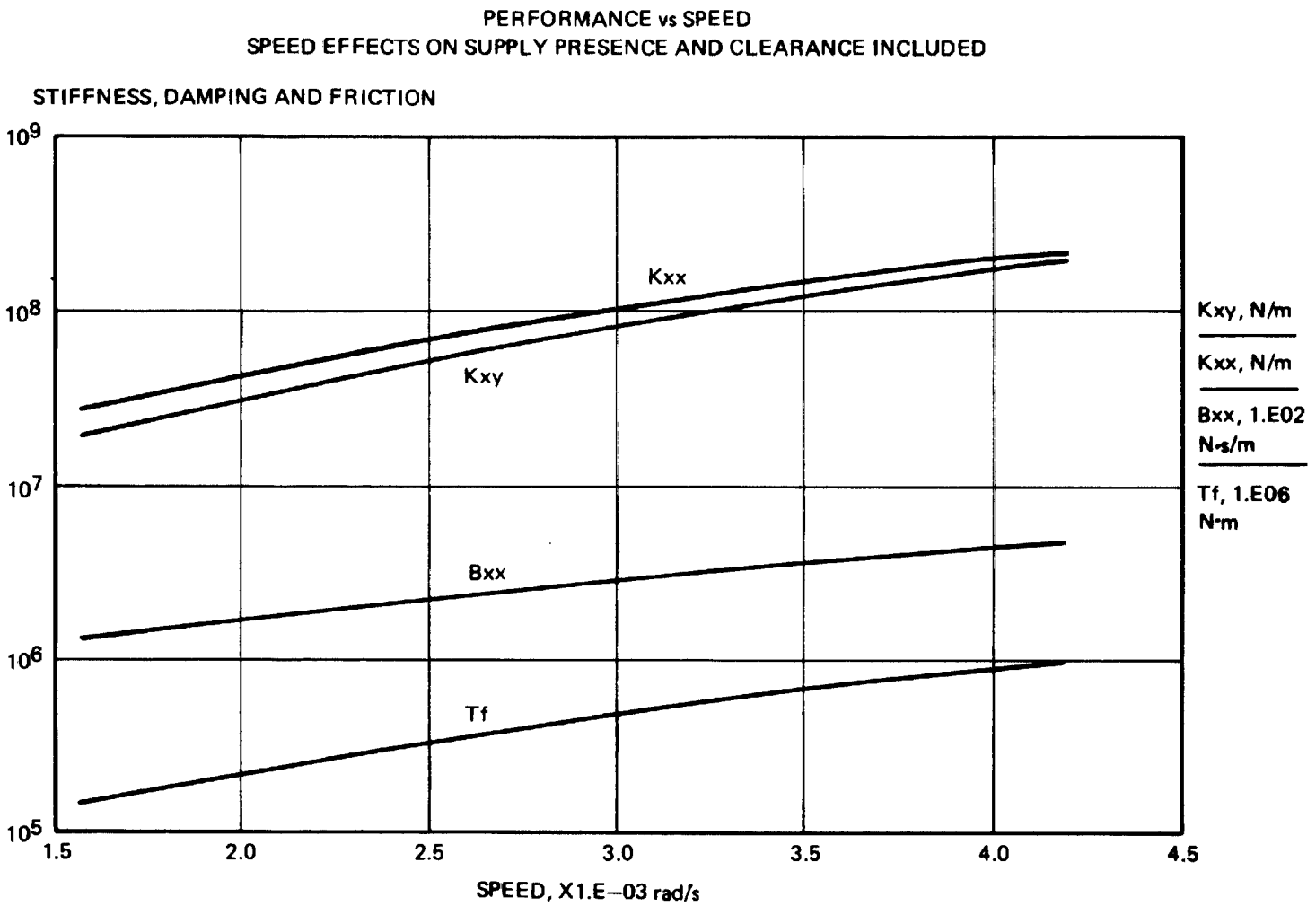

Figure 8. PLIN Hydrostatic Element Characteristics

HYDROSTATIC BEARING DESIGN

The hydrostatic bearings for this program were designed with emphasis on maximizing stiffness and damping and minimizing friction torque and flow rate. Designs for other applications will require prioritizing of these quantities to accommodate rotordynamic and other specific considerations. For example, maximum stiffness may not be desirable for a particular design. Also, low friction torque is more important for parallel speed hybrid bearings than for parallel load bearings.

Operating conditions, fluid properties, and bearing envelope are assumed to be governed by the turbopump configuration. Available supply (Ps) and ambient (Pa) pressures, fluid viscosity (μ) and density (ρ) and the shaft speed (N) are assumed to be set for the application. Bearing geometry nomenclature is illustrated in Fig. 9. The journal diameter (D) and bearing length (L) must be compatible with space constraints. The optimization process involves selecting the journal to bearing clearance (c), recess configuration, and orifice size (d_o) to achieve optimal performance. The following parameters are used to describe the recess configuration:

Number of recesses (n)
Recess to journal area ratio (A_r)
Number of rows (m)
Circumferential recess length (B_p)
Axial recess length (L_p)
Recess edge to bearing edge distance (L_p')

Considerations in selecting a candidate recess configuration include:

1. The number of recesses should be greater than four to avoid excessive directional stiffness variation. From this aspect, there is little benefit in using more than six recesses (Ref. 16)

2. Recess depth (h_r, Fig. 9)should be great enough to obtain uniform pressure over the recess area. Using the criterion of a 10% maximum pressure variation (Ref. 1),

$$\left(\frac{12\mu Q}{\pi^2 n\, G_p\, \bar{P}_R\, (P_s-P_a)\, (h_R+c)^3}\right)\left(\frac{2(B_p+L_p)}{d_o}-\pi\right) < .1$$

where: G_p is the Poiseuille correction factor for turbulence and is a function of the Poiseuille Reynolds' number (R_e^*).

Since:

$$Re^* = \frac{2\, c^3\, \rho\, (P_s-P_a)\, \bar{P}_R}{m^2\, (1-\frac{\bar{y}}{m})\, L}$$

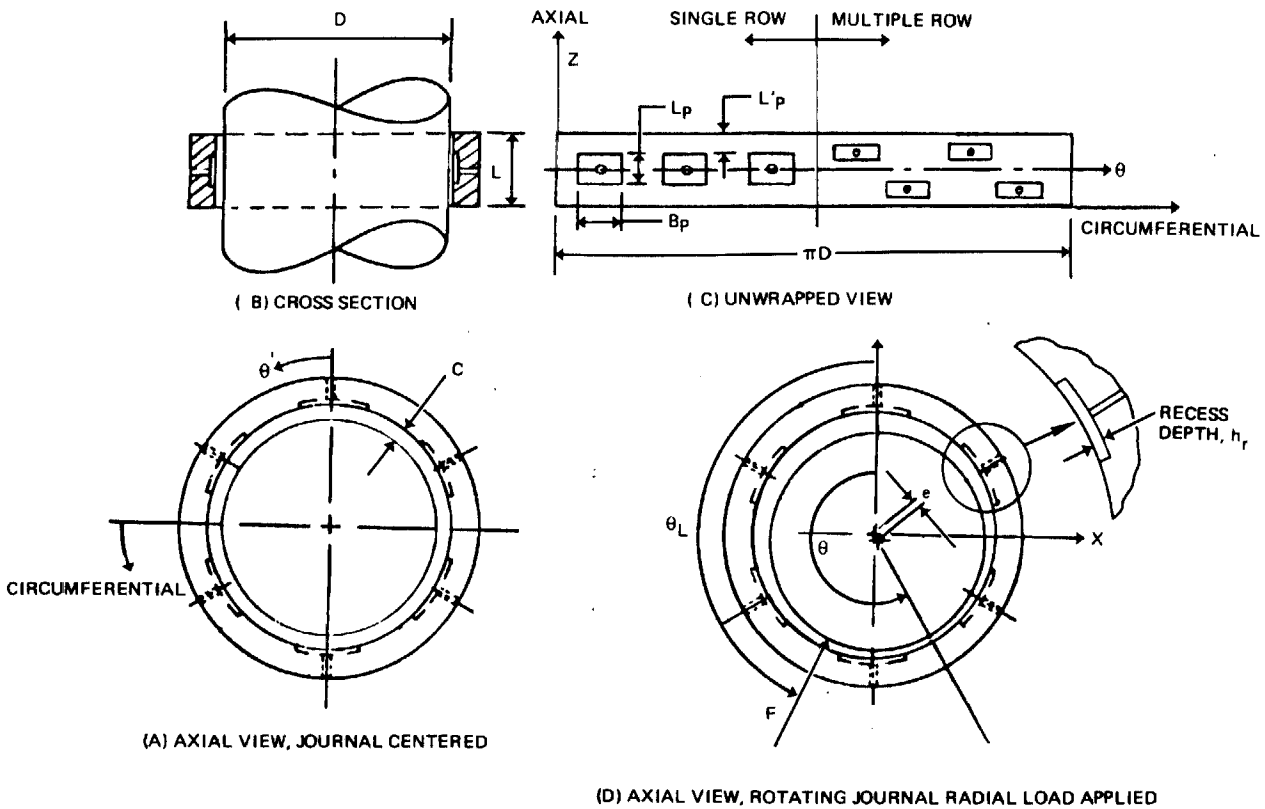

Figure 9. Orifice Compensated Hydrostatic Bearing

3. The recess volume should be kept small to avoid pneumatic hammer instability. Reference 1 suggests that the total volume of recess and compensating orifice not exceed the clearance volume in the land area for LH_2 hydrostatic bearings. Since LO_2 is less compressible, the permissible volume ratio can be as much as 2 for LO_2-fed bearings. This criterion can be expressed as

$$\frac{n[(h_R + c)\ L_p\ B_p]}{(\pi DL - n\ L_p\ B_p)\ c} \leq \begin{cases} 1.0 \text{ for } LH_2 \\ 2.0 \text{ for } LO_2 \end{cases}$$

4. Fluid velocities within the bearing flow path should be checked for choking, which will occur if the local velocity exceeds the sonic velocity.

When two rows of recesses are used, a staggered pattern is normally adopted, to give more uniform load support, although only a minor effect is expected for designs with more than four recesses per row. While the recess depth, corner radius, length of orifice, and surface finish do not have much calculable impact on performance, they require consideration as they do affect stability and choice of manufacturing process.

OPTIMIZED DESIGN

General Approach

Maximizing an Objective Function is the suggested way to quantify a desirable performance "score." The optimization process outlined below can be applied to any hydrostatic bearing design.

The expression for the Objective Function is determined by the relative importance of the performance goals and is formulated for each bearing design individually. An example of Objective Function use follows:

Given:

- The journal diameter (D),
- The fluid properties (μ, ρ),
- The operating speed (N),
- The supply (P_s) and ambient pressures (P_a) and
- The bearing load (W)

Required:

- The bearing length (L)
- The journal clearance (c)
- The recess configuration (n, m, A_r, B_p, L_p, L_p') which maximize the value of the objective function J.

where:

- $J = J\ (W_1 B,\ W_2 K,\ W_3 T_f,\ W_4\ \dot{m})$
- J is a function to be defined
- W_1 through W_4 are weights assigned to each element

J is to be maximized while satisfying the following constraints:

- $\varepsilon < \varepsilon_{max}$ to avoid rubbing
- $T_f < T_{max}$ to maintain a high film speed for parallel speed bearings
- $\dot{m} < \dot{m}_{max}$ where a limit can be set to maintain efficient pump performance.
- K and B within a certain envelope depending on the rotor configuration
- $d_o < d_{o_{min}}$ to avoid blockage by particulate contamination.

Formulation of the Objective Function (J) should be as specific as possible. In the absence of specific limits or constraints, subjective choices must be made based on judgment.

Hydrostatic Bearing Design Optimization

The optimization procedure used for the hydrostatic bearings is outlined above and is depicted in the block diagram of Fig. 10. The procedure started with a preliminary selection of the clearance (c) and bearing length (L) based on the following dimensionless quantities suggested in Ref. 15:

$$\frac{c}{R} = 0.001, \text{ and}$$

$$\frac{W}{(P_s - P_a)LD} = 0.25$$

To achieve maximum stiffness and damping, a recess pressure ratio of near 0.5 is required (Fig. 11). A candidate recess configuration was selected and, with the help of design curves, such as Fig. 12, (film resistance versus clearance) and Fig. 13, (orifice resistance versus orifice size) the orifice diameter was selected to achieve a pressure ratio (P_R) of 0.5.

The predicted performance of this trial design was then evaluated analytically using the computer program "HBEAR", which is described in Ref. 12. The results were then examined for matching of the objectives and constraints, and the Objective Function's value computed. Should the objectives not be met, the process was repeated after adjusting the candidate design elements. For example, the journal clearance and/or the bearing length was altered if permitted by constraints. The next adjustment, if necessary, was made to the recess configuration. This process was repeated until all constraints were satisfied. At this point, a feasible, but not necessarily optimal, design was achieved. The procedure could then again be repeated until the Objective Function value was maximized. This configuration was chosen as the final configuration, completing the design process.

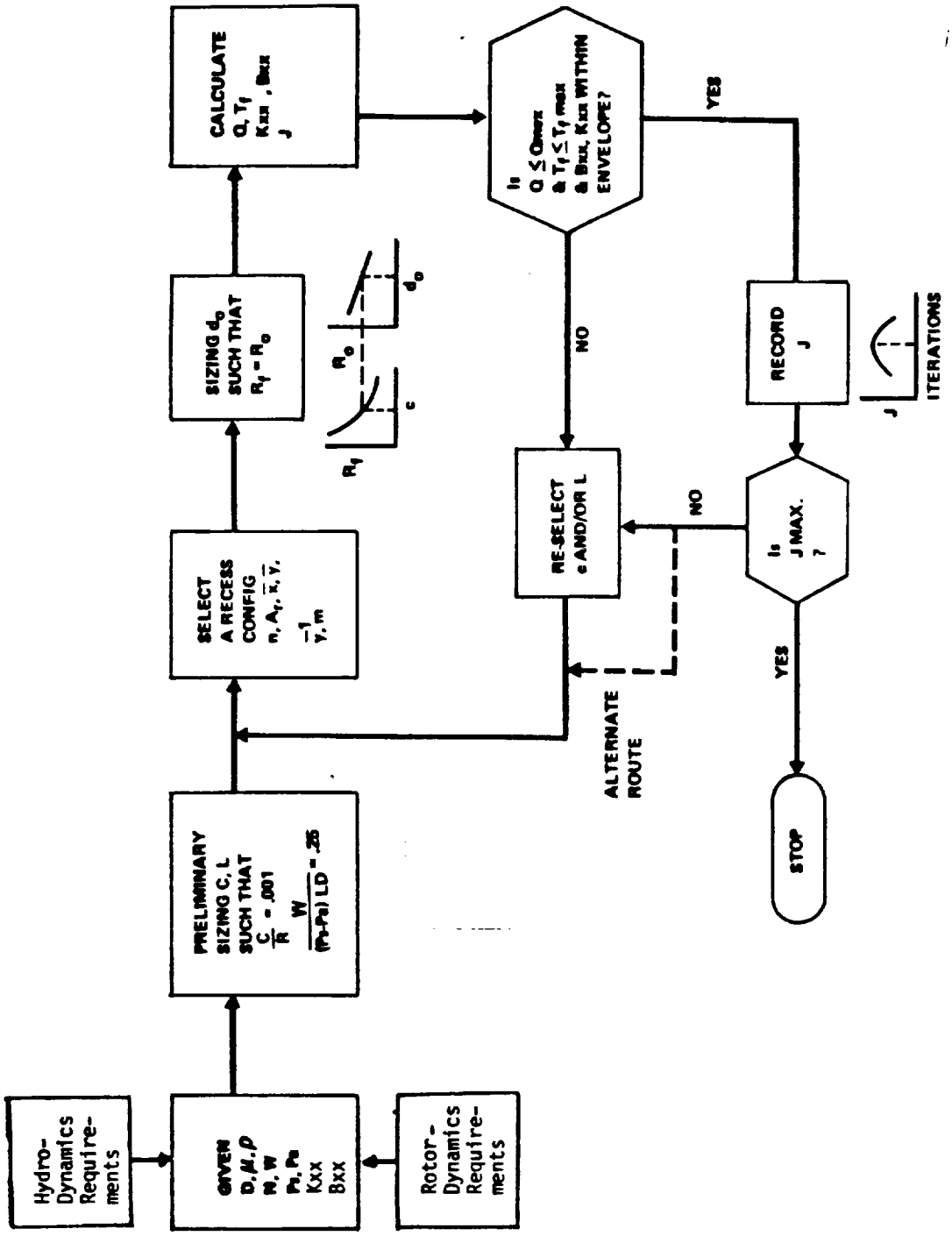

Figure 10. Optimization Block Diagram

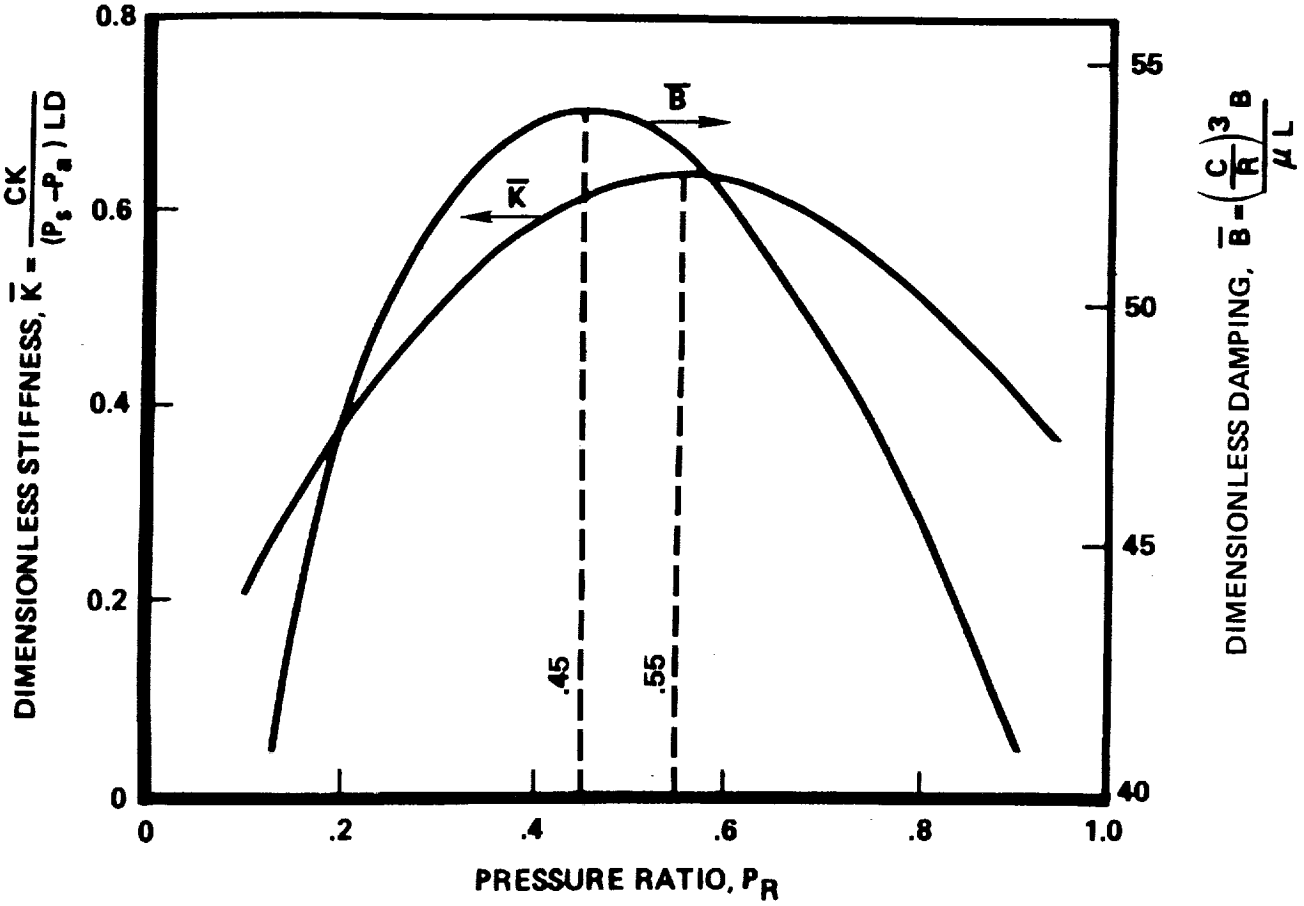

$$P_R = \frac{\text{RECESS PRESSURE} - \text{EXHAUST PRESSURE}}{\text{SUPPLY PRESSURE} - \text{EXHAUST PRESSURE}}$$

Figure 11. Pressure Ratio Effects

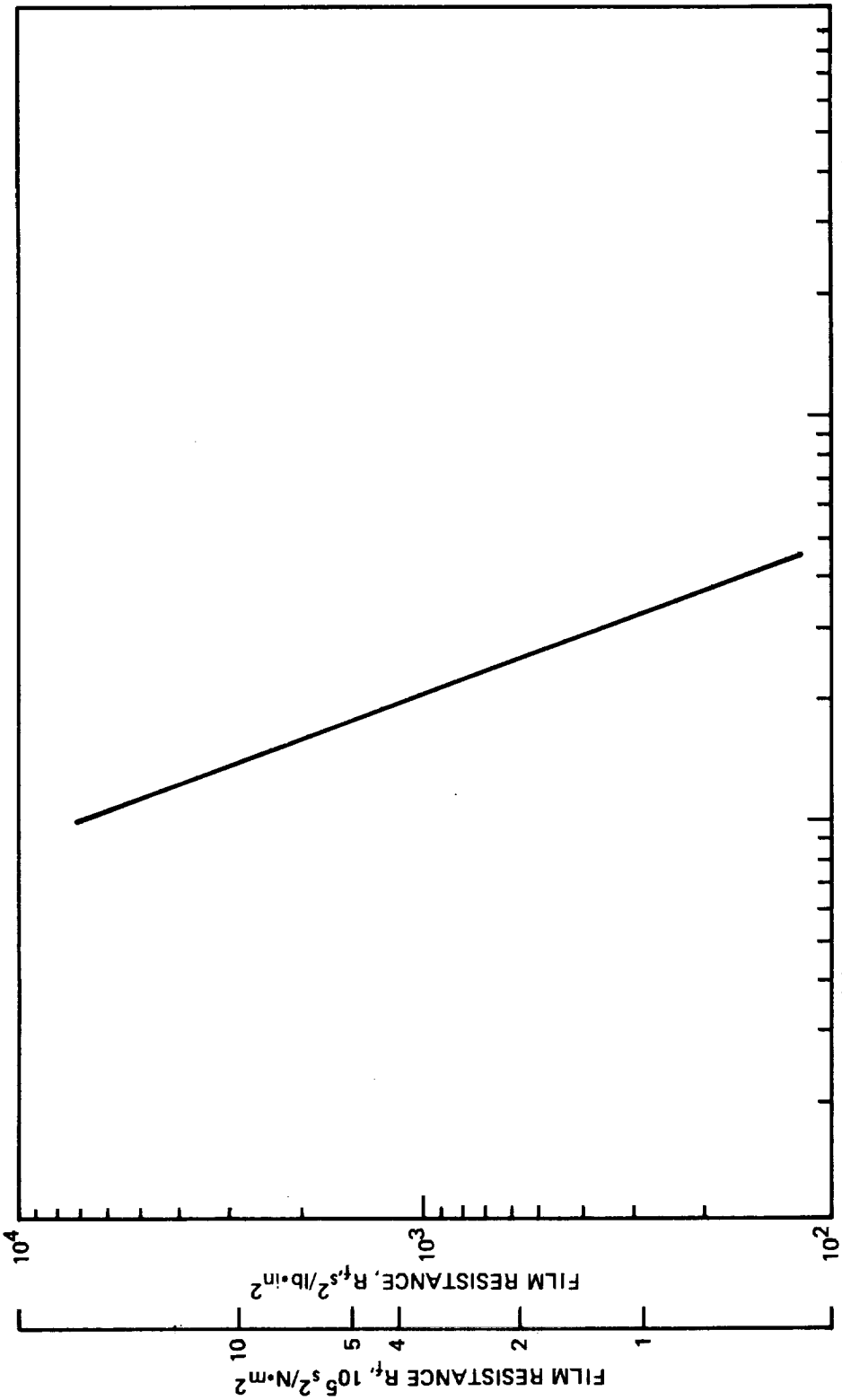

Figure 12. Film Resistance vs Radial Clearance

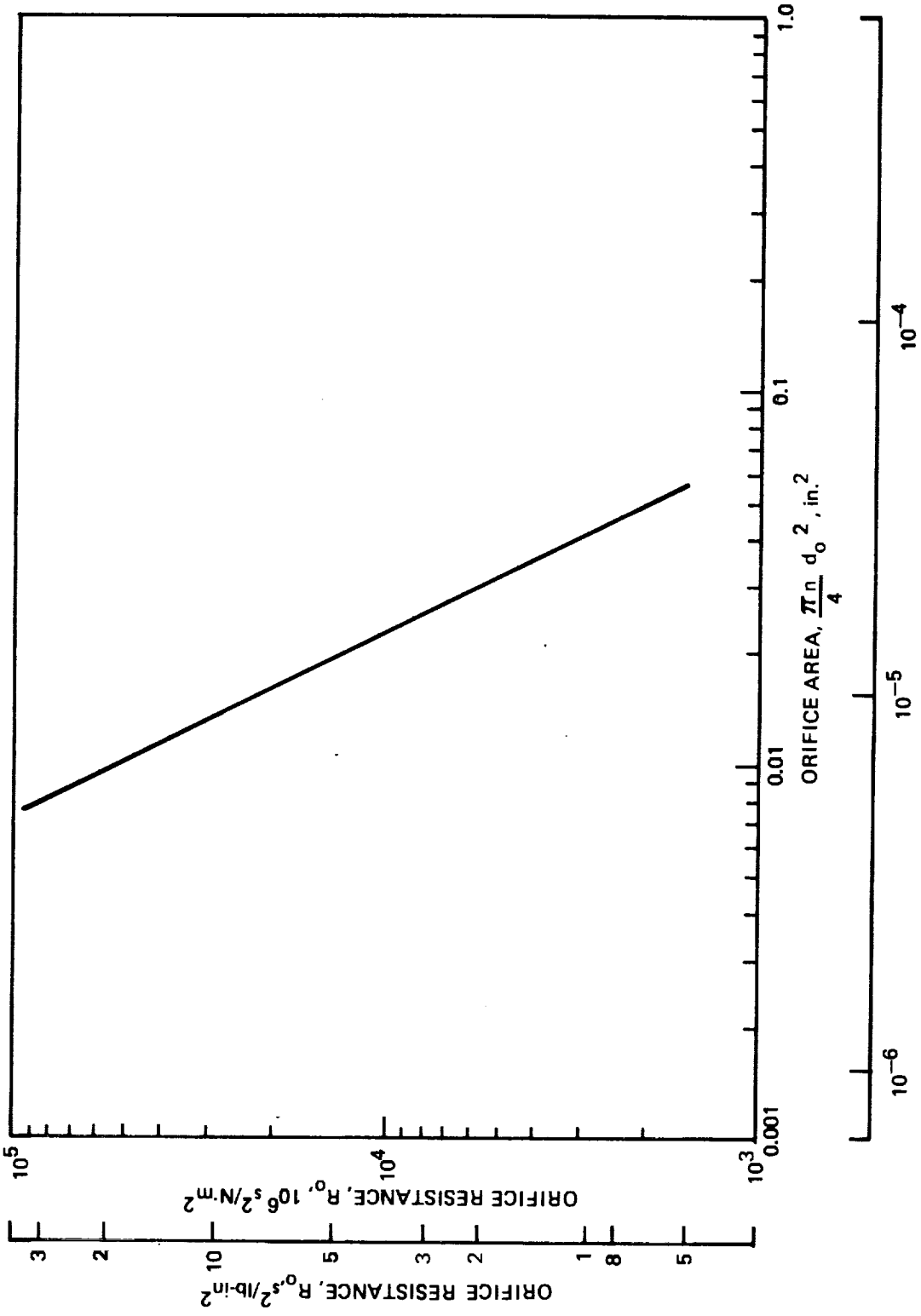

Figure 13. Orifice Resistance

HYDROSTATIC BEARING ANALYSIS

The following assumptions were adopted in the analysis:

1. The density change across the bearing is sufficiently small so that incompressible flow can be assumed.

2. The inertia force is negligible compared to the viscous force except at the film entrance from the recess; at this boundary, fluid is accelerated so fast that the static pressure loss must be considered.

3. Since fluid viscosity is a function of the pressure and temperature, the viscosity of the fluid at the inlet differs from that at the exit. An average value between these two will be used as the effective viscosity.

The type of bearing considered in this analysis is a full 360-degree orifice compensated hydrostatic journal bearing incorporating a number of feeding recesses in the bearing or journal. Fig. 9 presents a description of the geometry of the externally fed bearing shown in a schematic unwrapped view. Recesses are incorporated into the journal surface of the internally fed bearing. Each of the recesses is fed by flow from a high-pressure supply that passes through an orifice restrictor upstream of the recess.

Unusual factors concerning the use of cryogenic working fluids in hydrostatic bearings include the low values of kinematic viscosity coupled with high relative journal/bearing surface speed. As a result, the flow in the bearing film is vigorously turbulent. The level of turbulence is a function of the local velocity field, and the viscosity coefficient factors used as inputs to account for turbulence depend on the pressure distributions which are outputs to be determined. Solution thus requires an iterative procedure, which is incorporated into 'HBEAR'.

The analysis of the internally fed bearings was conducted similarly to that for the externally fed bearings, with stiffness and damping modified searately from the computer program to account for fluid swirl.

PARAMETRIC DESIGN STUDY

A parametric treatment was made of a hydrostatic bearing element (Table 5) by varying inputs individually to determine the effects on stiffness, damping, flow rate, and friction torque.

It was concluded from the parametric study that stiffness and damping are strongly affected by overall pressure ratio, bearing size, and clearance. Recess pressure ratio, controlled by choice of orifice diameter, is the most influential parameter in maximizing stiffness and damping for a given bearing. Other design and operating condition variables exert lesser influences on bearing performance. It is apparent that it is impractical to generate universally applicable nondimensional design charts for hydrostatic bearings owing to the large number of interacting relationships. A prohibitively large number of charts would be required to cover a wide range of variables. However, a relatively few curves can be utilized to characterize bearings that belong to the same category,

e.g., having the same recess configuration or operating under similar Reynold's numbers. A preliminary design can then be selected through interpolation or extrapolation of these charts. Final performance predictions should be refined with the computer code for the selected bearing geometry. Preliminary designs may be selected through use of the nondimensional charts, saving a considerable amount of computer time.

OPTIMUM DAMPING

Parametric treatments were made of the rotordynamic requirements for damping and the effect of bearing geometric features on the magnitude of damping attained.

Rotor Requirements for Damping

The effects of damping were analytically investigated to determine if a generalized relation could be developed between rotor responses and the magnitude of damping at the rotor supports. Simple rotor models were formulated, which had properties typical of rotors in gas turbines and rocket engine turbopumps. Fig. 14 and Table 8. present the rotor model properties. The bearing packages were set up to represent hydrostatic or hybrid bearings. The approach used was:

1. Assign values to the bearing stiffness, and the damping and stiffness of the bearing support

2. Calculate rotor synchronous responses over a range of speeds covering two critical speeds

3. Parametrically vary support stiffness, damping, and bearing stiffness

A unit unbalance was applied at J5 (Fig. 14), first with the bearing packages located at J2 and J4, then at J2 and J5. Parametric values were chosen to evaluate the effect of support stiffness and damping vs bearing stiffness.

The load in bearing No. 2 was chosen as the parameter for comparison among the various cases. With bearing No. 2 located at J4, increasing damping (for given bearing stiffness) decreases the resonant response up to a point. For greater damping the resonant speed is raised and the amplitude is larger than that with lower damping for some cases (Fig. 15).

For the same rotor with bearing No. 2 relocated to J5, increased damping raises response amplitudes in the vicinity of 25,000 rpm. Amplitudes are generally attenuated in the vicinity of 35,000 rpm for increased damping. The loci of peak responses as shown in Fig. 16 can be used to identify optimum damping for a given configuration.

This analysis indicated that there is no general relation governing response and damping for all rotors. It is evident that in some instances increasing damping may lead to a worse condition than previously existed. While there may be no general governing relation, a general approach to define optimum damping is to perform a parametric study such as that described to evaluate damping and stiffness interactions. The values used in the study do not necessarily have to be those for specific geometries of dampers or fluid film bearings but should cover

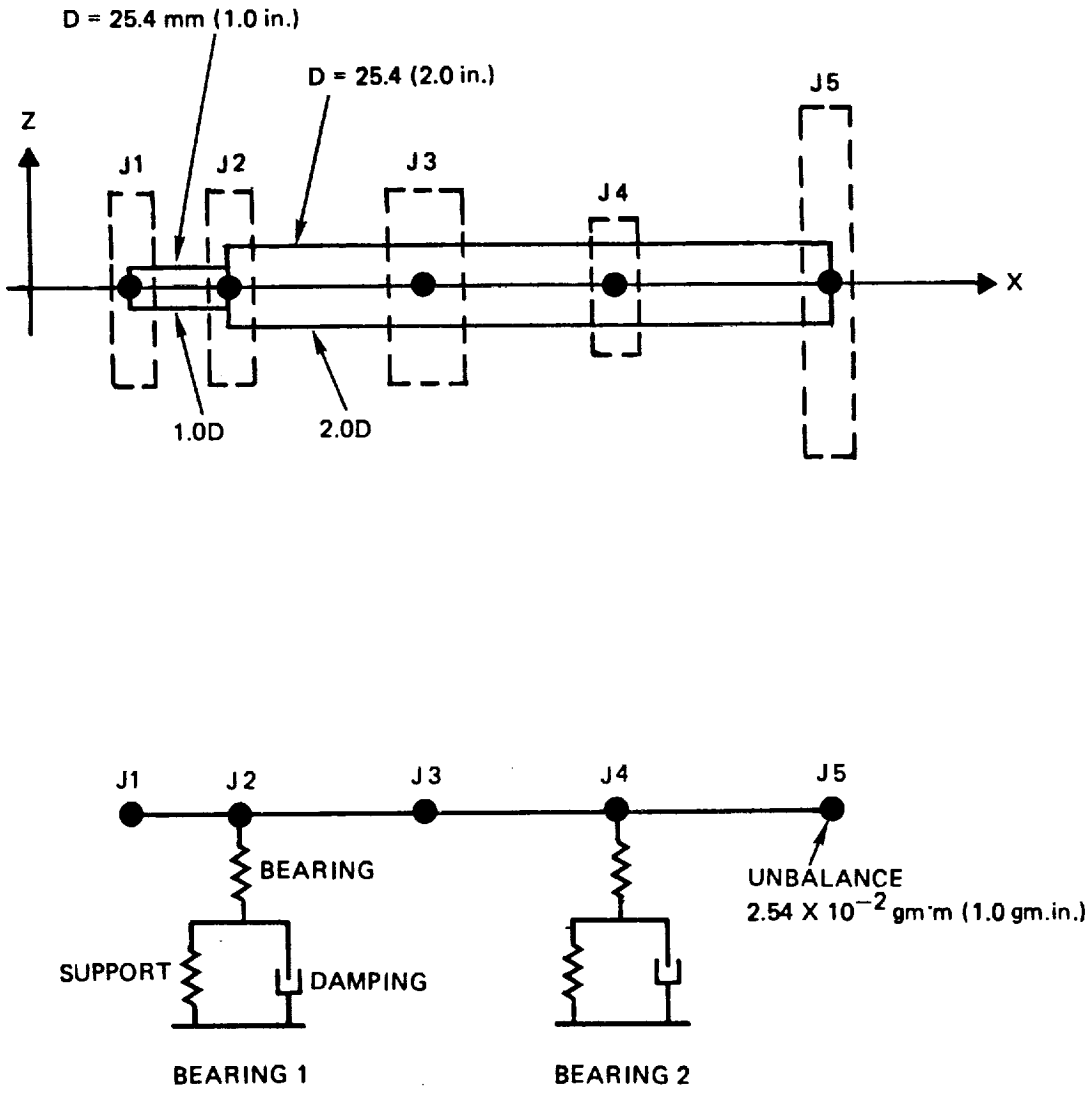

Figure 14. Rotor Models

TABLE 8. ROTOR MODEL PROPERTIES

JT	X	MASS	INERTIA MOMENTS		
			I_D	I_D	$I_D - I_p$
	m	kg	$N \cdot m^2$	$N \cdot m^2$	$N \cdot m^2$
1	0.0635	2.68	0.0278	0.0528	-0.0250
2	0.1270	2.68	0.0278	0.0528	-0.0250
3	0.2540	5.35	0.0640	0.1056	-0.0573
4	0.3810	0.964	0.0039	0.0068	-0.0029
5	0.5080	8.68	0.2820	0.5549	-0.2729
JT	inch	lbm	$lb \cdot in.^2$	$lb-in.^2$	$lb-in.^2$
1	2.5	5.89	9.69	18.41	-8.72
2	5.0	5.89	9.69	18.41	-8.72
3	10.0	11.78	22.33	36.82	-19.99
4	15.0	2.12	1.37	2.39	-1.02
5	20.0	19.10	98.29	193.39	-95.10

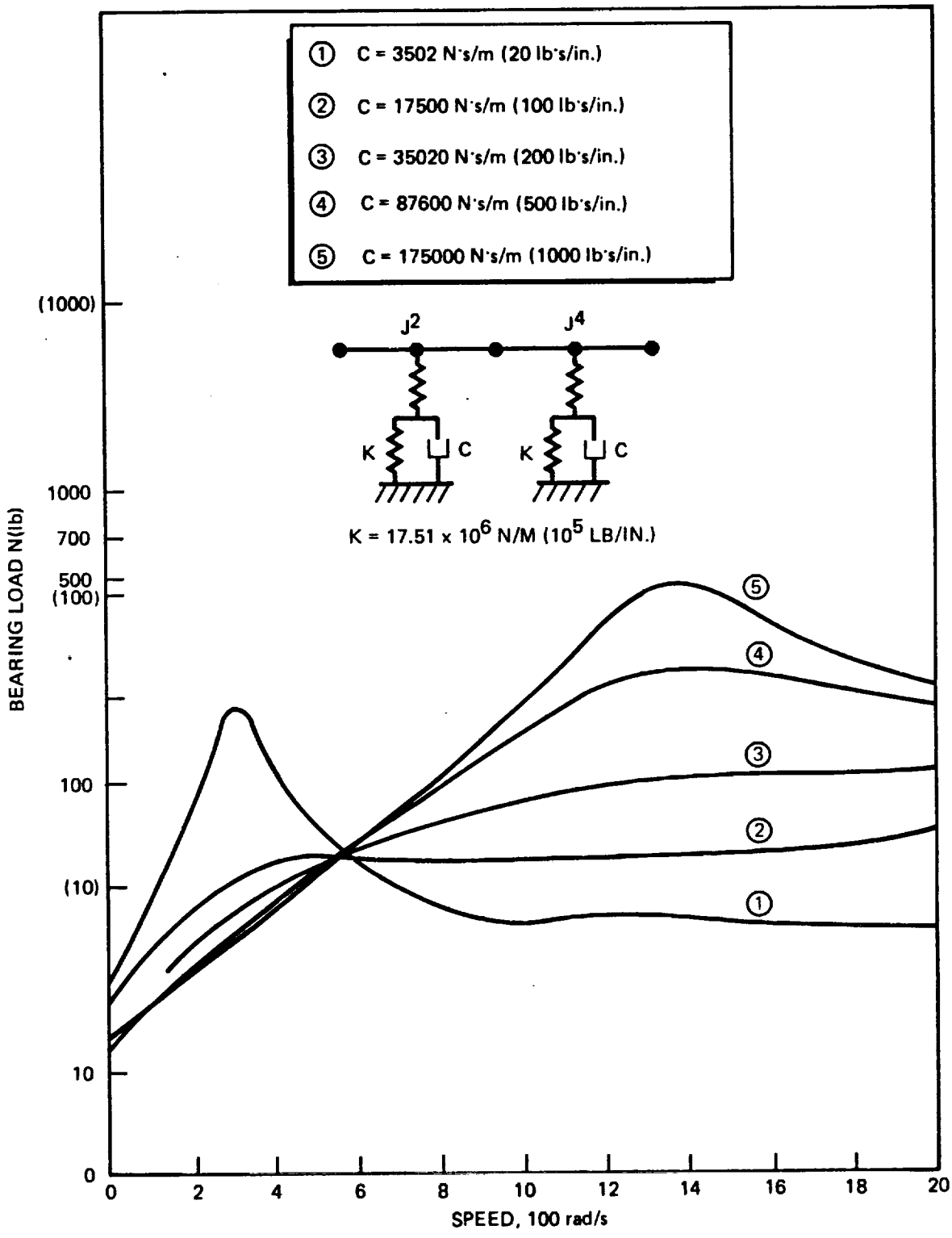

Figure 15. Overhung Rotor Response

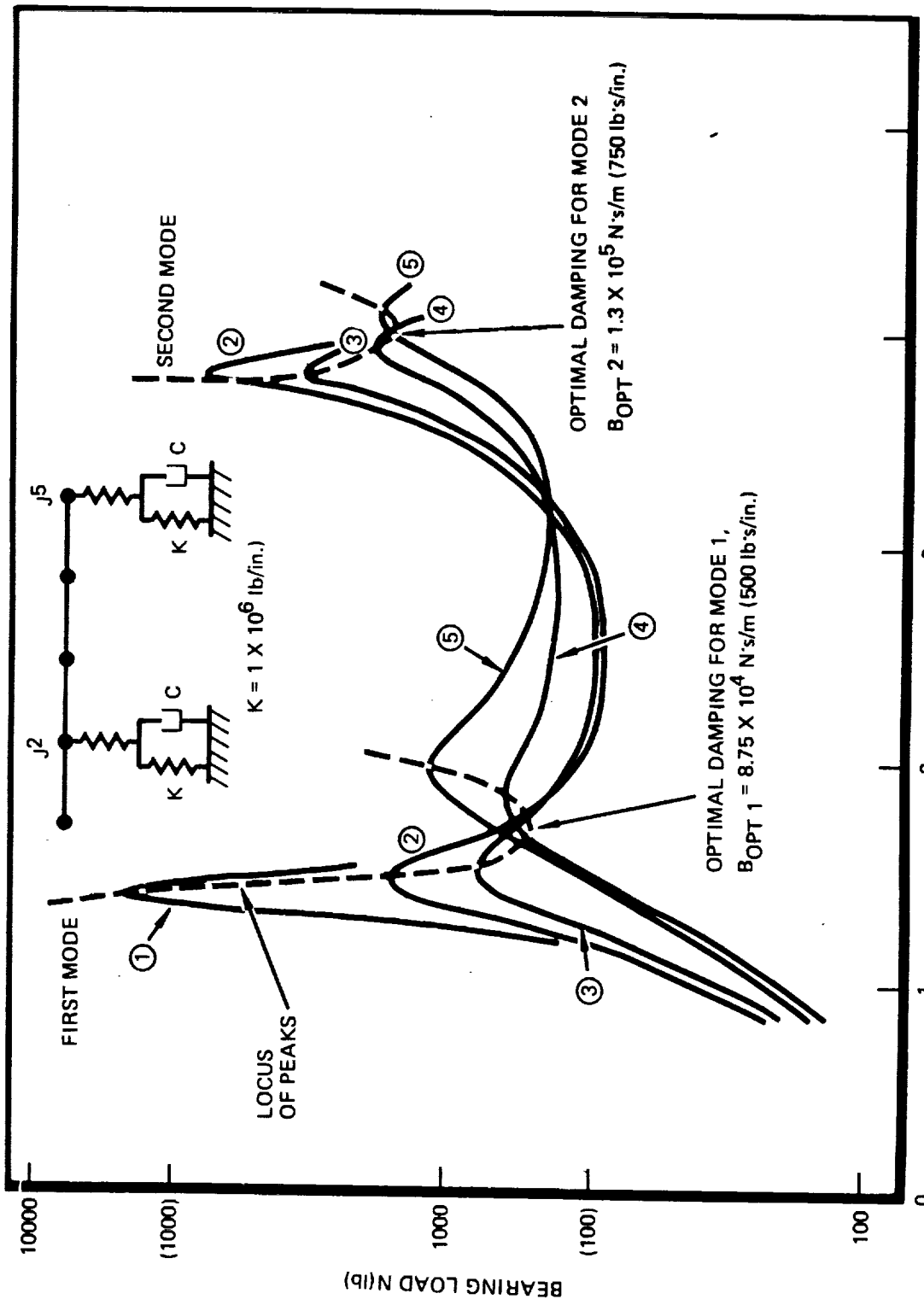

Figure 16. Straddled Rotor Response

(and exceed) the range of expected values. Since the bearing location significantly affects the results, rotordynamic analysis should be conducted concurrently with conceptual machine design.

The forgoing parametric treatment of rotor response included only the effects of damping. A complete rotor/bearing analysis should also include stability studies accounting for the cross-coupled stiffness added by the film bearing.

Bearing Design for Damping

The sensitivity of the magnitude of damping obtained to bearing design variables was assessed analytically by parametrically varying the geometry of a hydrostatic bearing using the design in Table 5 as the baseline. The results are Fig. 17 (LH_2) and 18 (LO_2). The effects of design and operational variables are discussed in the following sections. The term "damping" is used to denote the direct damping coefficient as calculated by the computer program HBEAR (Ref. 12).

Bearing Area. Increasing the projected bearing area, LD, produces a marked increase in damping (Fig. 19). However, the designer may not be free to increase diameter and length due to size restrictions. In addition, the increased frictional heat generated in a larger bearing (Fig. 20), and the reduced tolerance to misalignment must be balanced against the gain in damping from increased bearing area.

Radial Clearance. As shown in Fig. 21 reducing radial clearance will increase damping, however, the control over damping by clearance change alone will be limited in a practical situation because the bearing clearance will, in all probability, be determined by over-riding considerations other than damping, such as:

1. Allowance for centrifugal growth due to speed
2. Margin for tolerances and distortion of the bearing
3. The size of particles contained in the coolant
4. Heat generation rates that increase with decreased clearance
5. Allowances for unknown thermal effects

Journal diameter may be determined by considerations other than damping, such as shaft strength or, in the case of a hybrid bearing, by the rolling element bearing envelope. Varying the journal diameter may require adjustment of radial clearance; significant increases in L/D may result in higher friction losses and lower misalignment tolerance,

Overall Pressure Ratio. Higher supply-to-sump pressure ratio initially results in greater damping. However, when this ratio reaches approximately 5, no significant further increase in damping is achieved (Fig. 22). Pressure dependence of fluid properties was not considered. As shown subsequently, a damping increment results from an increase in fluid density at higher pressures. In a practical sense, the overall pressure ratio is normally a function of the required load capacity or the conditions inherent in the application, and would probably not be chosen to achieve greater damping.

PARAMETER	SYMBOL	RANGE	DAMPING, Bxx, % (0 100 200 300 400 500 600)
BEARING AREA	LD	1.38 TO 7.9 (x 10^{-3} m^2)	
RADIAL CLEARANCE	c	1.02 TO 7.62 (x 10^{-5} m)	
SPEED (OVERALL EFFECT)	N	0 TO 40,000 RPM	
L/D RATIO (LD = 3.39 x $10^{-3}m^2$)	L/D	1.2 TO 1.0	
PRESSURE DROP	(Ps—Pa)	6.90 TO 34.47 (x 10^6 Pa/m^2)	
SUPPLY/AMBIENT PRESSURE RATIO	Ps/Pa	1.5 TO 5.0	
PRESSURE RATIO	$\bar{P}_R$	0.1 TO 0.7	
FLUID DENSITY	ρ	42.77 TO 96.24 kg /m^3	
FLUID VISCOSITY	μ	3.447 TO 24.13 (x 10^{-6} N s/m^2)	
NUMBER OF RECESSES	n	6 TO 20	
ECCENTRICITY RATIO	ϵ	0 TO .9	
RECESS AREA RATIO	A_r	0.05 TO 0.15	
ORIFICE DIAMETER	d_o	8.13 TO 11.43 (x 10^{-4} m)	
SPEED (SOLE EFFECT)	N	0 TO 40,000 RPM	
SURFACE ROUGHNESS RATIO	RR	0 – 0.130	

DAMPING NOMINAL VALUE = 2.68 x 10^4 N s/m

Figure 17. Bearing Geometry Effects on Damping (LH_2)

PARAMETER	SYMBOL	RANGE
BEARING AREA	LD	1.58 TO 7.9 (x 10^{-3} m^2)
RADIAL CLEARANCE	C	1.02 TO 7.62 (x 10^{-5} m)
L/D RATIO (LD = 3.39 x 10^{-3} m^2)	L/D	0.2 TO 1.0
SPEED (OVERALL EFFECT)	N	0 TO 30,000 RPM
PRESSURE RATIO	P_R	0.1 TO 0.8
PRESSURE DROP	(Ps–Pa)	1.379 TO 13.79 (x 10^6 Pa/m^2)
PRESSURE RATIO	Ps/Pa	1.5 TO 6.0
ECCENTRICITY RATIO	ϵ	0.0 TO 0.9
FLUID DENSITY	ρ	8.55 TO 12.83 (x 10^2 kg /m^3)
SPEED (SOLE EFFECT)	N	0 TO 30,000 RPM
FLUID VISCOSITY	μ	4.137 TO 20.68 (x 10^{-5}N-s/m^2)
NUMBER OF RECESSES	n	6 TO 20
RECESS AREA RATIO	A_r	0.05 TO 0.15
ORIFICE DIAMETER	d_o	6.35 TO 17.02 (x 10^{-4}m)
SURFACE ROUGHNESS RATIO	RR	0 TO 0.130

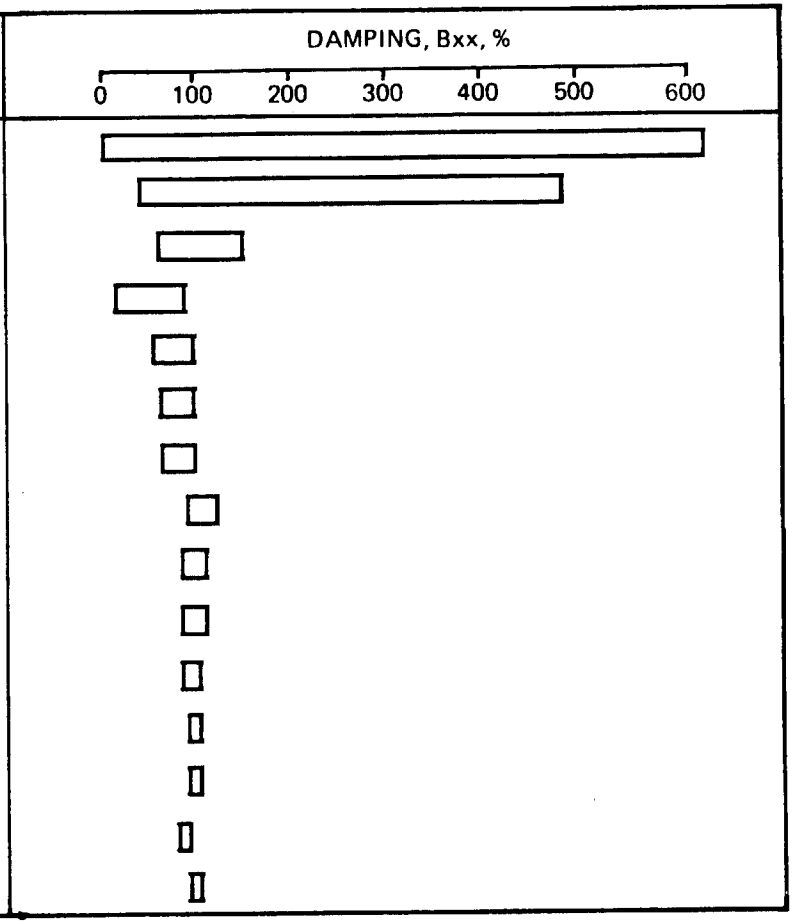

DAMPING NOMINAL VALUE = 1.148 x 10^5 N-s/m

Figure 18. Bearing Geometry Effects on Damping (LO_2)

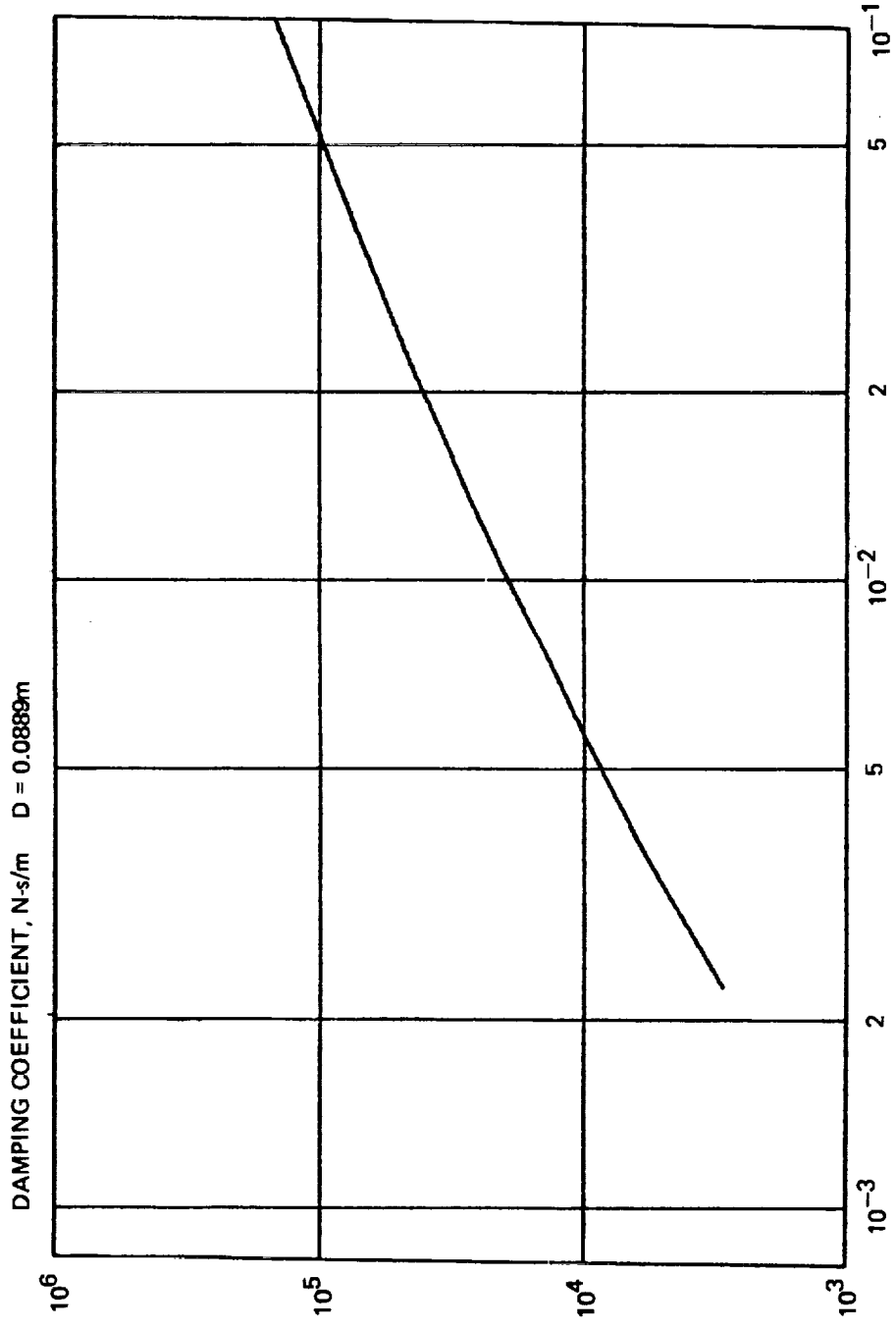

Figure 19. Size Effect on Damping

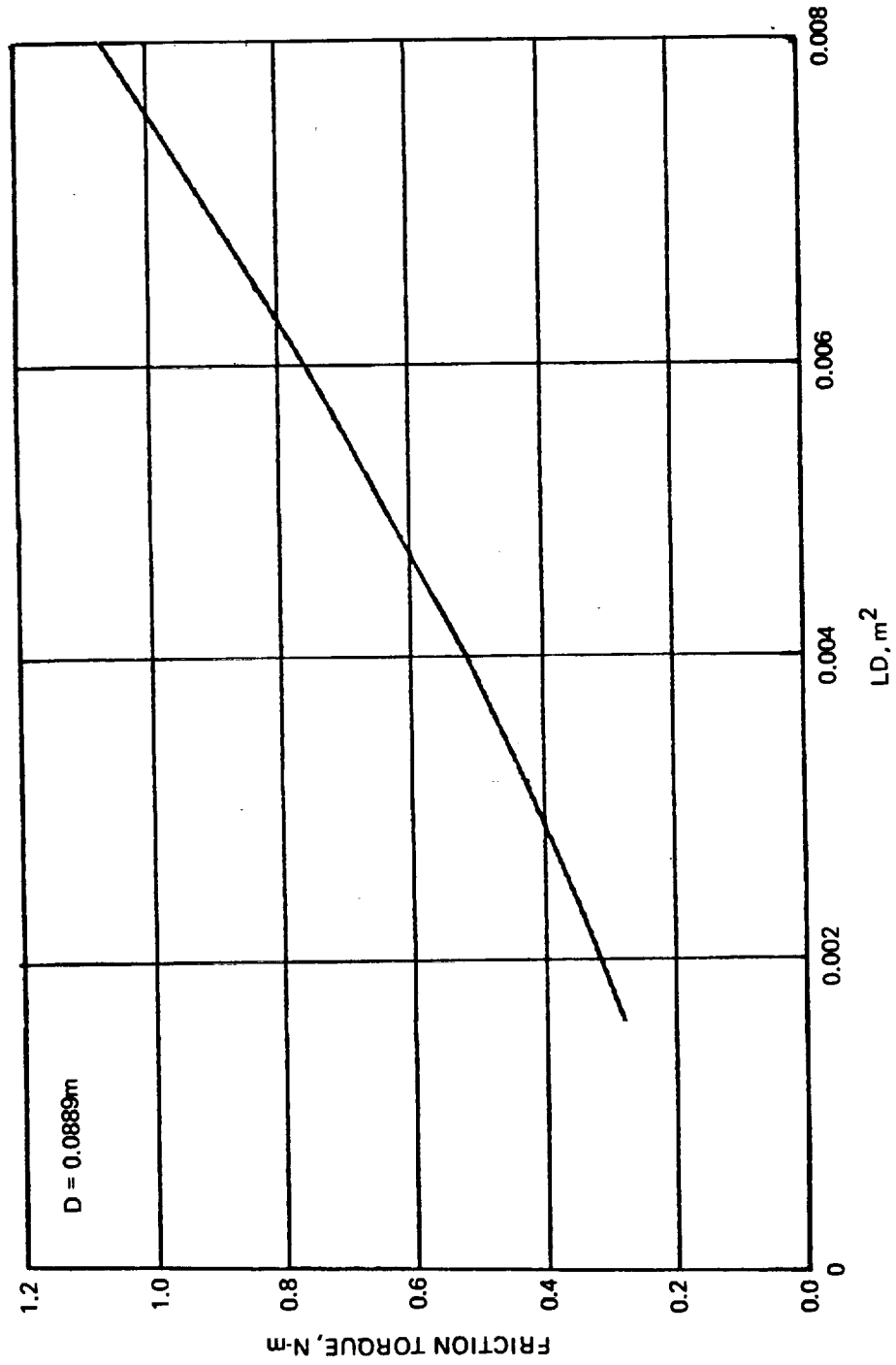

Figure 20. Size Effect on Drag

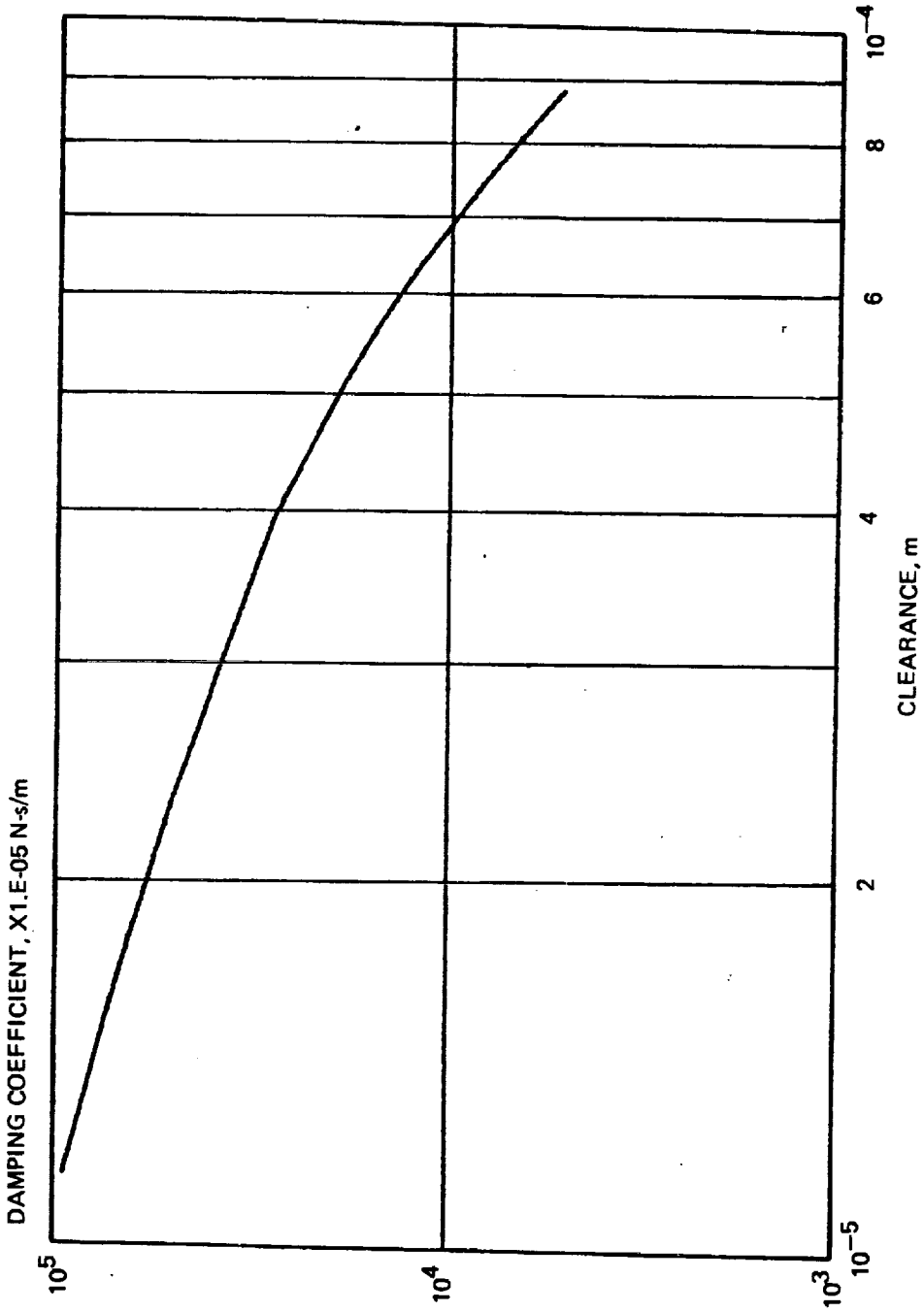

Figure 21. Clearance Effect on Damping

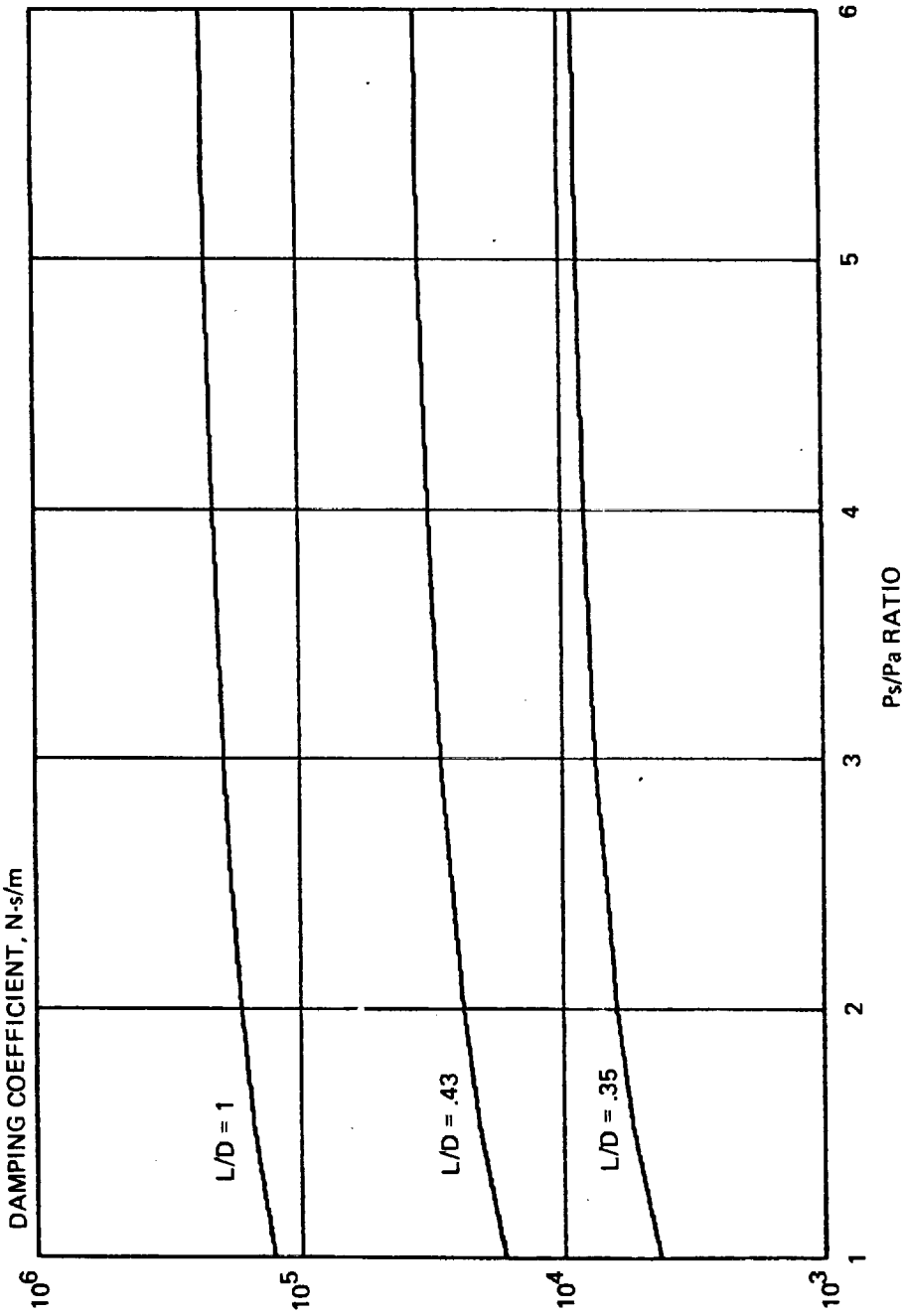

Figure 22. Overall Pressure Ratio Effect on Damping

Recess Pressure Ratio. Damping varies with the recess pressure ratio and attains a maximum at about P_R = 0.5 (Fig. 11), which approximates the condition producing maximum stiffness. The pressure ratio at which maximum damping occurs varies with recess geometry in an inverse relationship with the area ratio (A_r) Fig. 23.

Fluid Properties. Fluid properties influence damping as shown in Fig. 24 and 25 for H_2. In a practical sense, control over these variables is limited. Increasing either the fluid density or viscosity increases damping. Since the density and viscosity of H_2 (and to a lesser extent, of O_2), are affected by pressure as well as temperature, damping is increased by higher pressure or lower temperature. Therefore, variables that decrease friction in the bearing will increase damping.

Recess Configuration. A 10 to 15% range of variation in damping can be obtained by manipulating the recess configuration. A minor amount of control over damping can be obtained by varying the number of recesses as seen in Fig. 26. For larger numbers of recesses, some control is obtained by selection of area ratio (Fig. 23). A value of approximately 0.07 will result in maximum damping. There is no apparent correlation between the individual recess dimensions (i.e., x. y) and damping. An increase in the product x. y, which is the area ratio (A_r), decreases damping by reducing the proportion of bearing area with minimum clearance.

Excitation Frequency. For a bearing with fixed dimensions and operating conditions, the squeeze parameter is analogous to the excitation frequency of external vibration. For the bearing described in Table 5, Fig. 27 shows the sudden drop-off in damping when the squeeze parameter value exceeds 0.05, while there is practically no change in damping if the squeeze parameter is kept below 0.02. This infers that there exists a maximum allowable vibration frequency for which a bearing will maintain its inherent damping and stability properties. An additional aspect of the squeeze parameter is the critical mass, which is the largest mass that the bearing can support at the operating conditions, without the occurrence of half-frequency whirl. Figure 28 shows how the critical mass is affected by the squeeze parameter. It can be seen from Fig. 28 that the critical mass drops sharply when the squeeze parameter is 0.15, and is practically zero when it is 0.21.

Cross-Coupling Stiffness

If the design features incorporated to increase damping also increase the cross-coupling stiffness, rotor stability may be adversely affected.

A parametric approach was taken to identify the influence of hydrostatic bearing geometry on cross-coupling stiffness of the externally fed LH_2 hydrostatic bearing of Table 5. The results show that radial clearance affects the coefficients the most strongly of those features varied (Fig. 29), followed by speed. Other geometric variables exerted only limited effects. Bearing area (LD) has the most influence on cross-coupling stiffness for a bearing of the same size with LO_2 as the working fluid (Fig. 30).

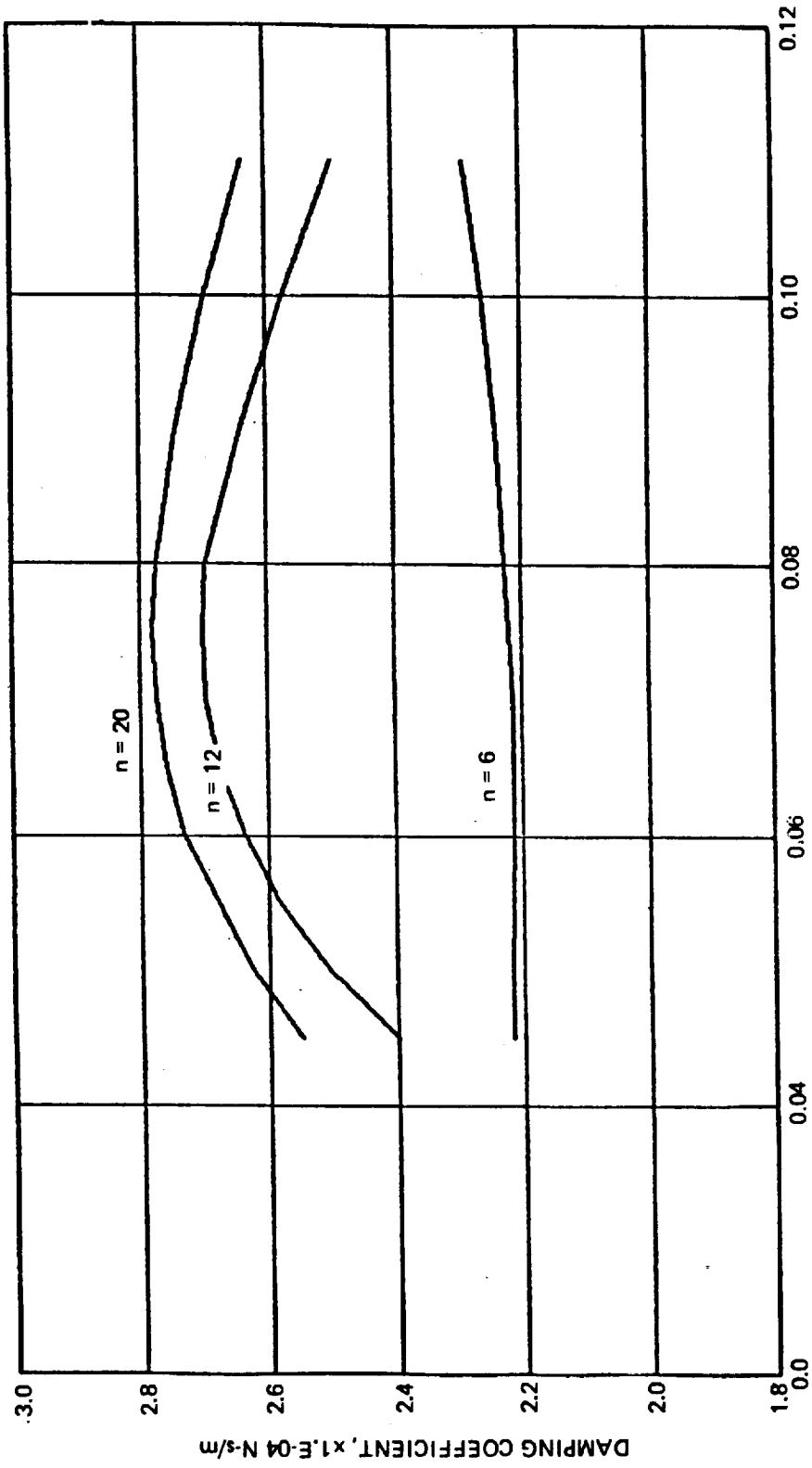

Figure 23. Area Ratio Effect on Damping

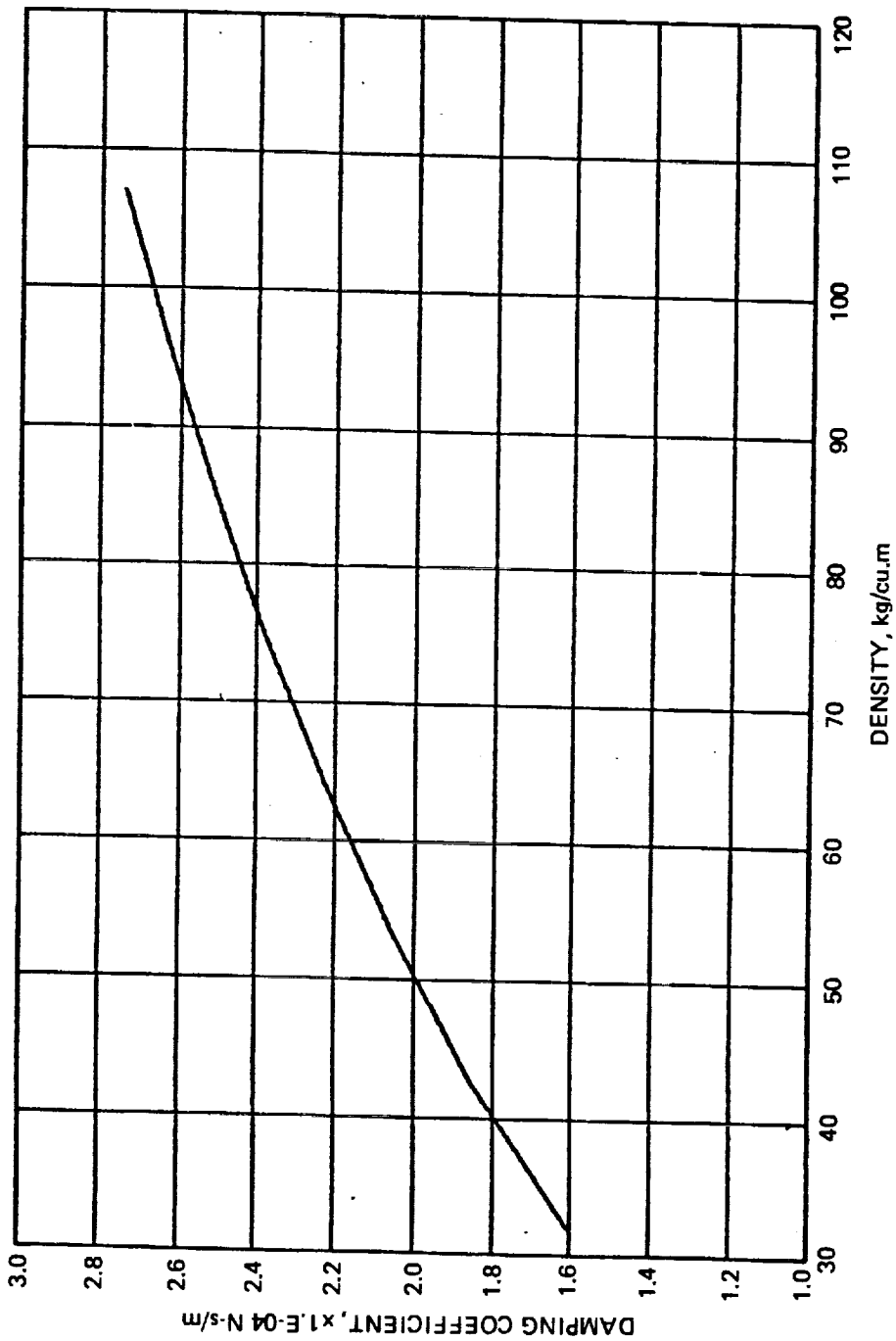

Figure 24. Density Effect on Damping

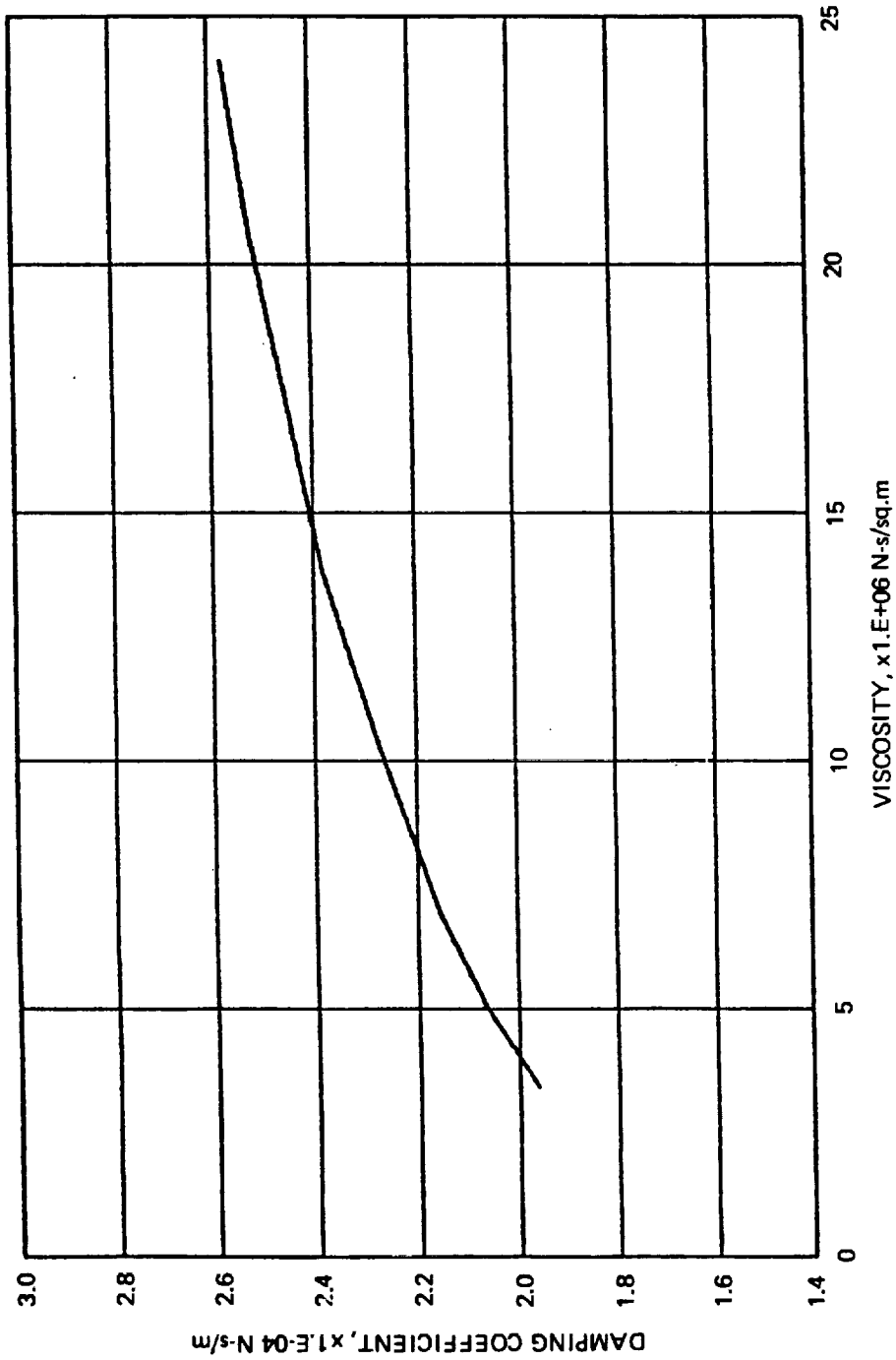

Figure 25. Viscosity Effect on Damping

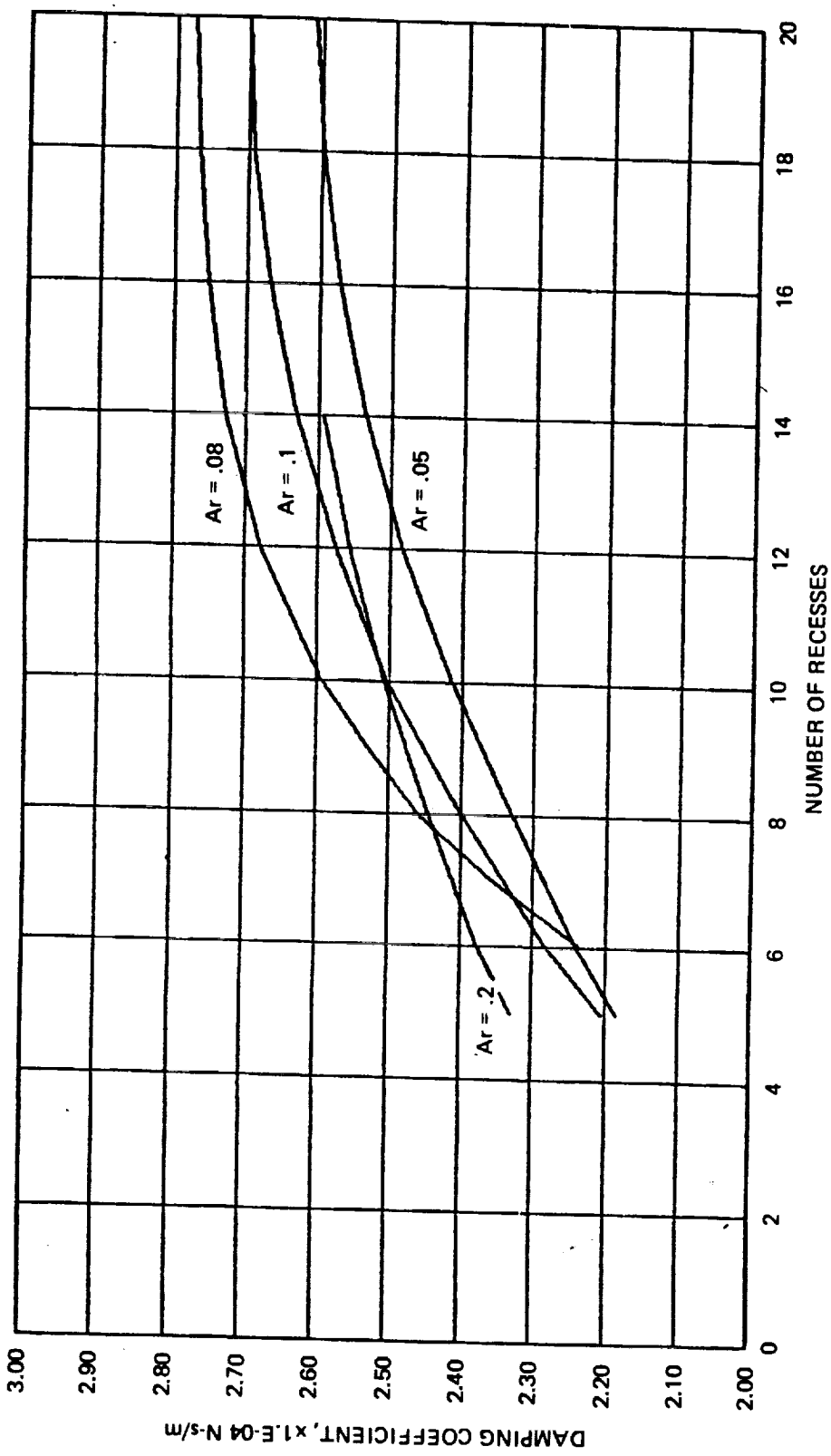

Figure 26. Number of Recesses - Effect on Damping

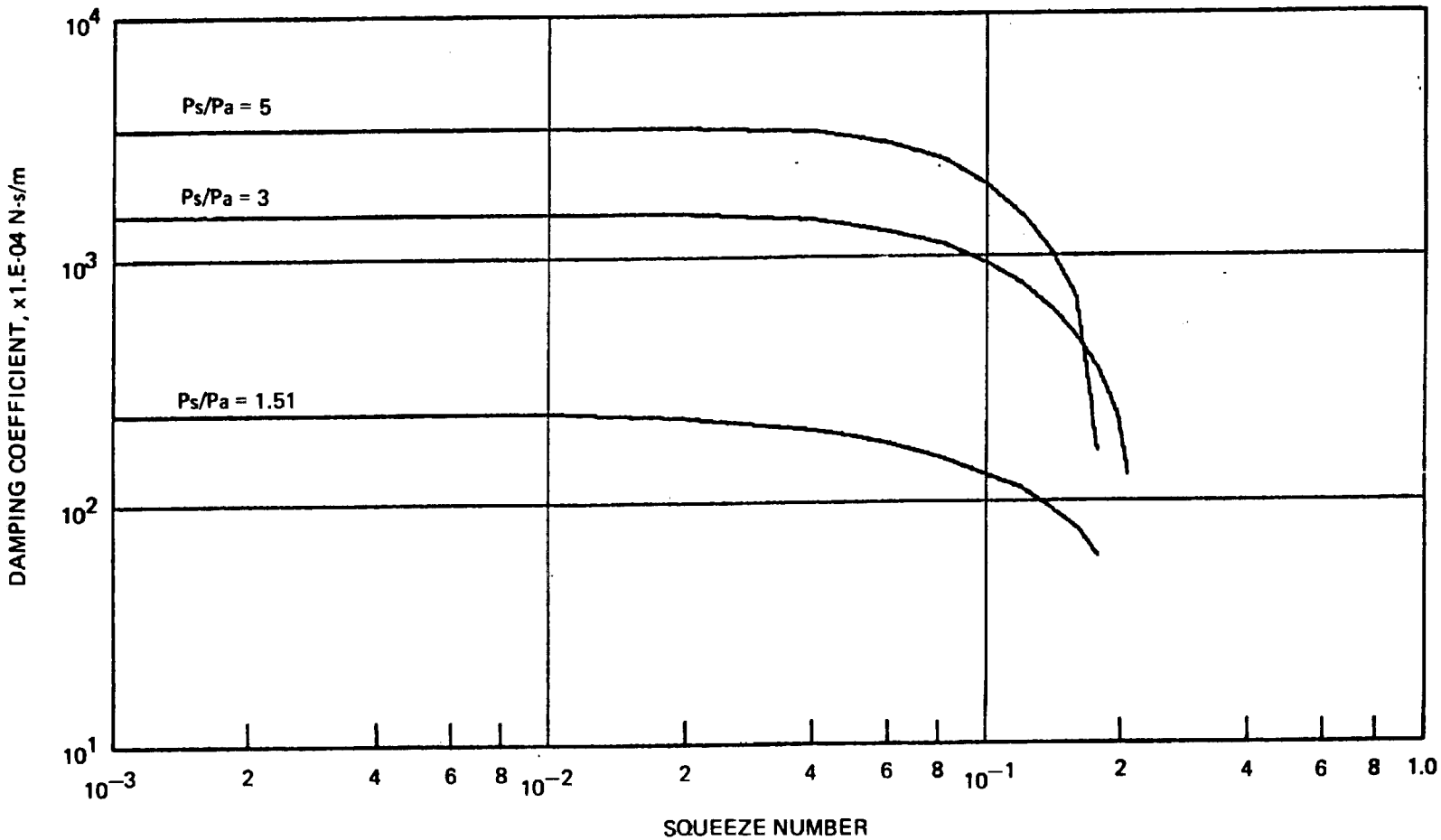

Figure 27. Squeeze Parameter Effect on Damping

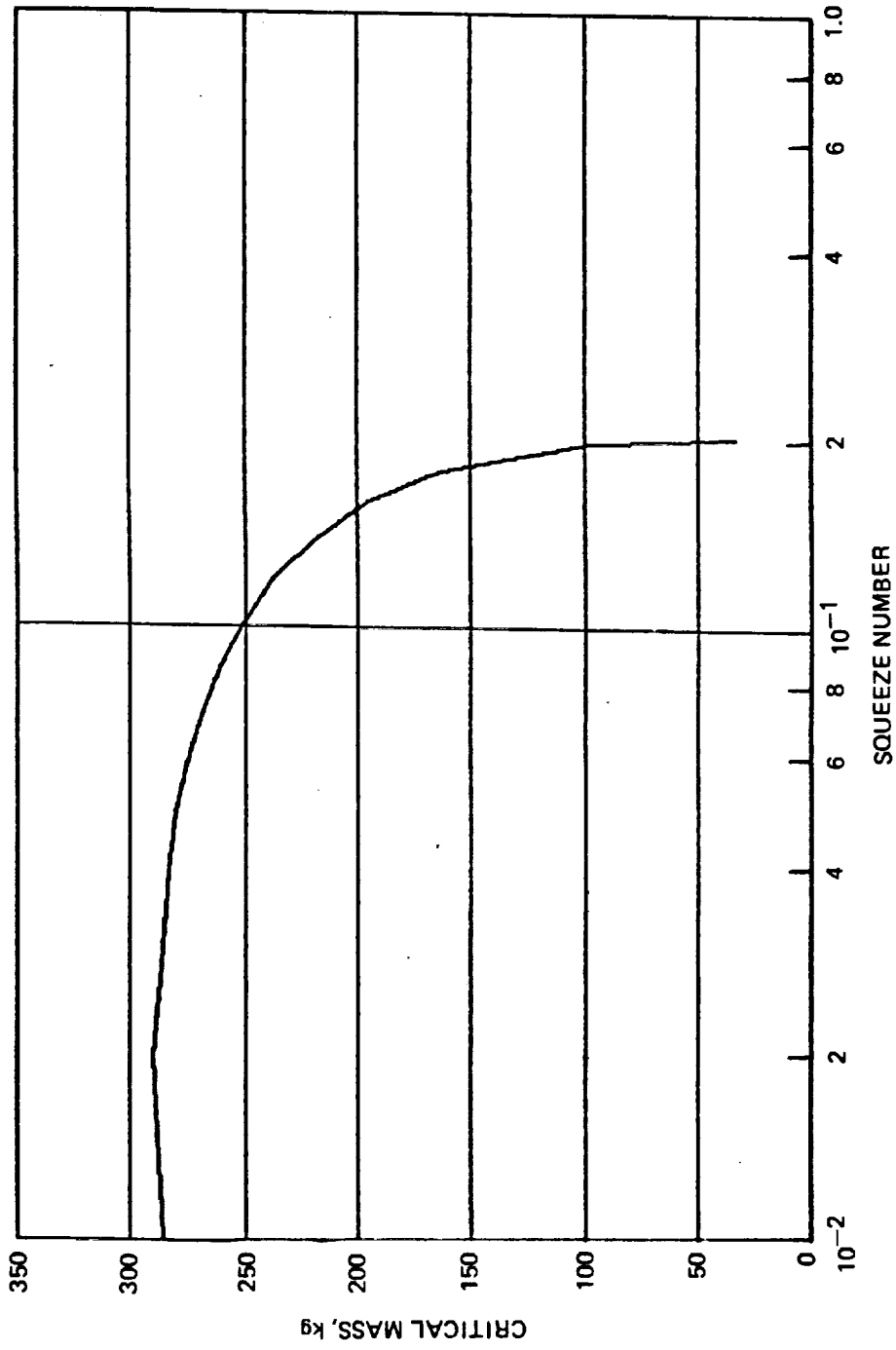

Figure 28. Squeeze Parameter Effect on Critical Mass

PARAMETER	SYMBOL	RANGE
RADIAL CLEARANCE	c	1.016×10^{-5} TO 7.62×10^{-5} m
SPEED (OVERALL EFFECT)	N	0 TO 4188.8 rad/s
SPEED (SOLE EFFECT)	N	0 TO 4188.8 rad/s
PRESSURE DROP	Ps–Pa	6.895×10^{6} TO 3.447×10^{7} N/m^2
L/D RATIO (LD = 3.35×10^{-3} m^2)	L/D	0.2 TO 1.0
BEARING AREA	LD	1.39×10^{-3} TO 7.9×10^{-9} m^2
SUPPLY/AMBIENT PRESSURE RATIO	Ps/Pa	1.5 TO 5.0
NUMBER OF RECESS	n	6 TO 20
FLUID DENSITY	ρ	42.77 TO 96.24 kg/m^3
ECCENTRICITY RATIO	ϵ	0 TO 0.9
FLUID VISCOSITY	μ	3.447×10^{-6} TO 2.413×10^{-5} N·s/m^2
ORIFICE DIAMETER	d_o	8.128×10^{-4} TO 1.143×10^{-3} m
RECESS AREA RATIO	Ar	0.05 TO 1.5

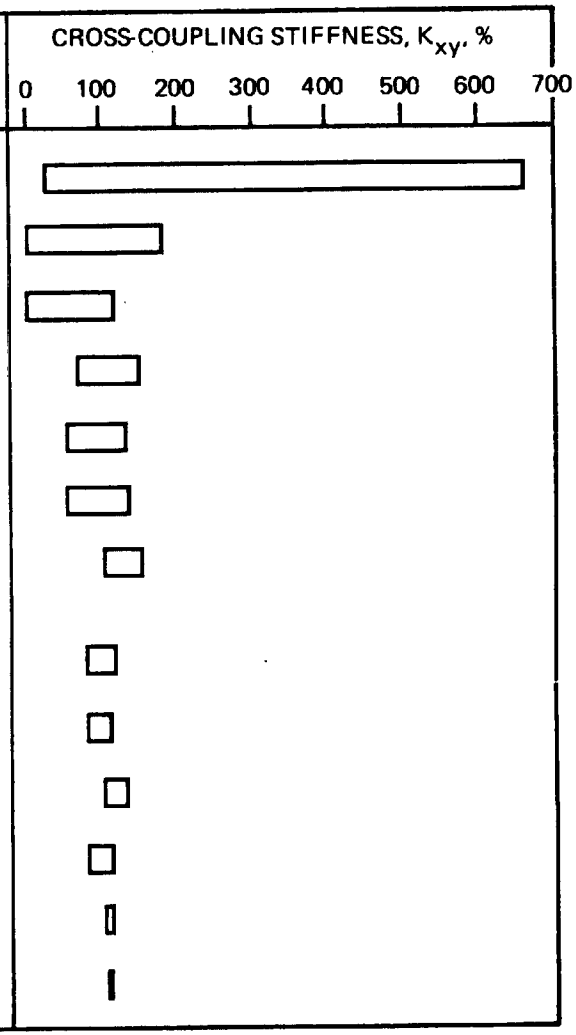

X–Cplg NOMINAL VALUE = 4.553×10^{7} N/m

Figure 29. Cross-Coupled Stiffness - Effects of Bearing Geometry (LH_2)

PARAMETER	SYMBOL	RANGE
BEARING AREA	LD	3.05×10^{-4} TO 8.78×10^{-5} m^2
RADIAL CLEARANCE	c	1.11×10^{-5} TO 8.89×10^{-5} m
SPEED (OVERALL EFFECT)	N	0 TO 418.9 rad/s
ECCENTRICITY RATIO	ϵ	0 TO 0.09
SPEED (SOLE EFFECT)	N	0 TO 418.9 rad/s
L/D RATIO (LD = $3.35 \times 10^{-3} m^2$)	L/D	0.2 TO 1.0
PRESSURE DROP (Ps–Pa)	Ps–Pa	1.4×10^6 TO 1.4×10^7 Pa
ORIFICE DIAMETER	d_o	9.07×10^{-4} TO 1.59×10^{-3} m
FLUID DENSITY	ρ	994.5 TO 1090.8 kg/m^3
NUMBER OF RECESSES	n	6 TO 20
RECESS AREA RATIO	Ar	0.05 TO 0.2
SUPPLY/AMBIENT PRESSURE RATIO	Ps/Pa	1.5 TO 6.0
FLUID VISCOSITY	μ	4.14×10^{-5} TO 1.24×10^{-4} $N \cdot s/m^2$

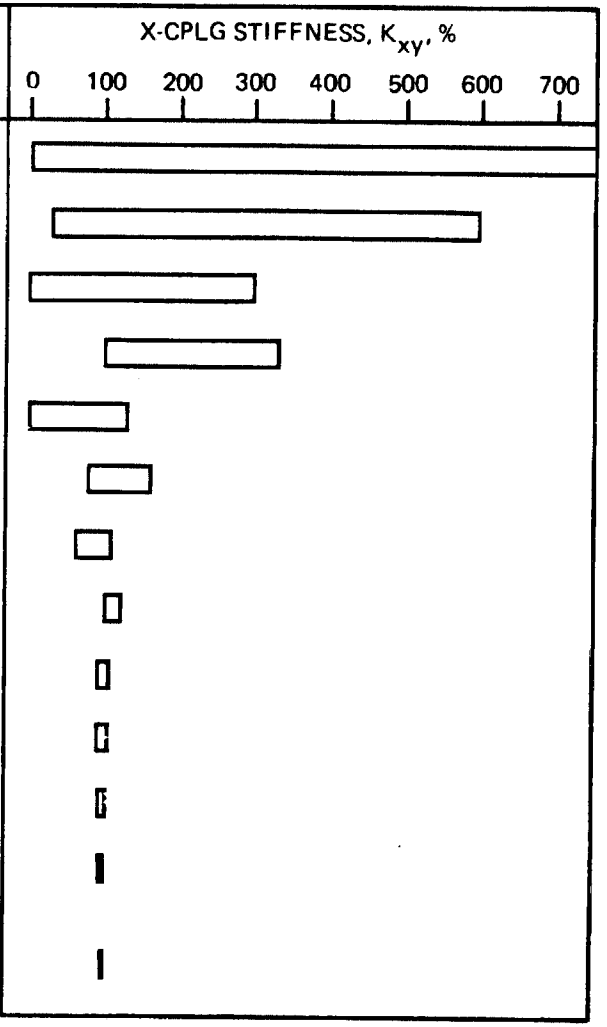

D = 88.9 mm

X-CPLG NOMINAL VALUE = 1.42×10^8 N/m

Figure 30. Cross-Coupling Stiffness - Effects of Bearing Geometry (LO_2)

Internally Fed Bearing Coefficients

In the internally fed bearing, additional cross-coupling is expected to arise due to the tangential velocity imparted to the fluid because the recesses are located in the journal surface. Modifying factors to compensate for this tangential velocity were calculated based on the predicted effects of fluid swirl and surface roughness.

Fluid swirl. The stiffness and damping coefficients of the internally fed bearing were modified to account for the tangential fluid velocity based on Childs' derivation of dynamic coefficients for annular seals with turbulent flow and inlet swirl (Ref. 17). Cross-coupling stiffness and damping are increased while direct stiffness declines slightly with speed (Fig. 31) when whirl effects are included.

Surface Roughness. Roughening one or both of the bearing surfaces has been shown to affect the damping and cross-coupling obtained in annular seals (Ref. 18, 19, 20). Analytic methods devised for seals were used to predict the effects of surface roughness in hydrostatic bearings. The result obtained depends upon whether the rough surface is on the stationary or the moving element. For example, increased roughness of the stator surface is expected to increase damping (Fig. 32). However, increasing the rotor surface roughness induces more fluid tangential velocity and is expected to increase the cross-coupling stiffness (Fig. 33).

The internally fed bearing is considered to be represented by an extreme degree of rotor surface roughening, since the recess depth is much greater than the radial clearance.

Coefficient Modification. Modifications were made to the coefficients predicted by the program HBEAR (Ref. 12) for a recessed hydrostatic bearing by applying a factor for fluid swirl over the entire surface and for journal roughness over the proportion of the bearing area swept by the recesses. The coefficients listed in Table 7 for the internally fed bearings have been modified. Results of testing the PLIN hydrostatic bearing with Freon indicate that there is a significant reduction in the value of coefficients compared with the unmodified predictions of HBEAR.

Material Selection

The materials of the hydrostatic elements of the experimental hybrid bearings are listed below:

	LH_2		LO_2	
CONFIGURATION	BEARING (STATIONARY)	JOURNAL (ROTATING)	JOURNAL ROTATING	BEARING STATIONARY
PLEX	Cr/718	718		
PLIN			Cr/718	Ag/718
PSIN			Cr/718	Ag/718

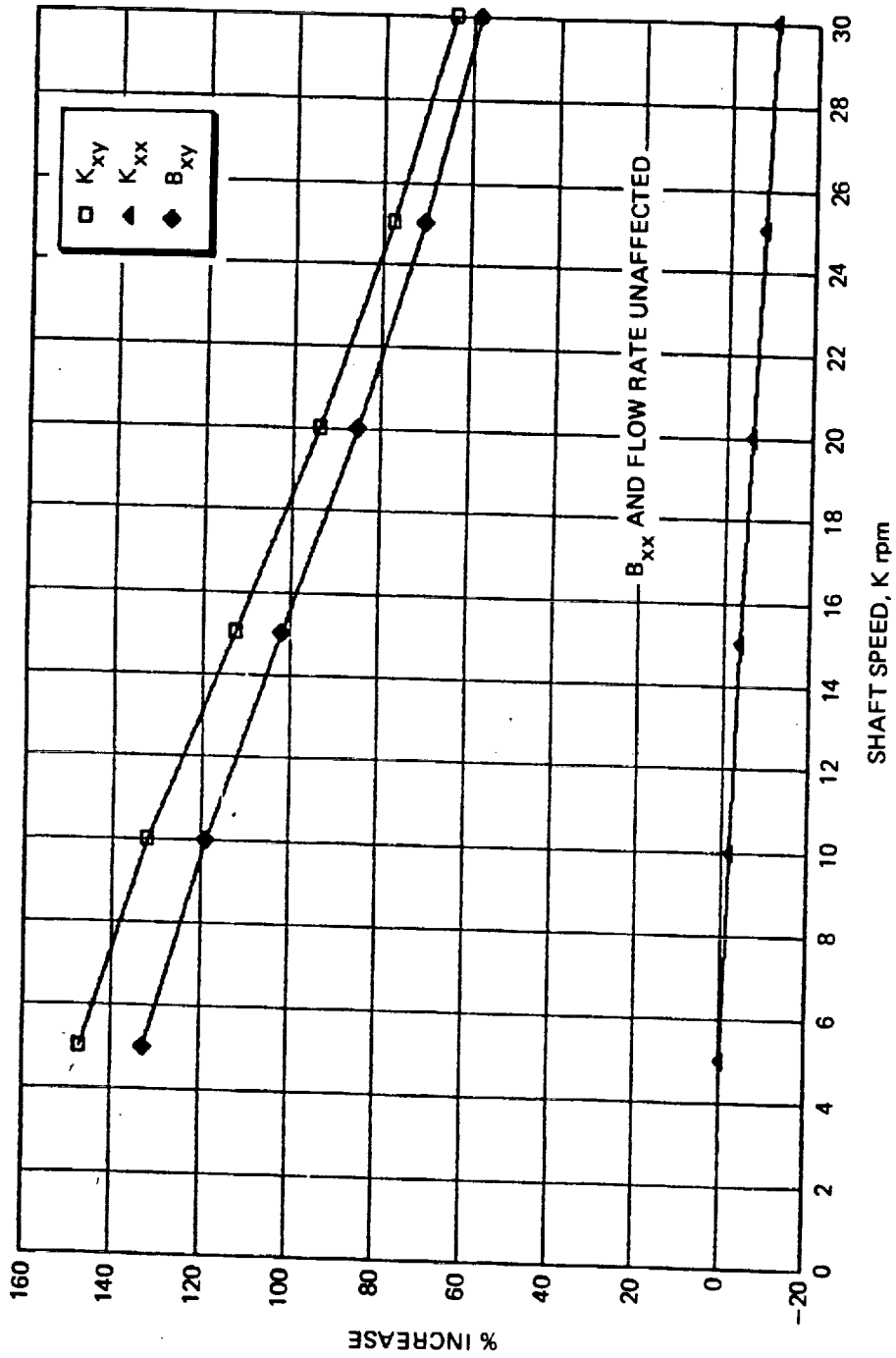

Figure 31. Fluid Swirl Effects

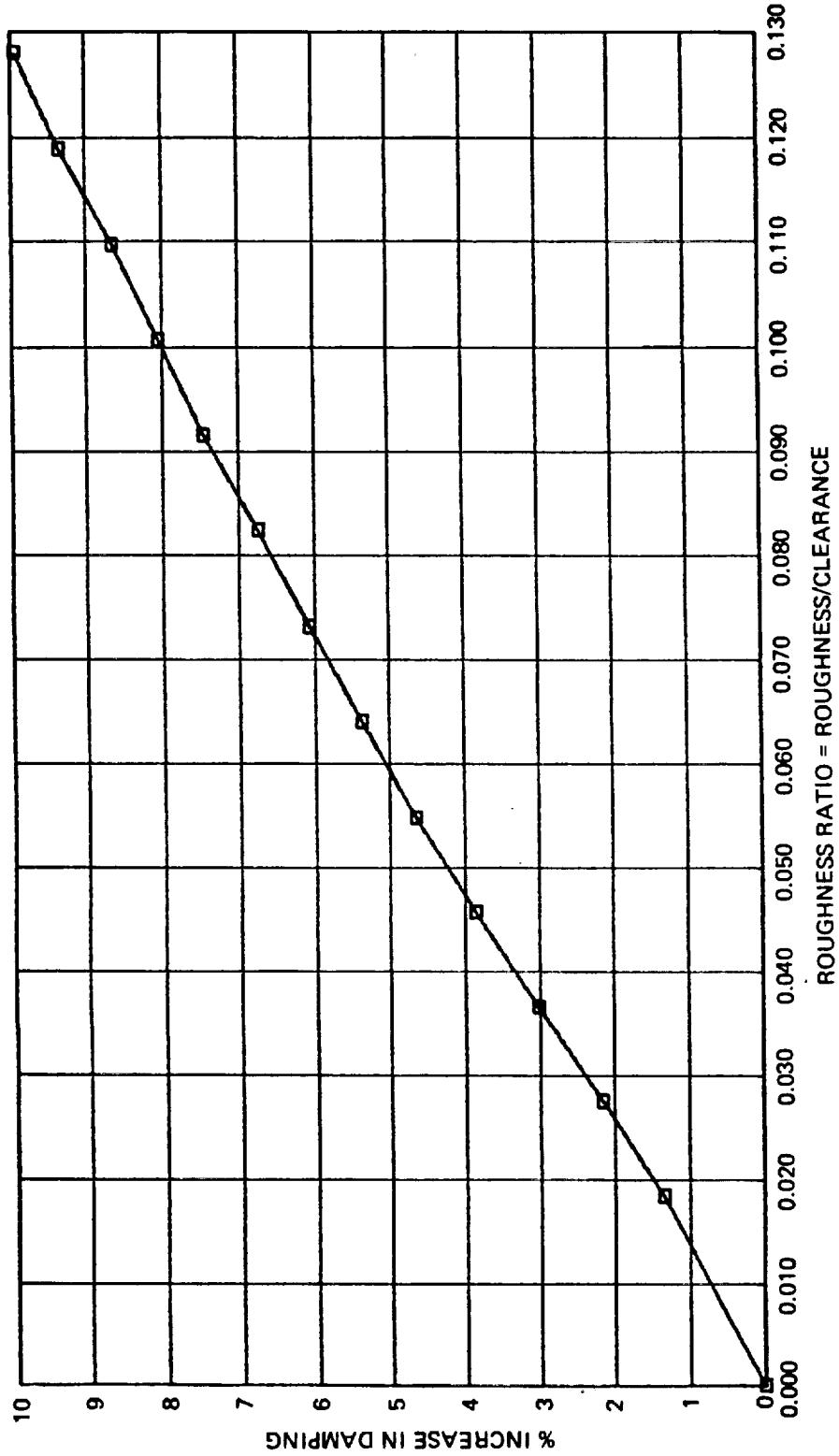

Figure 32. Surface Roughness Effects on Damping

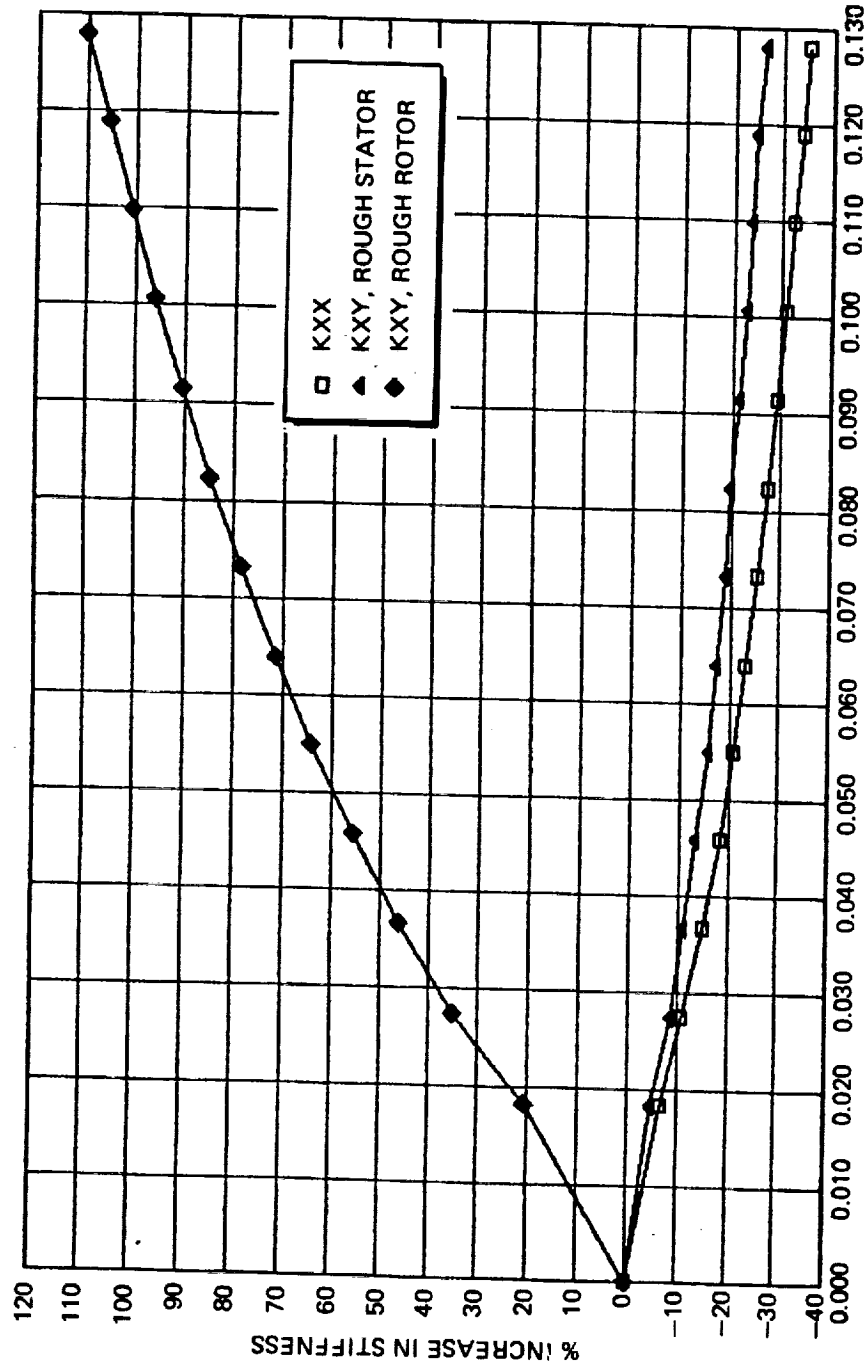

Figure 33. Surface Roughness Effects on Stiffness

The hydrostatic test bearing materials were selected for good performance in the following categories

1. Chemical compatibility with H_2 and O_2
2. Tensile strength - 90 Ksi minimum for journals
3. Adhesion of coatings and platings under thermal and mechanical shock
4. Corrosion resistance in moist air
5. Wear resistance
6. Thermal expansion/contraction compatibility with mating part
7. Producibility

LH_2 Bearing. Alloy 718 was used throughout for thermal uniformity, chemical compatibility, and strength. Thin dense chromium plating was used to enhance the wear resistance of the ball bearing mounting surface, and was extended through the hydrostatic bearing bore. Thin dense chromium plating was used not only for its wear resistance but also because no postplating machining is required, an important consideration for the recesses and orifices of the hydrostatic bearing. The journal was not plated, as rubbing contact is avoided with the parallel load design.

LO_2 Bearings. Alloy 718 was used for all hydrostatic bearing components for thermal and chemical compatibility and strength. The bearing inner diameters were silver plated, while the journal surfaces were chromium plated. Thin dense chromium was used for the parallel load bearing journal to avoid masking of or postplating machining the recess and orifices. In the parallel speed bearing, chromium was electroplated and ground to a finished thickness of 1.143×10^{-2} to 1.905×10^{-2} mm (0.00045 to 0.00075 in.). The silver was used primarily for resistance to ignition in the event of rubbing contact in the presence of LO_2.

Structural Analysis

Deflections caused by pressures and centrifugal forces were calculated using finite element analysis. The PSEX hydrostatic bearing was the most sensitive to the operating conditions due to its relatively large diameter of 88 mm (3.5 in.) and the high pressure of operation. Table 9 lists the deflections and the resulting clearances determined for a ΔP of 13.8 MPa (2000 psi) and 3832 rad/s (36,600 rpm). For all the bearing designs, the clearance at operation was selected from the optimized design procedure and corrections applied for speed and pressure to arrive at the drawing dimensions. The ball bearing mounting surfaces were the only dimensions requiring compensation for thermal differential contraction, since all hydrostatic bearing and tester components were constructed of Alloy 718.

TABLE 9. HYDROSTATIC BEARING OPERATIONS DEFLECTIONS

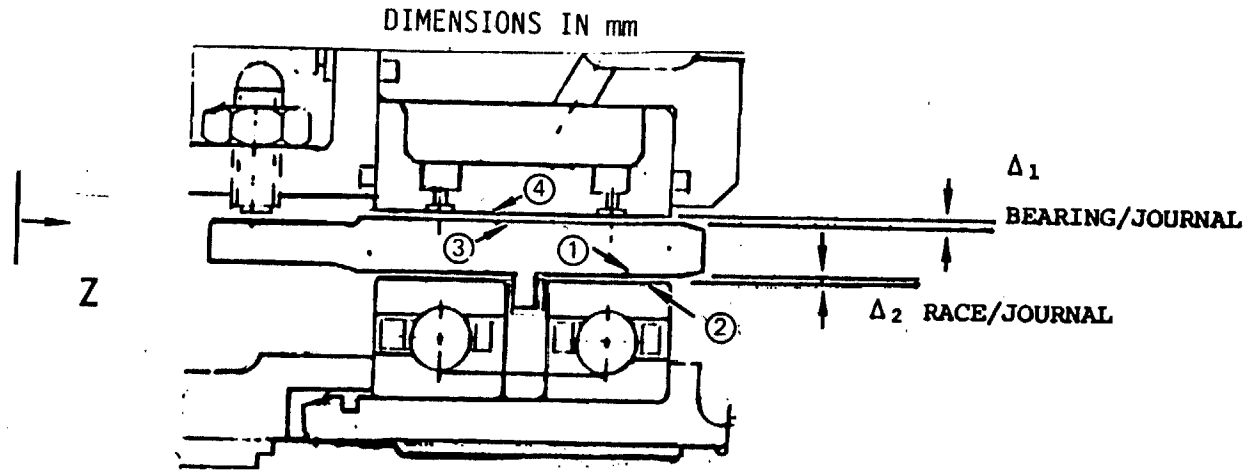

Z	45.11040	49.63160	56.41340	60.90920	67.69100	72.18680	81.20380	85.54720
δ_1	0.04318	0.04318	0.04318	0.04318	0.04318	0.04293	0.04267	0.04242
δ_2	0.03048	0.03048	0.03048	0.03048	0.03048	0.03048	0.03048	0.03048
δ_3	0.04242	0.04115	0.04089	0.04089	0.04089	0.04089	0.04064	0.04013
δ_4	-0.00025	-0.00254	-0.00660	-0.00787	-0.00889	-0.00711	-0.00356	-0.00229
Δ_1	-0.04267	-0.04369	-0.04750	-0.04877	-0.04978	-0.04801	-0.04420	-0.04242
Δ_2	0.01270	0.01270	0.01270	0.01270	0.01270	0.01245	0.01219	0.01194

FABRICATION

MATERIALS

All test bearings and the interfacing tester parts were constructed of nickel-base alloy (ALLOY 718). The large parts, including the bearings, were machined from forgings.

HEAT TREATMENT

Prior to final machining, all parts were solution heat treated and aged to stabilize dimensions and improve stength and hardness. The solution heat treatment consisted of 10 to 30 min at 1297 to 1339 K, followed by aging at 1033 K for 10 h then furnace cooled at 922 K for a total aging time of 20 h.

MACHINING

Conventional turning and milling were used to produce most dimensions, with grinding required for diameters with small tolerances. The recesses were produced by EDM (electrodischarge machining) with the exception of the recesses on the PSIN bearing journal, which were ground. The PSIN orifices were incorporated into inserts that were electron beam welded into the journal. This procedure was used to assure that the orifice entrances were free of burrs that could cause uneven flow division among the recesses.

PLATING

Thin dense chrome plating was applied to the bore of the PLEX bearing, and the outer diameter of the PLIN journal. No machining was done to these surfaces after plating. Thick (0.051 mm) electroplated chrome was applied to the journal of the PSIN journal, with the final diameter produced by grinding after plating. Thick (0.051 mm after final machining) silver was applied to the bores of the internally fed bearings.

TESTING

Parallel load hybrid bearings and their hydrostatic elements were tested to validate the design concepts and also to provide empirical data with which to anchor or modify the assumptions and analytic methods employed in the design of hydrostatic bearings. A summary of the testing is contained in the following table.

HYDROSTATIC BEARING TESTING

TEST CATEGORY	WORKING FLUID	TEST OBJECTIVE	RESULTS, REFERENCED TO THEORETICAL PREDICTION
• DYNAMIC CHARACTERISTICS	LH_2	MEASURE STIFFNESS AND DAMPING	INCONCLUSIVE
• EXTERNALLY FED BEARING	FREON	MEASURE STIFFNESS AND DAMPING	DIRECT COEFFICIENTS EQUIVALENT AT SPEED
• INTERNALLY FED BEARING	FREON	MEASURE STIFFNESS AND DAMPING	STIFFNESS: 70% LOWER DAMPING: EQUIVALENT
• STEADY-STATE OPERATION			
• EXTERNALLY FED BEARING	LH_2	MEASURE STEADY STATE STIFFNESS MEASURE FLOW	20% HIGHER 20% LOWER
• INTERNALLY FED BEARING	LH_2	MEASURE STEADY-STATE STIFFNESS MEASURE FLOW	5% LOWER 4% LOWER

DYNAMIC CHARACTERISTICS TESTS

Testing was conducted with LH_2 and Freon 113 as working fluids to measure the stiffness and damping of hydrostatic bearings. Data suitable for calculation of stiffness and damping were not obtained with LH_2 due to casing vibration. For a summary of dynamic coefficient testing conducted with LH_2, see Appendix A. After modification of the tester, testing with Freon 113 did produce satisfactory data from which stiffness and damping of both externally and internally fed bearings were determined. Direct and cross-coupled stiffness and damping coefficients were separated for tests in which the orbit ellipticity was sufficiently large. Otherwise, only net effective coefficients can be measured. The dynamic characteristic testing with Freon 113 is summarized in Table 10.

TEST METHOD AND THEORY OF OPERATION

The test method for determining dynamic coefficients of hydrostatic bearings involves generating a forced dynamic motion across the bearing fluid film, and measuring the resulting fluid film displacements and forces. These displacements and forces provide the means for computing the active set of rotordynamic coefficients.

TABLE 10. FREON HYDROSTATIC BEARING DYNAMIC TESTING SUMMARY

TEST TYPE	BRG TYPE INT OR EXT	RADIAL CLEAR E-6m	ECCEN. E-6m	TEST DATE	TEST NO.	SPEED Krad/s	TIME s	SUP. PRESS. MPa	SUMP PRESS. MPa	SUP. TEMP K	SUMP TEMP K	FLUID DENSITY kg/m^3	FLUID FLOW kg/sec	FLUID FLOW m^3/sec	COMMENTS
DAMPING COEFFICIENT, SMALL ECCENTRICTY	EXTERNAL	43.18	6.35	9-4-85	4		0	5.24	0	307.8	308.9	1.542e3	.33	2.15e-4	Film thickness signals distorted
					THRU	1.57	25	4.55	0	307.8	309.7	1.542e3	.31	2.02e-4	
					7		332	4.41	0	307.8	310.0	1.542e3	.31	1.99e-4	
REPEAT WITH NEW JOURNAL	EXTERNAL	43.18	6.35	9-10-85	8		0	4.27	0	308.9	308.9	1.540e3	.39	2.52e-4	Film thickness signals visually ok
						1.57	97	3.31	0	308.9		1.540e3	.25	1.64e-4	
							130	3.31	0	308.9		1.540e3	.36	2.33e-4	
REPEAT AT HIGHER PRESSURE	EXTERNAL	43.18	6.35	9-10-85	9		0	11.03	0	310.6	312.2	1.536e3	.62	4.04e-4	Speed limited by turbine gas supply
						1.78	67	10.48	0	310.6	315.6	1.536e3	.51	3.34e-4	Otherwise ok
							81	10.48	0	310.6	315.0	1.536e3	.59	3.85e-4	
REPEAT WITH INCREASED DRIVE PRESSURE	EXTERNAL	43.18	6.35	9-10-85	10		0	10.89	0	311.7	312.2	1.516e3	.61	4.04e-4	
						2.09	92	10.76	0	311.7	316.7	1.516e3	.48	3.15e-4	
							124	10.76	0	311.7	315.0	1.516e3	.59	3.91e-4	
DAMPING COEFFICIENT, LARGER ECCENTRICITY	EXTERNAL	43.18	12.70	10-14-85	11		0	10.34	0	293.3	297.2	1.576e3	.64	4.07e-4	Orbit appears truncated
						2.09	102	10.34	0	293.3	305.6	1.576e3	.48	3.07e-4	
							156	10.34	0	293.3	300.6	1.576e3	.64	4.07e-4	
REPEAT WITH ADDED SPEED RAMPS	EXTERNAL	43.18	12.70	10-15-85	13		0	10.34	0	295.6	297.2	1.571e3	.68	4.34e-4	Speed ramp cycles added to determine
						2.09	61	10.34	0	295.6	305.0	1.571e3	.51	3.26e-4	effect of acceleration vs deceleration
						1.26	98	10.34	0	295.6	302.2	1.571e3	.60	3.80e-4	Truncated orbit repeated.
						2.09	140	10.34	0	295.6	306.1	1.571e3	.50	3.21e-4	
						1.26	166	10.34	0	295.6	303.9	1.571e3	.59	3.73e-4	
						2.09	196	10.34	0	295.6	307.2	1.571e3	.50	3.17e-4	
							223	10.34	0	295.6	302.2	1.571e3	.66	4.21e-4	
REPEAT WITH ALTERNATE TEST BEARING	EXTERNAL	43.18	12.70	10-15-85	14		0	10.34	0	297.2	297.2	1.567e3	.67	4.25e-4	Alternate test bearing installed.
						2.09	52	10.34	0	297.2	307.2	1.567e3	.47	2.98e-4	Stator centered with dial indicator
						1.26	78	10.34	0	297.2	303.9	1.567e3	.58	3.71e-4	to within 0.0002 in.
						2.09	114	10.34	0	297.2	307.2	1.567e3	.45	2.90e-4	Truncated orbit repeated.
						1.26	131	10.34	0	297.2	305.0	1.567e3	.56		

TABLE 10. (Continued)

TEST TYPE	BRG TYPE INT OR EXT	RADIAL CLEAR in	ECCEN. in	TEST DATE	TEST NO. N-	SPEED Krpm	TIME s	SUP. PRESS. psig	SUMP PRESS. psig	SUP. TEMP F	SUMP TEMP F	SUPPLY FLUID DENSITY lb/ft^3	FLUID FLOW lbm/s	FLUID FLOW gal/min	COMMENTS
DAMPING COEFFICIENT, SMALL ECCENTRICTY	EXTERNAL	.0017	.00025	9-4-85	4	0	0	760	0	94	96	96.08	.73	3.40	Film thickness signals distorted
					THRU	15	25	660	0	94	97.5	96.08	.69	3.20	
					7	0	332	640	0	94	98	96.08	.67	3.15	
REPEAT WITH NEW JOURNAL	EXTERNAL	.0017	.00025	9-10-85	8	0	0	620	0	96	96	95.91	.85	4.00	Film thickness signals visually ok
						15	97	480	0	96		95.91	.56	2.60	
						0	130	480	0	96		95.91	.79	3.70	
REPEAT AT HIGHER PRESSURE	EXTERNAL	.0017	.00025	9-10-85	9	0	0	1600	0	99	102	95.66	1.36	6.40	Speed limited by turbine gas supply
						17	67	1520	0	99	108	95.66	1.13	5.30	Otherwise ok
						0	81	1520	0	99	107	95.66	1.30	6.10	
REPEAT WITH INCREASED DRIVE PRESSURE	EXTERNAL	.0017	.00025	9-10-85	10	0	0	1580	0	101	102	94.46	1.35	6.40	
						20	92	1560	0	101	110	94.46	1.05	5.00	
						0	124	1560	0	101	107	94.46	1.30	6.20	
DAMPING COEFFICIENT, LARGER ECCENTRICITY	EXTERNAL	.0017	.0005	10-14-85	11	0	0	1500	0	68	75	98.2	1.41	6.45	Orbit appears truncated
						20	102	1500	0	68	90	98.2	1.07	4.87	
						0	156	1500	0	68	81	98.2	1.41	6.45	
REPEAT WITH ADDED SPEED RAMPS	EXTERNAL	.0017	.0005	10-15-85	13	0	0	1500	0	72	75	97.88	1.50	6.88	Speed ramp cycles added to determine
						20	61	1500	0	72	89	97.88	1.13	5.16	effect of acceleration vs deceleration
						12	98	1500	0	72	84	97.88	1.31	6.02	Truncated orbit repeated.
						20	140	1500	0	72	91	97.88	1.11	5.09	
						12	166	1500	0	72	87	97.88	1.29	5.91	
						20	196	1500	0	72	93	97.88	1.09	5.02	
						0	223	1500	0	72	84	97.88	1.45	6.67	
REPEAT WITH ALTERNATE TEST BEARING	EXTERNAL	.0017	.0005	10-15-85	14	0	0	1500	0	75	75	97.63	1.47	6.74	Alternate test bearing installed.
						20	52	1500	0	75	93	97.63	1.03	4.73	Stator centered with dial indicator
						12	78	1500	0	75	87	97.63	1.28	5.88	to within 0.0002 in.
						20	114	1500	0	75	93	97.63	1.00	4.59	Truncated orbit repeated.
						12	131	1500	0	75	89	97.63	1.23	5.66	
						20	154	1500	0	75	96	97.63		4.59	
						0	180	1500	0	75	86	97.63		6.45	

TABLE 10. (Continued)

TEST TYPE	BRG TYPE INT OR EXT	RADIAL CLEAR E-6m	ECCEN. E-6m	TEST DATE	TEST NO.	SPEED Krad/s	TIME s	SUP. PRESS. MPa	SUMP PRESS. MPa	SUP. TEMP K	SUMP TEMP K	FLUID DENSITY kg/m^3	FLUID FLOW kg/sec	FLUID FLOW m^3/sec	COMMENTS
DYNAMIC CHARACTERISTIC TEST	EXT	43.18	12.70	10-15-85	15			10.34	0	298.3	299.4	1.565e3	.74	4.70e-4	ATTEMPTED SPEED RAMP FROM 20K-30K RPM. SPEED LIMITED BY
MODIFIED INLET TUBE INSTALLED. DOUBLE						2.20	30	10.34	0	298.3	306.7	1.565e3	.51	3.26e-4	TURBINE GAS SUPPLY CAPACITY.
INLET TO REDUCE FLOW NOISE.						2.20	35	10.34	0	298.3	307.2	1.565e3	.51	3.26e-4	
							63	10.34	0	298.3	303.9	1.565e3	.71	4.52e-4	
LARGE CLEARANCE, LARGE ECCENTRICITY	EXT	86.36	12.70	10-24-85	16			.83	0	292.2	292.2	1.579e3	-	0	VISIBLE TRUNCATION OF ORBIT ELIMINATED.
						2.09	94	3.45	0	292.2	298.9	1.579e3	.49	3.09e-4	HARMONICS APPEAR IN STATOR LOAD SIGNAL
							120	3.45	0	292.2	295.6	1.579e3	.50	3.15e-4	FOR THE FIRST TIME.
REPEAT WITH HIGHER SUPPLY PRESSURE	EXT	86.36	12.70	10-24-85	17				0	295.0	295.0	1.572e3		0	
						3.14	8	4.41	0	295.0	295.0	1.572e3	.56	3.53e-4	TURBINE GAS DRIVE CAPACITY LOW
						4.40	7	5.79	0	295.0	295.0	1.572e3	.63	3.97e-4	
						6.28		6.34	0	295.0	295.0	1.572e3	.66	4.23e-4	
REPEAT	EXT	86.36	12.70	10-25-85	18			.55	0	293.9	293.9	1.575e3	.21	1.32e-4	OPERATION OK. ORBIT OVAL AT LOW SPEED,BECOMES
						.13	52	6.21	0	293.9	293.9	1.575e3	.66	4.16e-4	8-SIDED AT APPROX. 13KRPM, THEN OVAL
						2.09	128	6.48	0	293.9	299.7	1.575e3	.66	4.16e-4	AT HIGHER SPEEDS.STATOR LOAD SIGNALS CONTAIN
							160	6.48	0	293.9	297.2	1.575e3	.67	4.23e-4	HARMONICS OF SHAFT SPEED.POSSIBLE RUBBING
REPEAT WITH HIGHER SUPPLY PRESSURE	EXT	86.36	12.70	10-25-85	19			.55	0	293.9	293.9	1.575e3	.22	1.39e-4	OPERATION OK. SIGNALS SMILAR TO TEST 19.
							52	7.72	0	293.9	293.9	1.575e3	.73	4.61e-4	JOURNAL SHOWED LIGHT RUBBING. SMALL
						2.09	134	8.00	0	293.9	300.6	1.575e3	.73	4.61e-4	METAL PARTICLE LODGED AT EDGE OF
							172	8.00	0	293.9	298.9	1.575e3	.76	4.79e-4	RECESS
REPEAT WITH NEW CENTERING METHOD.	EXT	86.36	12.70	10-28-85	20			1.10	0	293.9	293.3	1.575e3	.28	1.77e-4	SMOOTH ORBIT. HARMONICS IN LOAD AND STATOR
							17	4.14	0	293.9	293.9	1.575e3	.56	3.53e-4	SIGNALS
						2.09	62	7.31	0	293.9	297.2	1.575e3	.70	4.42e-4	
							86	6.76	0	293.9	297.2	1.575e3	.70	4.42e-4	
REPEAT WITH ORIGINAL INLET (SINGLE TUBE)	EXT	86.36	12.70	10-28-85	21			.28	0	293.9	293.9	1.575e3	.24	1.51e-4	SIMILAR PATTERN TO TEST 20
							60	8.00	0	293.9	294.4	1.575e3	.74	4.67e-4	
						2.09	86	8.14	0	293.9	298.9	1.575e3	.73	4.61e-4	
							115	8.14		293.9	297.2	1.575e3	.74	4.67e-4	

TABLE 10. (Continued)

TEST TYPE	BRG TYPE INT OR EXT	RADIAL CLEAR in	ECCEN. in	TEST DATE	TEST NO.	SPEED Krpm	TIME s	SUP. PRESS. psig	SUMP PRESS. psig	SUP. TEMP F	SUMP TEMP F	SUPPLY FLUID DENSITY lb/ft^3	FLUID FLOW lbm/s	FLUID FLOW gal/min	COMMENTS
DYNAMIC CHARACTERISTIC TEST MODIFIED INLET TUBE INSTALLED. DOUBLE INLET TO REDUCE FLOW NOISE.	EXT	.0017	.0005	10-15-85	15	0	0	1500	0	77	79	97.47	1.62	7.45	ATTEMPTED SPEED RAMP FROM 20K-30K RPM. SPEED LIMITED BY
						21	30	1500	0	77	92	97.47	1.12	5.16	TURBINE GAS SUPPLY CAPACITY.
						21	35	1500	0	77	93	97.47	1.12	5.16	
						0	63	1500	0	77	87	97.47	1.56	7.17	
LARGE CLEARANCE, LARGE ECCENTRICITY	EXT	.0034	.0005	10-24-85	16	0	0	120	0	66	66	98.36			VISIBLE TRUNCATION OF ORBIT ELIMINATED.
						20	94	500	0	66	78	98.36	1.07	4.90	HARMONICS APPEAR IN STATOR LOAD SIGNAL
						0	120	500	0	66	72	98.36	1.10	5.00	FOR THE FIRST TIME.
REPEAT WITH HIGHER SUPPLY PRESSURE	EXT	.0034	.0005	10-24-85	17	0	0	0	0	71	71	97.96			
						30	81	640	0	71	71	97.96	1.22	5.60	TURBINE GAS DRIVE CAPACITY LOW
						42	71	840	0	71	71	97.96	1.38	6.30	
						60	0	920	0	71	71	97.96	1.46	6.70	
REPEAT	EXT	.0034	.0005	10-25-85	18	0	0	80	0	69	69	98.12	.46	2.10	OPERATION OK. ORBIT OVAL AT LOW SPEED, BECOMES
						11	52	900	0	69	69	98.12	1.44	6.60	8-SIDED AT APPROX. 13KRPM, THEN OVAL
						20	128	940	0	69	79.5	98.12	1.44	6.60	AT HIGHER SPEEDS. STATOR LOAD SIGNALS CONTAIN
						0	160	940	0	69	75	98.12	1.46	6.70	HARMONICS OF SHAFT SPEED. POSSIBLE RUBBING
REPEAT WITH HIGHER SUPPLY PRESSURE	EXT	.0034	.0005	10-25-85	19	0	0	80	0	69	69	98.12	.48	2.20	OPERATION OK. SIGNALS SMILAR TO TEST 19.
						0	52	1120	0	69	69	98.12	1.60	7.30	JOURNAL SHOWED LIGHT RUBBING. SMALL
						20	134	1160	0	69	81	98.12	1.60	7.30	METAL PARTICLE LODGED AT EDGE OF
						0	172	1160	0	69	78	98.12	1.66	7.60	RECESS
REPEAT WITH NEW CENTERING METHOD.	EXT	.0034	.0005	10-28-85	20	0	0	160	0	69	68	98.12	.61	2.80	SMOOTH ORBIT. HARMONICS IN LOAD AND STATOR
						0	171	600	0	69	69	98.12	1.22	5.60	SIGNALS
						20	62	1060	0	69	75	98.12	1.53	7.00	
						0	86	980	0	69	75	98.12	1.53	7.00	
REPEAT WITH ORIGINAL INLET (SINGLE TUBE)	EXT	.0034	.0005	10-28-85	21	0	0	40	0	69	69	98.12	.52	2.40	SIMILAR PATTERN TO TEST 20
						0	60	1160	0	69	70	98.12	1.62	7.40	
						20	86	1180	0	69	78	98.12	1.60	7.30	
						0	115	1180	0	69	75	98.12	1.62	7.40	

TABLE 10. (Continued)

TEST TYPE	BRG FEED EXTERNAL OR INTERNAL	RADIAL CLEAR E-6m	ECCEN. E-6m	TEST DATE	TEST NO.	SPEED Krad/s	TIME s	SUP. PRESS. MPa	SUMP PRESS. MPa	SUP. TEMP K	SUMP TEMP K	FLUID DENSITY kg/m^3	FLUID FLOW kg/sec	FLUID FLOW m^3/sec	COMMENTS
DYNAMIC CHARACTERISTIC TEST. FAST RAMP TO 20KRPM, ATTEMPT SLOW RAMP TO 30KRPM	EXTERNAL	43.18	6.35	11-14-85	23	.00			.0	288.1	288.9	1.589e3		0	SPEED LIMITED BY TURBINE FLOW OF 0.8 lb/s MAX
						.00	11	6.21	.0	288.9	289.7	1.587e3	.56	3.54e-4	
						1.82	23	10.48	.0	288.9	295.0	1.587e3	.54	3.43e-4	THREE-SIDED ORBIT; FILM SIGNALS CONTAIN HARMONICS
						2.20	34	10.48	.0	288.9	300.6	1.587e3	.48	3.00e-4	LOAD SIGNALS DO NOT
						2.20	46	10.48	.0	288.9	303.9	1.587e3	.48	3.00e-4	
						1.26	48	10.48	.0	288.9	303.9	1.587e3	.58	3.65e-4	
						.00	50	10.48	.0	288.9	297.2	1.587e3	.68	4.29e-4	
ORBIT OBSERVATION WITHOUT FLUID	EXTERNAL	43.18	6.35	11-14-85	23A	.00			.0			0		0	STEADY 3-LOBE ORBIT AT ALL SPEEDS. JOURNAL OUT OF ROUND
						.57	4		.0			0		0	BY 0.00203 cm (80X10-6 INCH)
						.00	6		.0			0		0	JOURNAL REMOVED FOR INSPECTION AND REWORK.
						.00			.0			0		0	
DYNAMIC CHARACTERISTIC TEST WITH JOURNAL REWORKED FOR MINIMUM OUT-OF-ROUND. RAPID RAMP TO 20KRPM, SLOW RAMP TO 30K RPM ATTEMPT.	EXTERNAL	45.72	17.78	12-2-85	25	.00			.0	286.1	286.1	1.593e3		0	ORBIT APPEARS STEADY AND NORMAL.
						1.26	35	9.93	.0	287.2	291.7	1.591e3	.59	3.71e-4	
						2.38	75	8.83	.0	287.2	297.2	1.591e3	.48	3.00e-4	MAXIMUM SPEED LIMITED BY TURBINE DRIVE
						.00	92	8.41	.0	287.2	293.3	1.591e3	.60	3.77e-4	GAS FLOW CAPACITY.
REPEAT WITH MAXIMUM DRIVE GAS FLOW POSSIBLE	EXTERNAL	45.72	17.78	12-2-85	26	.00			.0	287.2	288.3	1.591e3		0	SIMILAR TO TEST 25 RESULTS
						.00	21	6.07	.0	287.2	288.3	1.591e3	.53	3.36e-4	
						1.26	41	10.20	.0	287.2	293.3	1.591e3	.59	3.71e-4	
						2.38	60	10.76	.0	287.2	296.7	1.591e3	.51	3.18e-4	
						.00	100	10.76	.0	287.2	295.0	1.591e3	.66	4.15e-4	

TABLE 10. (Continued)

TEST TYPE	BRG FEED EXTERNAL OR INTERNAL	RADIAL CLEAR in	ECCEN. in	TEST DATE	TEST NO.	SPEED Krpm	TIME s	SUP. PRESS. psig	SUMP PRESS. psig	SUP. TEMP F	SUMP TEMP F	SUPPLY FLUID DENSITY lb/ft^3	FLUID FLOW lbm/s	FLUID FLOW gal/min	COMMENTS
DYNAMIC CHARACTERISTIC TEST. FAST RAMP TO 20KRPM, ATTEMPT SLOW RAMP TO 30KRPM	EXTERNAL	.0017	.00025	11-14-85	23	.0	0	0	0	58.5	60	98.97			SPEED LIMITED BY TURBINE FLOW OF 0.8 lb/s MAX
						.0	11	900	0	60	61.5	98.85	1.24	5.61	
						17.4	23	1520	0	60	71	98.85	1.20	5.44	THREE-SIDED ORBIT; FILM SIGNALS CONTAIN HARMONICS
						21.0	34	1520	0	60	81	98.85	1.05	4.76	LOAD SIGNALS DO NOT
						21.0	46	1520	0	60	87	98.85	1.05	4.76	
						12.0	48	1520	0	60	87	98.85	1.27	5.78	
						.0	50	1520	0	60	75	98.85	1.50	6.80	
ORBIT OBSERVATION WITHOUT FLUID	EXTERNAL	.0017	.00025	11-14-85	23A	.0	0								STEADY 3-LOBE ORBIT AT ALL SPEEDS. JOURNAL OUT OF ROUND
						5.4	6								BY 0.00203 mm (8X10-6 INCH)
						.0	6								JOURNAL REMOVED FOR INSPECTION AND REWORK.
DYNAMIC CHARACTERISTIC TEST WITH JOURNAL REWORKED FOR MINIMUM OUT-OF-ROUND. RAPID RAMP TO 20KRPM, SLOW RAMP TO 30K RPM ATTEMPT.	EXTERNAL	.0018	.00070	12-2-85	25	.0	0	0	0	55	55	99.25			ORBIT APPEARS STEADY AND NORMAL.
						12.0	35	440	0	57	65	99.09	1.30	5.88	
						22.7	75	1280	0	57	75	99.09	1.05	4.76	MAXIMUM SPEED LIMITED BY TURBINE DRIVE
						.0	92	1220	0	57	68	99.09	1.32	5.98	GAS FLOW CAPACITY.
REPEAT WITH MAXIMUM DRIVE GAS FLOW POSSIBLE	EXTERNAL	.0018	.00070	12-2-85	26	.0	0	0	0	57	59	99.09			SIMILAR TO TEST 25 RESULTS
						.0	21	880	0	57	59	99.09	1.17	5.32	
						12.0	41	1480	0	57	68	99.09	1.30	5.88	
						22.7	60	1560	0	57	74	99.09	1.11	5.04	
						.0	100	1560	0	57	71	99.09	1.45	6.58	

TABLE 10. (Continued)

TEST TYPE	BRG TYPE INT OR EXT	RADIAL CLEAR E-6m	ECCEN. E-6m	TEST DATE	TEST NO.	SPEED Krad/s	TIME s	SUP. PRESS. MPa	SUMP PRESS. MPa	SUP. TEMP K	SUMP TEMP K	FLUID DENSITY kg/m^3	FLUID FLOW kg/sec	FLUID FLOW m^3/sec	COMMENTS
DYNAMIC CHARACTERISTIC TEST, INTERNALLY FED BEARING	INTERNAL	67.31	21.59	1-7-86	28	.00	31	10.62	.0	292.2	295.0	1.579e3	.53	3.36e-4	DATA WAVEFORMS LOOK GOOD, EXCEPT THAT ORBIT IS QUITE ROUND
						.44	38	10.55	.0	292.2	295.6	1.579e3	.52	3.27e-4	
						1.19	49	10.55	.0	292.2	297.2	1.579e3	.53	3.38e-4	DATA ANALYSIS REQUIRES MORE ELLIPTICITY IN ORBIT
						1.79	65	10.48	.0	292.2	298.9	1.579e3	.48	3.03e-4	
						.00	71	10.48	.0	292.2	297.2	1.579e3	.53	3.36e-4	
REPEAT OF PREVIOUS TEST, BUT WITH SOFT AXIS STRAIN STUDS REMOVED AND REPLACED WITH PROXIMITY PROBES TO INCREASE STATOR STIFFNESS ASYMMETRY TO ACHIEVE MORE ELLIPTIC ORBIT	INTERNAL	67.31	21.59	1-14-86	29	.00		10.48	.0	NOT RECORDED				0	GOOD WAVEFORMS.
						.00	20	10.48	.0					3.72e-4	
						1.57	40	10.48	.0					3.29e-4	
						2.09	55	10.48	.0					3.08e-4	
						2.09	60	10.48	.0					3.08e-4	
						.00	95	10.48	.0					3.72e-4	
REPEAT PREVIOUS TEST	INTERNAL	67.31	21.59	1-15-86	31	.00			.0					0	GOOD WAVEFORMS
						.00	12	10.20	.0					3.79e-4	
						1.01	20	9.93	.0					3.41e-4	
						2.07	38	10.07	.0					2.96e-4	
						2.02	40	10.07	.0					2.96e-4	
						2.02	44	10.07	.0	290.6	299.7	1.583e3		2.96e-4	
						.00	58	9.93	.0	290.6	295.6	1.583e3		3.67e-4	
REPEAT PREVIOUS TEST WITH SMALL ECCENTRICITY	INTERNAL	67.31	8.89	2-21-86	32	.00			.0	291.4	291.4	1.581e3		0	FILM THICKNESS SIGNALS NOISY, HAVE WEAK SECOND HARMONIC,
						1.91	50	11.03	.0	291.4	300.6	1.581e3	.53	3.38e-4	SMALL HIGHER HARMONICS. SIGNAL AFFECTED BY CABLE MOTION.
						.00	65		.0	291.4	295.6	1.581e3		0	
REPEAT PREVIOUS TEST WITH STATOR STIFFNESS ASYMMETRY REDUCED. STRAIN GAGED STUDS RE-INSTALLED IN THE SOFT AXIS.	INTERNAL	67.31	8.89	2-21-86	33	.00			.0	293.1	293.1	1.579e3		0	
						.00	10	9.52	.0	291.7	293.9	1.579e3	.64	4.04e-4	CABLES STRAPPED DOWN TO REDUCE NOISE. SIMILAR TO PREVIOUS TEST
						.34	20	10.20	.0	292.2	296.0	1.579e3	.63	4e-4	
						1.81	30	9.65	.0	292.2	298.9	1.579e3	.53	3.38e-4	
						2.01	40	9.10	.0	292.2	301.0	1.579e3	.56	3.18e-4	
						1.17	50	9.10	.0	292.2	300.6	1.579e3	.54	3.39e-4	
						.00	53	9.10	.0	292.2	298.9	1.579e3	.60	3.82e-4	
							55			292.2		1.579e3		0	

TABLE 10. (Concluded)

TEST TYPE	BRG TYPE INT OR EXT	RADIAL CLEAR in	ECCEN. in	TEST DATE	TEST NO.	SPEED Krpm	TIME s	SUP. PRESS. psig	SUMP PRESS. psig	SUP. TEMP F	SUMP TEMP F	SUPPLY FLUID DENSITY lb/ft^3	FLUID FLOW lbm/s	FLUID FLOW gal/min	COMMENTS
DYNAMIC CHARACTERISTIC TEST, INTERNALLY FED BEARING	INTERNAL	.00265	.00085	1-7-86	28	.0	31	1540	0	66	71	98.36	1.17	5.33	DATA WAVEFORMS LOOK GOOD, EXCEPT THAT ORBIT IS QUITE ROUND
						4.2	38	1530	0	66	72	98.36	1.14	5.19	
						11.4	49	1530	0	66	75	98.36	1.17	5.35	DATA ANALYSIS REQUIRES MORE ELLIPTICITY IN ORBIT
						17.1	65	1520	0	66	78	98.36	1.05	4.80	
						.0	71	1520	0	66	75	98.36	1.17	5.33	
REPEAT OF PREVIOUS TEST, BUT WITH SOFT AXIS STRAIN STUDS REMOVED AND REPLACED WITH PROXIMITY PROBES TO INCREASE STATOR STIFFNESS ASYMMETRY TO ACHIEVE MORE ELLIPTIC ORBIT	INTERNAL	.00265	.00085	1-14-86	29	.0	0	1520	0	NOT RECORDED					GOOD WAVEFORMS.
						.0	20	1520	0					5.90	
						15.0	40	1520	0					5.22	
						20.0	55	1520	0					4.88	
						20.0	60	1520	0					4.88	
						.0	95	1520	0					5.90	
REPEAT PREVIOUS TEST	INTERNAL	.00265	.00085	1-15-86	31	.0	0	0	0						GOOD WAVEFORMS
						.0	12	1480	0					6.00	
						9.6	20	1440	0					5.40	
						19.8	38	1460	0					4.69	
						19.3	40	1460	0					4.69	
						19.3	44	1460	0	63	79.5	98.61		4.69	
						.0	58	1440	0	63	72	98.61		5.81	
REPEAT PREVIOUS TEST WITH SMALL ECCENTRICITY	INTERNAL	.00265	.00035	2-21-86	32	.0	0	0.	0	64.5	64.5	98.49			FILM THICKNESS SIGNALS NOISY, HAVE WEAK SECOND HARMONIC,
						18.2	50	1600	0	64.5	81	98.49	1.18	5.36	SMALL HIGHER HARMONICS. SIGNAL AFFECTED BY CABLE MOTION.
						.0	65	0	0	64.5	72	98.49			
REPEAT PREVIOUS TEST WITH STATOR STIFFNESS ASYMMETRY REDUCED. STRAIN GAGED STUDS RE-INSTALLED IN THE SOFT AXIS.	INTERNAL	.00265	.00035	2-21-86	33	.0	0	0	0	67.5	67.5	98.36			
						.0	10	1380	0	65	69	98.36	1.40	6.40	CABLES STRAPPED DOWN TO REDUCE NOISE. SIMILAR TO PREVIOUS TEST
						3.2	20	1400	0	66	72.8	98.36	1.39	6.34	
						17.3	30	1400	0	66	78	98.36	1.17	5.35	
						19.2	40	1320	0	66	81.8	98.36	1.10	5.04	
						11.2	50	1320	0	66	81	98.36	1.18	5.38	
						.0	53	1320	0	66	78	98.36	1.33	4.06	
						.0	55	0	0	66		98.36			

The forced dynamic motion is generated as depicted in Fig. 34. The overhung test bearing is located on the outboard end of a test shaft supported by two duplex pair of ball bearings. The rotating part of the test bearing has been given an intentional eccentricity (i.e., runout) at the test bearing location. When the shaft rotates, the eccentricity generates an orbital pattern synchronous with shaft speed. This orbital pattern is measured with a pair of eddy current displacement probes mounted directly in the stator of the test bearing. In this way, should the stator element also be in motion, the displacement probes will directly measure the desired relative deflection across the fluid film.

The stator element is supported by eight tubes (flexure arms), one of which is shown in Fig. 34. These tubes also direct the supply of fluid to the externally fed test bearing. In addition to the stiffness of the flexure arms, the stator element is elastically constrained in the radial direction by two pair of preloaded strain gaged studs (Fig. 35 and 36). The studs were calibrated for load sensitivity and stiffness by applying known static loads directly to the stator at midplane of the test bearing. Under test conditions, the strain gage readings will then reflect the sum of the fluid film forces and the inertia force of the stator mass. As determination of rotordynamic coefficients requires the fluid film force by itself, the stator inertia force must be subtracted from the load cell readings. With the mass of the stator known, this is done as follows:

$$F_y = -\bar{F}_y + m_s \, (d^2/dt^2) \, (-\bar{F}_y/K_{sy}) \tag{1}$$

$$F_z = -\bar{F}_z + m_s \, (d^2/dt^2) \, (-\bar{F}_z/K_{sz}) \tag{2}$$

where

$\bar{F}_{y,z}$ = components of load cell reaction force acting on stator

$F_{y,z}$ = components of fluid film force acting on stator

m_s = stator mass

$K_{sy,sz}$ = stator support stiffness, can be asymmetric

The technique of using strain gage load data to compute the inertia term was found equally effective as using stator-mounted accelerometers, and was employed here since it involves processing fewer data channels.

The most general type of relative fluid film displacement orbits permissible in linear systems are elliptic in nature. Therefore, the goal of the measurement process is to identify the ellipse that describes the relative displacement as a function of time in the following form (relative = rotor - stator):

$$y(t) = a(\cos\omega t) + b(\sin\omega t) \tag{3}$$

$$z(t) = g(\cos\omega t) + h(\sin\omega t) \tag{4}$$

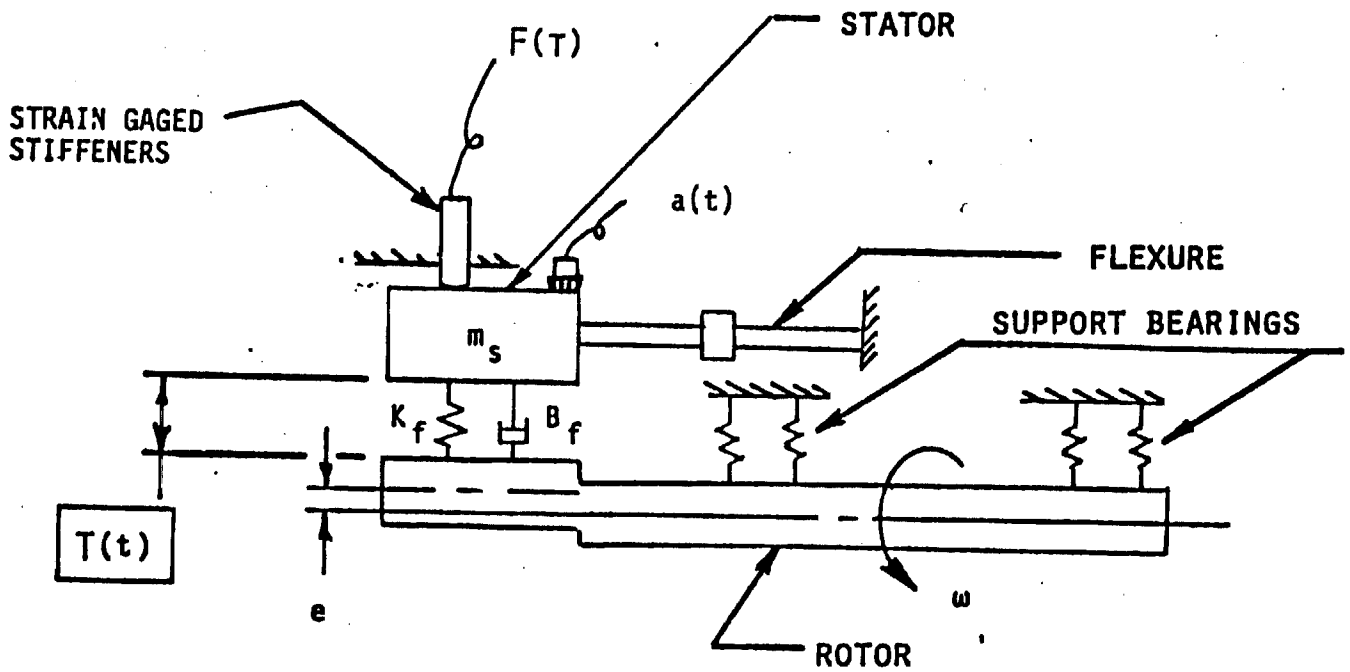

METHOD:

DYNAMIC FORCE & MOTION DATA
USED TO SOLVE FOR B_f

Figure 34. Damping Measurement Technique

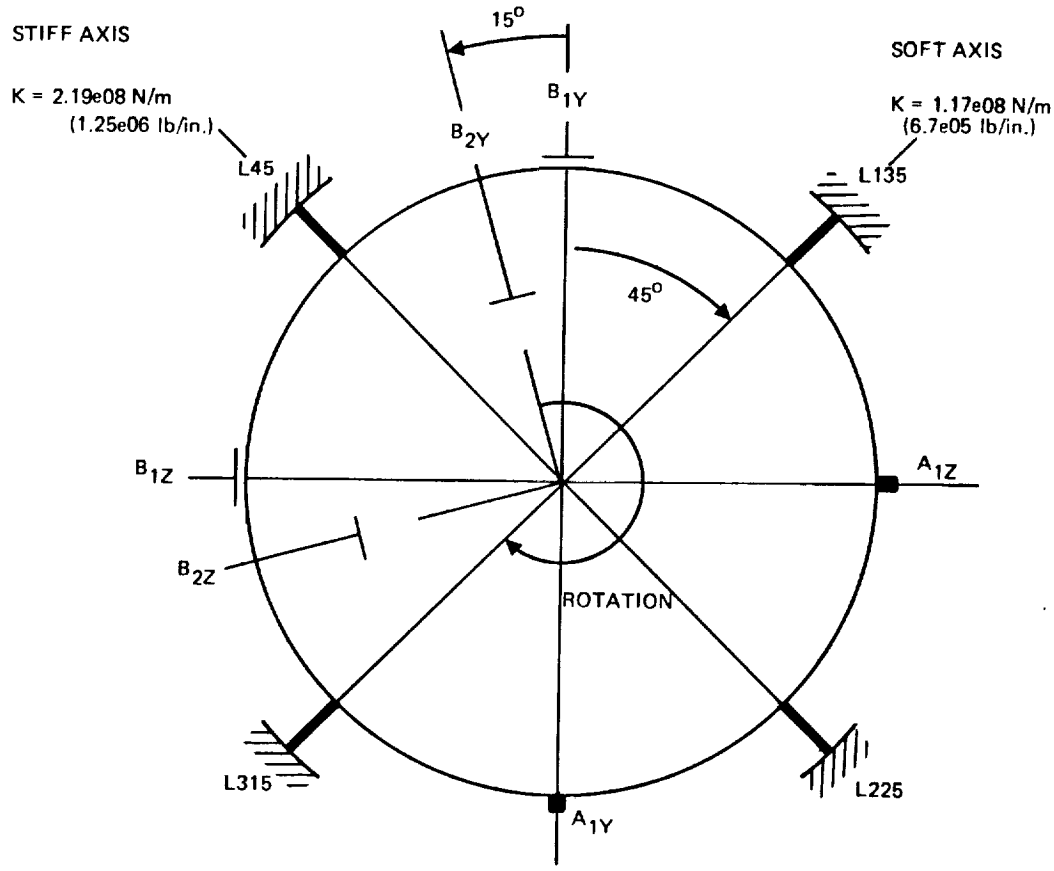

Figure 35. Sensor Orientation

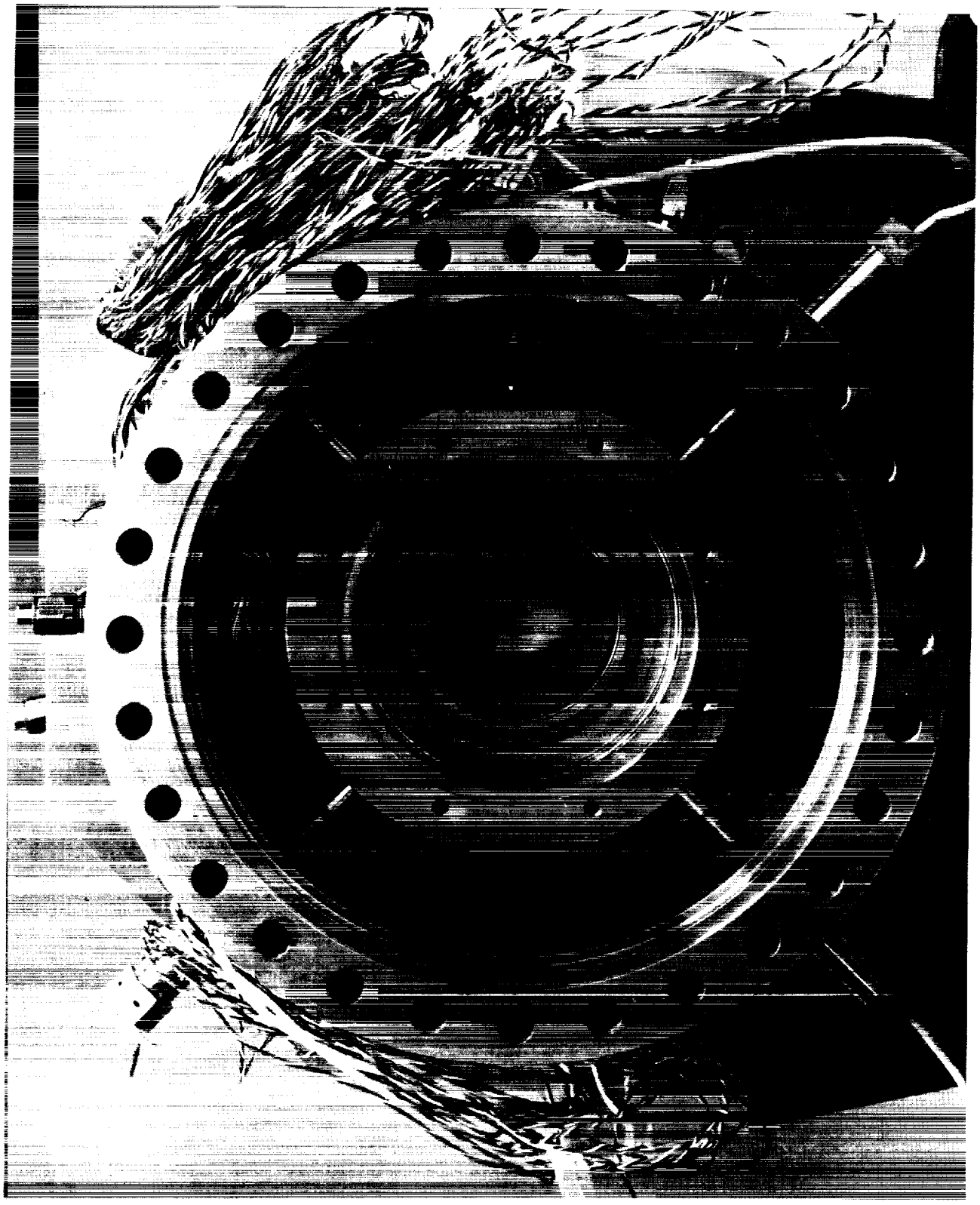

Figure 36. Compression Studs Installed

The four coefficients "abgh" are termed Fourier coefficients, and ω is the tester speed in radians per second. They can be obtained in one of two ways: (1) by processing each data channel with an analog tracking filter to obtain synchronous amplitude and phase, and then transforming these to cosine and sine components or, (2) compute the frequency spectrum of each data channel and obtain the Fourier coefficients directly. The second method was employed here as it permitted the easiest processing of all data channels simultaneously.

The same procedure is applied to the load data to obtain Fourier coefficients in the following form:

$$\bar{F}_y = \bar{m}(\cos\omega t) + \bar{n}(\sin\omega t) \tag{5}$$

$$\bar{F}_y = \bar{p}(\cos\omega t) + \bar{q}(\sin\omega t) \tag{6}$$

The equations correcting for stator inertia now become

$$F_y = -[\bar{m}(\cos\omega t) + \bar{n}(\sin\omega t)] + (m_s/K_{sy})\,(\bar{m}\omega^2(\cos\omega t) + \bar{n}\omega^2(\sin\omega t)) \tag{7}$$

$$F_z = -[\bar{p}(\cos\omega t) + \bar{q}(\sin\omega t)] + (m_s/K_{sz})\,(\bar{p}\omega^2(\cos\omega t) + \bar{q}\omega^2(\sin\omega t)) \tag{8}$$

or

$$F_y = m(\cos\omega t) + n(\sin\omega t) \tag{9}$$

$$F_z = p(\cos\omega t) + q(\sin\omega t) \tag{10}$$

where

$$m = \bar{m}(-1+(m_s\omega^2/K_{sy})) \text{ etc.}$$

mnpq = Fourier coefficients for fluid film force (acting on stator)

With the fluid film force and the displacement across the fluid film now known as functions of time, rotordynamic coefficients can be computed. The generally accepted form for the relationship between these three sets of quantities is as follows:

$$\begin{Bmatrix} F_y \\ F_z \end{Bmatrix} = \begin{bmatrix} K_{yy} & K_{yz} \\ K_{zy} & K_{zz} \end{bmatrix} \begin{Bmatrix} y \\ z \end{Bmatrix} + \begin{bmatrix} B_{yy} & B_{yz} \\ B_{zy} & B_{zz} \end{bmatrix} \begin{Bmatrix} \dot{y} \\ \dot{z} \end{Bmatrix} + \begin{bmatrix} M_{yy} & M_{yz} \\ M_{zy} & M_{zz} \end{bmatrix} \begin{Bmatrix} \ddot{y} \\ \ddot{z} \end{Bmatrix} \tag{11}$$

The displacements and forces were defined above using Fourier coefficients. The velocities and accelerations are obtained by differentiation with respect to time. There are several ways to approach the problem of identifying the 12

unknown rotordynamic coefficients. It should be noted that the measured forces and displacements will vary with tester rotational speed. In fact, complete sets of Fourier coefficients can typically be made available for any rotational speed within the tester's speed range. Thus, one straightforward approach for computing the K's, B's and M's would be to simply rearrange the above matrix equation into the following alternate form (substituting in the Fourier coefficients):

$$\begin{bmatrix} -a\omega_2^2 & -g\omega_2^2 & b\omega & h\omega & a & g & o & o & o & o & o & o \\ -b\omega^2 & -h\omega^2 & -a\omega & -g\omega & b & h & o_2 & o_2 & o & o & o & o \\ o & o & o & o & o & o & -a\omega_2^2 & -g\omega_2^2 & b\omega & h\omega & a & g \\ o & o & o & o & o & o & -b\omega^2 & -h\omega^2 & -a\omega & -g\omega & b & h \end{bmatrix} \begin{Bmatrix} M_{yy} \\ M_{yz} \\ B_{yz} \\ B_{yy} \\ K_{yz} \\ K_{yy} \\ M_{zy} \\ M_{zz} \\ B_{zy} \\ B_{zz} \\ K_{zy} \\ K_{zz} \end{Bmatrix} = \begin{Bmatrix} m \\ n \\ p \\ q \end{Bmatrix} \quad 12)$$

Note that the 12 rotordynamic coefficients are the unknowns in this matrix equation, and that the two equations of the former relation have been resoslved into sinωt and cosωt components (or real and imaginary). Since there are more unknowns than equations, one could use data from multiple values of tester speed, writing 4 equations for each. Data from 3 different speeds would yield 12 equations, and Gaussian elimination could be used to find the solution. Another method would be to use more than 3 speed points, and a least squares equation solver to find the "best fit" coefficient solution. Neither of these approaches will prove successful, however, since the coefficient solution will not be unique. To circumvent this problem, the inertia coefficients must be eliminated from the list of unknowns. This yields the following:

$$\begin{bmatrix} b\omega & h\omega & a & g & o & o & o & o \\ -a\omega & -g\omega & b & h & o & o & o & o \\ o & o & o & o & b\omega & h\omega & a & g \\ o & o & o & o & -a\omega & -g\omega & b & h \end{bmatrix} \begin{Bmatrix} B_{yy} \\ B_{yz} \\ K_{yz} \\ K_{yy} \\ B_{yz} \\ B_{zy} \\ K_{zz} \\ K_{zy} \\ K_{zz} \end{Bmatrix} = \begin{Bmatrix} m \\ n \\ p \\ q \end{Bmatrix} \quad (13)$$

Since data from multiple speed points must be used, it is necessary that the speeds span as wide a range as possible to give the best definition of the coefficients.

This type of coefficient solution yields one general asymmetric set of constant stiffness and damping coefficients to fit the given data. In practice, however, these coefficients could vary appreciably with speed. Efforts to expand the set of unknown coefficients to include speed dependent terms will once again be unsuccessful due to nonunique solutions. This occurs because in certain cases a speed dependent set of skew-symmetric coefficients and a set of constant asymmetric coefficients can both be solutions for the same data.

For the type of fluid film element being measured here, the fluid inlet is made circumferentially uniform by using 6 equally spaced, identical hydrostatic pressure pockets, while the test bearing is centered in its clearance space with no applied static load. These conditions dictate that the rotordynamic coefficients will be skew-symmetric (i.e., $K_{yy}=K_{zz}$, $K_{yz}=-K_{zy}$, and similarly for B and M). This reduces the number of unknowns so that the matrix equation for rotordynamic coefficients becomes:

$$\begin{bmatrix} b & h & a & g \\ -a & -g & b & h \\ h & -b & g & -a \\ -g & a & h & -b \end{bmatrix} \begin{Bmatrix} B_{yy}\omega \\ B_{yz}\omega \\ K_{yy}-M_{yy}\omega^2 \\ K_{yz}-M_{yz}\omega^2 \end{Bmatrix} = \begin{Bmatrix} m \\ n \\ p \\ q \end{Bmatrix} \tag{14}$$

where

ω is the excitation frequency (rad/sec)

Ω is the shaft rotation frequency (rad/sec)
for all "synchronous only rigs" $\omega=\Omega$ always
and all coefficients are functions of Ω.

Define:

$$K'_{yy} = K_{yy}-\Omega^2 M_{yy} \tag{15}$$

$$K'_{yz} = K_{yz}-\Omega^2 M_{yz} \tag{16}$$

Note that the two unknown inertia coefficients have been combined with the stiffness coefficients to form a combined pair of unknowns. This is necessary to ensure a unique solution to the matrix. Since there are now only four unknowns, the matrix solution can be carried out with data from only one speed point. Also, for convenience, the shaft speed has been placed in the unknown column vector instead of in the matrix elements.

The coefficients K_{yy}, K_{yz}, B_{yy}, B_{yz}, M_{yy} and M_{yz} will, in general, vary with rotational speed Ω, and since only linear model characteristics are desired, they do not vary with excitation frequency ω. Tester data can be used with the above matrix to determine how K'_{yy}, K'_{yz}, B_{yy} and B_{yz} vary with synchronous frequency $\omega=\Omega$. Note that the damping terms are completely separated from the stiffness terms without the need to vary tester speed. However, this requires that the fluid film displacement orbit be elliptic. If only circular orbits were possible, the above 4 by 4 matrix would become 2 by 2, and the stiffness and damping terms would need to be combined.

To show how such a separation is possible, and how effective this separation is, consider the displacement orbit shown in Fig. 37. Any displacement ellipse can be transformed into the ellipse of Fig. 37 without any loss in generality, and without altering the coefficient solution (a special result for the skew-symmetric coefficient arrangement). The same transformation is also enacted on the corresponding force ellipse. This transformation (in space and time) results

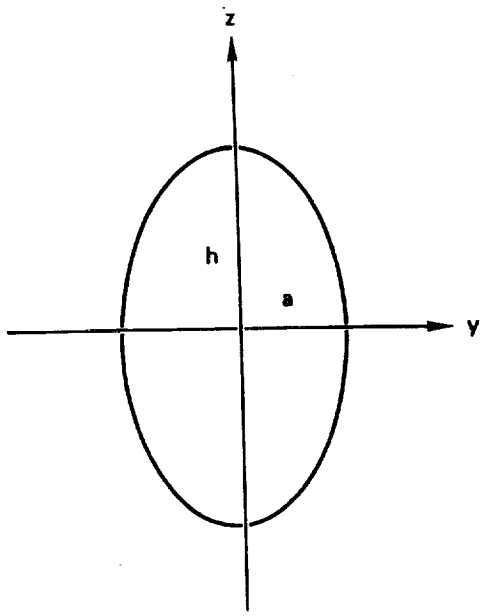

COORDINATES OF DISPLACEMENT ELLIPSE:

$$y = a\cos\omega t + \not{b}^{0}\sin\omega t$$

$$z = \not{g}^{0}\cos\omega t + h\sin\omega t$$

CORRESPONDING FORCE ELLIPSE

$$F_y = m\cos\omega t + n\sin\omega t$$

$$F_z = p\cos\omega t + q\sin\omega t$$

Figure 37. Displacement Ellipse Transformation

in b=g=0 for the fluid film displacements, and establishes an easy solution for the unknown coefficients as follows:

$$B_{yy}\omega = -(an+hp)/(a^2-h^2) \tag{17}$$

$$B_{yz}\omega = (aq-hm)/(a^2-h^2) \tag{18}$$

$$K'_{yy} = (am-hq)/(a^2-h^2) \tag{19}$$

$$K'_{yz} = -(ap+hn)/(a^2-h^2) \tag{20}$$

It is immediately apparent that for a circular displacement orbit (i.e., a=h) the solution becomes undefined, and for a nearly circular orbit the solution is ill defined. An adequate solution thus requires a sufficient amount of ellipticity in the displacement orbit.

A further understanding of what is taking place is gained by rearranging the above solution into a slightly different form:

$$B_{yz}\omega+K'_{yy} = (m+q)/(a+h) \tag{21}$$

$$-B_{yz}\omega+K'_{yy} = (m-q)/(a-h) \tag{22}$$

$$B_{yy}\omega+K'_{yz} = (p+n)/(-a+h) \tag{23}$$

$$-B_{yy}\omega+K'_{yz} = (p-n)/(a+h) \tag{23}$$

In this "sum and difference form," half of the solution is well defined even for circular orbits, while the other half is not. Synchronous excitation test rigs specifically designed to deliver circular orbits (e.g., Ref. 19) can be used only to measure $(B_{yz}\omega+K'_{yy})$ and $(B_{yy}\omega-K'_{yz})$. The remainder of the solution cannot be identified from circular orbits. The quantity $(K'_{yy}+B_{yz}\omega)$ is often referred to as the net effective stiffness, and the quantity $(B_{yy}\omega-K'_{yz})/\omega$ as the net effective damping.

An error analysis has been performed on the coefficient solution to quantify the sensitivity of the computed coefficients to experimental error as a function of the ellipticity ratio defined as follows:

$$\text{ellipticity ratio} = f = h/a \tag{25}$$

Small percentage changes in the data become excessively magnified in the coefficient solution when f approaches one (i.e., when the displacement orbit approaches a circle). As a function of f this error magnification is approximated as follows:

$$\text{error magnification} = (f/2)/(1-f) \tag{26}$$

Figure 38 shows this magnification plotted versus f. For the work reported here, f was required to be outside of the range $0.87<f<1.175$ so the magnification would be less than 3.5. When f is outside this range, stiffness and damping constants can be separated and quoted along with the net effective values. When f is inside this range, only the net effective stiffness and damping values can be obtained. With the test apparatus used here, the stator elastic support was made intentionally asymmetric, $K_{sy} \neq K_{sz}$, in order to generate the required ellipticity.

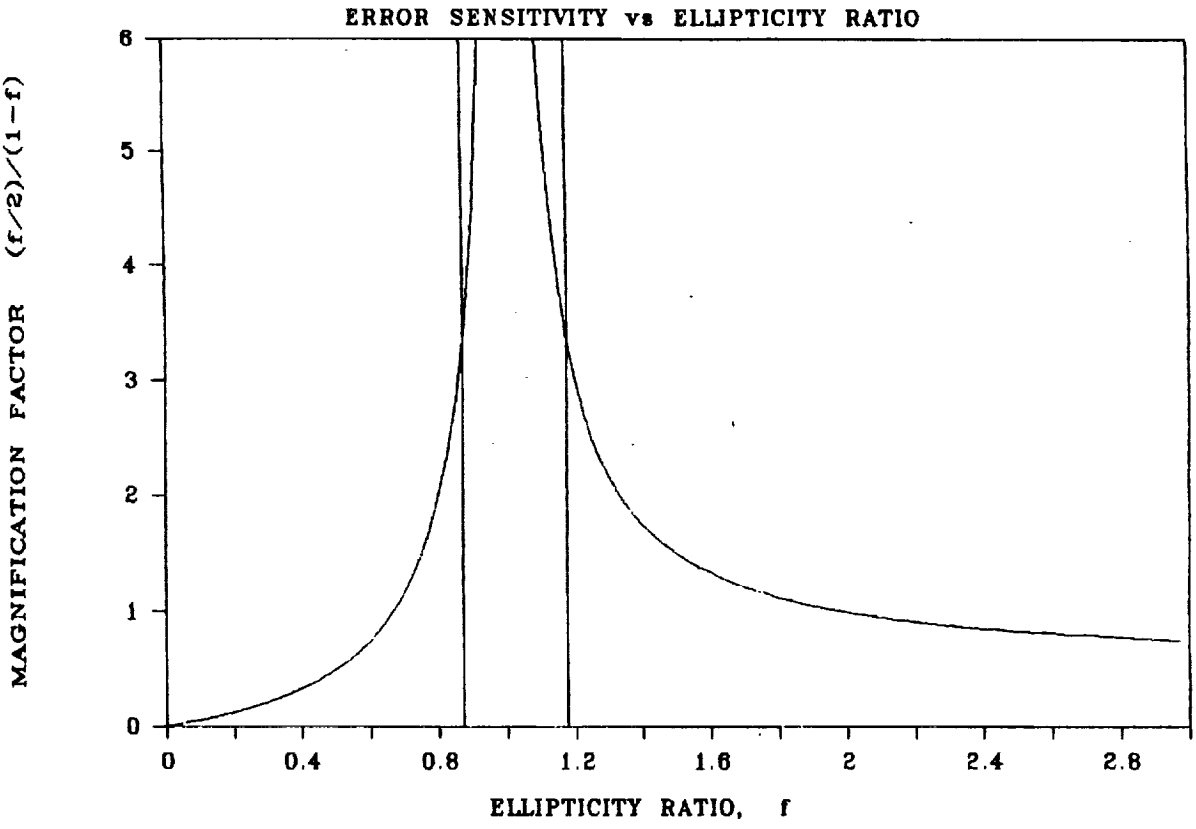

Figure 38. Error Sensitivity to Orbit Ellipticity

Test Equipment

Externally Fed Test Bearing - The externally fed test bearing is the hydrostatic element of the PLEX bearing shown in Fig. 2a. It is nominally 75 mm in diameter and 25 mm long, with six recesses in the bore of the bearing, with geometry described in Table 2. Figure 39 depicts the bearing and journal. In the tester (Fig. 40), the working fluid flows through the tubular flexure arms, and into the

ORIGINAL PAGE IS
OF POOR QUALITY

Figure 39. PLEX Bearing and Journal

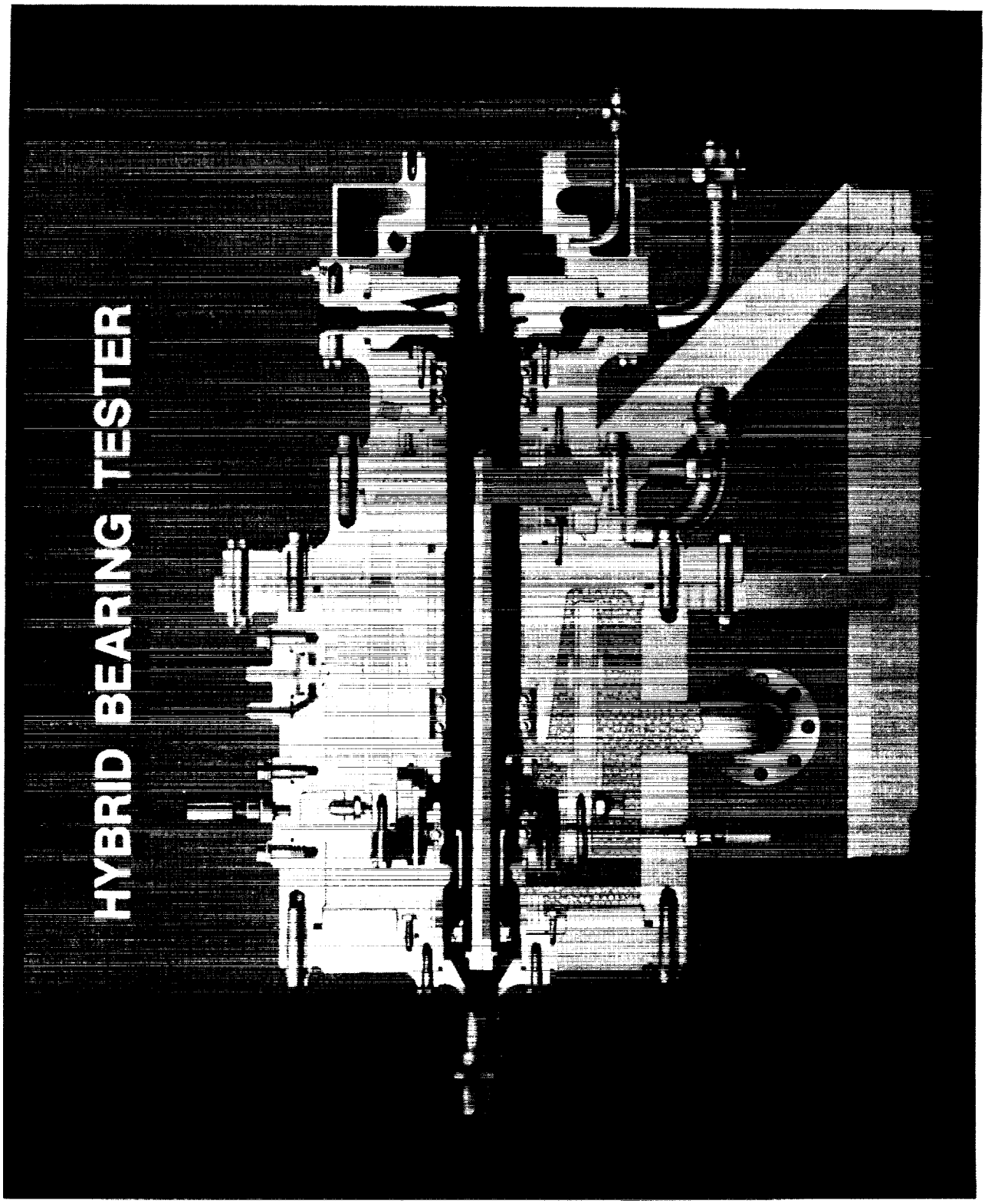

Figure 40. Bearing Tester Cross Section (Above Centerline-Externally Fed; Below Centerline-Internally Fed)

bearing annulus, through the orifices to the recesses and finally through the bearing's radial clearance to the sump. Relative radial motions of the journal are measured with two orthogonally placed proximity probes located in the center of the bearing, but displaced 15 degrees from the vertical axis to avoid interference with the recesses.

Internally Fed Test Bearing - Six recesses and compensating orifices are incorporated into the 54.6 mm (2.15 in.) diameter journal of the internally fed hydrostatic test bearing shown in Fig. (41). The geometric features of the bearing are listed in Table 3, and its cross-section in Fig. 2b. In operation, fluid is introduced to the 12.7 mm diameter hole in the shaft center through four slots 25.4 mm long by 6.35 mm wide by pressurizing the cavity between the two shaft-riding seals located at the turbine end of the tester shaft as shown below the centerline in Fig. 40. The bearing is then fed from the inner diameter of the journal. The 25.4 mm (1 in.) long bearing (Fig. 42) has a plain cylindrical bore. Relative journal/bearing motions are measured by eddy current probes, which scan an extension of the journal surface.

Bearing Tester - The bearing tester, shown in cross section in Fig. 40 was especially designed to test hybrid and hydrostatic bearings with LH_2 and LO_2, although it is suitable for use with most fluids. The shaft is supported on two preloaded pairs of 45 mm bore bearings, and is capable of operation at speeds to 5325 rad/sec (50,000 rpm) driven by the radial inflow turbine operated by ambient temperature gaseous hydrogen or gaseous nitrogen. Maximum speed achieved during the testing was 4107 rad/sec (39,229 rpm) in the LH_2 test series. In the test bearing location, the tester is constructed of Alloy 718 throughout to avoid dimensional variations due to material thermal contraction differentials. The test bearing is mounted in a stator housing, which is supported on a flexure consisting of eight tubes. To obtain sufficient radial stiffness of the stator to ensure adequate relative motion within the fluid film for the dynamic characteristics tests, four strain-gaged compression studs were incorporated as shown in Fig. 36. When preloaded against the stator, sufficient deflection is imposed to prevent unloading of any stud under maximum load.

Tester Assembly - Prior to testing with cryogenic fluids, the tester components were cleaned for propellant service and tester assembly was performed in a clean room environment. Installation of components with interference fits was accomplished by chilling with LN_2, or warming with a heat gun, or a combination of both. The assembled tester is shown from the drive turbine end (Fig. 43), and from the test bearing end prior to installation of the end cover (Fig. 44).

Instrumentation - For the LH_2 tests, the instrumentation listed in Tables 11, 12 and 13 were used to monitor control of the tester and performance of the test bearing. The high-frequency force and motion data required for definition of the dynamic characteristics were recorded on FM tape for subsequent analysis in the analog facility. Film thickness and force measurements were made in orthogonal (separated by 90 degrees of arc) planes to provide required input for calculation of stiffness and damping coefficients. Figure 35 depicts the sensor orientation for the externally fed bearing for all dynamic testing. Low-frequency parameters, such as pressures and temperatures, were digitally recorded on magnetic tape and were later reduced to CRT plots. During the actual test, real-time variations of key input and control test parameters, such as fluid pressures and temperatures,

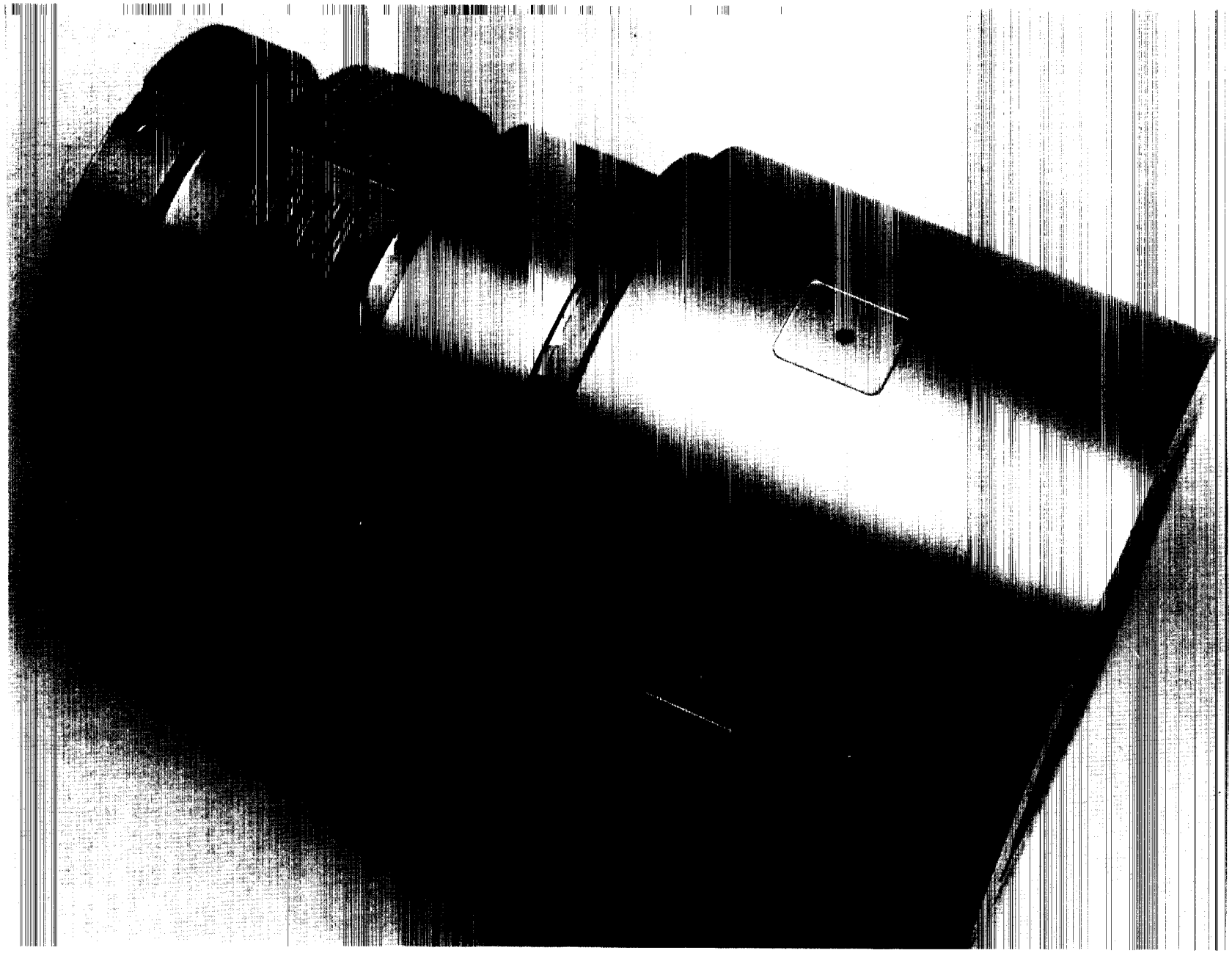

Figure 41. PLIN Bearing Journal

Figure 42. PLIN Bearing

Figure 43. Tester Assembly, Turbine End

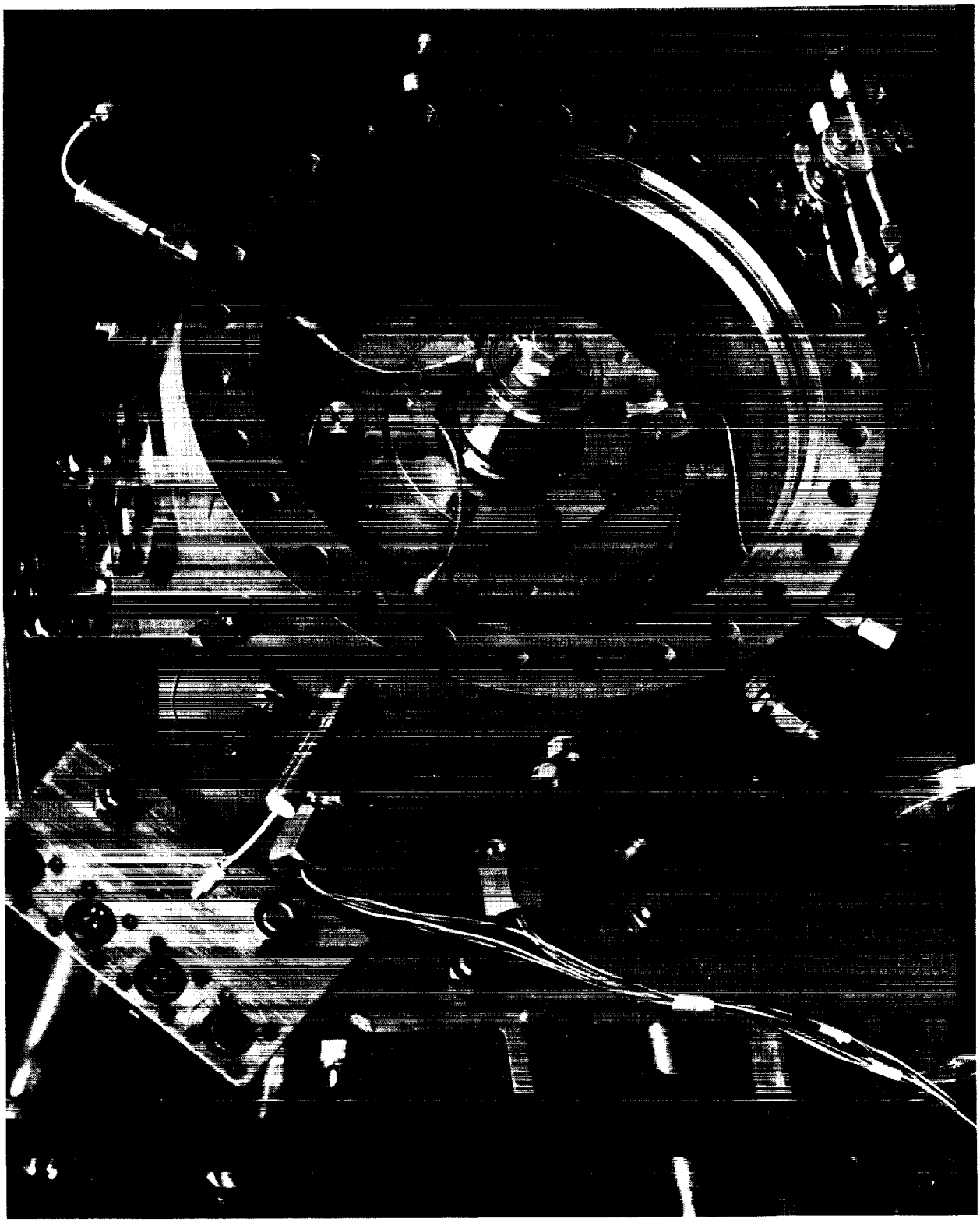

Figure 44. Tester Assembly, Test Bearing End

TABLE 11. HIGH-FREQUENCY INSTRUMENTATION

TAPE TRACK NO.	PARAMETER	TAPE CALIBRATION		
		KEY NUMBER	(KN)*	mV TO TR
1	SHAFT RPM NO. 1 (RAW)	10,000	mV	2000
2	A1Y ACCELEROMETER	140.6	GPP	2000
3	BEARING/HOUSING MOTION $-B_1Y$	2000	mV	2000
4	FLUID FILM THICKNESS - B_2Y	400	mV	2000
5	BEARING HOUSING MOTION $-B_1Z$	2000	mV	2000
6	FLUID FILM THICKNESS - B_2Z	400	mV	2000
7	STRAIN GAGE LG1	4	mV	2000
8	STRAIN GAGE LG2	4	mV	2000
9	STRAIN GAGE LG3	4	mV	2000
10	STRAIN GAGE LG4	4	mV	2000
11	SHAFT RPM NO. 2 (SCALED)	21,942	RPM	2000
12	A1Z ACCELEROMETER	140.2	GPP	2000
13	CASING ACCEL	51.2	GPP	2000
14	IRIG 'B'			-

TABLE 12. LOW-FREQUENCY INSTRUMENTATION HYDROGEN TESTS

APTF--	LIMA STAND (BEARING)	MSI--04/18/84
076076	TEST BRG SUPU PR	5000GP3951.9
075075	SUMP PR	3000GP2387.4
074074	RECESS 1 PR	5000GP4000.3
073073	RECESS 2 PR	5000GP4000.7
072072	OBD BRG CLNT SUP PR	5000GP3974.4
071071	TRB BRG CLNT SUP PR	5000GP4017.9
070070	TRB INLET PR	500GP 399.6
069069	TRB BRAKE PR	500GP 399.1
068068	LOAD CYLINDER PR	5000GP4001.6
067067	TST BRG VENT IN PR	5000GP3978.4
066066	LH2 TK11 PR	5000GP3968.2
065065	LH2 RUN LINE PR	5000GP4037.9
064064	V650 LH2 TANK PR	200GP 157.2
095095	GH2 SUPPLY PR	5000GP4009.8
094094	GH2 PREVALVE PR	5000GP3986.4
093093	SPIN VENT U/S PR	2000GP1599.8
092092	V650 DO-MOT SUP PR	2000GP1600.3
091091	HYDRAULIC PR	5000GP4008.7
090090	TST BRG VENT DP	250DP 200.4
089089	SPIN VENT DP	250DP 200.8
018018	SPIN VENT GH2 T	CA 8.00
017017	BENTLY BOX T	CA 8.00
107107	TANK 11 VENT T	-425T1 398.9
106106	TST BRG SUP T	-425T1 147.2
105105	SUMP T	-425T1 399.4
104104	OBD BRG SUP T	-425T1 400.8
103103	TRB BRG SUP T	-425T1 400.0
102102	LH2 PREVALVE TEMP	-425T1 402.5
101101	LH2 RUN LINE T	-425T1 405.3
048048	THROTTLE VALVE	PL 107.9
049049	BRG LH2 SUP VALVE	PL 106.1
050050	SPIN VALVE	PL 106.2
051051	RAD BRG LOAD VALVE	PL 106.5
079079	BRG TMP CONTROLV VALVE	PL 107.4
084084	SHAFT RPM #1	RM27428.
083083	SHAFT RMP #2	RM27428.
052052	XDUCER POWER	5.00 V 8.00
999999		
END		

TABLE 13. VISUAL RECORDER DATA LIST

LIBWAT

016 046 094 95210

WATANABE

LIMA STAND (BEARING TEST)

DATE 09/10/84

CHANL	SYS	DG SEQ	-ZERO-	-SPAN-	KEY. NO	RANGE	PARAMETER	
EVENT							SEQUENCE START	
1-1	SP5	123	0 DIV	32 DIV	3952	500 MV	TEST BRG SUP PR	
1-2	SP2	121	0 DIV	32 DIV	2395	500 MV	SUMP PR	
1-3	056	001	0 DIV	32 DIV	4004	500 MV	RECESS 1 PR	
1-4	029	002	0 DIV	32 DIV	4001	500 MV	RECESS 2 PR	
1-5	812	118	0 DIV	20 DIV	27428	1 VOLT	SHAFT RPM #1	
1-6				2 DIV		20 VLT	IRIG "B" TIMING	

CHANL	SYS	SEQ	-ZERO-	-SPAN-	KEY. NO	RANGE	PARAMETER	
EVENT							SEQUENCE START	
2-1	047	003	0 DIV	32 DIV	399.6	500 MV	TRE INLET PR	*
2-2	051	004	0 DIV	32 DIV	399.1	500 MV	TRB BRAKE PR	*
2-3	SP4	122	0 DIV	32 DIV	3983	500 MV	LOAD CYLINDER P	
2-4	808	120	10 DIV 48.8 OHM	30 DIV	147.2 OHM	500 MV	TEST BRG SUP T	
2-5	039	005	10 DIV 4.9 OHM	30 DIV	399.4 OHM	1 VLT	SUMP TEMP	
2-6				2 DIV		20 VLT	IRIG "B" TIMING	

CHANL	SYS	SEQ	-ZERO-	-SPAN-	KEY. NO	RANGE	PARAMETER
EVENT							SEQUENCE START
3-1	SVO	116	0 DIV	40 DIV	100 %	1 VOLT	BRG TMP CNT VLV
3-2	SVO	126	0 DIV	40 DIV	100 %	1 VOLT	RAD BRG LOAD VLV
3-3	SVO	125	0 DIV	40 DIV	100 %	1 VOLT	SPIN VALVE
3-4	SVO	124	0 DIV	40 DIV	100 %	1 VOLT	BRG LH2 SUP VLV
3-5	SVO	115	0 DIV	40 DIV	100 %	1 VOLT	THROTTLE VALVE
3-6				2 DIV		20 VLT	IRIG "B" TIMING

* NO ZERO VALVE
MAKE SURE CONSOLE R-CAL IS OFF BEFORE SETTING SERVO VALVE PARAMETERS.

C-2

shaft speed, and servovalve opening positions were presented on strip chart recorders for visual tracking during the test runs. Pretest and posttest calibrations of all signal paths were performed for each test. Calibration of the temperature and pressure transducers is performed on a regularly scheduled basis.

The proximity devices used to measure journal motion were calibrated at ambient temperature and at 77.6 K (-320 F). The output voltage was determined for known gaps by inserting shims a short distance into the bearing clearance at each end of the journal while applying a uniform load toward the sensor with a spring clamp. Cryogenic calibration required immersion of the entire test bearing with shims and clamp in place into LN_2. The output voltage reading was taken when all boiling stopped. It was found that, while there was a DC shift in the signal voltage, the scale factor (slope of voltage vs gap) did not change significantly with temperature. The calibration of the strain gaged spoke members was also performed at ambient and at 77.6 K. The temperature compensation of the full bridge gages was effective in maintaining the same scale factor at ambient and cryogenic temperature.

Instrumentation signal conductors required to pass through the tester housing were routed through fittings sealed with Polyurethane adhesive. Since some leakage did occur along the signal conductors, jets of inert gas were directed at instrument cable fittings to dilute the hydrogen gas. Positive static seals were used at all ports and connections to prevent leakage of the test working fluid.

Liquid Hydrogen Tests

Seven tests were conducted to determine the dynamic characteristics of the externally fed hydrostatic bearing. These tests are summarized in Appendix A. Data analysis of the hydrogen tests was not successful primarily due to an irreconciled anomaly in the phase relations between displacements and loads, which has been concluded to be the result of tester mount resonances. Modifications were made to stiffen the mount and to install additional instrumentation prior to further tests for dynamic characteristics.

Testing With Freon

Dynamic characteristic testing was continued using Freon 113 with 5% lubricating oil as the test fluid after these modifications had been made to the tester:

1. The stiffness of the mounting was increased by adding brackets to both ends of the tester.

2. Accelerometers were mounted on the casing in the vertical and horizontal directions in the plane of the test bearing.

3. Load measuring capability in both planes and asymmetric stiffness was obtained by installing strain-gaged studs of higher stiffness in the 45-degree plane. A stiffness ratio of 1.88 was achieved in order to enforce an elliptic orbit.

Fourteen sets of tests were conducted with the revised tester at speeds to 2377 rad/sec (22,700 rpm or 378 Hz) as summarized in Table 10.

Externally Fed Test Bearing - The externally fed hydrostatic bearing tested with LH_2 was used without alteration in the Freon testing. The bearing geometry is described in Table 2; it is shown in cross section in Fig. 2a.

Internally Fed Test Bearing - The internally fed bearing is described in Table 3 with the exception that the radial clearance was 0.067 mm (0.00265 in.).

Test Facility - Freon tests were conducted using a test arrangement shown schematically in Fig. 45. The installation of the tester appears in Fig. 46. Test bearing fluid supply flow is obtained by pressurizing the run tank with GN_2. From the tester drain, Freon enters a catch tank and is returned to the run tank for the next test. The speed regulation and overspeed protection functions were performed by a manually operated valve control unit.

Instrumentation - Dynamic data (Table 11), including signals from proximitors, accelerometers, strain gages, and raw speed signals, were recorded on magnetic tape. Phase relations were established by injecting oscillator signals simultaneously into each data channel so that corrections for tape head alignment and effects of transmission lines can be made if necessary. Low-frequency data, including pressures, temperatures, and analog speed, were recorded on strip charts.

Test Procedure - The Freon run tank was pressurized to start fluid flow prior to applying GN_2 to the drive turbine. The tester speed was manually controlled to produce a slow speed ramp from rest to maximum and return.

Testing - The testing conducted to measure dynamic characteristics of both externally and internally fed hydrostatic bearings is outlined in Table 10. It was found that in order to successfully produce stiffness and damping coefficients, the data must meet certain criteria:

1. The journal motion must have a minimum ellipticity ratio of 1.175 to obtain separated coefficients of direct damping and cross-coupled stiffness. The same requirement also applies to separating direct stiffness and cross-coupled damping.

2. Harmonics of synchronous frequency in the motion or load data are not acceptable. Two sources of harmonics were experienced:

   a. Minor deviations from a true circular form of the journal surface; A three-lobe out of roundness of 0.002 mm was found to produce excessive signal degradation.
   b) Rubbing of the journal in the bearing bore. Particular attention to centering of the journal within the bearing clearance was required.

Freon Testing Procedure - The flow chart in Fig. 47 illustrates the sequence of the major steps of the procedure for tester operation and calibration, data acquisition, and data reduction.

All transducer signals used in computing coefficients are stored in analog form on a single 14 channel FM tape. To ensure that channel-to-channel phase differences are preserved for data reduction, a series of sine waves are simultaneously

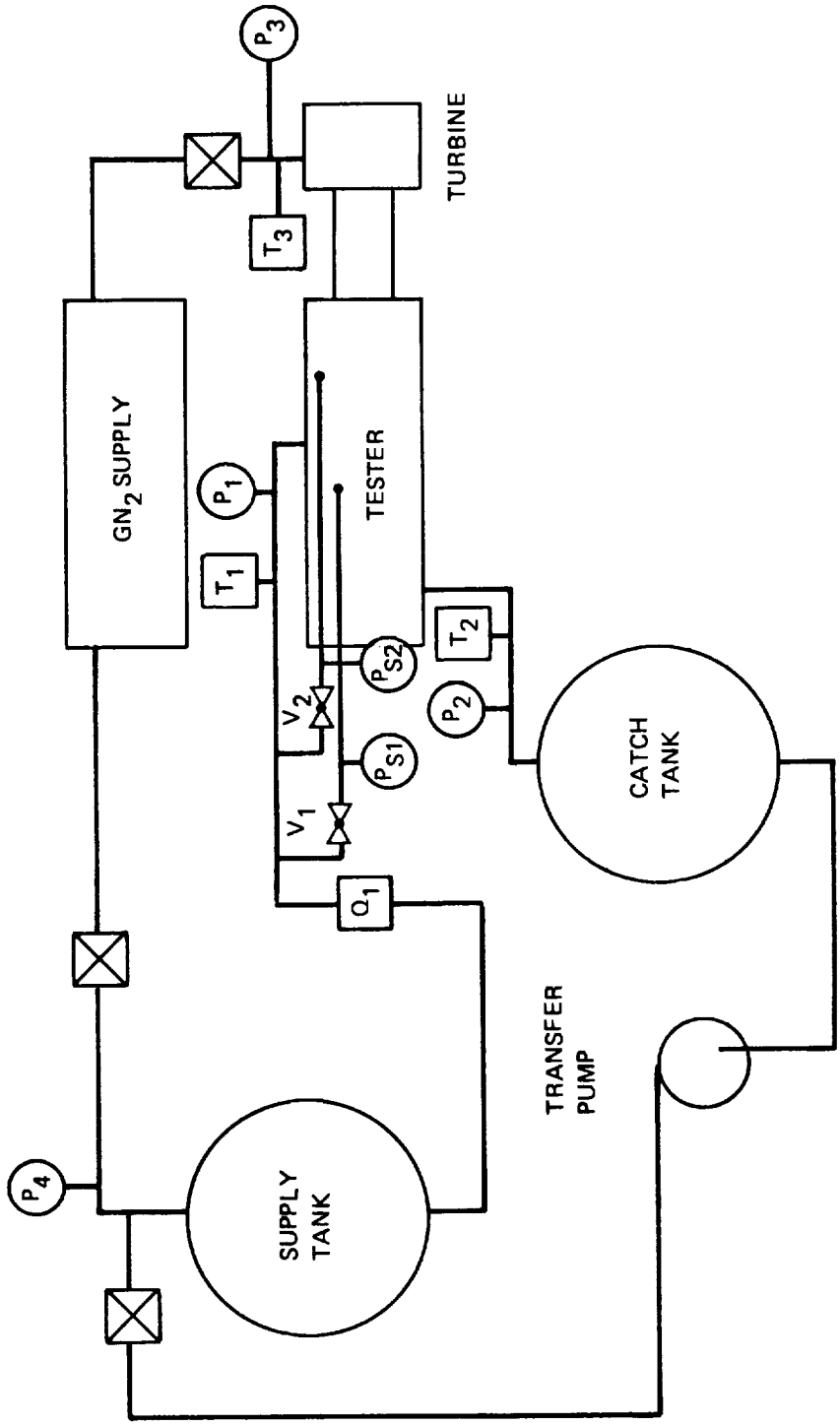

Figure 45. Freon Test Schematic

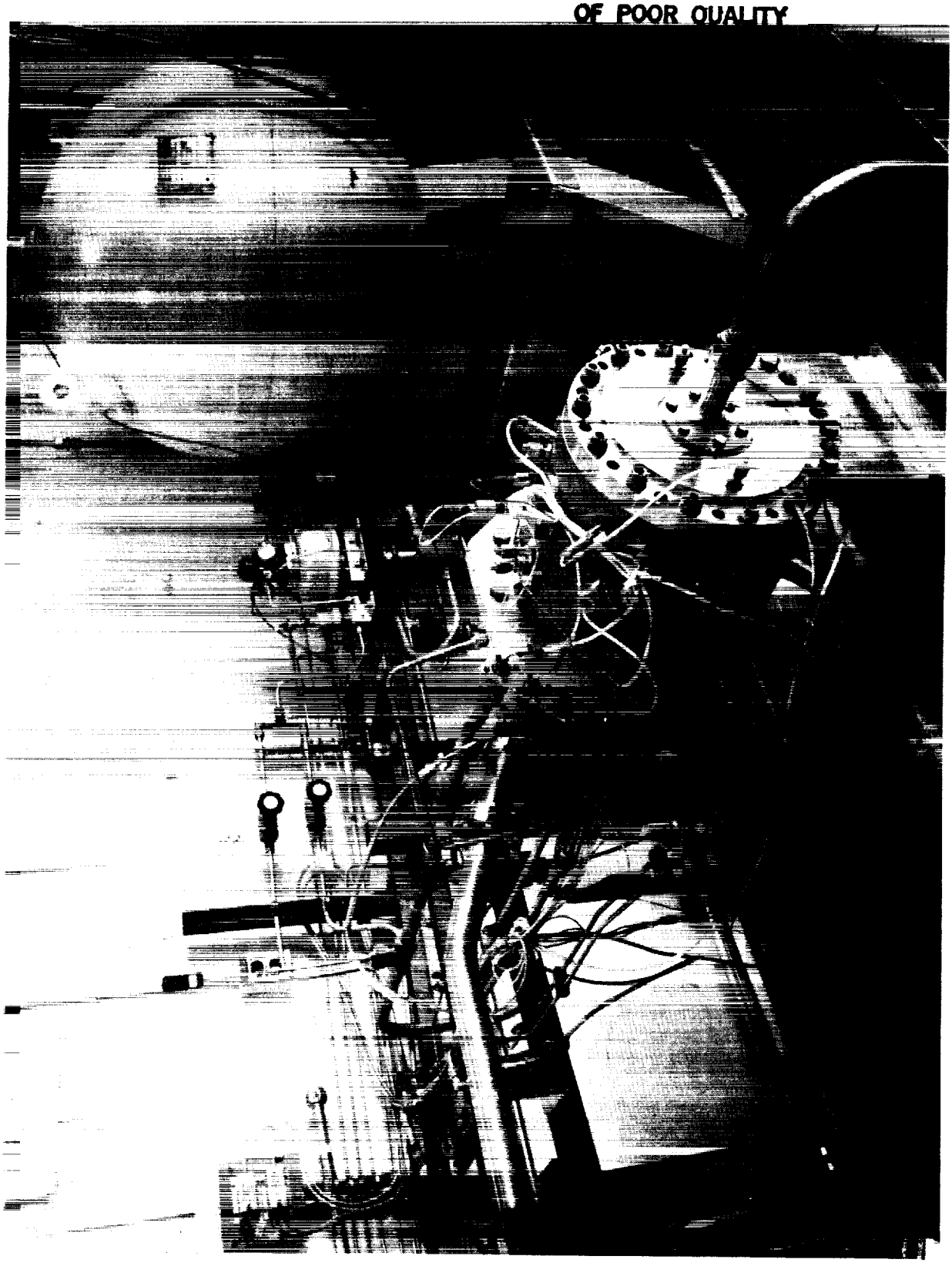

Figure 46. Freon Test Installation

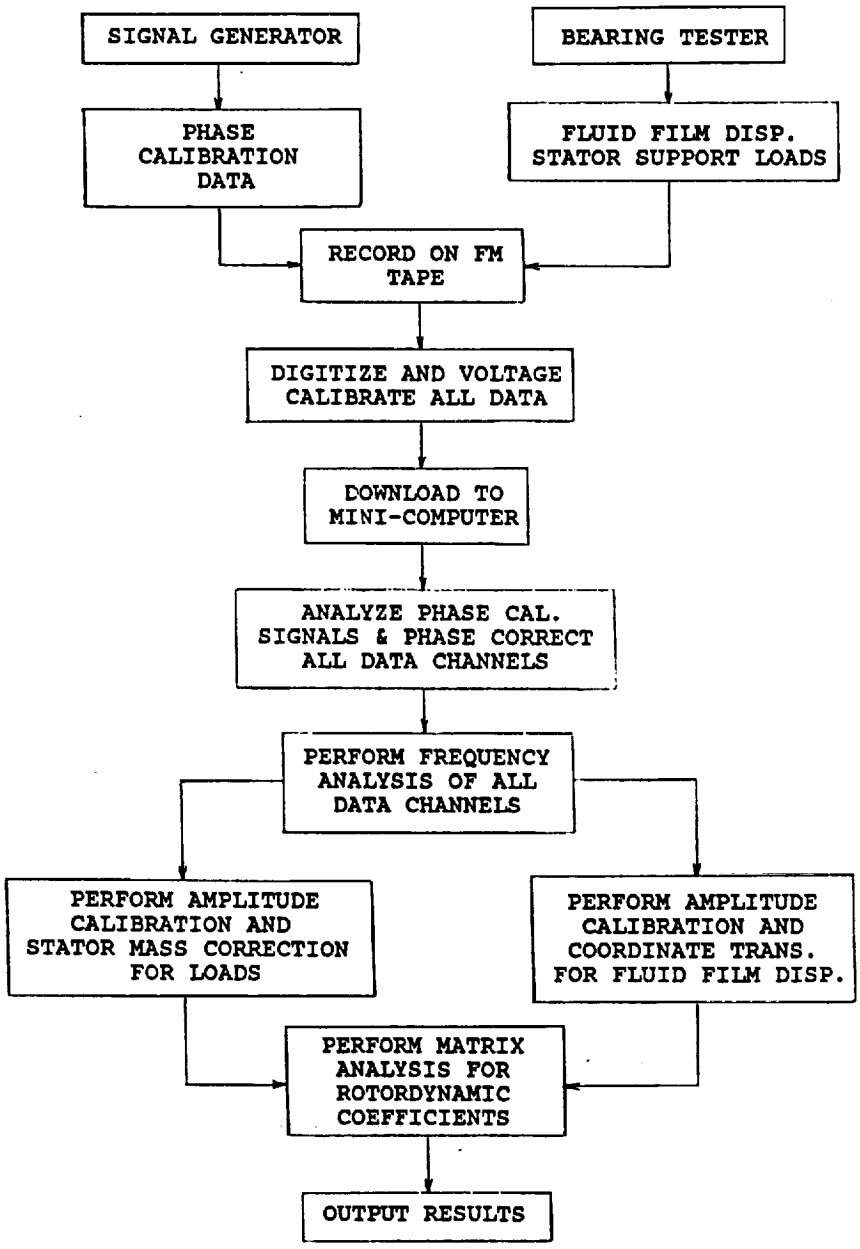

Figure 47. Test Data Acquisition and Reduction Flow Diagram

recorded on all tape channels from a common source generator before every test. On playback, any detectable phase differences between these sine waves are measured and used to correct subsequent phase errors for actual test data signals.

Before every test, calibration signals are also recorded on all active data channels as a way of accurately documenting the effect of all gain amplifiers used to individually optimize each signal amplitude for recording on tape. This defines the ratio of transducer output voltage to tape recorded voltage for each channel.

During data acquisition the supply pressure is held constant while the rotational speed is slowly ramped across the desired speed range. The speed range of the tester operating in Freon was 0 to 2377 rad/s (22,700 rpm or 378 Hz). The duration of any one test was limited to approximately 6 minutes for the externally fed bearing and 3 minutes for the internally fed bearing by the capacity of the Freon tank.

The analog data stored on FM tape, including the phase calibration data, are then digitized at 5000 samples/s and downloaded to a minicomputer. During this step the digitized FM tape voltages are scaled back to transducer output voltages.

The first task performed on the minicomputer is to analyze the phase calibration signals and phase correct all data channels. Next, the complex frequency spectrum is computed for each channel. The frequency spectrum operation performs the same function as a tracking filter by providing the synchronous amplitude and phase of each channel. The amplitude and phase are equivalent to the Fourier coefficients described earlier. The frequency analysis is performed all along the speed ramp, essentially providing a sequence of snapshots at discrete values of tester speed.

As the flow chart shows, the load signal amplitudes (from data channels F45 and F135 in Fig. 35) are converted to units of force using the static load calibration constants, and the stator inertia loads are subtracted as shown previously. Data from the pair of displacement probes (B2y and B2z) are converted to units of length, and are rotated via a coordinate transformation to be compatible with the orientation of the load sensors.

The data are now ready for use in computing rotordynamic coefficients via the matrix analysis method previously described. Test results are obtained directly from the output of this program.

Freon Testing Results and Discussion - Successful dynamic characteristic tests were achieved using Freon 113 at ambient temperature as the working fluid. Both an externally fed and an internally fed bearing configuration was tested. The dimensions of each configuration appear in Tables 2 and 3. Thirty-three tests in 14 series were conducted. However, data from only 4 of the 14 test series could be used to calculate rotordynamic coefficients. Only 2 of these had orbits that were elliptic enough to permit separation of direct and cross-coupled coefficients for stiffness and damping.

The externally fed bearing was tested with 2 different radial clearances and three different amounts of journal eccentricity. The various combinations were achieved by changing both the journal and the eccentric shaft sleeve onto which the bearing journal is mounted. Usable data were obtained only for the smaller clearance with the smallest and largest eccentricities, and separated coefficients were obtained only for the smaller eccentricity.

The internally fed configuration was tested with two journals with the same clearance, but different eccentricities. Only the test with the large eccentricity had sufficient ellipticity to permit separating the rotordynamic coefficients. For that particular test, one pair of load studs in one axis (F135 and F315 of Fig. 35) was removed and replaced with eddy current displacement probes. This increased the stator support stiffness asymmetry ratio (K_{sz}/K_{sy}) from 1.88 to 4.48, and increased the ellipticity of the relative journal orbit.

Externally Fed Bearing - The ellipticity ratio and the computed set of skew-symmetric rotordynamic coefficients are shown for both upramp and downramp in Fig. 48 through 50 for the externally fed bearing of test number F10 (Table 14).

Also shown in the figures are the predicted values for these coefficients obtained numerically with the computer program HBEAR described in Ref. 12. The orbit ellipticity ratio was greater than 1.175 and, therefore, separated stiffness and damping terms were obtained. Measured coefficients exhibit the speed trends predicted. The measured direct stiffness values are about 20% less than predicted, and the measured direct damping values are roughly equal to the predicted values. The measured cross-coupled stiffness is less than predicted, and is actually a stabilizing influence at low speed where $K_{yz}<0$.

For the test bearing configurations, the analytical code predicts low values of cross-coupled damping, whereas the test measurements show a significant amount of cross-coupled damping. To help place these results in proper perspective it should be noted that one effect of cross-coupled damping is to either add to, or detract from, the amount of asymmetry in the direct stiffness. The coefficient reduction method employed here assumes symmetric direct stiffness. One way that asymmetry in the direct stiffness can manifest itself is by the prediction of nonzero cross-coupled damping coefficients. A moderate amount of stiffness asymmetry would account for the cross-coupled damping found. In this particular case, roughly 17.5 MN/m (100,000 lb/in.) of asymmetry could produce the cross-coupled damping coefficients shown.

Since neither of the stiffness curves show a strong variation with speed squared, it is concluded that the bearing does not possess a significant inertia effect over this speed range.

A major difference between test results and theory was that the empirical K_{yz} was found to be negative rather than positive, as predicted. It is not currently understood how a negative cross-coupled stiffness can arise in a hydrostatic bearing; however, two observations can be made concerning potential causes. One possible explanation is that unexpected asymmetry may exist in the direct stiffness (not accounted for during data reduction). It can be shown theoretically that this asymmetry can produce an apparent shift in the cross-coupled stiffness value. As an example, a bearing with a direct stiffness

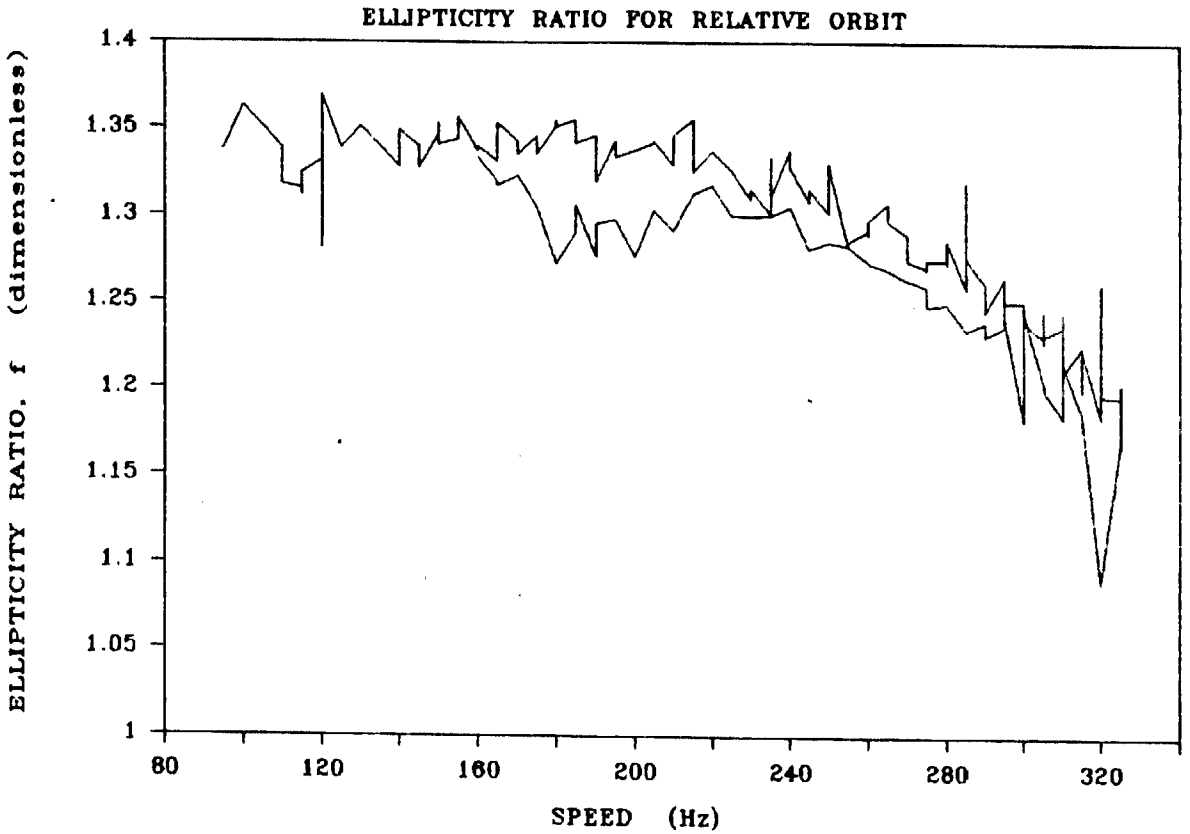

Figure 48. Orbit Ellipticity Ratio - Test F10

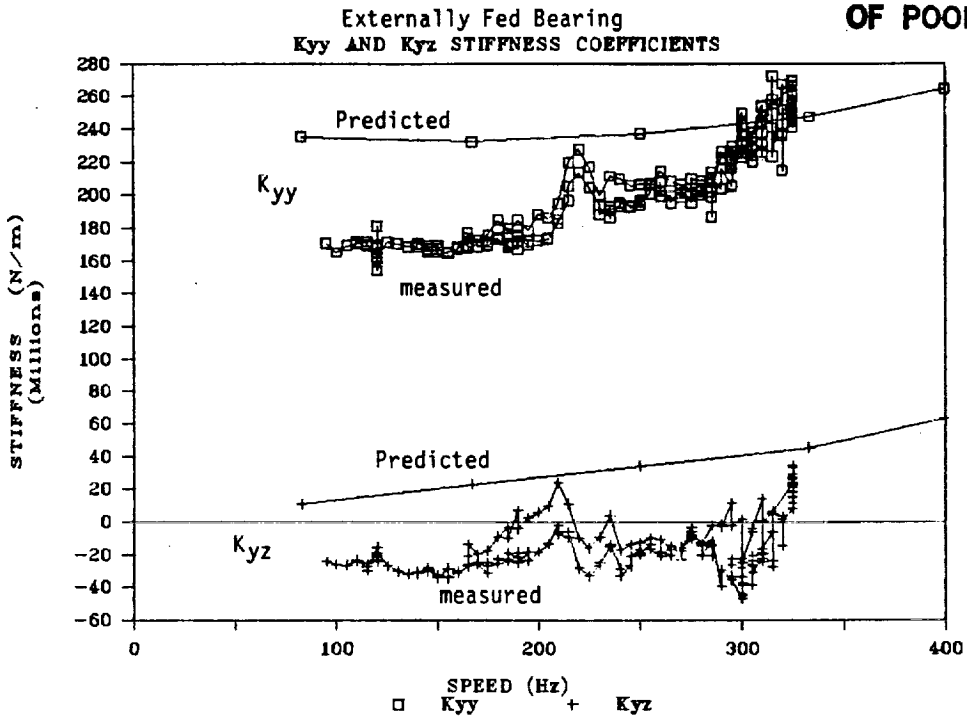

Figure 49. Stiffness Coefficient, Test F10

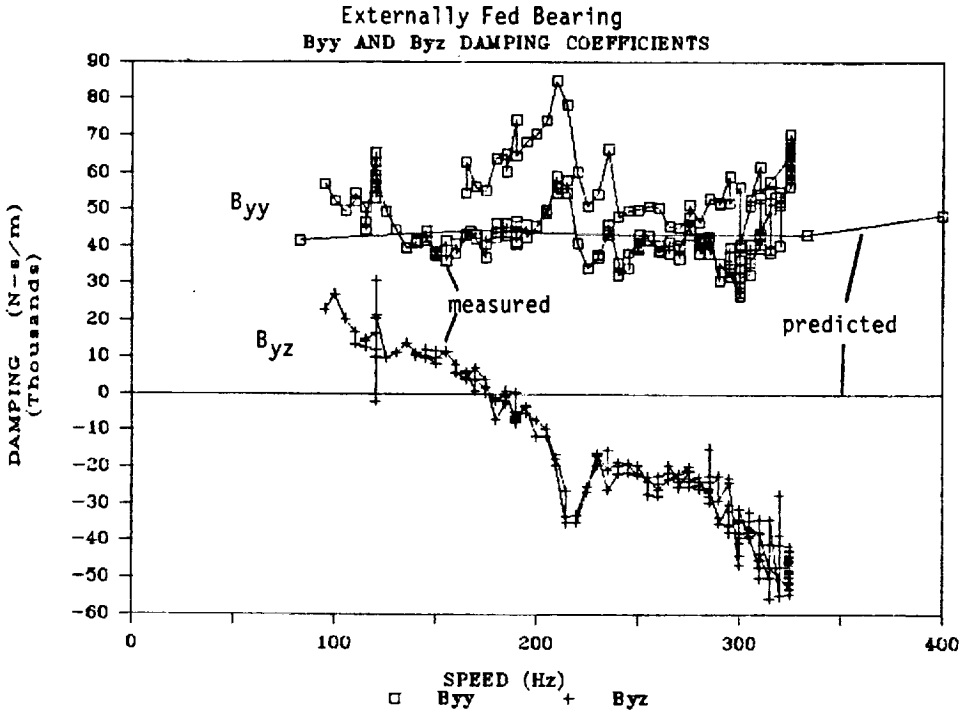

Figure 50. Damping Coefficients, Test F10

TABLE 14. HYDROSTATIC BEARING FREON TESTS SERIES

TEST NO	DATE	BEARING TYPE	INLET PRESSURE (MPa)	RADIAL CLEARANCE (E-6 m)	FREE ECCENTRICITY (E-6 m)	STATOR STIFFNESS RATIO	COEFFICIENTS SEPARATED	REASON			
								SIGNAL HARMONICS		ORBIT TOO CIRCULAR	CONCLUDED CAUSE
								FILM	LOADS		
1-3	8/30/85	EXT	10.3	43.2	6.4	1.88	NO				INSTRUMENTATION
4-7	9/4/85	EXT	10.3	43.2	6.4	1.88	NO	X			WAVY JOURNAL
8	9/10/85	EXT	3.4	43.2	6.4	1.88	YES				NEW JOURNAL
9,10			10.3								
11-13	10/14/85	EXT	10.3	43.2	12.7	1.88	NO	X			RUBBING
14,15	10/15/85	EXT	10.3	43.2	12.7	1.88	NO	X			RUBBING
16,17	10/24/85	EXT	10.3	86.4	12.7	1.88	NO		X		RUBBING
18,19	10/25/85	EXT	10.3	86.4	12.7	1.88	NO		X		PARTICLE FOUND
20,21	10/28/85	EXT	10.3	86.4	12.7	1.88	NO		X		RUBBING
22-23A	10/28/85	EXT	10.3	43.2	6.4	1.88	NO	X			WAVY JOURNAL
25,26	12/2/85	EXT	10.3	45.7	17.8	1.88	NO			X	
28	1/7/86	INT	10.3	67.3	21.6	1.88	NO			X	
29-31	1/14/86	INT	10.3	67.3	21.6	4.48	YES				
32	2/21/86	INT	10.3	67.3	8.9	4.48	NO				INSTRUMENTATION
33	2/21/86	INT	10.3	67.3	8.9	1.88	NO				INSTRUMENTATION

of 3.67e8 N/m (1.2 million lb/in.), cross-coupled stiffness of 1.75e7 N/m (100,000 lb/in.), and direct damping of 6.13e4 N·S/m (350 lb/in.) was analytically given 1.75 x 10^7 N/m (100,000 lb/in.) of direct stiffness asymmetry (i.e., K_{yy} increased by 1.75e7 and K_{zz} decreased by 1.75e7). Computing the cross-coupled stiffness according to the symmetric coefficient reduction method resulted in a negative Kyz of -1.22e7 N/m (-70,000 lb/in.). To explore this effect on the test bearing, the dynamic data from test F10 was reduced to a single pair of stiffness and damping matrixes with equal and opposite cross-coupled stiffness terms which permits the orthorgonal direct stiffnesses to be different. When this was done, the direct stiffness did become asymmetric, but K_{yz} remained negative (see page 114). Thus, direct stiffness asymmetry is not necessarily, or may be only partly, responsible for a negative empirical K_{yz}.

It may also be conjectured that sign reversal of cross-coupled stiffness may arise from the synchronous journal motion used in the test method, which is different from that of a hydrodynamic bearing operating at a fixed eccentric position. In the film with synchronous motion, the zone of decreasing radial clearance, and, therefore, maximum film pressure, leads the location of minimum film thickness, producing the damping force. Concurrently, the film thickness is expanding behind the site of minimum clearance, reducing the film pressure rise normally responsible for cross-coupled stiffness. If this effect is not entirely contained in the damping term, a reduction or actual reversal of the assumed positive sense of the force attributed to cross-coupled stiffness may occur.

Orbit ellipticity makes it possible to separate the stiffness from damping, so if the orbits were too nearly circular, only net effective stiffness and damping defined by Eq. 21 and 24 could be determined. Figures 51 and 52 show a comparison of the measured and predicted net effective stiffness and damping values. For use in analytical rotordynamic models, net effective values will suffice for performing unbalance response studies of symmetrically supported rotors, but they are not adequate for performing rotordynamic stability studies, or for unbalance studies of asymmetrically supported rotors. As an example, direct damping and cross-coupled stiffness represent energy transferral mechanisms. The cross-coupled stiffness adds energy to the system and the direct damping dissipates it. The energy balance between them determines: (1) system stability and (2) response amplitudes to forcing functions. This energy balance is dependent on the frequency of motion and whirl orbit shape. This dependency is properly modelled only by separate stiffness and damping coefficients. Combined, or net effective, values give the correct balance only for the special case of circular synchronous orbits (i.e., for unbalance response of symmetrically supported rotors).

The bearing of test F10 was operated with a bearing inlet pressure of 10.3 MPa (1500 psi). In test F8 the same bearing was tested with an inlet pressure of 3.4 MPa (500 psi). Figures 53 through 57 show the ellipticity ratio and comparisons of measured and predicted stiffness and damping. The results are similar to those for test F10 except for the correspondingly lower magnitudes due to the lower inlet pressure. Also, agreement with the predictions is not as close as for test F10. Figures 58 and 59 directly compare the net effective values and show them to be very nearly proportional to inlet pressure.

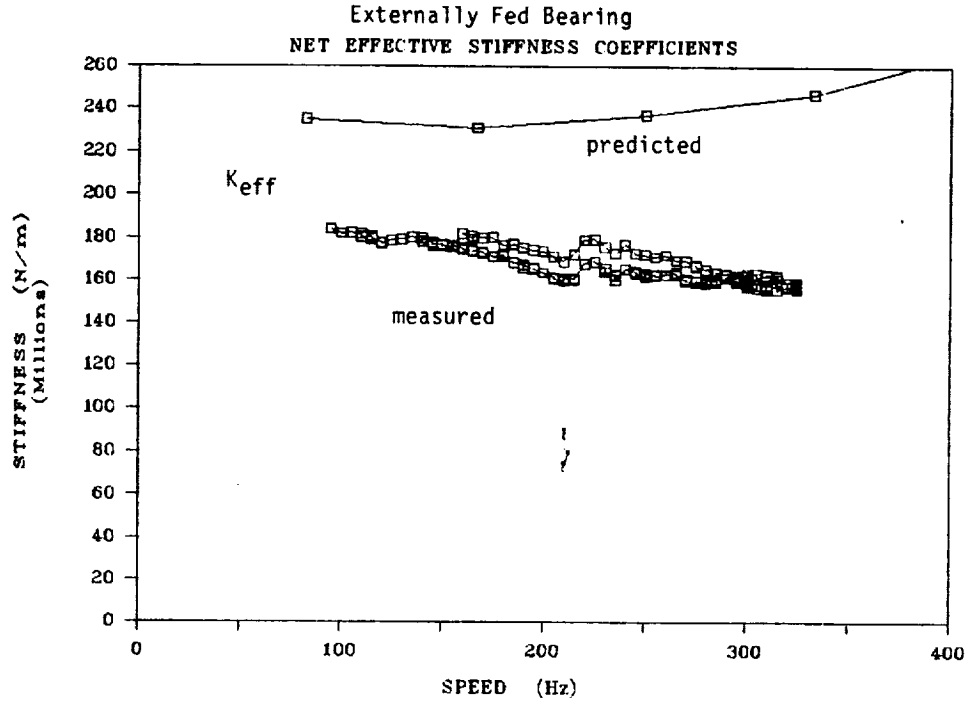

Figure 51. Net Effective Stiffness Coefficients, Test F10

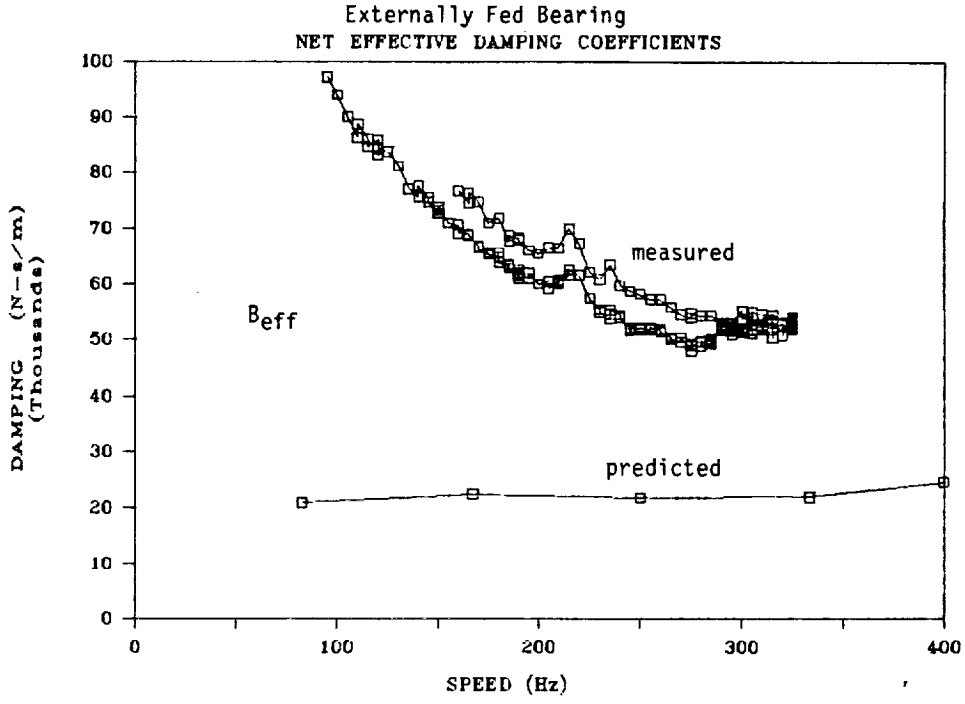

Figure 52. Net Effective Damping Coefficients - Test F10

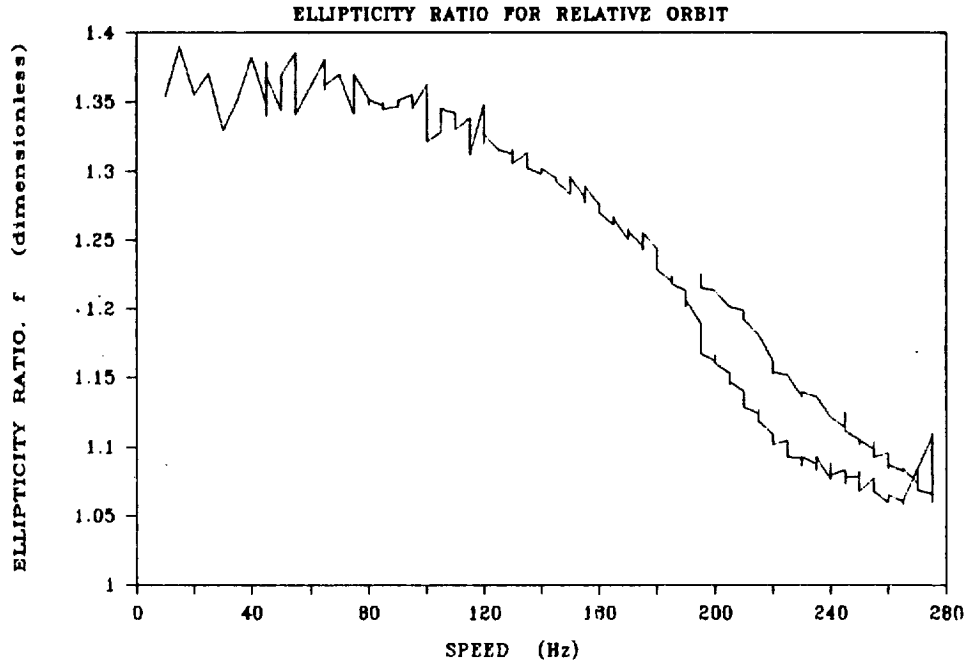

Figure 53. Orbit Ellipticity Ratio, Test F8

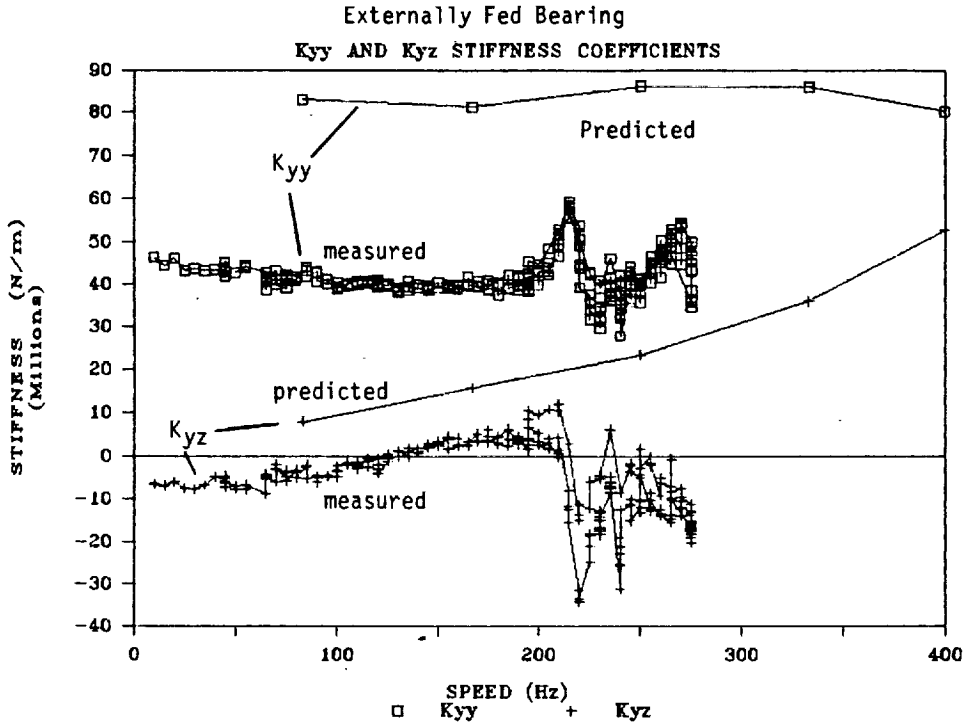

Figure 54. Stiffness Coefficients, Test F8

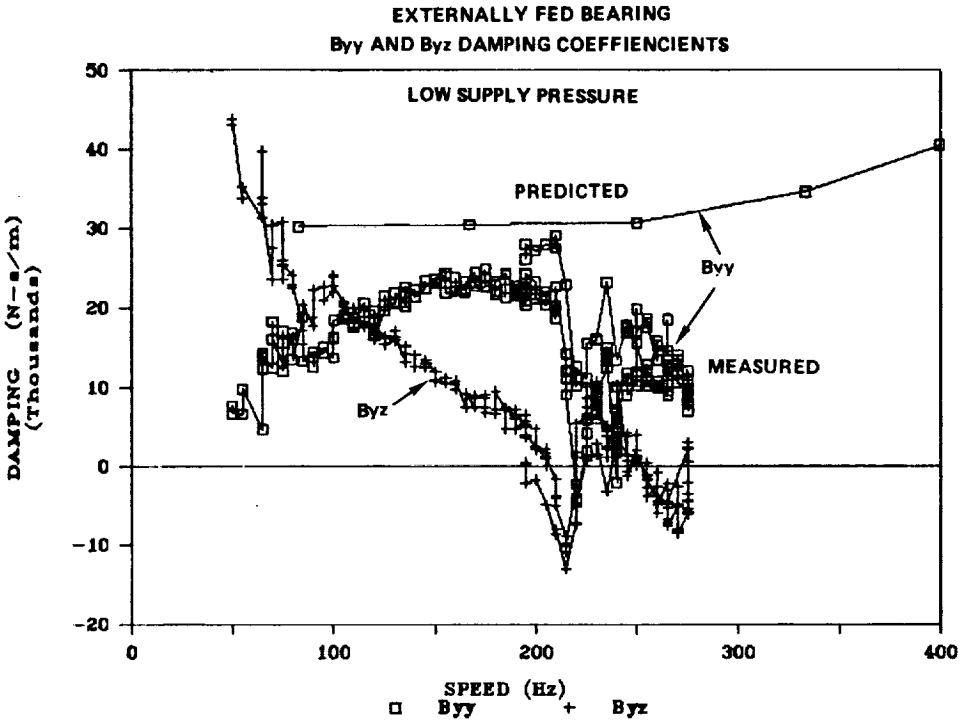

Figure 55. Damping Coefficients, Test F8

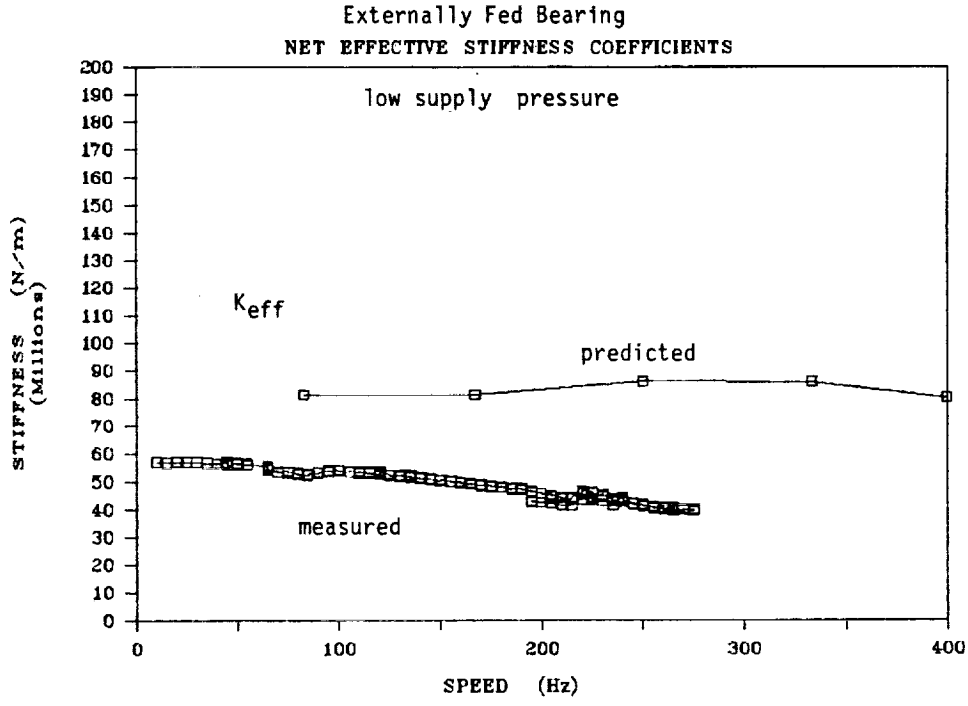

Figure 56. Net Effective Stiffness Coefficients, Test F8

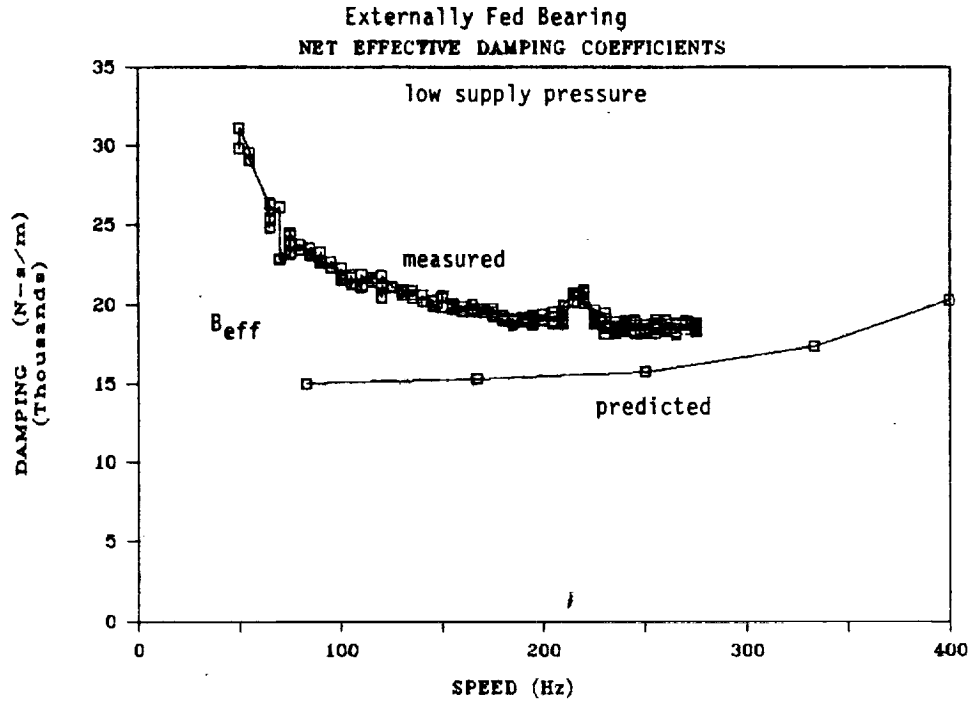

Figure 57. Net Effective Damping Coefficients, Test F8

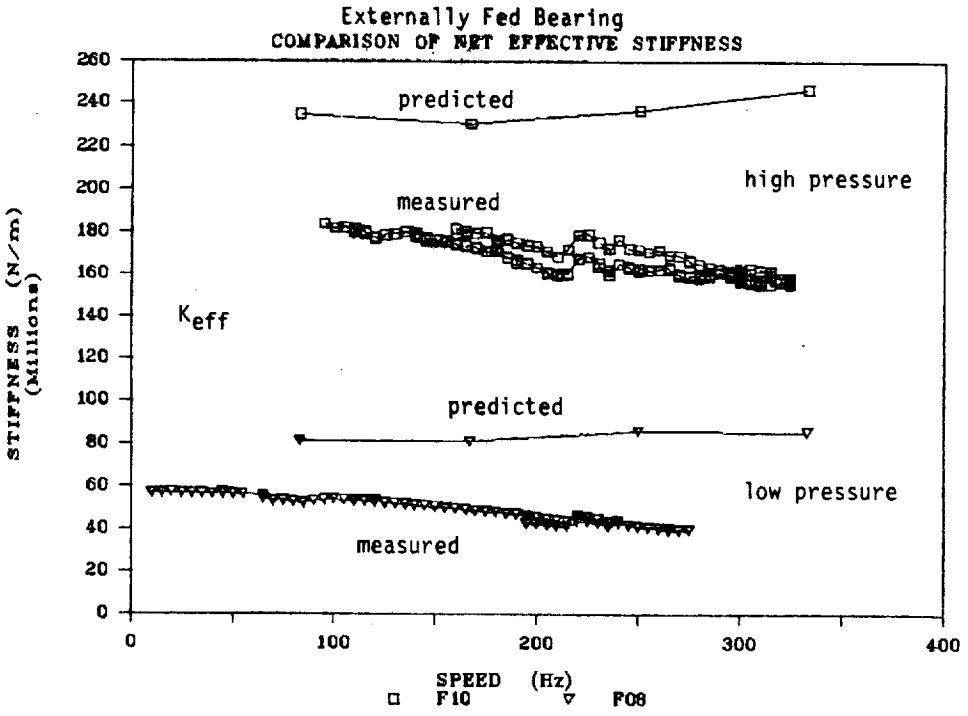

Figure 58. Net Effective Stiffness at Two Supply Pressures

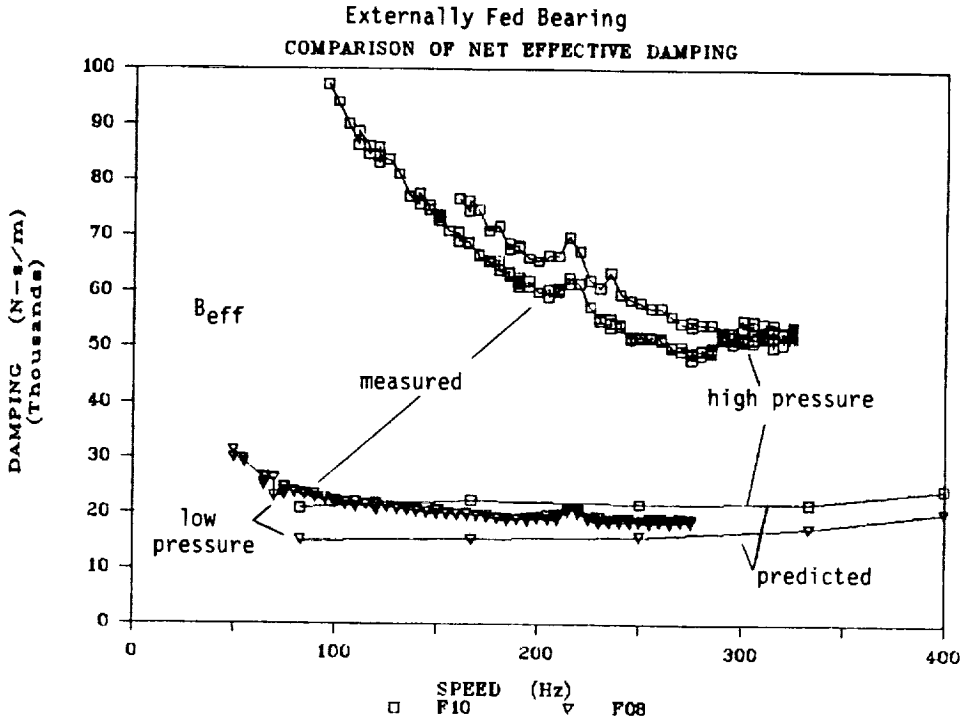

Figure 59. Net Effective Damping at Two Supply Pressures

In Test F8, as tester speed surpassed 200 Hz, the ellipticity ratio fell below the 1.175 criteria for separable data (Fig. 53). At this point, the curves for the separated coefficients become more erratic (Fig. 54 and 55). The net effective values of Fig. 56 and 57 should not, and are not, affected by the orbit becoming more circular.

Since the bearing was much softer for test F8, larger displacements were experienced which resulted in a larger signal to noise ratio than for test F10. As a result, the data of test F10 are slightly more erratic than that of test F8. In test F10, the relative displacements across the fluid film were on the order of 0.6 to 1.0 μm (25 to 40 μ in), contrasted to the 1.5 to 2.5 μm (60 to 100 μ in) for test F8.

The difference in coefficient values formed during upramp versus downramp may be due to differences in orbit ellipticity (Fig. 48). It is not known why the direct damping (Fig. 50) and cross-coupled stiffness (Fig. 49) are affected more than direct stiffness and cross-coupled damping.

Test F26 of the externally fed configuration yielded data that could be reduced for rotordynamic coefficients. Test F26 (Table 14) was essentially a repeat of test F10 but with larger shaft eccentricity. Also, it employed a very fast speed ramp rate up to about 250 Hz shaft speed. The displacement orbits were too circular to permit separation of stiffness from damping, and thus only the net effective values can be quoted. Figures 60 and 61 compare the stiffness and damping obtained in tests F10 and F26. The net effective stiffness was somewhat higher and damping lower for test 26. Although the operating conditions will not theoretically affect the coefficients, test 26 was conducted with a larger eccentricity and higher speed ramp rates.

Internally Fed Bearing - Two successful tests, F28 and F31, were conducted with the internally fed bearing. In test F28 the ellipticity ratio was extremely close to 1, and thus only net effective values can be quoted. The probable cause for small ellipticity is that the internally fed bearing produces a much lower overall stiffness than the externally fed bearing, and thus generated less motion of the asymmetrically supported stator. It is forced motion of the stator that causes the relative orbits to be elliptic. For test F31 two load studs were removed from one axis, as described earlier, and replaced with displacement probes. This action increased the amount of stator support stiffness asymmetry, and resulted in an ellipticity ratio that satisfied the 1.175 criteria. Another consequence of removing the load studs from one axis was the reduction of control over centering of the stator in that axis. The bearing's stator element is centered about the bearing journal by adjusting the preloads in the load cells. When the load cells were removed, the ability to provide positive centering in that axis was lost. If the shaft is not centered, significant asymmetry in the fluid film coefficients may result.

Figures 62 through 64 show the ellipticity ratio and the measured and predicted net effective stiffness and damping for test F28. The differences between predictions and measurements are qualitatively the same as those noted for the externally fed bearing. The net effective stiffness was overpredicted by 100 to 150% versus about 20% for the externally fed bearing. The net effective damping was both predicted and measured to be very small, and was underpredicted as it was for the externally fed bearing. Meaningful percentage differences cannot be quoted in this case as the measured and predicted values are of opposite sign.

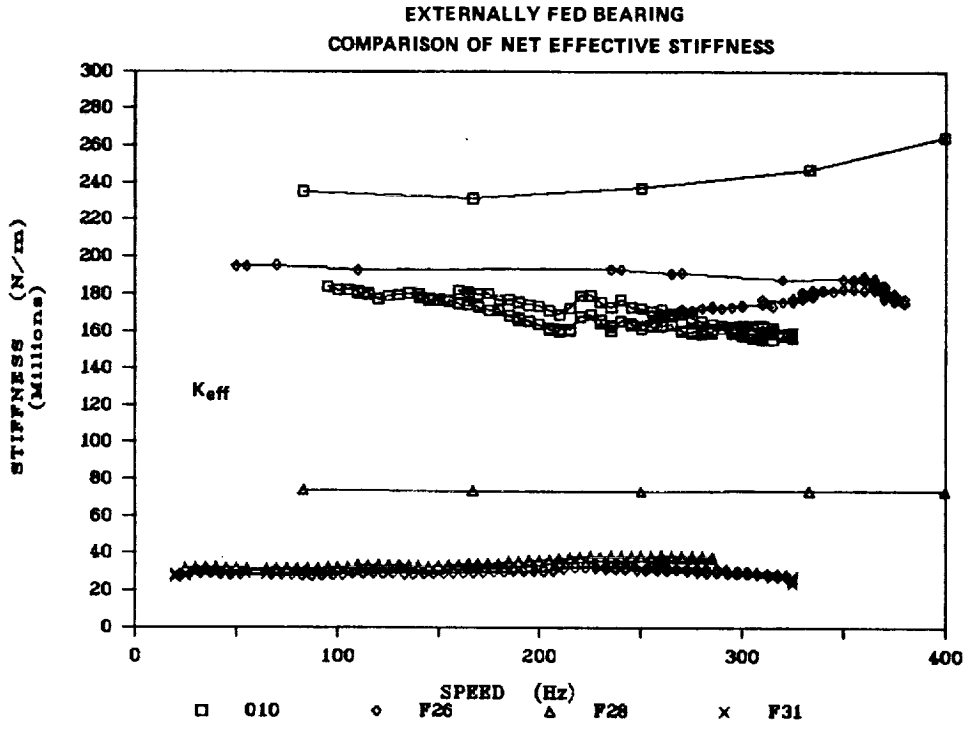

Figure 60. Net Effective Stiffness, Tests F10 and F26

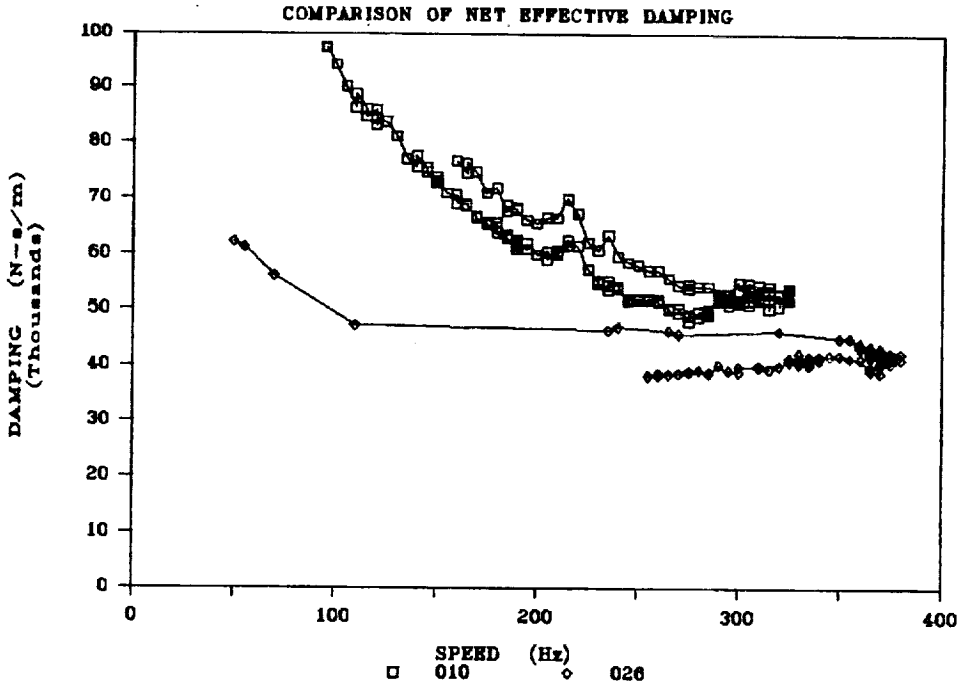

Figure 61. Net Effective Damping, Tests F10 and F26

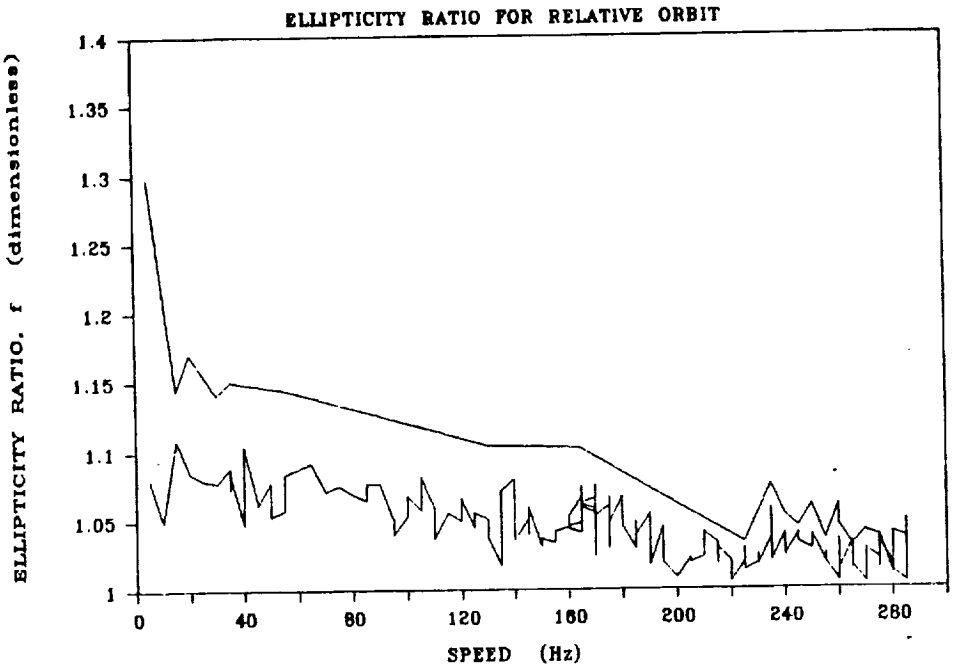

Figure 62. Orbit Ellipticity Ratio, Test F28

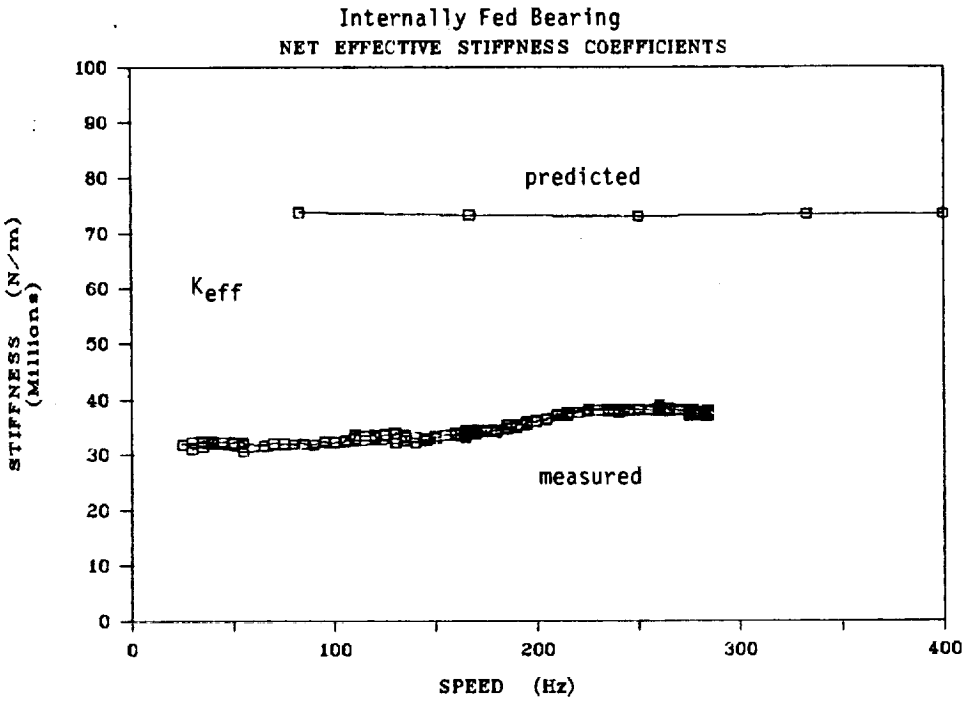

Figure 63. Net Effective Stiffness, Internally Fed Bearing, Test F28

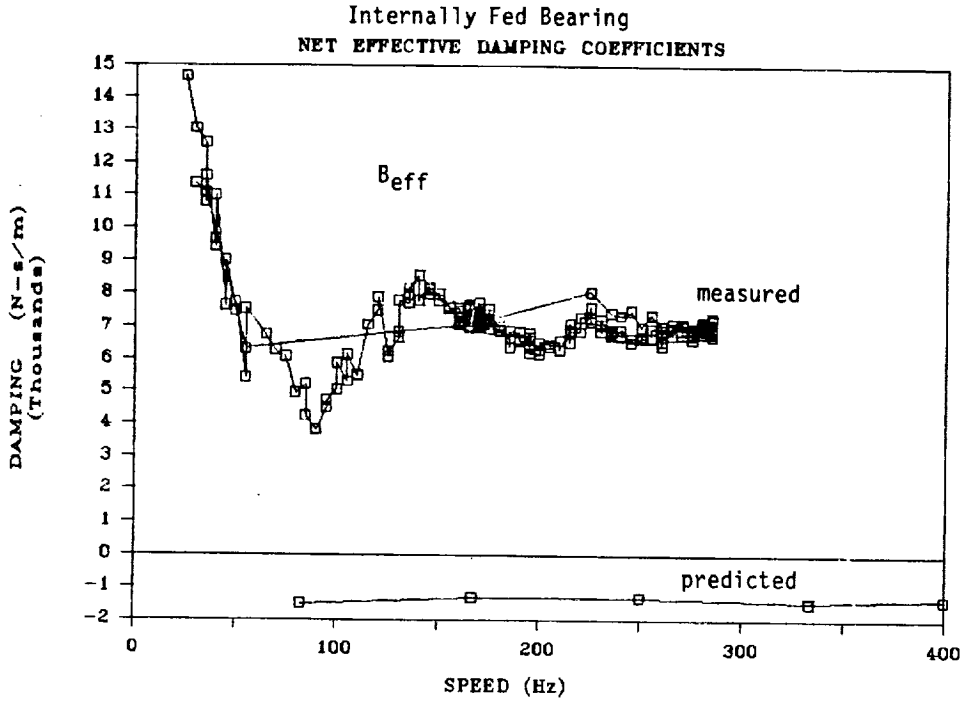

Figure 64. Net Effective Damping, Internally Fed Bearing, Test F28

Figures 65 through 69 show the ellipticity ratio and all measured and predicted coefficients for test F31 (in which two load studs were removed). The separated stiffness and damping coefficients do not exhibit the qualitative agreement with predictions that the externally fed bearing shows. The measured and predicted direct stiffness actually agree quite well in magnitude at high speed, but the measurements show a major speed dependence not predicted. The direct damping was measured to be negative at low speed, and also shows a major speed dependency not predicted.

The net effective stiffness and damping values for test F31 compare favorably to those of test F28, which had consistent correlation between measurement and theory. Two potential causes exist for the prominent speed dependency exhibited by the internally fed bearing:

1. The effect of fluid tangential velocity induced by the rotating recesses may have more influence than anticipated in the analysis (see Internally Fed Bearing Coefficients, page 55).
2. A static eccentricity (radial displacement of stator and shaft centers) may be the cause of speed dependency, although the value in the test bearing was low. Feeler gage checks of the test bearing clearance indicated that the bearing was centered within 0.0016 mm (0.0003 in.).

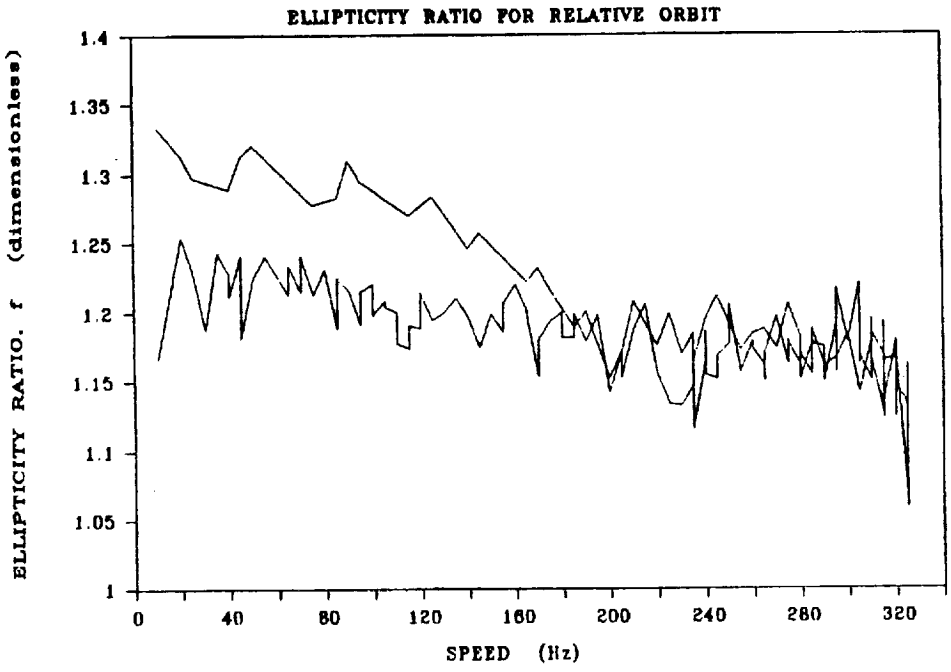

Figure 65. Orbit Ellipticity, Internally Fed Bearing, Large Stator Stiffness Asymmetry

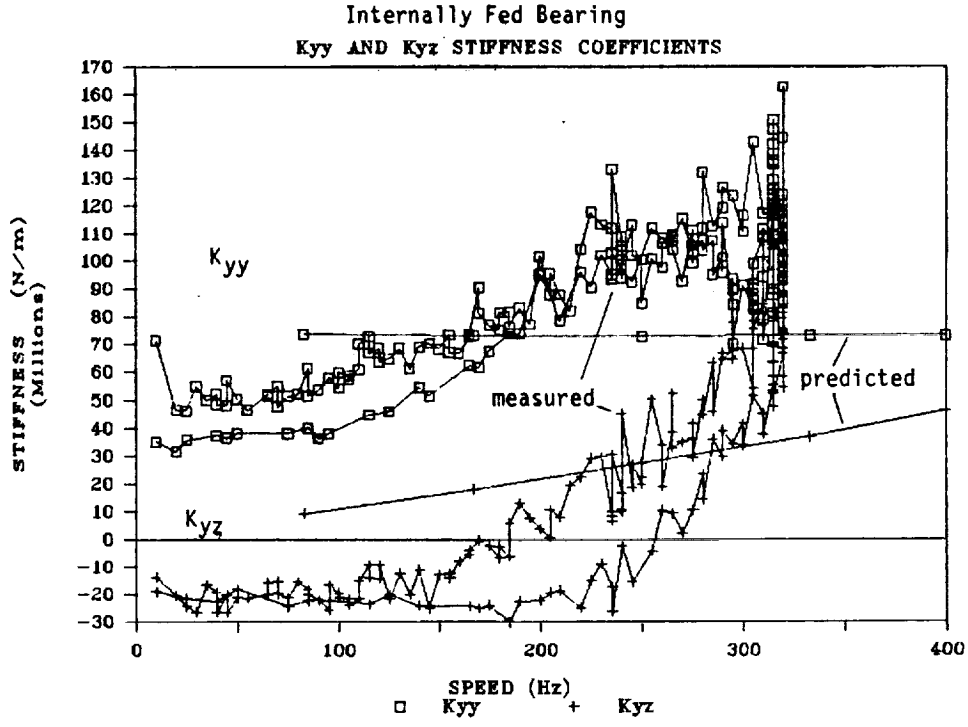

Figure 66. Stiffness Coefficients, Internally Fed Bearing, Test F31

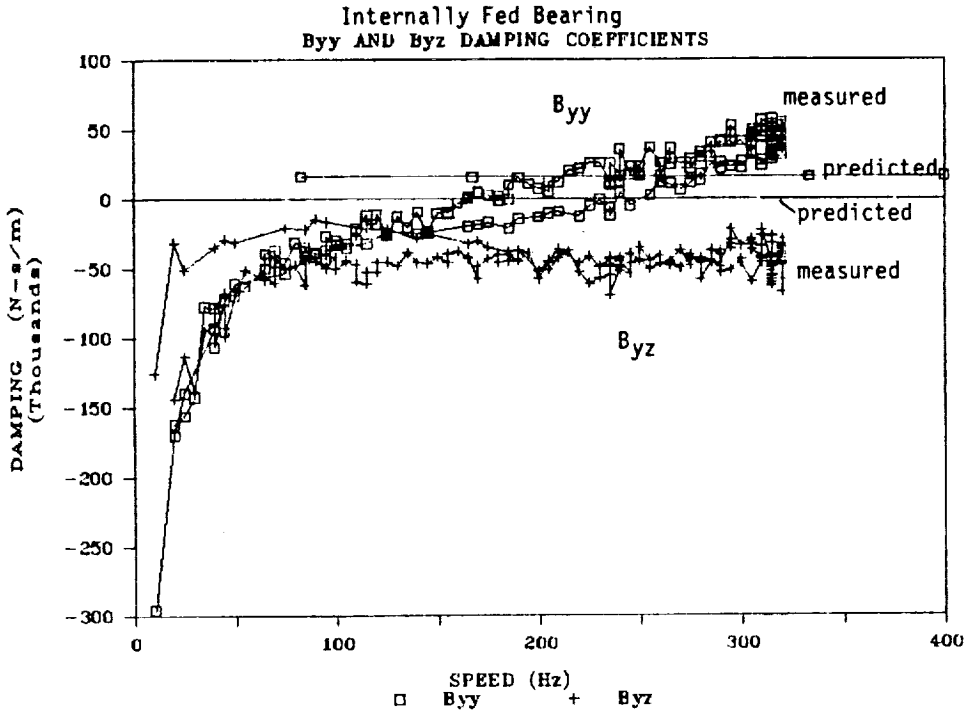

Figure 67. Damping Coefficients, Internally Fed Bearing, Test F31

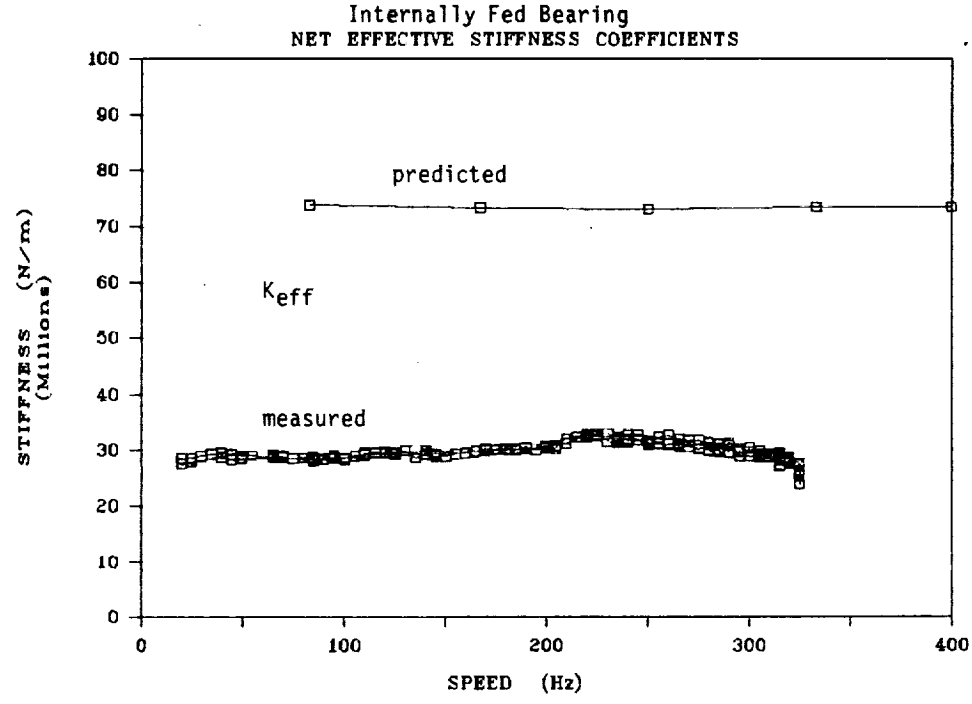

Figure 68. Net Effective Stiffness Coefficients, Internally Fed Bearing, Test F31

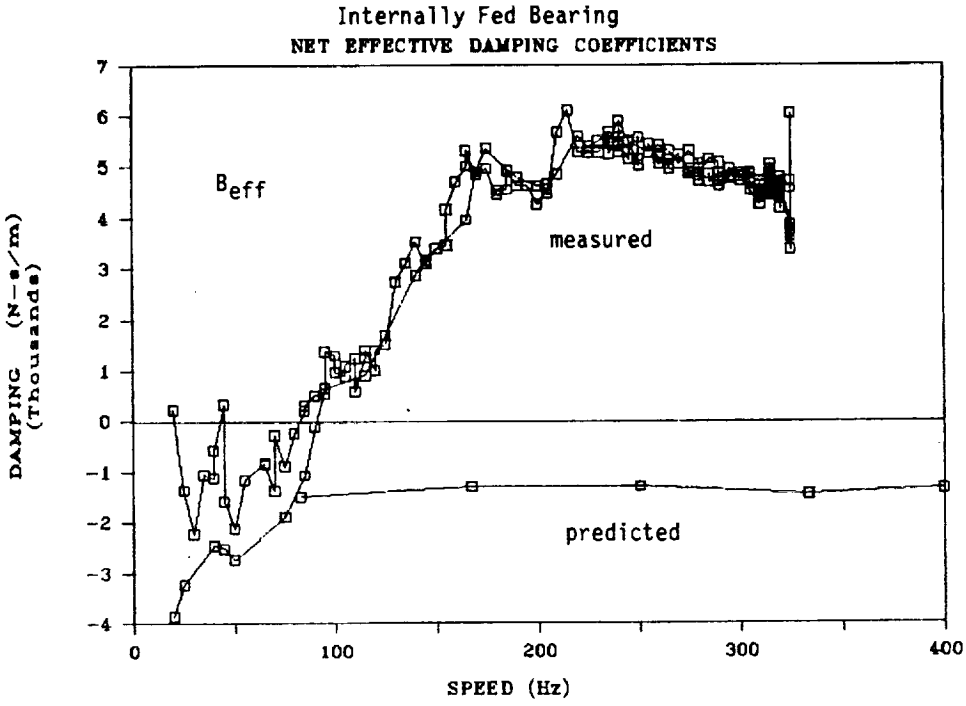

Figure 69. Net Effective Damping Coefficients, Internally Fed Bearing, Test F31

The data reduction process of Eq. 14 assumes the rotordynamic coefficients to be skew-symmetric. If, in fact, they are not skew-symmetric as a result of bearing asymmetry or miscentering, this condition will manifest itself in the data reduction process by causing the calculated coefficients, assumed to be skew-symmetric, to vary with speed.

Speed Dependency vs Asymmetry - If the data for the internally fed bearing of test F31 are reduced according to the asymmetric method of Eq. 13, the following set of stiffness and damping values are produced:

$$\begin{bmatrix} K_{yy} & K_{yz} \\ K_{zy} & K_{zz} \end{bmatrix} = \begin{bmatrix} 22.3 & 2.9 \\ -2.9 & 34.6 \end{bmatrix} \text{ MN/m}$$

$$\begin{bmatrix} B_{yy} & B_{yz} \\ B_{zy} & B_{zz} \end{bmatrix} = \begin{bmatrix} -.96 & 2.13 \\ -.62 & 13.0 \end{bmatrix} \text{ kN-s/m}$$

These values are dependent on the arbitrary orientation of the yz coordinate system. Stiffness and damping values computed for the yz coordinate system of Fig. 35 have been rotated to make the cross-coupled stiffness values of equal magnitude and opposite sign. In this case, the required rotation is 28 degrees counterclockwise. However, by enforcing skew-symmetry in K_{yz} and K_{zy}, large asymmetry arises in the direct coefficients. The resulting direct stiffness values are different by a factor of 1.55, and the direct damping values are different by a factor of 13.5, and are of opposite sign.

The same procedure applied to the externally fed bearing test F10 results in:

$$\begin{bmatrix} K_{yy} & K_{yz} \\ K_{zy} & K_{zz} \end{bmatrix} = \begin{bmatrix} 211 & -46 \\ +46 & 174 \end{bmatrix} \text{ MN/m}$$

$$\begin{bmatrix} B_{yy} & B_{yz} \\ B_{zy} & B_{zz} \end{bmatrix} = \begin{bmatrix} 20.5 & -30.4 \\ +.98 & 32.0 \end{bmatrix} \text{ kN-s/m}$$

Asymmetry in the direct stiffness and damping is much less pronounced for test F10 with ratios of only 1.2 and 1.6, respectively.

Both reduction methods result in stiffness and damping values that produce excellent correlation between the measured forces and displacements. Therefore, deciding which method is more correct involves choosing between the existence of general asymmetry and speed dependency for the rotordynamic coefficients. One set of coefficients contains asymmetry, but is unaffected by speed. The other set assumes skew-symmetry, but yields a direct measure of speed dependency. The choice must be dictated by which of the two conditions is expected to be most significant.

All predicted coefficients are skew-symmetric and vary with speed. Figures 49 and 50 for test F10 show that the measured speed dependency parallels the predicted speed dependency. The asymmetric coefficient set for test F10 indicates only minor asymmetry of direct stiffness and damping. Figures 66 and 67 for the internally fed bearing in test F31, however, show a dramatic difference between measured and predicted speed dependency for skew-symmetric coefficients. At the same time, the asymmetric coefficient set for test F31 shows large differences in the direct stiffness and damping.

Thus, for test F31 either the coefficients are approximately skew-symmetric and the measured speed dependency is real, or the coefficients are in reality asymmetric and the measured speed dependency in the skew-symmetric coefficients is part real and part due to asymmetry.

The most plausible source of significant coefficient asymmetry is static miscentering of the stator about the bearing journal. The feeler gage checks previously described indicated that the bearing was centered within 12% of the clearance. Analysis of generic fluid film components has shown that miscentering must be as much as 50% of the clearance to produce significant asymmetry. Thus, the internally fed hydrostatic bearing may be more sensitive to miscentering than other types of fluild film elements.

Summary: Internally vs Externally Fed - Figures 70 and 71 show the net effective stiffness and damping for all tests run at a common bearing supply pressure of 10.3 MPa (1500 psi). The internally fed bearing was physically smaller than the externally fed bearing, and also had larger clearance. Both these differences tend to lower the stiffness and damping, but are accounted for in the predicted values. The most important aspects of a direct comparison of the internally versus externally fed configurations are as follows:

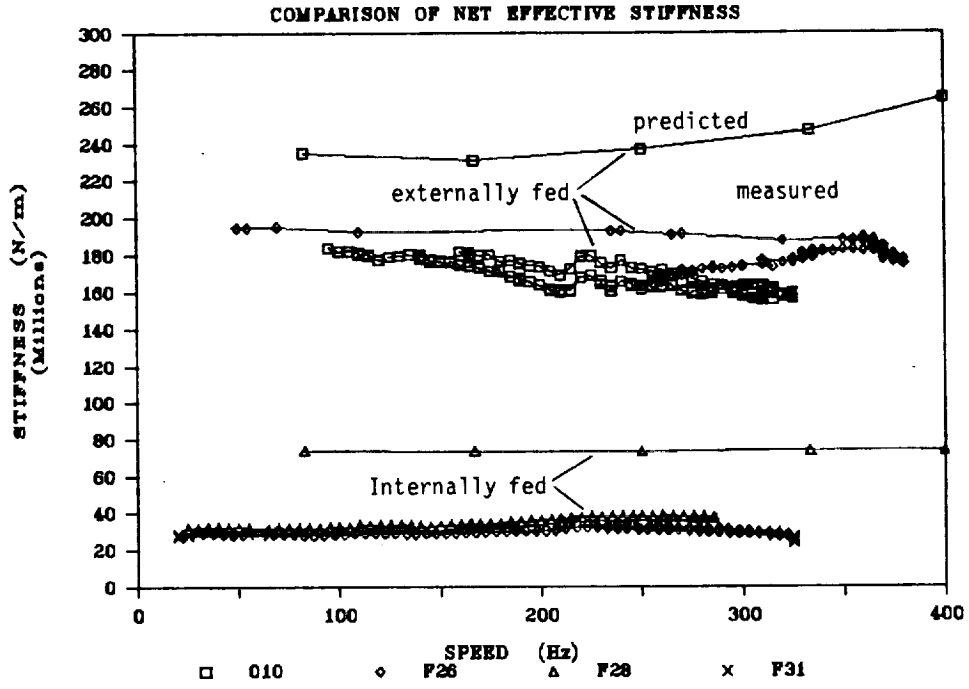

Figure 70. Comprison of Net Effective Stiffness, Externally and Internally Fed Bearings

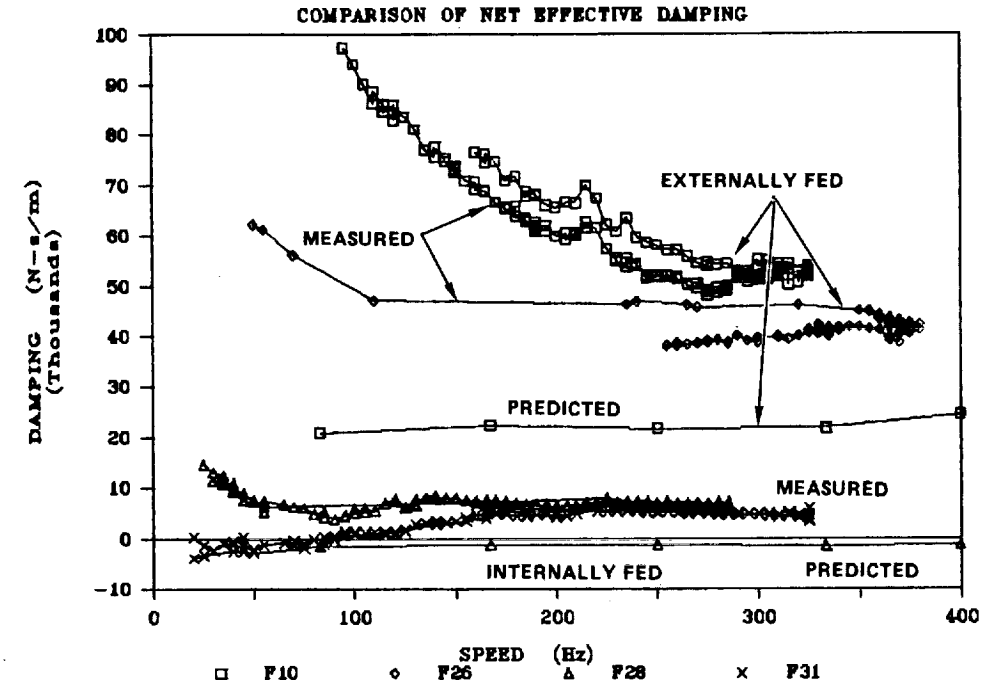

Figure 71. Comparison of Net Effective Damping, Externally and Internally Fed Bearings

1. Both configurations had measured net stiffness values that were lower than predicted, but the externally fed bearing was only 20 to 25% lower whereas the internally fed bearing was 70% lower.
2. Both configurations had measured damping values that were higher than predicted. The externally fed bearing was predicted, and shown, to have significant damping. The internally fed bearing analysis, as modified to account for fluid swirl, predicted low net effective damping. Test results showed the bearing to have practically neutral net effective damping.

The low net effective damping attained by the internally fed bearing is considered to be due mainly to fluid swirl. Fluid entering the bearing has the full tangential velocity of the journal surface. Circumferential flow of this nature is predicted to have a detrimental effect on net effective damping because of the large increase in cross-coupled stiffness (Fig. 31). The damping performance of the internally fed bearing may be significantly enhanced by providing some type of circumferential flow attenuating device, or by giving the stator increased surface roughness, or both.

Freon Bearing Flow Rate - In addition to the dynamic characteristics determination, the testing with Freon included measurement of the flow rate of the internally fed bearing and comparison to the theoretically predicted values.

Bearing flow rate was determined by deducting the seal leakage from the total flow entering the tester. Seal leakage rates were measured as a function of supply pressure by pressurization of the feed system while a nondrilled journal was installed in the test bearing position, blanking off the exit of the shaft flow channel. The seal leak rate was negligibly affected by speed.

The proportion of the total fluid flowing through the bearing remained relatively constant over the pressure range (Fig. 72). Flow rate declined 7% as speed increased to 2094 rad/s (20,000 rpm). Since recess pressure was not known, the measured flow rate was reconciled with that predicted by trial and error calculations. A solution was obtained if the film entrance loss coefficient Ke was set as 0.5 with an orifice coefficient C'_d of 0.6 (see Fig. 73 for locations where coefficients apply). The relatively low C'_d value contains both the discharge coefficient and the orifice entry loss which is expected to be large because there is no lead-in chamfer or counterdrill of the orifice entrance at the journal inner diameter.

STEADY-STATE AND TRANSIENT TESTING

Testing was conducted to determine the steady-state stiffness and flow characteristics of the PLEX and PLIN hybrid bearings and their hydrostatic elements. A fixed radial load was applied after establishing steady-state speed and supply pressure. Film thickness changes were measured with eddy current proximity devices. It was found that the measured stiffness was higher than that predicted, while the measured flow was lower than predicted.

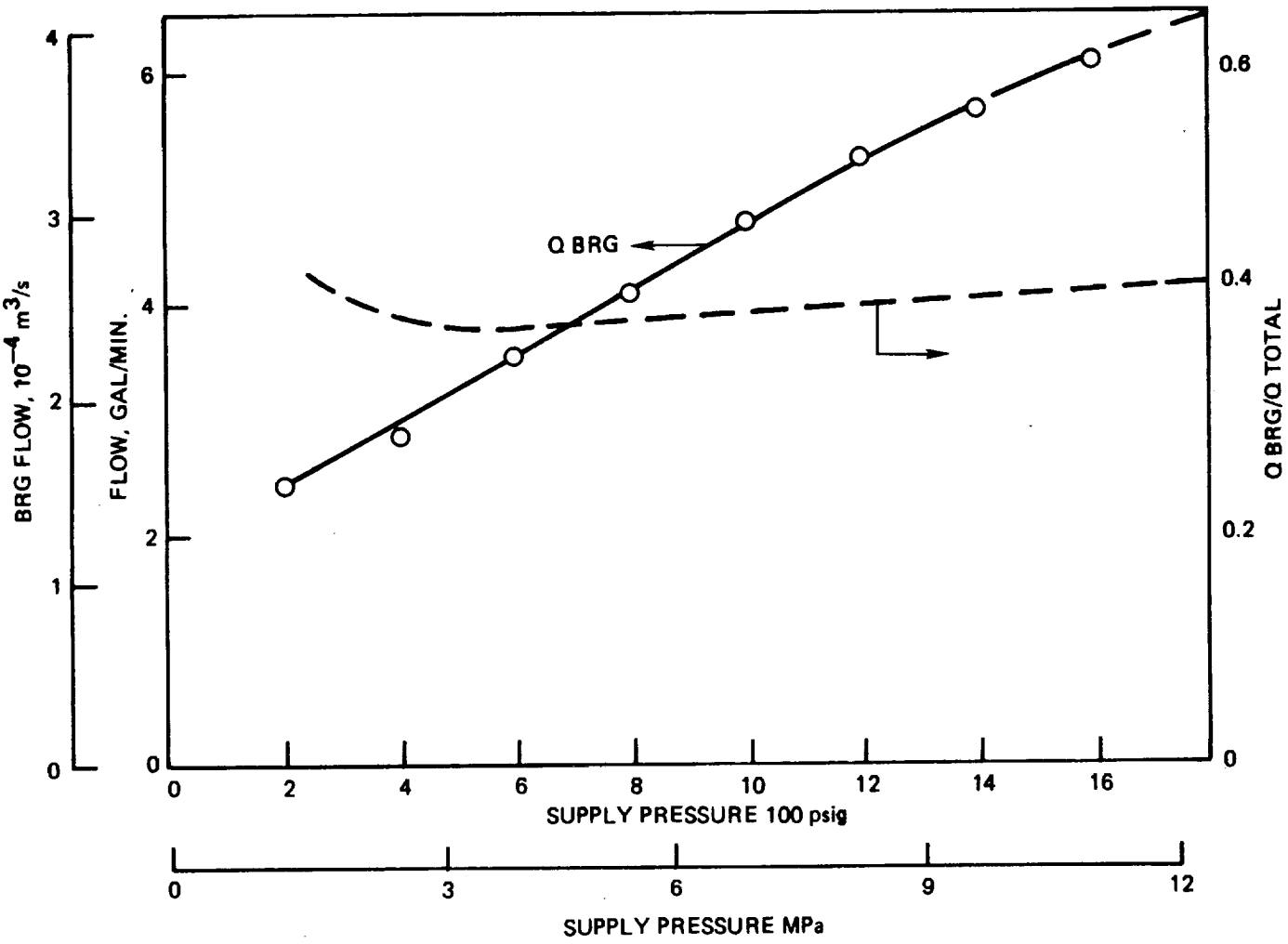

Figure 72. Internally Fed Bearing Flow, Freon

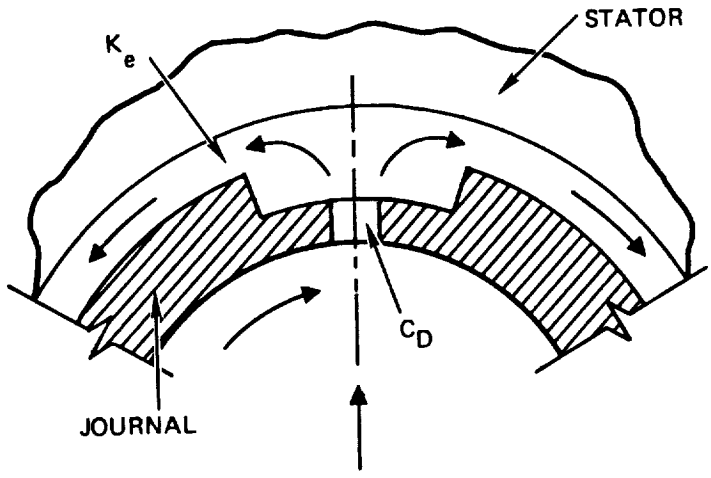

Figure 73. Flow Coefficient Locations

LH_2 Testing

Liquid Hydrogen Test Facility. The liquid hydrogen test facility, shown schematically in Fig. 74, includes a 750 liter (200 gallon) run tank rated at 34.5 MPa (5000 psia) for bearing supply. Gaseous hydrogen from a high-pressure source was used to transfer fluid, pressurize the working fluid, and drive the turbine. Servocontrolled valves regulated test bearing supply and sump pressure, and shaft speed. Set points for each of these parameters were preprogrammed for each test. Test control and data flow are shown schematically in Fig. 75.

Liquid Hydrogen Tests. Prior to initiating the chill operation, the tester housing was warmed for 8 to 12 h, then purged with GH_e (gaseous helium) to remove air and moisture. The run tank and tester were chilled by hydrogen flowing from the low-pressure LH_2 storage tank through the tank, feed system, and tester to the vent stack. The exhausted gas was ignited and continuously burned to prevent a buildup of potentially explosive gas. The chilling process was maintained until the flow to the tester was then closed, and the run tank filled.

LH_2 Steady-State Testing. Test 19 (Table 15) was conducted to measure the steady-state stiffness of the PLEX hybrid bearing. After chilling, LH_2 was supplied at 16.2 MPa (2350 psia) and shaft speed raised to 3770 rad/s (36,000 rpm). After steady- state was reached, a fixed radial load was applied to the test bearing three times by pressurizing the load piston (Fig. 40). The load was measured through strain gages bonded to the stator flexure arms. An average radial stiffness of 5.8×10^8 N/m (3.33×10^6 lb/in.) was found, exceeding the predicted value by 21%.

Table 16 summarizes steady-state stiffness tests of the hydrostatic bearing element of the PLEX hybrid bearing. In test 43, static (no rotation) stiffness and flow were determined for three values of supply pressure. Stiffnesses at three speeds were determined for the design supply pressure of 16.2 MPa (Test 47), and for half the design pressure drop (Test 48). As shown in Fig. 76, radial stiffness was found to increase with speed, an effect considered to be mainly the result of decreasing clearance due to centrifugal growth of the journal, with some additional contribution from hydrodynamic action. Measured stiffness was found to exceed that predicted by approximately 23%.

Flow rate declined with speed, probably in response to decreasing clearance. At full speed, the volumetric flow rate measured for the hydrostatic bearing was approximately 6% more than for the hybrid bearing, because the ball bearing outer race was not present to restrict fluid exit from the film bearing. On a mass basis, flow in the latter test was approximately 16% greater than during the hybrid bearing test. This larger difference was caused at least in part by the 8% increase in fluid density due to the lower supply temperature achieved during Test 47.

The results of steady state testing, e.g., stiffness higher and flowrate lower than predicted, are similar to other tests of LH_2-fed hydrostatic bearings (Ref. 22).

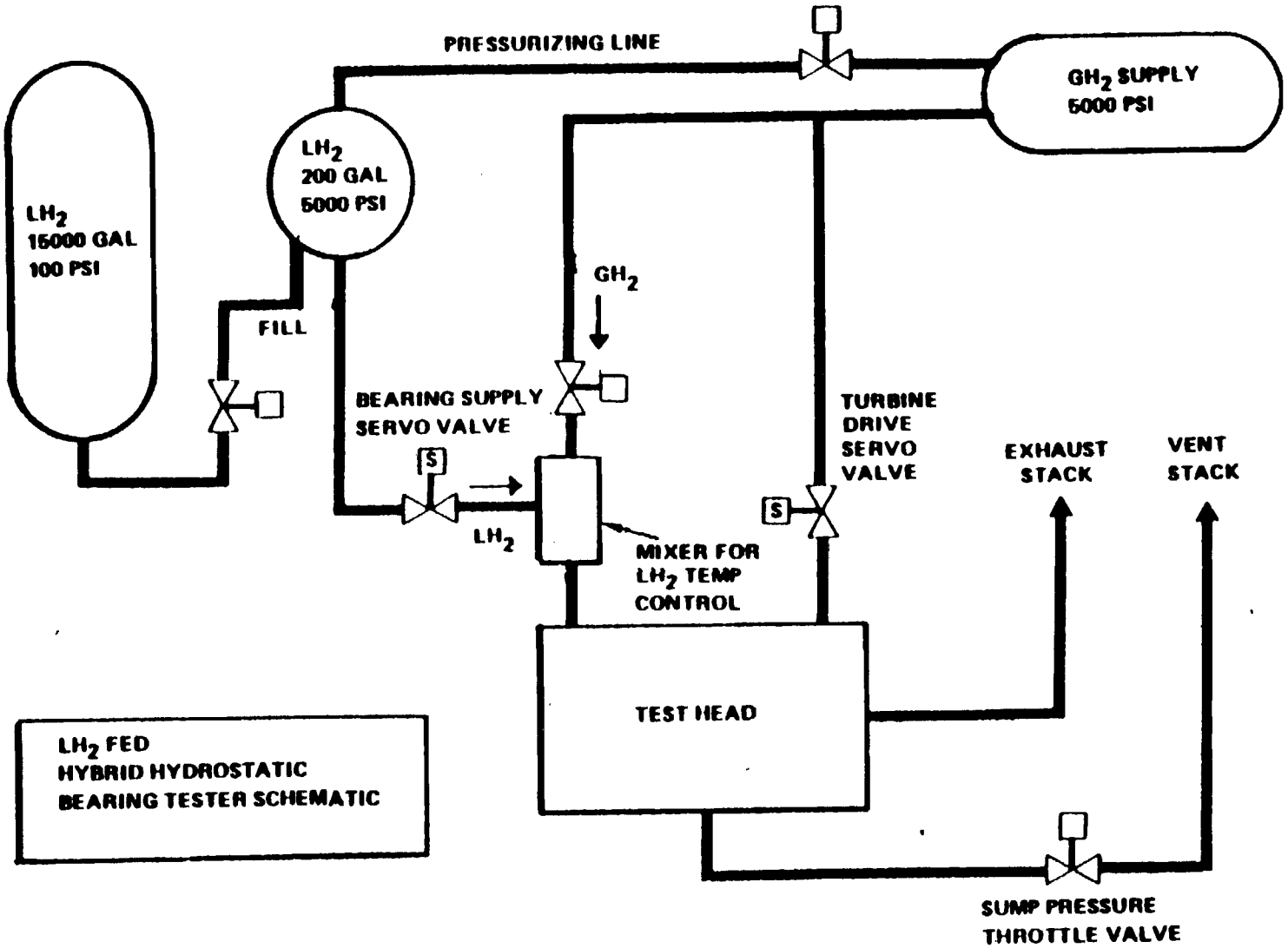

Figure 74. LH_2 Test Schematic

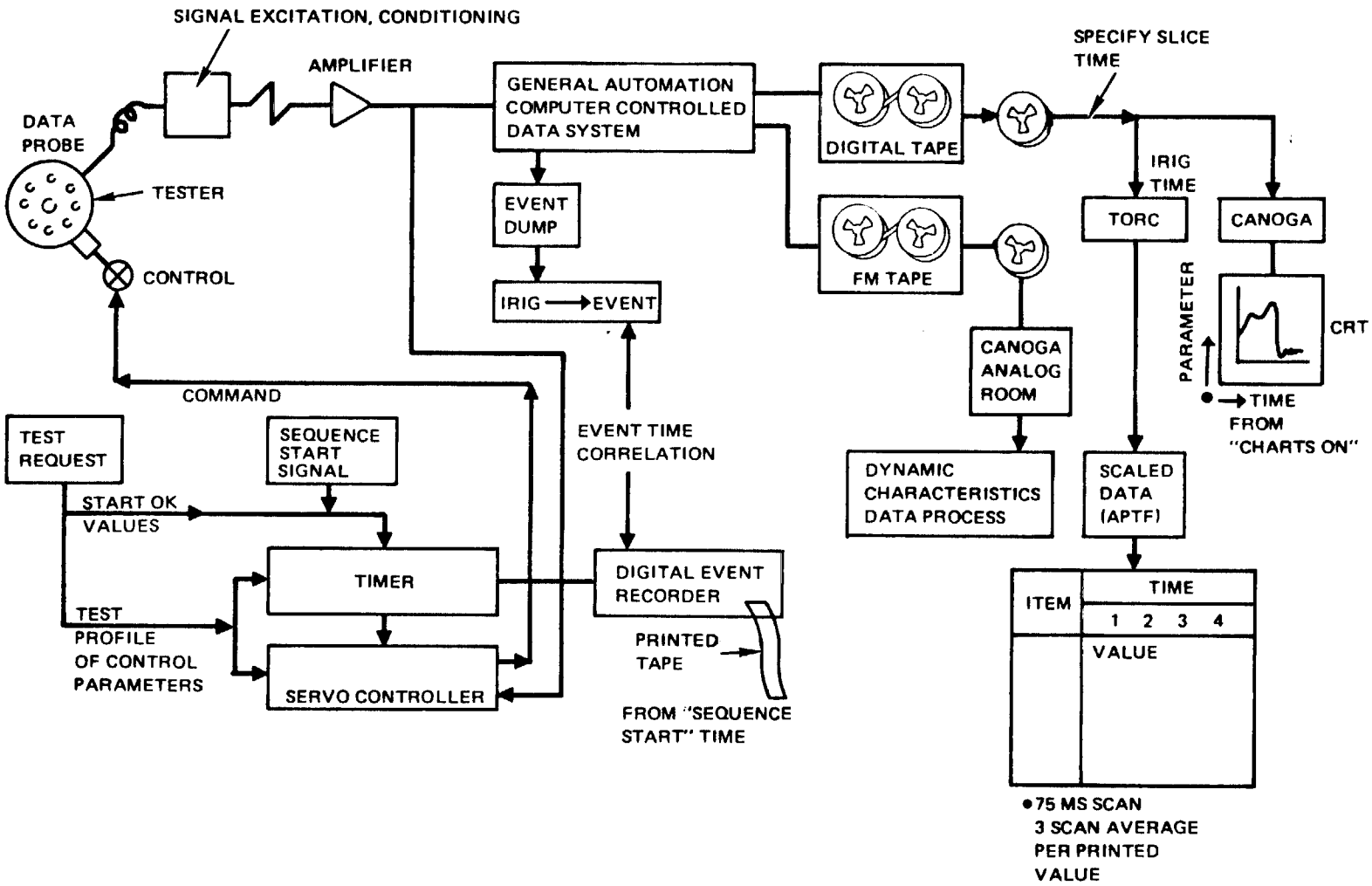

Figure 75. Test Control and Instrumentation Schematic

TABLE 15. LH_2 HYBRID BEARING TESTING SUMMARY-STEADY STATE AND TRANSIENT

TEST TYPE	TEST DATE	TEST NO.	SPEED Krpm	TIME s	SUP. PRESS. psig	SUMP PRESS. psig	RECESS 1 PRESS psig	RECESS 2 PRESS psig	SUP. TEMP R	SUMP TEMP R	RAD. LOAD lbf	FILM DEFLECT. in	BRG. STIFF. lb/in	SUPPLY FLUID DENSITY lb/ft^3	FLUID FLOW lbm/s	FLUID FLOW gal/min
AMBIENT H2 SPIN	3-2-84	6	10.15	68	1002	307	730	793	540		0			.38	.070	8.267e1
		TO	10.21	79	2362	308	1761	1884	540		0			.78	.130	7.48e1
		11	6.82	96	2360	306	1762	1887	540		0			.78	.120	6.905e1
			4.02	133	2361	307	1758	1880	540		0			.78	.120	6.905e1
			10.31	284	2360	307	1778	1897	540		0			.78	.120	6.905e1
COLD H2 SPIN	3-9-84	12	8.03	15	2357	352	1515	1517	104	87.0	0			3.56	.370	4.664e1
		TO	19.66	28	2360	352	1585	1600	106	90.0	0			3.51	.350	4.475e1
		15	32.80	48	2361	353	1778	1799	112	97.0	0			3.36	.310	4.141e1
			36.68	57	2360	349	1859	1891	118	102.0	0			3.22	.290	4.042e1
STEADY STATE STIFFNESS, HYBRID BEARING	3-14-84	16	38.56	37	2328	346	1820	1894	91	82.0	0			3.88	.320	3.701e1
		TO	36.07	50	2325	350	1816	1783	93	83.0	166	4.9e-5	3.37e6	3.82	.310	3.642e1
		19	36.20	57	2324	349	1763	1831	93	83.0	0			3.82	.320	3.760e1
			35.62	64	2325	350	1869	1723	95	84.0	340	1.08e-4	3.16e6	3.77	.320	3.809e1
			36.45	68	2326	350	1773	1845	95	84.0	0			3.78	.320	3.799e1
			35.82	74	2323	351	1891	1716	95	84.0	386	1.11e-4	3.45e6	3.77	.320	3.809e1
			35.98	81	2325	351	1761	1834	96	84.0	0			3.78	.320	3.799e1
			36.00	83	2320	352	1760	1840	96	84.0				3.75		0
			22.00	84	2310	360	1600	1600	93	83.0				3.75		0
			.00	96	220	96	190	180	64	58.0						0
			.00	100	0	0	0	0	62	60.0						0
TRANSIENT, FLIGHT PROFILE	3-19-84	22	.00	0	100	10	40	40	56	52.0	0					0
		k	39.23	32	2106	284	1763	1726	84	81.0	386			4.00	.260	2.917e1
		23	36.96	40	2252	349	1853	1788	90	82.0	43			3.91	.330	3.708e1
			27.63	55	1704	270	1246	1168	94	76.0	295			3.45	.320	4.163e1
			37.26	75	2264	352	1876	1798	94	84.0	434			3.81	.320	3.769e1
			15.67	94	1611	258	1041	1039	96	78.0	93			3.31	.320	4.339e1
			.00	100	0	0	0	0	60	56.0	0					0

TABLE 15. (Concluded)

TEST TYPE	TEST DATE	TEST NO.	SPEED Krad/s	TIME s	SUP. PRESS. MPa	SUMP PRESS. MPa	RECESS 1 PRESS MPa	RECESS 2 PRESS MPa	SUP. TEMP K	SUMP TEMP K	RAD. LOAD N	FILM DEFLECT. m	BRG. STIFF. N/m	FLUID DENSITY kg/m^3	FLUID FLOW kg/sec	FLUID FLOW m^3/sec
AMBIENT H2 SPIN	3-2-84	6	1.06	68	6.909	2.117	5.019	5.452	300					6.10	.032	5.22e-3
		TO	1.07	79	16.29	2.124	12.107	12.953	300					12.52	.059	4.72e-3
		11	.71	96	16.27	2.110	12.114	12.973	300					12.52	.055	4.36e-3
			.42	133	16.28	2.117	12.086	12.925	300					12.52	.055	4.36e-3
			1.08	284	16.27	2.117	12.224	13.042	300					12.52	.055	4.36e-3
COLD H2 SPIN	3-9-84	12	.84	15	16.25	2.427	10.416	10.429	57.8	48.3				57.15	.168	2.94e-3
		TO	2.06	28	16.27	2.427	10.897	11.000	58.9	50.0				56.34	.159	2.82e-3
		15	3.43	48	16.28	2.434	12.224	12.368	62.2	53.9				53.93	.141	2.61e-3
			3.84	57	16.27	2.406	12.781	13.001	65.6	56.7				51.69	.132	2.55e-3
STEADY STATE STIFFNESS, HYBRID BEARING	3-14-84	16	4.04	37	16.05	2.386	12.513	13.021	50.6	45.6				62.28	.145	2.34e-3
		TO	3.78	50	16.03	2.413	12.485	12.258	51.7	46.1	738.	1.24e-6	5.90e8	61.32	.141	2.30e-3
		19	3.79	57	16.02	2.406	12.121	12.588	51.7	46.1				6..32	.145	2.37e-3
			3.73	64	16.03	2.413	12.849	11.846	52.8	46.7	1512	2.73e-6	5.53e8	60.52	.145	2.40e-3
			3.82	68	16.04	2.413	12.189	12.684	52.8	46.7				60.68	.145	2.40e-3
			3.75	74	16.02	2.420	13.001	11.798	52.8	46.7	1717	2.82e-6	6.04e8	60.52	.145	2.40e-3
			3.77	81	16.03	2.420	12.107	12.609	53.3	46.7				60.68	.145	2.40e-3
			3.77	83	16.00	2.427	12.100	12.650	53.3	46.7				60.20		0
			2.30	84	15.93	2.482	11.000	11.000	51.7	46.1				60.20		0
			.00	96	1.517	.6619	1.306	1.238	35.6	32.2						0
			.00	100					34.4	33.3						0
TRANSIENT, FLIGHT PROFILE	3-19-84	22	.00	0	.6895	.0690	.275	.275	31.1	28.9						0
		&	4.11	32	14.52	1.958	12.121	11.866	46.7	45.0	1717			64.21	.118	1.84e-3
		23	3.87	40	15.53	2.406	12.739	12.293	50	45.6	191.1			62.76	.150	2.39e-3
		-	2.89	55	11.75	1.862	8.566	8.030	52.2	42.2	1312			55.38	.145	2.63e-3
			3.90	75	15.61	2.427	12.898	12.361	52.2	46.7	1930			61.16	.145	2.38e-3
			1.64	94	11.11	1.779	7.157	7.143	53.3	43.3	414.1			53.13	.145	2.74e-3
			.00	100					33.3	31.1						0

TABLE 16. LH_2 HYDROSTATIC BEARING TESTING SUMMARY-STEADY STATE

TEST TYPE	TEST DATE	TEST NO.	SPEED Krad/s	TIME s	SUP. PRESS. MPa	SUMP PRESS MPa	RECESS 1 (TOP) PRESS MPa	RECESS 2 (BOTTOM) PRESS MPa	SUP. TEMP K	SUMP TEMP K	RAD. LOAD N	FILM DEFLECT. m	BRG. STIFF. N/m	FLUID DENSITY kg/m^3	FLUID FLOW kg/sec	FLUID FLOW m^3/sec
STATIC STIFFNESS	8-31-84	43	.00	0	"DNA"			"DNA"	"DNA"		0	0	0	.00		0
			.00	32	5.875	2.420	3.685	2.846	47.8	44.4	0	0	0	42.22	.132	3.12e-3
			.00	41	5.861	2.331	2.702	3.286	48.3	42.8	2015	2.26e-5	8.93e7	41.25	.132	3.20e-3
			.00	47	9.357	2.406	3.692	4.641	48.9	42.8	0	0	0	52.49	.150	2.86e-3
			.00	55	9.357	2.344	5.218	3.568	48.9	43.3	1993	1.65e-5	1.21e8	52.49	.159	3.03e-3
			.00	63	9.329	2.379	3.630	4.606	49.4	42.2	0	0	0	51.85	.159	3.07e-3
			.00	68	16.27	2.379	6.951	8.119	46.7	41.7	0	0	0	64.21	.200	3.11e-3
			.00	75	16.27	2.358	8.642	6.827	46.7	42.2	1801	6.78e-6	2.66e8	64.21	.205	3.19e-3
			.00	82	16.29	2.379	6.930	8.181	47.2	41.7	0	0	0	65.011	.209	3.22e-3
STEADY STATE STIFFNESS	9-11-84	47	1.28	34	16.13	2.448	7.081	8.656	45.6	41.7	0	0	0	66.13	.173	2.61e-3
			1.34	41	16.14	2.393	8.814	7.356	45	43.3	2006	8.51e-6	2.33e8	66.62	.177	2.66e-3
			1.28	49	16.14	2.434	7.006	8.704	45.6	41.1	0	-8.0e-6	0	66.13	.177	2.68e-3
			2.68	59	16.13	2.413	8.216	9.728	45.6	41.1	0	0	0	66.13	.168	2.54e-3
			2.62	68	16.14	2.468	9.666	8.463	45.6	43.9	2064	6.83e-6	2.03e8	66.13	.168	2.54e-3
			2.61	75	16.14	2.441	8.092	9.694	46.1	41.1	0	-5.8e-6	0	65.65	.168	2.56e-3
			3.85	84	16.15	2.406	10.065	11.536	46.1	41.7	0	0	0	65.65	.150	2.28e-3
			3.81	91	16.14	2.393	11.199	10.498	46.1	44.4	2046	5.05e-6	4.12e8	65.65	.155	2.35e-3
			3.73	98	16.14	2.406	9.797	11.364	46.1	42.2	0	-5.8e-6	0	65.65	.150	2.28e-3
STEADY STATE STIFFNESS	9-11-84	48	1.30	35	9.239	2.475	3.823	4.826	48.9	42.8	0	0	0	52.17	.150	2.88e-3
			1.24	41	9.267	2.427	5.459	3.692	48.3	46.1	2104	2.24e-5	9.46e7	52.97	.127	2.40e-3
			1.24	.345	9.232	2.420	3.585	4.847	48.9	43.9	0			52.97	.127	2.40e-3
			2.71	60	9.246	2.406	4.180	5.308	49.4	42.8	0	0	0	51.69	.123	2.37e-3
			2.61	67	9.253	2.393	5.761	4.214	48.9	46.7	2104	1.83e-5	1.12e8	52.33	.123	2.35e-3
			2.60	76	9.232	2.420	4.276	5.280	49.4	43.9	0	-1.8e-5	0	51.53	.123	2.38e-3
			3.85	85	9.239	2.399	5.397	6.146	49.4	43.3	0	0	0	51.69	.109	2.11e-3
			3.76	91	9.253	2.427	6.518	5.177	49.4	46.1	2131	1.19e-5	1.79e8	51.69	.109	2.11e-3
			3.76	101	9.246	2.420	5.280	6.064	50	44.4	0	-1.2e-5	0	51.05	.114	2.23e-3

TABLE 16. (Concluded)

TEST TYPE	TEST DATE	TEST NO.	SPEED	TIME	SUP. PRESS.	SUMP PRESS.	RECESS 1 (TOP) PRESS	RECESS 2 (BOTTOM) PRESS	SUP. TEMP	SUMP TEMP	RAD. LOAD	FILM DEFLECT.	BRG. STIFF.	SUPPLY FLUID DENSITY	FLUID FLOW	FLUID FLOW
			Krpm	s	psig	psig	psig	psig	R	R	lbf	in	lb/in	lb/ft^3	lbm/s	gal/min
STATIC STIFFNESS	8-31-84	43	.00	0	0	0	0	0								
			.00	32	852	351	536	414	86	80.0	0	0		2.63	.290	49.49
			.00	41	850	338	393	478	87	77.0	453	8.9e-4	5.1e5	2.57	.290	50.64
			.00	47	1357	349	537	675	88	77.0	0	0		3.27	.330	45.29
			.00	55	1357	340	759	519	88	78.0	448	6.5e-4	6.9e5	3.27	.350	48.04
			.00	63	1353	345	528	670	89	76.0	0	0		3.23	.350	48.63
			.00	68	2360	345	1011	1181	84	75.0	0	0		4.00	.440	49.37
			.00	75	2360	342	1257	993	84	76.0	405	2.67e-4	1.52e6	4.00	.450	50.49
			.00	82	2362	345	1008	1190	85	75.0	0	0		4.05	.460	50.97
STEADY STATE STIFFNESS	9-11-84	47	12.20	34	2340	355	1030	1259	82	75.0	0			4.12	.380	41.39
			12.80	41	2341	347	1282	1070	81	78.0	451	3.35e-4	1.33e6	4.15	.390	42.18
			12.18	49	2341	353	1019	1266	82	74.0	0	-3.2e-4		4.12	.390	42.48
			25.60	59	2340	350	1195	1415	82	74.0	0			4.12	.370	40.30
			25.00	68	2341	358	1406	1231	82	79.0	464	2.69e-4	1.16e6	4.12	.370	40.30
			24.90	75	2341	354	1177	1410	83	74.0	0	-2.3e-4		4.09	.370	40.60
			36.80	84	2342	349	1464	1678	83	75.0	0			4.09	.330	36.21
			36.40	91	2341	347	1629	1527	83	80.0	460	1.99e-4	2.35e6	4.09	.340	37.31
			35.60	98	2341	349	1425	1653	83	76.0	0	-2.3e-4		4.09	.330	36.21
STEADY STATE STIFFNESS	9-11-84	48	12.38	35	1340	359	556	702	88	77.0				3.25	.330	45.57
			11.85	41	1344	352	794	537	87	83.0	473	8.8e-4	5.4e5	3.30	.280	38.08
			11.88	50	1339	351	520	703	88	79.0		-9.5e-4		3.25	.280	38.67
			25.85	60	1341	349	608	772	89	77.0				3.22	.270	37.63
			24.89	67	1342	347	838	613	88	84.0	473	7.2e-4	6.4e5	3.26	.270	37.17
			24.88	76	1339	351	622	768	89	79.0		-6.9e-4		3.21	.270	37.75
			36.78	85	1340	348	785	894	89	78.0				3.22	.240	33.45
			35.90	91	1342	352	948	753	89	83.0	479	4.7e-4	1.02e6	3.22	.240	33.45
			35.88	101	1341	351	768	882	90	80.0		-4.9e-4		3.18	.250	35.28

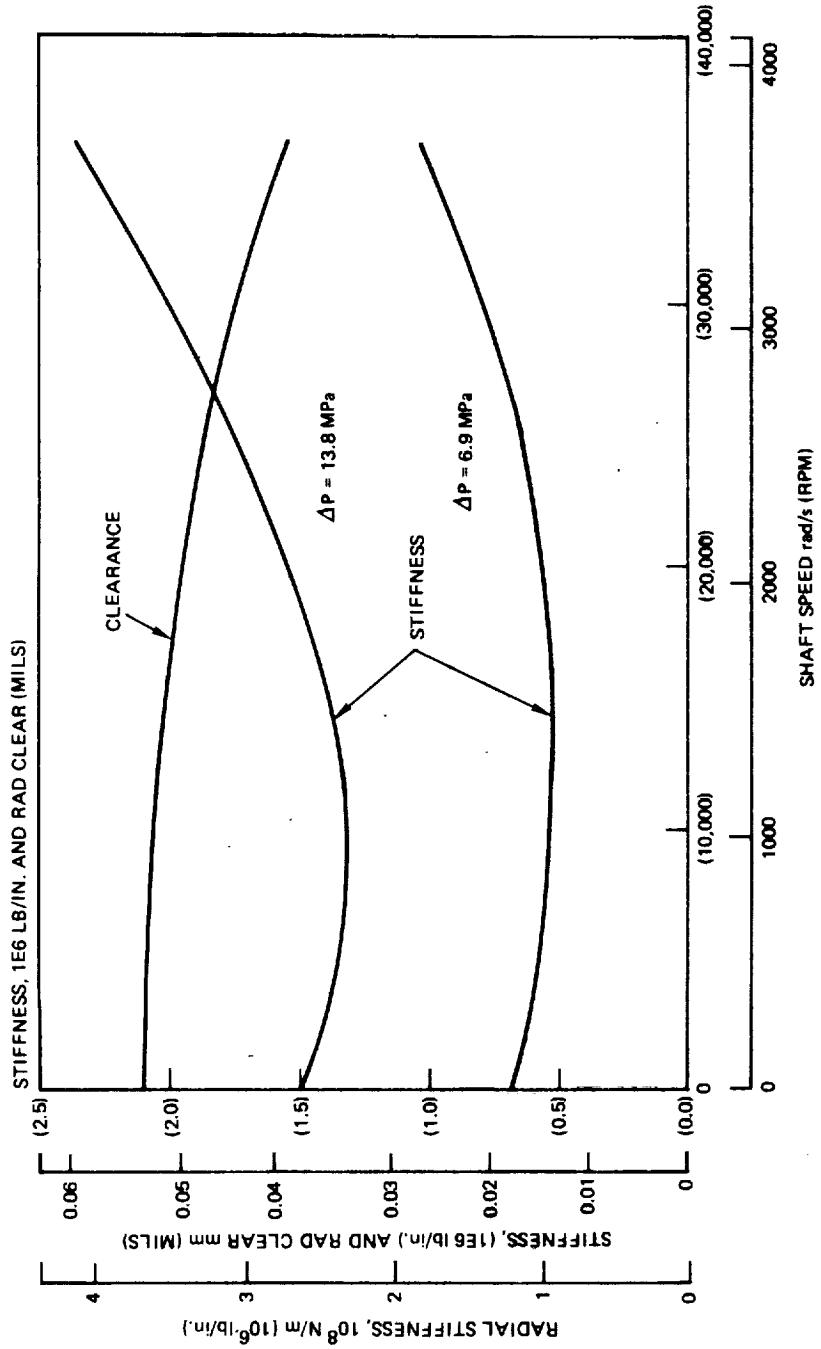

Figure 76. Speed Effects on Stiffness, (LH_2)

The theoretically determined flow rate was reconciled with measured values by applying varying values of orifice discharge and film entrance loss coefficients (Fig. 77) to match measured conditions of supply pressure, flow rate, and recess pressure to yield graphically a compatible pair of coefficients (Fig. 78). The film entrance loss due to inertial effects, K_e was lower than assumed at 0.39 rather than 0.5 probably because the recess edges are not completely sharp. The orifice coefficient C_d contains not only the discharge coefficient, but also entrance loss; its value is 0.94 rather than the assumed value of unity.

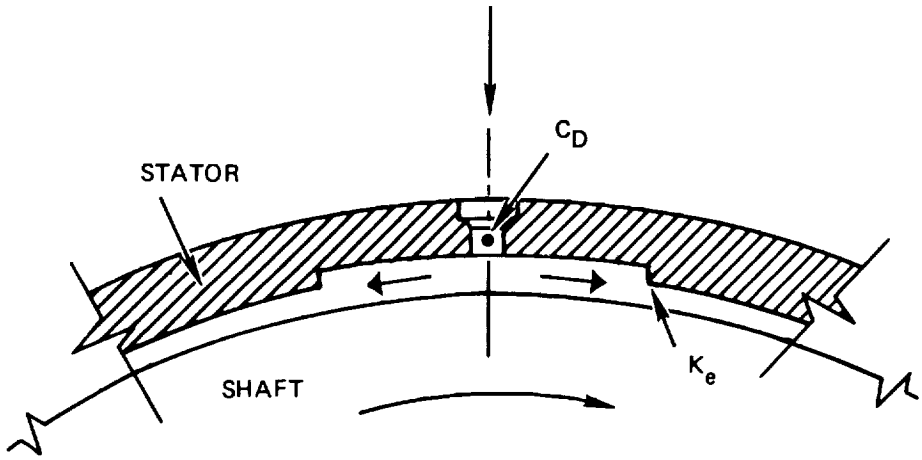

Figure 77. Flow Coefficient Locations, Externally Fed Bearing

LH_2 Transient Testing. Two transient tests of the PLEX hybrid bearing were conducted in which simultaneous speed ramp rates, load changes, and speed changes were imposed with the profile shown in Fig. 79, 80, and 81. The conditions were based on the flight duty profile of the SSME during launch, throttling, and shutdown. Table 15, Tests 22 and 23, summarizes the tests, which proceeded as planned with no anomalies.

The transient simulation demonstrated the capability of the PLEX bearing to start and stop without rubbing contact of the hydrostatic journal. The tester's loading capability was limited to 1930 N (434 lbs) by piston size and available gas pressure, representing the lower range of expected SSME engine component loads; loading to 4000 N (900 lbs) would have been desirable. A different loading system has been fabricated since the tests reported that will permit loading to 10,000 N (2250 lbs).

Accuracy of Results. Reported values are considered to be accurate within the following limits:

Pressures	1% full scale
Temperatures	0.5 K
Flow	5% of quoted value

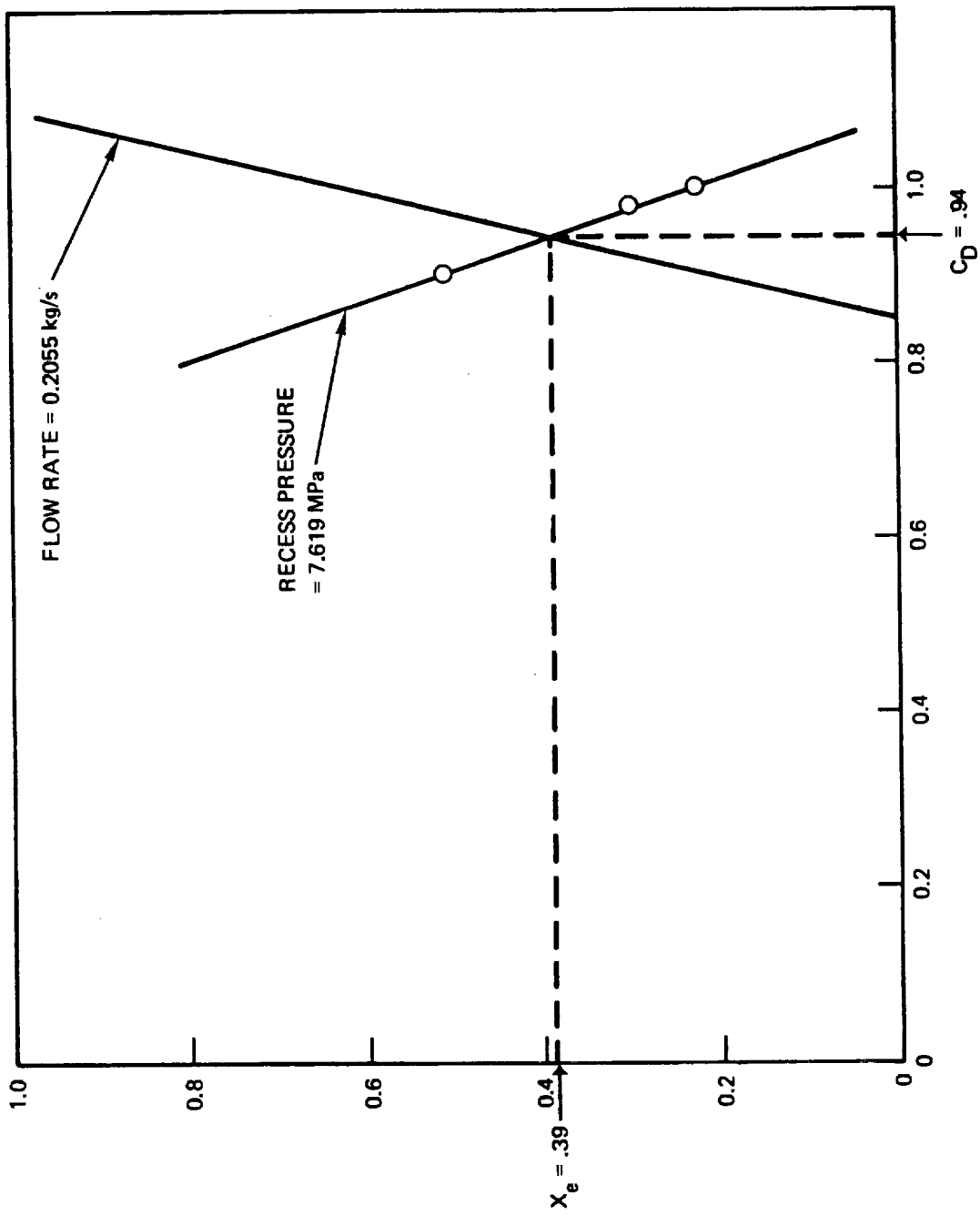

Figure 78. Flow Coefficient Matching (LH_2)

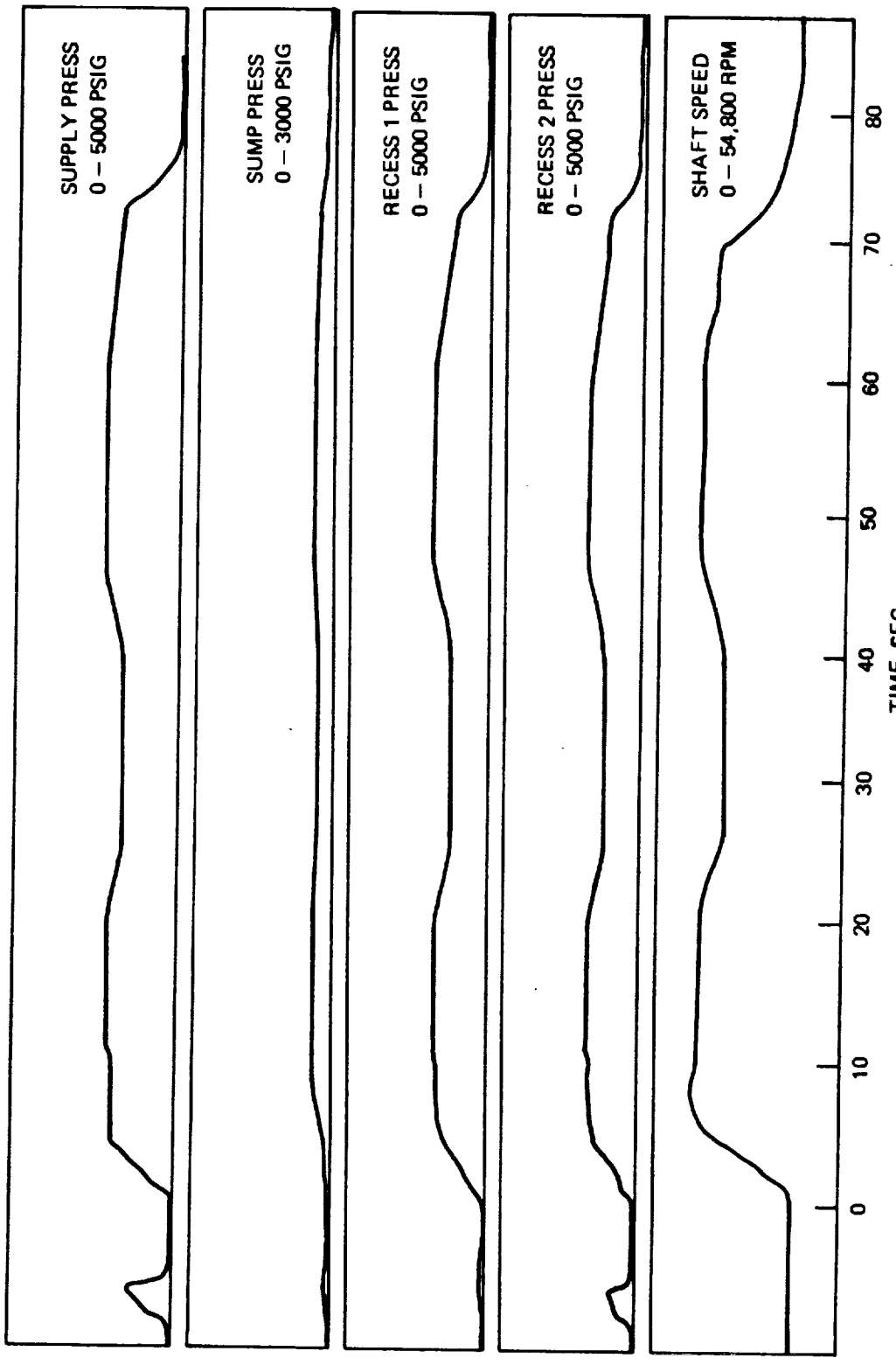

Figure 79. Transient Test; Pressure, Speed Profile

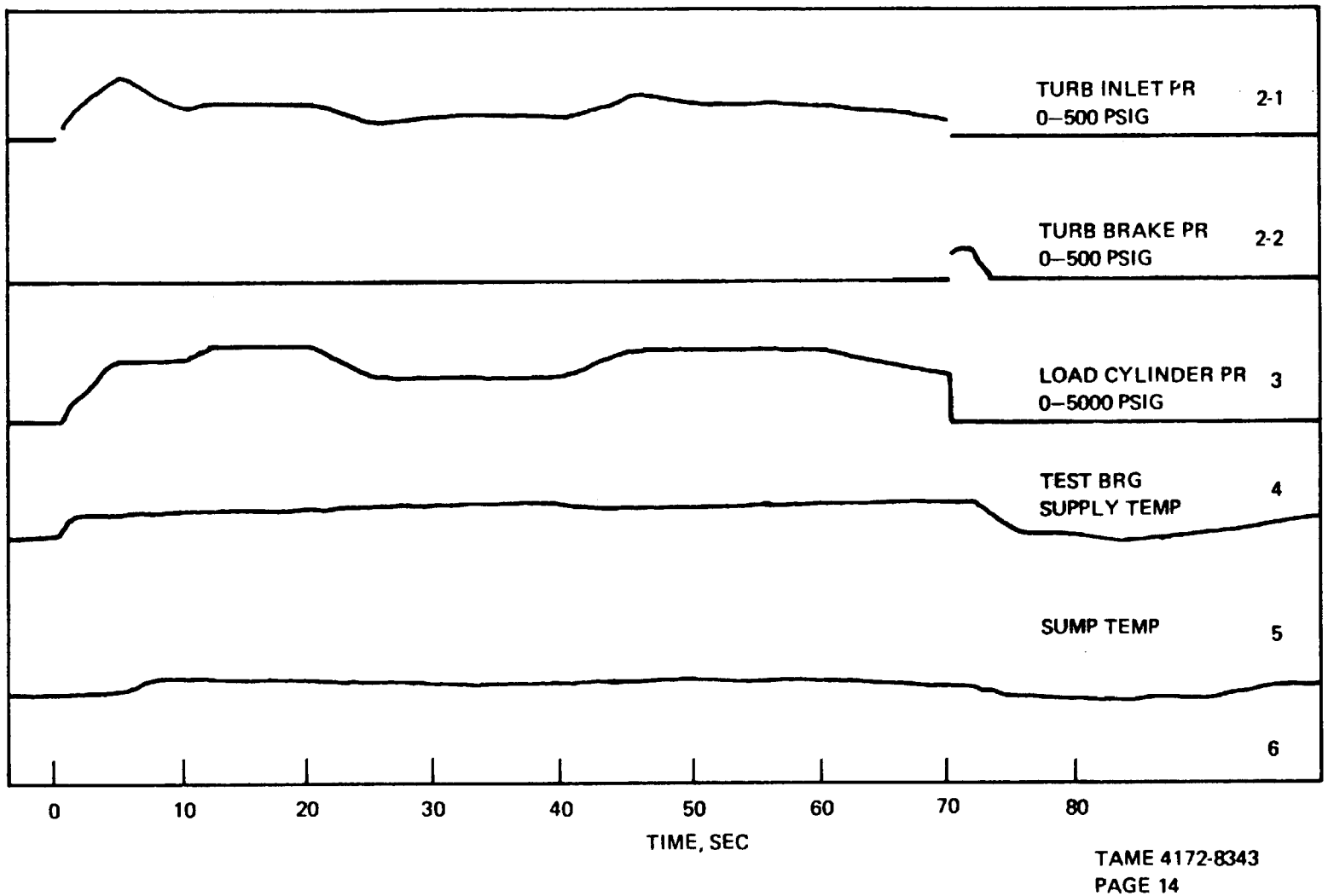

Figure 80. Transient Test Profile, Page 2

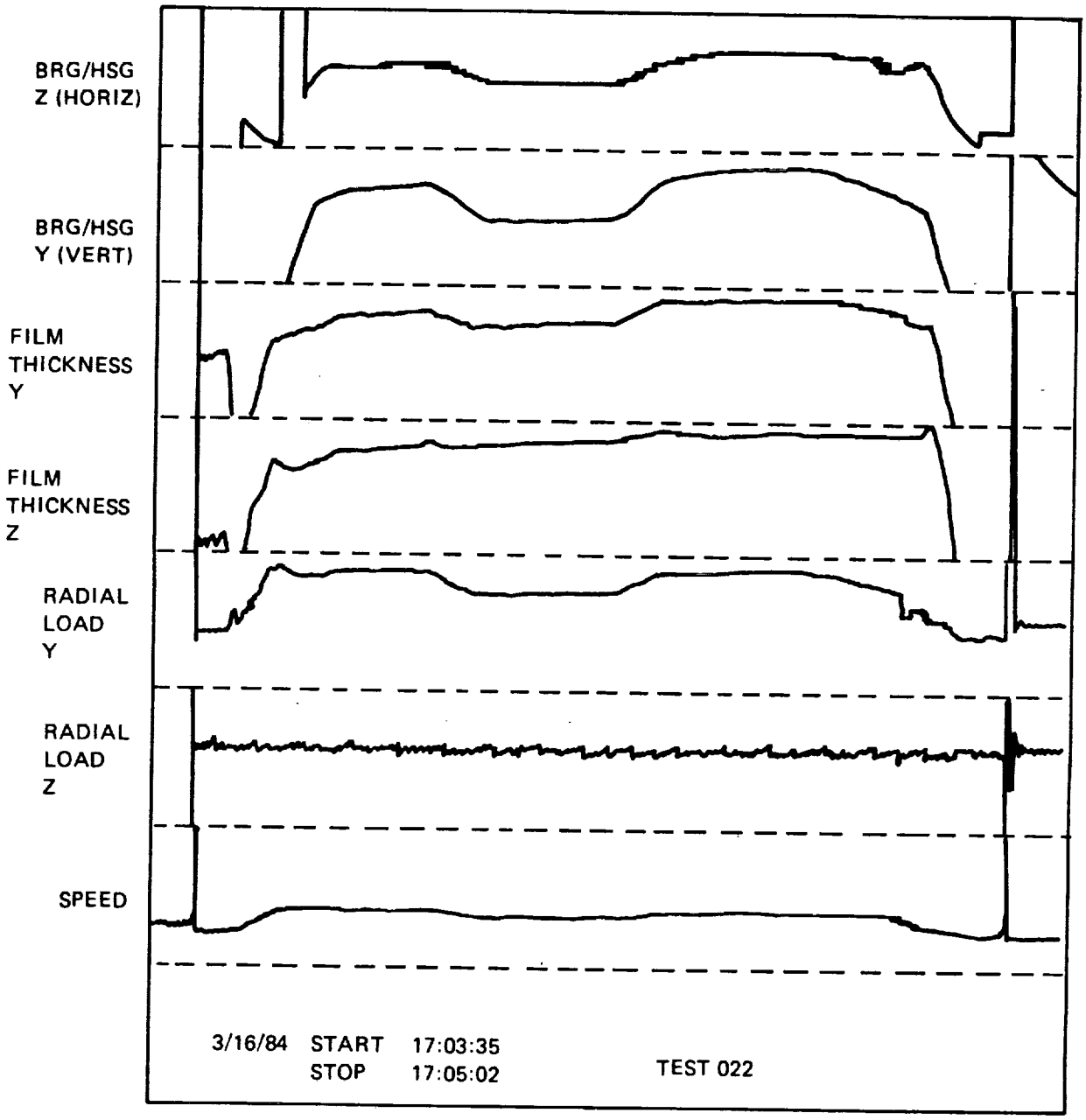

Figure 81. Transient Test Profile; Proximity, Load

Speed	1% of quoted value
Stiffness	25% of quoted value
Load	15% of quoted value
Deflection	9% of quoted value

Stiffness. Since stiffness values are based on both deflection and load measurements, 25% accuracy is expected for the highest stiffness calculated. Better accuracy is probable for the other tests conducted at lower speeds and pressures because the deflections are larger.

Deflection Measurement Accuracy, LH_2 Tests. The measured deflections used to calculate stiffness are considered to be accurate within 9% at the minimum deflection magnitudes of 0.005 mm (0.0002 in.), producing a signal voltage change of 45 mV. The overall deflection accuracy estimate is based upon the accumulation of accuracies for the proximity measurement system (2%) instrumentation system (2%) and visual interpretation of the graphical output of the analog data processing devices (5%). It was assumed that all effects of cryogenic temperature are included in the scale factor determined by calibration at LN_2 temperature (77 K).

Load Measurement Accuracy. The load values were determined by strain gage outputs and are considered to be accurate within 15% due to the accumulation of inaccuracies in calibration (5%), the amplification of the signal (2%), the excitation voltage (2%) and the visual interpretation of the processed data (5%). Effects of temperature were assumed to be included in the calibration at LN_2 temperature.

Recess Pressures - Externally Fed Bearing

The pressures measured in the top and bottom recesses (clock positions of 12:00 and 6:00) were responsive to speed, radial load and the presence of the parallel ball bearing during hybrid bearing tests. During the hybrid bearing testing (Tests 12 through 23), the recess pressure ratio $P_r = P_r-P_a/P_s-P_a$ was approximately 0.75, whereas the ideal value would lie in the range of 0.45 to 0.55 for maximum stiffness and damping. The high recess pressure in these tests probably resulted from flow resistance added by the ball bearing's proximity to the fluid exit from the hydrostatic bearing. The recess pressures and P_r were reduced when the hydrostatic bearing was tested alone in Tests 43, 47, and 48, becoming approximately 0.6 at full speed. Speed dependence was shown as P_r increased with speed primarily in response to decreasing internal clearance. Optimum P_r could be established at full speed by a slight reduction in orifice diameter or increase in clearance.

Variation between the opposing recess pressures under no-load operation was approximately 4% with the ball bearing present, but for hydrostatic bearing alone increased to approximately 15% at full speed and supply pressure. This difference is considered to be due to the centering influence of the ball bearing. After a load cycle, recess pressures returned to the preload value within approximately 3%.

Conclusions

Conclusions drawn from the LH_2 testing were:

1. The hydrostatic element of the parallel bed externally fed hybrid bearing has high values of radial stiffness and, thus, can be used to increase radial stiffness of the ball bearing and increase its life under radial load. The ball bearing prevents rubbing contact of the hydrostatic bearing during transient conditions.

2. Analytic stiffness prediction by current methdods is conservative for steady-state operation with LH_2 as the working fluid.

3. Analytic flowrate predictions for LH_2 service are conservative with an orifice coefficient of 1.0 and a film entry loss coefficient of 0.5. Accurate prediction of flow requires lower values of these coefficients, representing slightly greater orifice losses and lower film entrance losses.

LN_2 Testing

The PLIN hybrid bearing was subjected to steady-state stiffness and flow testing (Table 17). LN_2 was used in these tests to check the bearing's operation with a cryogenic working fluid while avoiding the risk involved with operation with LO_2. In seven Tests, fixed radial loads were applied at speeds from 1256 rad/s (12,000 rpm) to 3822 rad/s (36,500 rpm) to determine stiffness. Supply pressure and speed were ramped simultaneously in four tests to simulate turbopump start conditions.

The single test (Test N15) of the hydrostatic element of the PLIN bearing was terminated after 24 s of operation at 1256 rad/s (12,000) rpm by jamming of the bearing due to accumulation of globules of silver plating from the bearing inner diameter. No erratic journal motion was noted prior to the sudden stoppage of the shaft. The most probable initiating cause of silver accumulation was metallic debris particles from a weld joint that failed upstream of the bearing. The bearing bore was subsequently machined 0.05 mm (0.002 in.) oversize, restoring the original surface texture. The same bearing was used in testing with Freon in a later test series.

TABLE 17. LN_2 BEARING TESTING SUMMARY

TEST TYPE	TEST DATE	TEST NO. N-	SPEED Krad/s	TIME s	SUP. PRESS. MPa	SUMP PRESS. MPa	SUP. TEMP K	SUMP TEMP K	RAD. LOAD N	FILM DEFLECT. m	BRG. STIFF. N/m	FLUID DENSITY kg/m^3	FLUID FLOW kg/sec	FLUID FLOW m^3/sec	
STEADY STATE ROTATION	1-9-85	4		42	3.54	.696	89.4	94.4	0	0	0	770.50	.418	5.00e-4	START
		1	1.27	44	14.92	.648	89.4	94.4	0	0	0	770.50	.582	8.18e-4	ACCELERATION
			1.27	69	14.92	2.889	89.4	96.1	0	0	0	770.50	.682	9.47e-4	STEADY STATE 12KRPM
			2.20	75	14.92	2.868	90.0	98.3	0	0	0	770.50	.668	9.26e-4	ACCELERATION
			2.20	107	14.92	2.786	90.0	100.0	0	0	0	770.50	.664	9.17e-4	SPEED LIMITED TO 21KRPM
			1.78	110	14.92	2.979	90.0	99.4	0	0	0	770.50	.668	9.24e-4	
			1.80	118	14.92	2.855	90.0	98.9	0	0	0	770.50	.668	9.24e-4	
STEADY STATE STIFFNESS	1-17-85	6		37	3.54	2.634	97.8	99.4		0	0			0	FULL DURATION TEST; SPEED LIMITED TO 32KRPM BY AVAILABLE
		1	1.26	58	14.93	2.855	95.0	102.2	903	2.70e-6	2.16e5	770.50	.695	9.62e-4	TURBINE DRIVE GAS PRESSURE.
			2.47	77	14.93	2.882	95.6	103.9	-867	-2.6e-6	2.17e5	770.50	.677	9.39e-4	
			2.32	85	14.93	2.875	95.6	106.1	890	2.67e-6	2.77e5	770.50	.673	9.29e-4	STIFFNESS TEST AT LOWEST RADIAL LOAD VALUE.
			3.11	102	14.93	2.882	95.6	109.4	-850	-3.0e-6	1.43e5	770.50	.650	9.02e-4	
			3.35	111	14.92	2.875	95.6	112.2	881	2.58e-6	2.20e5	770.50	.650	8.97e-4	
			3.35	118	14.92	2.882	95.6	112.8	-792	-1.6e-6	3.24e5	770.50	.645	8.95e-4	
STEADY STATE STIFFNESS	1-17-85	7	1.27	52	14.92	2.827	90.6	97.2		0	0	786.55	.686	9.30e-4	DURATION TEST; NEXT LEVEL RADIAL LOAD.
			1.27	61	14.91	2.827	90.6	97.8	1,619	3.01e-6	3.47e5	786.55	.686	9.32e-4	
			2.35	78	14.92	2.827	90.6	100.0	-1,557	-3.9e-6	2.55e5	786.55	.664	9.03e-4	
			2.52	86	14.92	2.827	91.1	102.2	1,610	5.23e-6	1.99e5	786.55	.659	8.95e-4	
			3.07	100	14.93	2.889	91.1	104.4	-1,468	-5.2e-6	1.81e5	786.55	.645	8.78e-4	
			3.35	111	14.93	2.875	91.1	110.0	1,597	2.86e-6	3.60e5	786.55	.636	8.61e-4	
			3.35	118	14.91	2.875	91.1	110.6	-1,441	-3.9e-6	2.36e5	786.55	.641	8.67e-4	
STEADY STATE STIFFNESS	1-17-85	8	1.27	52	14.91	2.861	91.7	99.4		0	0	786.55	.686	9.34e-4	DURATION TEST AT HIGHEST RADIAL LOAD LEVEL.
			1.27	60	14.91	2.882	91.7	100.0	2,068	5.37e-6	2.49e5	786.55	.686	9.30e-4	
			2.36	77	14.91	2.896	91.7	101.1	-1,948	-5.4e-6	2.34e5	786.55	.673	9.11e-4	
			2.50	85	14.91	2.903	91.7	103.9	409	4.28e-6	6.17e4	786.55	.664	8.98e-4	
			3.39	100	14.94	2.875	92.2	106.7	-1,810	-4.3e-6	2.72e5	786.55	.645	8.75e-4	
			3.19	111	14.91	2.903	92.2	110.6	1,899	5.35e-6	2.29e5	786.55	.641	8.71e-4	
			3.17	118	14.91	2.875	92.2	110.0	-1,699	-5.4e-6	2.04e5	786.55	.645	8.78e-4	

TABLE 17. (Continued)

TEST TYPE	TEST DATE	TEST NO. N-	SPEED Krpm	TIME s	SUP. PRESS. psig	SUMP PRESS. psig	SUP. TEMP R	SUMP TEMP R	RAD. LOAD lbf	FILM DEFLECT. in	BRG. STIFF. lb/in	SUPPLY FLUID DENSITY lb/ft^3	FLUID FLOW lbs/s	FLUID FLOW gal/min	COMMENTS
STEADY STATE ROTATION	1-9-85	4	.00	42	514	101	161	170	0	0		48	.92	9.20	START
			12.10	44	2164	94	161	170	0	0		48	1.28	12.97	ACCELERATION
			12.10	69	2164	419	161	173	0	0		48	1.50	15.01	STEADY STATE 12KRPM
			21.00	75	2164	416	162	177	0	0		48	1.47	14.67	ACCELERATION
			21.00	107	2164	404	162	180	0	0		48	1.46	14.54	SPEED LIMITED TO 21KRPM
			17.00	110	2164	432	162	179	0	0		48	1.47	14.64	
			17.20	118	2164	414	162	178	0	0		48	1.47	14.64	
STEADY STATE STIFFNESS	1-17-85	6	.00	37	514	382	176	179	0	0					FULL DURATION TEST; SPEED LIMITED TO 32KRPH BY AVAILABLE
			12.03	58	2165	414	171	184	203	1.06e-4	1.91e6	48	1.53	15.24	TURBINE DRIVE GAS PRESSURE.
			23.63	77	2163	418	172	187	-195	-1.0e-4	1.92e6	48	1.49	14.88	
			24.10	85	2166	417	172	191	200	8.16e-5	2.45e6	48	1.48	14.73	STIFFNESS TEST AT LOWEST RADIAL LOAD VALUE.
			29.75	102	2165	418	172	197	-191	-1.5e-4	1.27e6	48	1.43	14.29	
			32.00	111	2164	417	172	202	198	1.02e-4	1.95e6	48	1.43	14.22	
			32.02	118	2164	418	172	203	-178	-6.2e-5	2.87e6	48	1.42	14.19	
STEADY STATE STIFFNESS	1-17-85	7	12.13	52	2164	410	163	175		0		49	1.51	14.74	DURATION TEST; NEXT LEVEL RADIAL LOAD.
			12.13	61	2162	410	163	176	364	1.18e-4	3.07e6	49	1.51	14.78	
			22.43	78	2164	410	163	180	-350	-1.6e-4	2.26e6	49	1.46	14.31	
			24.03	86	2164	410	164	184	362	2.06e-4	1.76e6	49	1.45	14.18	
			29.28	100	2165	419	164	188	-330	-2.1e-4	1.60e6	49	1.42	13.91	
			32.00	111	2166	417	164	198	359	1.13e-4	3.19e6	49	1.40	13.64	
			32.00	118	2163	417	164	199	-324	-1.6e-4	2.09e6	49	1.41	13.74	
STEADY STATE STIFFNESS	1-17-85	8	12.15	52	2163	415	165	179		0		49	1.51	14.81	DURATION TEST AT HIGHEST RADIAL LOAD LEVEL.
			12.10	60	2163	418	165	180	465	2.11e-4	2.2e6	49	1.51	14.74	
			22.51	77	2163	420	165	182	-438	-2.1e-4	2.07e6	49	1.48	14.44	
			23.84	85	2163	421	165	187	92	1.68e-4	5.46e5	49	1.46	14.23	
			32.40	100	2167	417	166	192	-407	-1.7e-4	2.41e6	49	1.42	13.87	
			30.45	111	2163	421	166	199	427	2.11e-4	2.03e6	49	1.41	13.81	
			30.31	118	2163	417	166	198	-382	-2.1e-4	1.81e6	49	1.42	13.91	

TABLE 17. (Continued)

TEST TYPE	TEST DATE	TEST NO.	SPEED Krad/s	TIME s	SUP. PRESS. MPa	SUMP PRESS. MPa	SUP. TEMP K	SUMP TEMP K	RAD. LOAD N	FILM DEFLECT. m	BRG. STIFF. N/m	FLUID DENSITY kg/m^3	FLUID FLOW kg/sec	FLUID FLOW m^3/sec	
STEADY STATE STIFFNESS	11-17-85	9	1.29	50	14.91	2.875	90.6	96.7		0	0.	786.55	.709	9.63e-4	DURATION TEST, MAX SPEED=36500 RPM.
			1.26	58	14.89	2.868	90.6	97.8	2,117	5.73e-6	2.38e5	786.55	.705	9.56e-4	
			2.30	74	21.81	2.882	91.1	99.4	-1,917	-5.4e-6	2.27e5	786.55	.691	9.38e-4	
			2.51	83	14.92	2.875	91.7	102.8	2,086	6.24e-6	2.16e5	786.55	.682	9.27e-4	
			3.10	97	14.91	2.882	91.7	104.4	-1,824	-6.2e-6	1.89e5	786.55	.673	9.14e-4	
			3.58	107	14.91	2.882	92.2	110.0	1,930	0	0	786.55	.645	8.76e-4	
			3.17	115	14.91	2.903	92.2	111.7	-1,744	0	0	786.55	.650	8.81e-4	
TRANSIENT START, STEADY STATE STIFFNESS	11-17-85	10	1.27	52	14.92	2.875	90.6	96.1		0	0	770.50	.700	9.67e-4	REPEAT OF PREVIOUS TEST WITH SIMULTANEOUS SUPPLY PRESSURE AND SPEED RAMP FROM 0.441 MPa (64 psia)
			1.26	60	14.91	2.875	90.6	97.2	2,064	5.72e-6	2.33e5	770.50	.695	9.61e-4	
			2.32	76	14.91	2.875	91.1	98.9	-1,917	-5.7e-6	2.16e5	770.50	.682	9.44e-4	
			2.52	84	14.91	2.875	91.1	101.7	1,966	6.64e-6	1.91e5	770.50	.677	9.38e-4	
			3.24	101	14.93	2.889	91.7	105.0	-1,757	-6.6e-6	1.71e5	770.50	.655	9.09e-4	
			3.60	109	14.91	2.882	92.2	110.0	1,926	5.76e-6	2.16e5	770.50	.641	8.85e-4	
			3.74	117	14.91	2.896	92.2	112.2	-1,721	-4.8e-6	2.32e5	770.50	.636	8.79e-4	
TRANSIENT START	11-17-85	11		42	.23	.545	94.4	95.0		0	0	770.50	.105	1.46e-4	START TRANSIENT SIMULATED BY INCREASING SPIN VALVE
			.33	42	.23	.545	94.4	95.0		0	0			0	OPENING RATE. TEST CUT FOR SUMP PRESSURE MAX REDLINE.
			1.47	43	5.27	.614	98.3	96.1		0	0			0	REDUCED SUMP THROTTLE VALVE INITIAL OPENING FOR NEXT TEST.
			1.69	44	7.82	.683	96.7	97.8		0	0			0	
			1.24	52	14.51	3.951	92.2	100.6		0	0			0	
										0	0			0	
TRANSIENT START RADIAL STIFFNESS	11-17-85	14		36	.18	.059	96.1	96.1		0	0	770.50	.073	9.91e-5	DURATION TEST; 36510 RPM MAX
			1.26	67	14.47	2.861	98.9	98.9	2,082	0	5.20e5	770.50	.682	9.44e-4	
			2.33	76	14.47	2.861	95.0	101.7	-1,908	0	3.95e5	770.50	.664	9.21e-4	
			2.51	83	14.47	2.848	95.6	105.0	2,019	0	3.95e5	770.50	.655	9.07e-4	
			3.35	101	14.45	2.882	97.2	110.0	-1,833	0	2.03e5	770.50	.627	8.69e-4	
			3.77	108	14.47	2.882	97.8	114.4	1,926	0	5.08e5	770.50	.618	8.57e-4	
			3.82	116	14.46	2.910	97.8	116.1	-1,859	0	2.37e5	770.50	.614	8.47e-4	
HYDROSTATIC BEARING ONLY	11-31-85	15		36	3.45	1.724	132.8	100.6		0	0			0	FIRST TEST OF INTERNALLY FED HYDROSTATIC BEARING. SEIZURE
			1.30	40	13.79	2.482	95.6	102.8	1,245	0	0	770.50	.673	9.34e-4	OCCURRED 2 SECONDS AFTER REMOVAL OF RADIAL LOAD.
			1.28	60	14.76	2.758	96.1	102.8		0	0	770.50		0	FILM THICKNESS SIGNALS NOT READABLE.
				61	14.76	2.792	96.1	102.8		0	0			0	

TABLE 17. (Concluded)

TEST TYPE	TEST DATE	TEST NO. N-	SPEED Krpm	TIME s	SUP. PRESS. psig	SUMP PRESS. psig	SUP. TEMP R	SUMP TEMP R	RAD. LOAD lbf	FILM DEFLECT. in	BRG. STIFF. lb/in	SUPPLY FLUID DENSITY lb/ft^3	FLUID FLOW lbm/s	FLUID FLOW gal/min	COMMENTS
STEADY STATE STIFFNESS	1-17-85	9	12.32	50.0	2162	417	163	174		0		49	1.56	15.26	DURATION TEST, MAX SPEED=36500 RPM.
		1	12.07	58.0	2160	416	163	176	476	.000226	2.11e6	49	1.55	15.15	
			21.97	74.0	3163	418	164	179	-431	-.00021	2.01e6	49	1.52	14.87	
			23.94	83.0	2164	417	165	185	469	.000246	1.91e6	49	1.50	14.70	
			29.60	97.0	2163	418	165	188	-410	-.00025	1.67e6	49	1.48	14.48	
			34.17	107.0	2163	418	166	198	434	0		49	1.42	13.89	
			30.31	115.0	2162	421	166	201	-392	0		49	1.43	13.97	
TRANSIENT START, STEADY STATE STIFFNESS	1-17-85	10	12.15	52.0	2164	417	163	173		0		48	1.54	15.32	REPEAT OF PREVIOUS TEST WITH SIMULTANEOUS SUPPLY PRESSURE
			12.06	60.0	2163	417	163	175	464	.000225	2.06e6	48	1.53	15.23	AND SPEED RAMP FROM 0.441 MPa (64 psia)
			22.15	76.0	2163	417	164	178	-431	-.00023	1.91e6	48	1.50	14.97	
			24.07	84.0	2163	417	164	183	442	.000262	1.69e6	48	1.49	14.84	
			30.93	101.0	2165	419	165	189	-395	-.00026	1.51e6	48	1.44	14.41	
			34.43	109.0	2163	418	166	198	433	.000227	1.91e6	48	1.41	14.02	
			35.70	117.0	2162	420	166	202	-387	-.00019	2.05e6	48	1.40	13.93	
TRANSIENT START	1-17-85	11	.00	41.9	34	79	170	171				48	.23	2.32	START TRANSIENT SIMULATED BY INCREASING SPIN VALVE
			3.30	42.0	34	79	170	171				UN-	UN-	UN-	OPENING RATE. TEST CUT FOR SUMP PRESSURE MAX REDLINE.
			14.00	43.0	764	89	177	173				DEFINED	DEFINED	DEFINED	REDUCED SUMP THROTTLE VALVE INITIAL OPENING FOR NEXT TEST.
			16.10	44.0	1134	99	174	176				"	"	"	
			11.80	52.1	2104	573	166	181				"	"	"	
			.00												
TRANSIENT START RADIAL STIFFNESS	1-17-85	14	.00	36.0	26	8.6	173	173				48	.16	1.57	DURATION TEST; 36510 RPM MAX
			12.02	57.0	2099	415	178	178	468		4.6e6	48	1.50	14.97	
			22.30	76.0	2099	415	171	183	-429		3.5e6	48	1.46	14.60	
			23.95	83.0	2099	413	172	189	454		3.5e6	48	1.44	14.38	
			32.04	101.0	2096	418	175	198	-412		1.8e6	48	1.38	13.78	
			35.96	108.0	2099	418	176	206	433		4.5e6	48	1.36	13.59	
			36.51	116.0	2097	422	176	209	-418		2.1e6	48	1.35	13.42	
HYDROSTATIC BEARING ONLY	1-31-85	15	.00	36.3	500	250	239	181							FIRST TEST OF INTERNALLY FED HYDROSTATIC BEARING. SEIZURE
			12.40	40.1	2000	360	172	185	280			48	1.480	14.80	OCCURRED 2 SECONDS AFTER REMOVAL OF RADIAL LOAD.
			12.20	60.4	2140	400	173	185	1			48			FILM THICKNESS SIGNALS NOT READABLE.
			.00	60.5	2140	405	173	185							

LN_2 Steady-State Testing. After static flow tests and prior to initiating powered rotating tests, the test bearing became jammed during hand rotation. Particulate matter had apparently entered the bearing through the orifices and been caught at the recess edges. Rotation caused plowing of the silver plating from the bearing inner diameter by these particles. The silver galled and accumulated into globules large enough to jam the bearing clearance. The silver protruding above the surface was removed and the tester reassembled. The total area of grooving was a small percent of the total bearing area and the radial clearance outside the area swept by the recesses was not affected. The jamming of the bearing demonstrated that pure silver is not a suitable material for bearings with close clearances that particles may enter. Silver was selected for this application because in rubbing contact, it is the most resistant material to ignition in a LO_2 environment. The thin dense chromium plated surface of the journal was not damaged. Since rubbing contact is precluded in the parallel load hybrid bearings, a harder bearing material could be used to advantage.

After preliminary tests (N1 through N4, Table 17), Tests N6 through N9 were conducted to determine direct radial stiffness of the hybrid bearing, with LN_2 supplied at 14.9 MPa (2165 psia) and with sump pressure maintained at 2.87 MPa (417 psia). Fixed radial loads were applied at speeds of from 1256 rad/s (12,000 rpm) to 3577 rad/s 34,170 rpm). The speed attained was limited by turbine gas supply source pressure, which was increased a small amount for each test to avoid inadvertant overspeed until a maximum speed of 3821 rad/s (36,500 rpm) was achieved.

LN_2 Combined Transient Testing. Tests N10 through N14 combined transient start/stop ramps with stiffness measurements. The supply pressure was reduced to 0.44 MPa (64 psia) at start of rotation. The pressure was then ramped to full inlet pressure in 4 s. Shaft acceleration of 1288 rad/s^2 (12,300 rpm/s) was achieved on start. In all tests, the fluid supply valve was shut simultaneously with the turbine spin supply valve, while the turbine brake was activated, giving a deceleration rate of 2458 rad/s^2 (23,500 rpm/s) from full speed to rest. Supply pressure decayed from 14.9 MPa to zero gage pressure in 1.5 s, which is less than the 4 s period of deceleration in the engine shutdown profile.

Measured flow, which included the leakage of the two shaft seals used to force flow into the shaft, was approximately 4% greater than predicted. Bearing flow rates listed were derived by deducting calculated seal leakage from the total measured flow.

LN_2 Hybrid Bearing Stiffness Values - The steady-state tests resulted in stiffness values with large variation which was caused in part by noise in the deflection signals. If the extreme values are dropped, the average stiffness from 14 test points becomes 2.27×10^8 N/m (1.75×10^6 lb/in.) for the hybrid bearing. When the ball bearings calculated stiffness is deducted, the hydrostatic bearing stiffness becomes 3.06×10^8 N/m (1.29×10^6 lb/in.), or 5% lower than predicted. This result is in reasonable agreement with the dynamic tests conducted with Freon, wherein the magnitude of separated direct stiffness (Test F31) was approximately as predicted at 1256 rad/s (12,000 rpm). The speed dependence of stiffness indicated in test F31 was not predicted and is not currently explained. The radically lower net effective stiffness of the internally fed bearing found in

tests F28 and F31 are the result of combining direct stiffness and cross-coupled damping. Since the damping force arises from dynamic shaft motion, it is probable that its effect would not be shown in the steady-state tests. The low effective dynamic stiffness may not be a significant detrimental consideration for applications with predominantly steady-state radial loading.

Test N15 - The ball bearing was removed prior to Test 015 so that the radial stiffness of the hydrostatic bearing element alone could be measured. The test was cut at 24 s by underspeed redline when the tester shaft stopped from 1256 rad/s (12,000 rpm) in 0.7 s. At disassembly, the condition of jamming was similar to that experienced prior to Test N1. After test N15, LN_2 testing was discontinued to concentrate effort on developing the damping test method. Consequently, the tester was removed for modification in preparation for dynamic coefficient testing which was subsequently performed with Freon.

The conditions of the bearing and journal after test N15 are shown in Fig. 82 and 83.

Conclusions drawn from the LN_2 testing were:

1. The parallel load internally fed (PLIN) hybrid bearing is a viable concept for load sharing and life extension of ball bearings in propellant cooled service; when particles were excluded, no rubbing contact of the hydrostatic bearing occurred. Since the ball bearing supports radial load during start and shutdown and prevents rubbing of the hydrostatic bearing, this bearing configuration is a good candidate for use in LO_2 turbopumps. Although dynamic tests with Freon showed the stiffness and damping provided by the internally fed bearing is low compared to that of the externally fed bearing, the damping supplied by the hydrostatic bearing is substantially increased over that of a rolling bearing.

2. Systems using hydrostatic bearings must include filters or the bearing materials must be hard and seizure resistant to prevent damage by particulate contamination of the bearing clearance.

3. In locations where rubbing can occur, pure silver is not suitable as a hydrostatic bearing material because of its tendency to gall, accumulate and jam the bearing clearance.

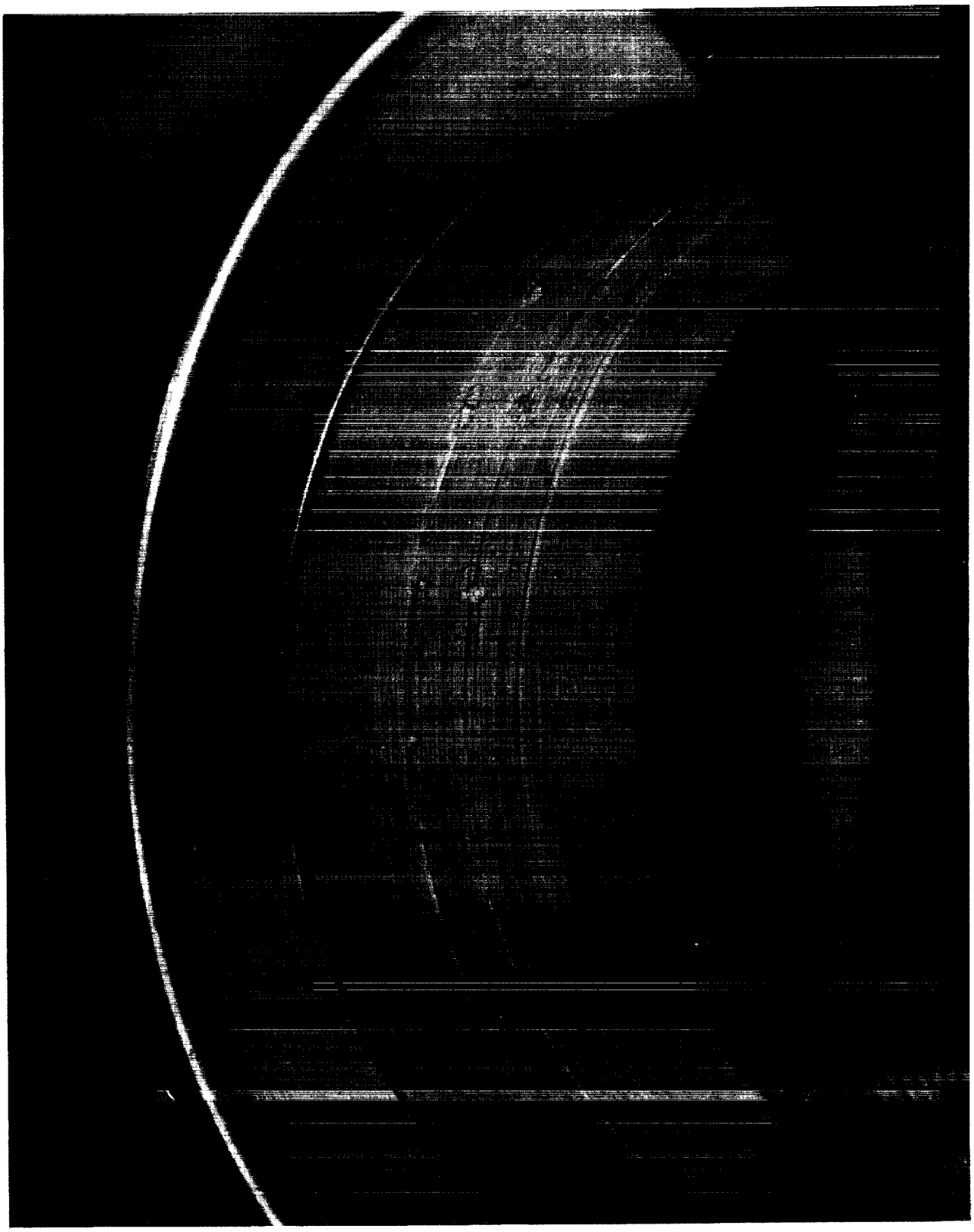

Figure 82. PLIN Bearing, Silver Accumulation, Posttest N15

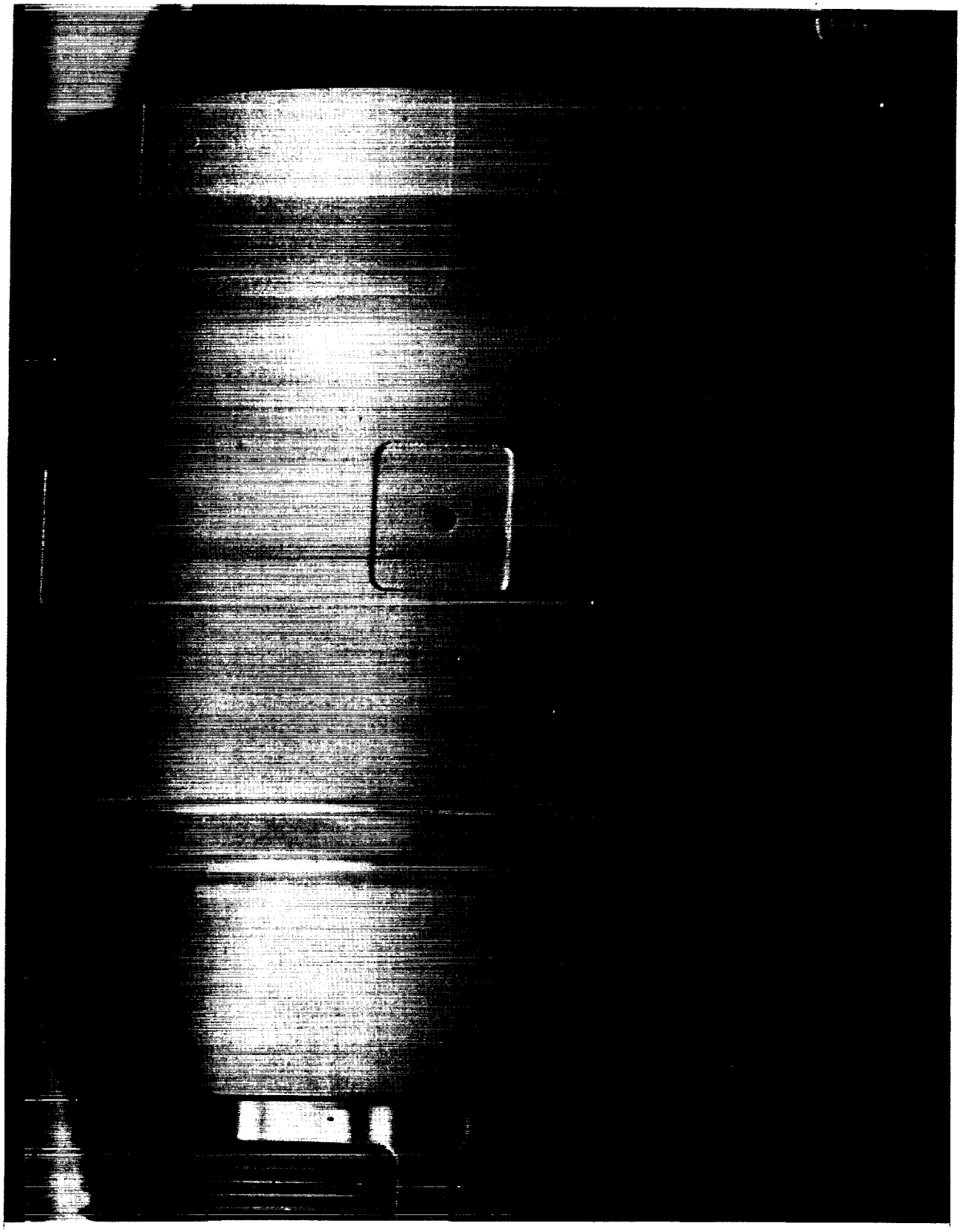

Figure 83. PLIN Bearing Journal, Posttest N15

SUMMARY OF RESULTS

The SSME Long-Life Bearing Program encompassed analytic and empirical treatments of hybrid and hydrostatic bearings for cryogenic turbopumps.

ANALYTIC RESULTS

Parallel load hybrid bearings can be used to extend ball bearing life, increase radial load capacity, and provide additional stiffness and damping. The prevention of rubbing of the hydrostatic bearing surface during start and shutdown is especially valuable for applications with reactive working fluids such as LO2. Since the ball bearing must operate at full rotor speed, speed limits are not raised, and the life extension is limited to that achieved by load reduction. Inclusion of the fluid swirl effects in the internally fed bearing analysis reduces the direct stiffness and increases the cross-coupling stiffness.

The most effective design variables affecting load capacity, stiffness and damping are: (1) bearing size, (2) radial clearance, (3) recess pressure ratio (the pressure drop from recess to sump divided by total pressure drop across the bearing). This quantity is controlled by balancing the flow resistances of the film and the orifice. It should be close to 0.5 for maximum stiffness and damping.

EMPIRICAL RESULTS

Dynamic stiffness and damping coefficients were determined for a 75 mm diameter externally fed and a 55 mm diameter internally fed hydrostatic bearing using Freon 113 as the working fluid with a supply pressure of 10.3 MPa (1500 psig). The externally fed bearing had a direct stiffness value approximately 20% lower than predicted at 1.75e08 N/m (1.0e06 lb/in.). Damping was approximately as predicted at 40,000. N•s/m (228 lb•s/in.). Cross-coupling stiffness of -2.0e7 N/m (-114,000 lb/in.) was measured compared with a predicted value of +4.0e7 N/m (+228,000 lb/in.). Separated coefficients of the internally fed bearing were quite speed-dependent. The net effective stiffness of the internally fed bearing at 3.0e07 N/m (171,000 lb/in.) was only about 30% of the predicted value. Measured damping was also low, at 7000 N•s/m (40 lb•s/in) but exceeded the analytic value adjusted for fluid swirl. Separated coefficients could only be determined if the journal orbit ellipticity exceeded 1.175.

Steady-state direct stiffness of the externally fed bearing operating with LH_2 as determined by application of a fixed radial load was found to be 4.12e08 N/m (2.35e06 lb/in.) with a supply pressure of 16.14 MPa (2340 psia) at a speed of 3810 rad/s (36,400 rpm). Steady state-stiffness increased with speed and supply pressure.

Steady-state stiffness of the parallel load internally fed hybrid bearing with LN2 as the working fluid was indicated to be 5% lower than predicted when the calculated stiffness of the ball bearing was deducted, the hydrostatic element stiffness was indicated to be 2.3e08 N/m (1.5e06 lb/in.). No significant test results were obtained with the hydrostatic element alone.

Flowrates were found to be lower than predicted. For the externally fed bearing operating with LH2, adjustment of the orifice coefficient from 1.0 to 0.94 and reduction of the film entrance loss coefficient to 0.36 from the assumed 0.5 reconciled the predicted and measured flow. For the internally fed bearing, Freon tests also indicated flowrates lower than predicted. Since recess pressures for the internally fed bearing were not measured, separation of the orifice and film entrance loss coefficients was not possible. However, coefficient values of 0.6 and 0.5 for orifice and film entrance coefficients, respectively, is consistent with overall measured flow.

CONCLUSIONS

ANALYTICAL CONCLUSIONS

Hybrid bearings are an effective concept for increasing the capabilities of ball bearings and are applicable to LH2 and LO2 turbopumps as well as other types of rotating machinery.

Parallel load hybrid bearings can be used to increase the load capacity, stiffness, and damping provided by rolling bearings. Life of the rolling bearings will be improved if the life-limiting factor is radial load.

Hydrostatic bearing design factors most strongly affecting load capacity, stiffness, and damping are bearing area, radial clearance, and recess pressure ratio. Operating conditions of overall pressure ratio, fluid properties, and speed also affect these bearing support characteristics.

Maximum damping is not necessarily the optimum in terms of unbalance response. Rotordynamic analysis for turbomachinery designs should include determination of the optimum damping and also the effect of the cross-coupling stiffness introduced by the hydrostatic bearing on rotor stability. Transient analysis should include speed-dependent factors; supply pressure and centrifugal growth will affect bearing stiffness, introducing the potential for a rotor resonance to track shaft speed.

TESTING CONCLUSIONS

Parallel load hybrid bearings are applicable to cryogenic turbomachinery; the ball bearings are effective in preventing rubbing contact of the hydrostatic bearing element.

Externally fed hydrostatic bearings provide significant direct stiffness and damping at speed, which can be predicted with current analytical procedures. Net effective coefficients are affected by speed; actual stiffness appears to be lower and damping higher than theoretical values.

Steady-state stiffness in response to a fixed direction unvarying radial load is conservatively predicted.

Internally fed hydrostatic bearings with recesses in the journal surface provide low values of net effective stiffness and damping under dynamic loading due to the effects of fluid swirl. Steady-state stiffness in response to fixed radial load is reduced to a lesser extent and can be predicted analytically with good accuracy.

Hard, wear resistant materials are necessary for hydrostatic bearing surfaces that are subject to rubbing. Silver plating is not a suitable material for close-clearance bearings since it tends to accumulate into globules that will jam the bearing.

Filtering or other means are required to exclude particles from the working fluid to avoid blockage of the clearance. Particles tend to accumulate at the recess edges, causing flow restrictions wear, and potentially jamming the bearing. A 10 micron nominal filter was found to be effective in preventing serious contamination for the test bearings with clearances of 0.038 mm (0.0015 in.).

RECOMMENDATIONS

Further testing is recommended to characterize hydrostatic bearing damping and stiffness, since only a limited number of dynamic coefficients were obtained. One of the major drawbacks of the tester configuration used is the need for elliptic orbits in order to separate stiffness from damping. Since the elliptic orbits are obtained by having an asymmetric stator support stiffness, the tester will be effective only when the fluid film stiffness is well matched with the support stiffness. If the support is too soft or too stiff, sufficient ellipticity will not be obtained.

Another drawback is the inability to measure asymmetric fluid film coefficients as functions of speed. The only way to lift this restriction is to use an asynchronous excitation source. Figure 83 shows one way in which the current test apparatus can be modified to have an asynchronous excitation source. Mounted on the tester shaft just outboard of the test bearing is a disk that can rotate at a speed independent of test shaft speed. Unbalance masses added to this disk will then impart orbital motion to the test shaft at a frequency equal to the speed of the disk. By operating on the measured displacements and forces (using Fourier coefficients as before) at the frequency of the rotating disk, the full general set of 12 asymmetric rotordynamic coefficients can be identified as functions of test shaft speed. Such a tester would make it possible to measure bearing nonlinearity and the effects of fixed radial eccentricity.

To conduct testing with an independent rotating disk, it will be necessary to have accurate active control of both the test shaft speed and rotating disk speed. While the speed of the disk is changing, the shaft speed must be held constant. Also, the tester should have the capability to rotate the exciter disk in both the forward and reverse directions.

ALTERNATE MATERIALS

Material development for hydrostatic bearings should continue with studies of alternate materials with good compatibility, strength and wear resistance. Materials considered to have good potential for use in LH_2 and LO_2 service, including those requiring development evaluation are listed in Table 18. Material categories are for base materials of construction, materials that should be contained as inserts due to lack of tensile strength, and platings and coatings that have potential for wear resistance.

An attractive alternate material for both journal and bearing surfaces is Stellite 6B. It is highly wear and corrosion resistant, but has marginal strength based on ambient temperature properties. Strength increases due to cryogenic temperatures are unknown at present. Stellite 6B has good resistance to impact and thermal shock, at elevated temperature, with an estimated 40% reduction in ductility at -400 F. It has excellent wear resistance in air, with a stator coefficient of friction of 0.119 against itself. With an adhesive galling threshold of over 72 KSI, the Stellite/Stellite combination should have excellent resistance to seizure. High cost is a drawback for heavy sections of Stellite 6B. With development of oxy-acetylene deposition or plasma arc surfacing, significant cost savings might be obtained. Some techniques for accommodating residual stresses for these applied coatings would be required to assure permanent adhesion to substrate, however.

DAMPING MEASUREMENT WITH NON-SYNCHRONOUS EXCITATION

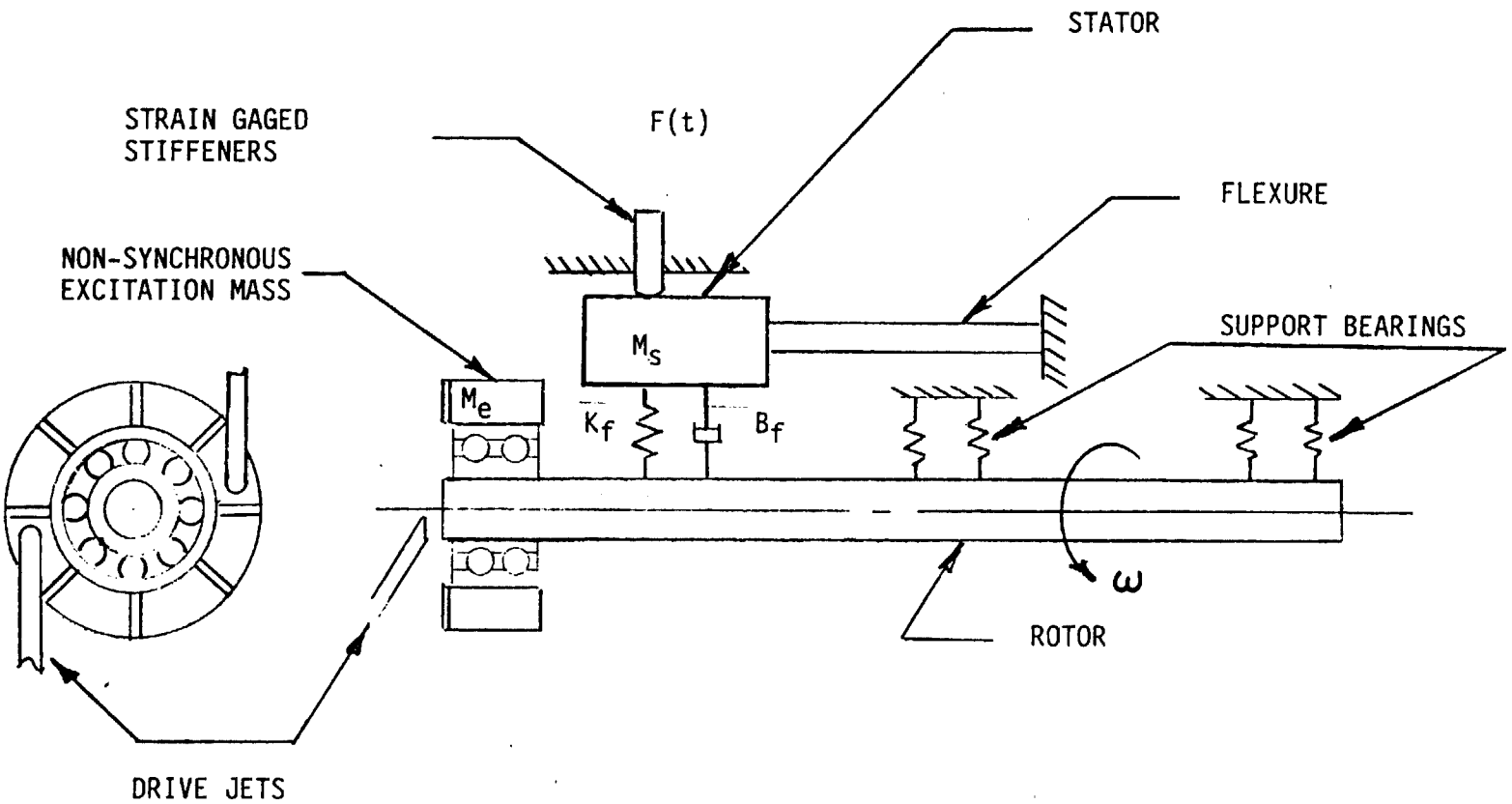

METHOD: SWEEP FREQUENCY WITH M_e AT SEVERAL VALUES OF ω

DYNAMIC FORCE & MOTION DATA USED TO SOLVE FOR B_f, K_f

Figure 84. Asynchronous Tester Schematic

TABLE 18. HYDROSTATIC BEARING MATERIALS RECOMMENDED FOR STUDY

				CURRENT RATING								
JOURNAL MATERIALS	FORM	BEARING MATERIALS	FORM	COMPATIBILITY	STRENGTH	CORROSION RESISTANCE	WEAR RESISTANCE	THERMAL SHOCK RESISTANCE	PRODUCIBILITY	FRICTION COEFFICIENT	MECHANICAL SHOCK RESISTANCE	COST
ALLOY 718	BASE	ALLOY 718	BASE	F	F	F	D	F	F	D	F	F
STELLITE 6B, WROUGHT	SLEEVE	STELLITE 6B, WROUGHT	INSERT	F	D	F	F	D	D	F	D	D
STELLITE 6B	HARD COAT	STELLITE	HARD COAT	F	F	F	F	D	D	F	D	D
SILICON CARBIDE	SLEEVE	SILICON CARBIDE	INSERT	F	D	F	F	D	D	F	D	D
CHROMIUM	THIN DENSE			F	F	F	D	F	F	D	F	F
TUNGSTEN CARBIDE	HARD COAT			F	F	F	F	D	F	F	D	F
		CARBON GRAPHITE COMPOSITES	INSERT	D	D	F	F	D	F	F	D	F
FERRO-TIC			COATING	D	D	D	F	D	D	D	U	D
NY CARB			PLATING	D	D	D	D	D	D	D	D	D
BORIDE COATINGS			COATING	D	D	D	D	D	D	D	D	D
		SILICONIZED CARBON GRAPHITE	INSERT	D	D	F	D	D	F	D	D	F
		METGLASS	HARD COAT	D	D	D	D	D	D	D	D	D

RATING KEY: F - FAVORABLE D - DEVELOPMENT OR EVALUATION REQUIRED U - SATISFACTORY

An attractive insert material is silicon carbide, which has shown good wear resistance in rolling bearings. Made into inserts and kept under compression, silicon carbide could prove to be an excellent hydrostatic bearing material. If the sleeve could be hot pressed to net shape, difficult machining could be avoided.

The ultimate goal of the material study should be identification of materials that are sufficiently wear resistant that transient rubbing can be tolerated, so that the necessity for including rolling bearings can be eliminated.

REFERENCES

1. Young, W. E., and J. M. Reddecliffe: "Investigation of Hydrostatic Bearings for use in High Pressure Cryogenic Turbopumps," PWA FR-2343; AFRPL-TR-67-130, United Aircraft Corp., West Palm Beach, FL; Air Force Rocket Propulsion Lab., Edwards AFB, CA, 15 May 1967.

2. Reddecliffe, J. M., and J. H. Vohr: "Hydrostatic Bearings for Cryogenic Rocket Engine Turbopumps," Journal of Lubrication Technology, July 1969.

3. Winn, L. W.: "Development and Test of Long-Life Hybrid Boost Thrust Bearings for Small High-Speed Jet Engine Application," June MT169-TR17, 1969 Contract No. N00019-68-C-0269.

4. Winn, L. W. and R. Badgley: "Development of Long-Life Jet Engine Thrust Bearings," NASA CR-72744, 1970.

5. Anderson, W. J., D. P. Fleming, and R. J. Parker: "The Series Hybrid Bearing: A New High-Speed Bearing Concept," ASME Paper 71-Lub-15, 1971.

6. Nypan, L. J., H. W. Scibbe and B. J. Hamrock: "Optimal Speed Sharing Characteristics of a Series - Hybrid Bearing," 1971.

7. Wolf, J. E.: "Mark 25 Hybrid Hydrostatic Bearing Test at Nuclear Rocket Development Station," Rockwell International, Rocketdyne Division, Canoga Park, CA. Report R-9117, Contract SNSN-65, 20 November 1972.

8. Wilcock, D. F., and L. W. Winn: United States Patent 3,708,215, Hybrid Bearing Boost Assembly, 2 January 1973.

9. Gu, A., M. Eusepi and L. W. Winn: "Evaluation of a Series Hybrid Thrust Bearing at DN Values to 3 Million I-Analysis and Design," NASACR-2366, January 1974.

10. Scibbe, H. W., L. W. Winn, and M. Eusepi: "Design and Evaluation of a 3 Million DN Series - Hybrid Thrust Bearing," ASME Paper 76-LubS-17, 1976. Also printed in the Journal of Lubrication Technology, Vol 98, No. 4, October 1976.

11. Hannum, N. P., and C. E. Nielson: "The Performance and Application of High-Speed Long-Life LH_2 Bearings for Reusable Rocket Engine Turbomachinery," NASA TM-83417, AIAA83-1389, June 1983.

12. Artiles, A., J. Wallowit, and W. Shapiro: "Analysis of Hybrid, Fluid Film Journal Bearings with Turbulence and Inertia Effects," Advances in Computer - Aided Bearing Design, Proceedings of ASME-ASLE Lubrication Conference, October 1982, American Society of Lubrication Engineers, New York, NY.

13. Jones, A. B.: Rolling-Element Bearing Analysis Program, 1978.

14. Black, H. F., P. E. Allaire, and L. E. Barrett: "Inlet Flow Swirl in Short Turbulent Annular Seal Dynamics," presented at 9th International Conference on Fluid Sealing, BHRA Fluid Engineering, Leeuenhorst, Netherlands, April 1981.

15. RPI-MTI Gas Bearing Design Course, 1967.

16. Aston, R. L. and J. P. O'Donoghue: "The Effect of the Number of Recesses on the Performance at Externally Pressurized Multirecess Journal Bearings," Tribology, May 1971, pp. 94-96.

17. Childs, D. W.: "Finite Length Solution for Rotordynamic Coefficients of Turbulent Annular Seals," Journal of Lubrication Technology, July 1983, Vol. 105, pp. 437-445.

18. Von Pragenau, G. L.: "Damping Seals for Turbomachinery NASA," Technical Paper 1987, 1982.

19. Childs, D. W., Kim. C. H.: "Analysis and Testing for Rotordynamic Coefficients of Turbulent Annular Seals with Different, Directionally Homogeneous Surface-Roughness Treatment for Rotor and Stator Element," Rotordynamics Instability Problems in High-Performance Turbomachinery, Workshop held at Texas A&M University, NASA Conference Publication 2338, pp. 313-340, May 1984.

20. Chen, W. C., and E. D. Jackson: "A Generalized Theory for Eccentric and Misalignment Effects in High-Pressure Annular Seals ASLE," Preprint No. 86-AM-3G-4. Presented at 41st Annual Meeting, Toronto, Canada, 12 through 15 May, 1986.

21. Miller, D. S.: "Internal Flow Systems," Vol. 5, BHRA Fluid Engineering Series.

22. Spica, P. W., N. P. Hannum, and S. D. Meyer: Evaluation of a Hybrid Hydrostatic Bearing for Cryogenic Turbopump Application, NASA Technical Memorandum 87255, April 1986.

APPENDIX A

LH_2 DYNAMIC CHARACTERISTICS TESTS

Seven tests (test numbers 033 through 042, Table 19) were conducted to determine the dynamic characteristics of the hydrostatic bearing of the PLEX bearing pressurized with liquid hydrogen. The tester housing was electrically heated for 8 to 12 hours, followed by a gaseous helium (GHe) purge to eliminate air and moisture prior to introducing cold hydrogen flowing from the low-pressure LH_2 storage tank through the test hardware to the vent stack. The exhausted hydrogen was ignited at the top of the vent stack and continuously burned to prevent a buildup of explosive gas. The chilling process was continued until the fluid temperature in the tester approached 50 K (90 R). The flow to the tester was stopped, and the run tank topped off and pressurized. The test was then started as soon as possible, as the temperature of the hydrogen in the run tank rises due to heat from the ambient surroundings.

In the dynamic characteristics tests, the test bearing was subjected to the pressure and speed profile shown in Fig. 85. Dynamic force and motion data were recorded for later analysis.

TESTS 033, 034

A test bearing journal length of 25.4 mm (1 inch) was used. Bearing supply pressure was 16.1 MPa (2350 psia) with a sump pressure of 2.4 MPa (350 psia). B2, or journal deflection data were satisfactory, indicating a magnitude of 1.37e-2 mm (0.00054 inch) p-p; however, dynamic load data were not obtained. Since it was expected that load values could be recovered from the stator accelerometer signals, the tester was prepared for the next test by installing a longer journal (L = 35 mm (1.375 inch) while data analysis was initiated. It was found that the journal motion signals had a nonsinusoidal wave form, preventing successful analysis for dynamic coefficients of data from these tests.

TESTS 035, 036

Tests 035 and 036 were run with the same total fluid pressure drop at supply pressures of 16.2 and 18.6 MPa, respectively. The flowrate was not significantly affected by the higher supply pressure. Although hydrogen is slightly compressible under these conditions, its density was essentially the same for both tests because of the compensating effect of the higher supply temperature resulting from more heating by the additional pressurizing gas required to achieve higher run tank pressure.

TEST 038, 039

With the same long journal, an identical alternate test bearing with different proximity probes was installed in an attempt to obtain undistorted B2 (film thickness or relative journal motion) signals. Peak amplitudes of signals differed from the previous tests due to different scale factors of the new probes; however, signal distortion was repeated, precluding successful data analysis. Bearing supply/sump pressure drop was 13.8 MPa (2000 psi) and 6.9 MPa (1000 psi), respectively, for the two tests. Flowrates differed approximately by the square root of the pressure drops.

TABLE 19. LH_2 HYDROSTATIC BEARING DYNAMIC TESTING SUMMARY

TEST TYPE	TEST DATE	TEST NO.	SPEED Krad/s	TIME s	SUP. PRESS. MPa	SUMP PRESS. MPa	SUP. TEMP K	SUMP TEMP K	FLUID DENSITY kg/m^3	FLUID FLOW kg/sec	FLUID FLOW m^3/sec	COMMENTS
DAMPING COEFFICIENT	5-18-84	33	1.10	8	16.25	2.427	47.8	42.22	64.5290	.200	3.10e-3	NO RADIAL LOAD SIGNALS RECORDED
BEARING LENGTH=25.4mm		&	1.48	30	16.21	2.434	47.8	42.22	64.5290	.205	3.17e-3	
SUPPLY PRESSURE=16.2MPa (2350 psia)		34	2.38	34	16.23	2.427	47.8	42.22	64.5290	.195	3.03e-3	
DELTA P=13.8MPa (2000 psi)			2.73	55	16.23	2.434	48.3	42.22	64.0475	.191	2.98e-3	
			3.41	59	16.20	2.420	48.3	42.78	64.0475	.186	2.91e-3	
			3.75	80	16.21	2.434	48.9	42.78	63.5659	.177	2.79e-3	
DAMPING COEFFICIENT	6-12-84	35	1.15	15	16.18	2.406	46.1	41.11	65.6527	.186	2.84e-3	FILM THICKNESS SIGNALS DISTORTED
BEARING LENGTH=35mm			1.47	27	16.18	2.413	46.1	41.11	65.6527	.191	2.91e-3	
SUPPLY PRESSURE=16.2MPa (2350 psia)			2.35	33	16.19	2.406	46.7	41.67	65.3316	.186	2.85e-3	
DELTA P=13.8MPa (2000 psi)			2.73	50	16.18	2.413	46.7	41.67	65.3316	.182	2.78e-3	
			3.41	56	16.20	2.399	47.2	42.22	64.8501	.168	2.59e-3	
			3.80	73	16.18	2.406	47.8	42.22	64.3685	.159	2.47e-3	
DAMPING COEFFICIENT	6-12-84	36	1.18	6	18.60	4.427	50.6	44.44	65.0106	.132	2.03e-3	FILM THICKNESS SIGNALS DISTORTED
BEARING LENGTH=35mm			1.51	26	18.60	4.854	51.1	45.56	64.6896	.195	3.02e-3	
SUPPLY PRESSURE=18.6MPa (2700 psia)			2.33	30	18.62	4.854	51.1	45.56	64.6896	.191	2.95e-3	
DELTA P=13.8MPa (2000 psia)			2.72	47	18.60	4.861	51.7	46.67	64.208	.182	2.83e-3	
DELTA P=13.8MPa			3.72	53	18.62	4.847	52.2	46.67	63.8870	.173	2.70e-3	
			3.72	68	18.60	4.854	52.2	46.67	63.8870	.164	2.56e-3	
DAMPING COEFFICIENT	6-21-84	38	1.06	9	13.71	.6888	50.6	33.89	58.1082	.136	2.35e-3	SIMILAR FILM THICKNESS SIGNALS
BEARING LENGTH=35mm			1.48	29	16.25	2.427	49.4	42.22	62.6028	.191	3.05e-3	WITH NEW BEARING AND PROBES
NEW BEARING & FILM PROBES			2.32	35	16.26	2.406	50	42.78	62.6028	.182	2.90e-3	
SUPPLY PRESSURE=16.2MPa			3.81	55	16.25	2.413	51.1	43.33	60.9976	.177	2.91e-3	
DELTA P=13.8MPa			3.35	60	16.26	2.406	51.1	43.89	60.9976	.164	2.68e-3	
			3.82	80	16.26	2.420	52.8	45	60.195	.155	2.57e-3	
DAMPING COEFFICIENT	6-21-84	39	1.20	9	9.322	.7516	51.7	43.89	49.7612	.127	2.56e-3	SIMILAR TO PREVIOUS TESTS
SUPPLY PRESSURE=9.3MPa (1350 psia)		&	1.48	29	9.329	2.413	53.3	44.44	48.156	.141	2.93e-3	EXCHANGED SIGNAL CONDUCTOR
DELTA P=6.9MPa (1000 psia)		40	2.35	35	9.336	2.406	53.9	45	47.3534	.136	2.88e-3	LINES FOR TEST 40
			2.73	55	9.329	2.413	55	46.11	45.7482	.132	2.88e-3	
			3.76	80	9.343	2.413	57.2	47.78	44.143	.118	2.68e-3	

TABLE 19. (Concluded)

TEST TYPE	TEST DATE	TEST NO.	SPEED Krpm	TIME s	SUP. PRESS. psig	SUMP PRESS. psig	SUP. TEMP R	SUMP TEMP R	SUPPLY FLUID DENSITY lb/ft^3	FLUID FLOW lbm/s	FLUID FLOW gal/min	COMMENTS
DAMPING COEFFICIENT BEARING LENGTH=25.4mm	5-18-84	33	11.24	8	2357	352	86	76	4.02	.440	4.912e1	NO RADIAL LOAD SIGNALS RECORDED
		&	14.12	30	2351	353	86	76	4.02	.450	5.024e1	
		34	22.74	34	2354	352	86	76	4.02	.430	4.801e1	
			26.04	55	2354	353	87	76	3.99	.420	4.724e1	
			32.53	59	2349	351	87	77	3.99	.410	4.612e1	
			35.84	80	2351	353	88	77	3.96	.390	4.42e1	
DAMPING COEFFICIENT BEARING LENGTH=35mm SUPPLY PRESSURE=16.2MPa (2350 psia) DELTA P=13.8MPa (2000 psi)	6-12-84	35	10.95	15	2347	349	83	74	4.09	.410	4.499e1	FILM THICKNESS SIGNALS DISTORTED
			14.04	27	2347	350	83	74	4.09	.420	4.609e1	
			22.45	33	2348	349	84	75	4.07	.410	4.521e1	
			26.08	50	2347	350	84	75	4.07	.400	4.411e1	
			32.52	56	2350	348	85	76	4.04	.370	4.110e1	
			36.27	73	2346	349	86	76	4.01	.350	3.917e1	
DAMPING COEFFICIENT BEARING LENGTH=35mm SUPPLY PRESSURE=18.6MPa (2700 psia) DELTA P=13.8MPa (2000 psia)	6-12-84	36	11.24	6	2697	642	91	80	4.05	.290	3.214e1	FILM THICKNESS SIGNALS DISTORTED
			14.46	26	2698	704	92	82	4.03	.430	4.789e1	
			22.21	30	2700	704	92	82	4.03	.420	4.677e1	
			26.01	47	2698	705	93	84	4	.400	4.488e1	
			35.52	53	2700	703	94	84	3.98	.380	4.285e1	
			35.53	68	2698	704	94	84	3.98	.360	4.059e1	
DAMPING COEFFICIENT BEARING LENGTH=35mm NEW BEARING & FILM PROBES SUPPLY PRESSURE=16.2MPa DELTA P=13.8MPa	6-21-84	38	10.13	9	1988	97	91	61	3.62	.300	3.719e1	SIMILAR FILM THICKNESS SIGNALS
			14.12	29	2357	352	89	76	3.9	.420	4.833e1	WITH NEW BEARING AND PROBES
			22.19	35	2358	349	90	77	3.9	.400	4.603e1	
			36.35	55	2357	350	92	78	3.8	.390	4.606e1	
			32.00	60	2358	349	92	79	3.8	.360	4.252e1	
			36.46	80	2358	351	95	81	3.75	.340	4.069e1	
DAMPING COEFFICIENT SUPPLY PRESSURE=9.3MPa (1350 psia) DELTA P=6.9MPa (1000 psia)	6-21-84	39	11.48	9	1352	109	93	79	3.1	.280	4.054e1	SIMILAR TO PREVIOUS TESTS
		&	14.12	29	1353	350	96	80	3	.310	4.638e1	EXCHANGED SIGNAL CONDUCTOR
		40	22.41	35	1354	349	97	81	2.95	.300	4.564e1	LINES FOR TEST 40
			26.04	55	1353	350	99	83	2.85	.290	4.567e1	
			32.14	60	1353	349	100	84	2.8	.280	4.488e1	
			35.92	80	1355	350	103	86	2.75	.260	4.243e1	

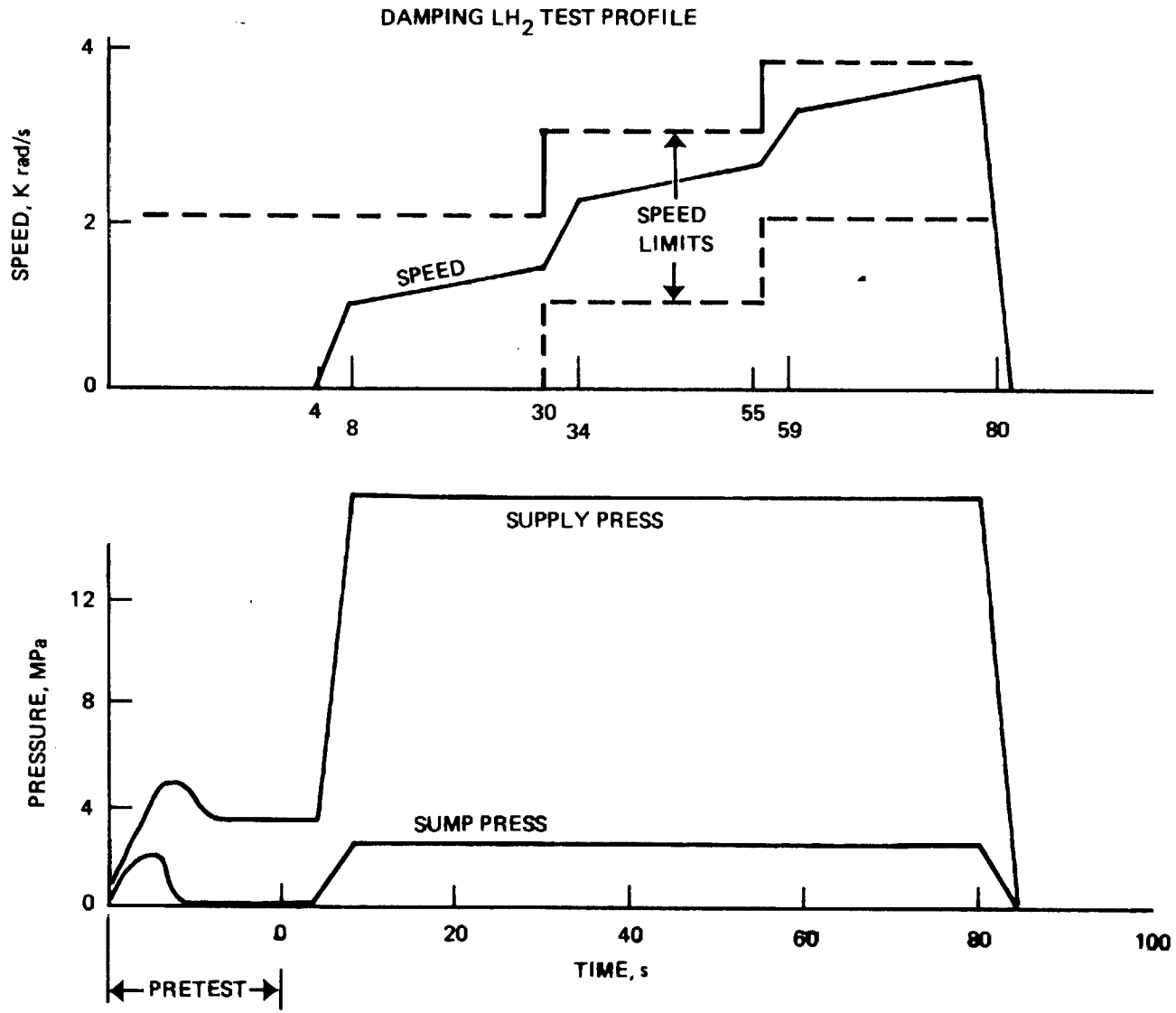

Figure 85. Damping Test Profile, LH_2

TEST 040

In this repeat of test 039, journal and stator proximity probe cables were interchanged to identify the source of the B2 signal distortion, which remained with the journal motion signals. This result indicated that the difficulty lay with the journal. In more recent testing, it has been found that minor deviations from a true circular journal surface introduces harmonics into the displacement signals. The possibility that the observed distortion is due to deflection signal artifacts arising from residual magnetism of the journal was explored with eddy current inspection equipment used to detect grinding burns in balls and ball bearing races. As would be expected for Alloy 718, no indications were found. In view of the more recent experience cited, the probable cause of the B2 signal distortion was journal surface waviness in excess of 1.2e-3 mm (50e-6 inch).

TESTS 040, 041

In an attempt to achieve an elliptic journal orbit, the strain-gaged studs in the 45-degree plane were removed, thus providing an asymmetric stator stiffness. Stator accelerometer signals were to be used to replace the missing strain gage load readings. This action was taken as a result of discussion with Dr. Dara Childs in which he indicated that the journal orbit must be elliptic for the eccentric journal test method used to produce data that can be successfully analyzed for separate stiffness and damping coefficients. The shorter journal was reinstalled to avoid the signal distortion noted in the previous tests. As in the previous tests, the pressure drops across the test bearing were set at 13.8 and 6.9 MPa (2000 and 1000 psi) for tests 040 and 041, respectively. Visual assessment of oscilloscope traces of the signal suggested that the data were good.

Data analysis of tests 33 and 34 indicated that there was a definite phase difference of approximately 90 degrees between force and displacement vectors. In addition, there was a 180-degree phase shift of these vectors at 530 Hz. The stator motion ceased, while the film motion continued, which could be interpreted as a loss of capacity at this frequency. This response was not found in the other dynamic tests. Additional checks of the instrumentation and data systems showed no phase shifts from these sources. The data signal quality was sufficient for processing by the analysis program, which was checked out with a trial problem. Various trial phase shifts were imposed to determine if the solution could be stabilized. The resulting coefficients were inconsistent.

Prior to test 41, two load-measuring studs were removed to produce elliptical orbits for coefficient separation by creating asymmetric stator stiffness. The data analysis program produced consistent but unrealistic coefficients at all speeds. A stator resonance was produced at 525 Hz because of the softened support in one axis. Previously, the stator support stiffness was sufficient to prevent resonances from occurring in the operating speed range.

It was concluded that the inability to extract realistic coefficients stemmed from interference by casing resonances, and no further efforts were made to analyze the data from tests 033 through 042, and all activities were directed toward modification of the tester to eliminate housing resonances that would interfere with production of reducible data. Subsequent testing was conducted using Freon 113 as the working fluid, with the results noted in the main body of the report.

APPENDIX B

DISTRIBUTION LIST FOR FINAL REPORT

CONTRACT NAS3-23263

	No. of Copies
National Aeronautics & Space Administration Lewis Research Center 21000 Brookpark Road Cleveland, Ohio 44135	
Attn: Contracting Officer, MS 500-305	1
Adm. Assistant, MS 500-200	
Technical Utilization Office, MS 7-3	1
Report Control Office, MS 60-1	1
AFSC Liaison Office, MS 501-3	2
Library, MS 60-3	2
Office of Reliability & Quality Assurance, MS 500-211	1
P. W. Spica, MS 500-219	15
National Aeronautics & Space Administration Headquarters Washington, D. C. 20546	
Attn: OFFICE OF AERONATUICS & SPACE TECHNOLOGY	
Director for Space/RS	1
Deputy Director (Space & Energy)/RP1	1
F. W. Stephenson/RP	1
OFFICE OF SPACE FLIGHT	
Chief, Advanced Transportation/MTT	1
D. L. Winterhalter/MP	1
H. T. Gawrylowicz/MPE	1
National Aeronautics & Space Administration Ames Research Center Moffett Field, CA 94035	
Attn: Library	1
National Aeronautics & Space Administration Flight Research Center P. O. Box 273 Edwards, CA 93523	
Attn: Library	1

National Aeronautics & Space Administration
George C. Marshall Space Flight Center
Huntsville, Alabama 35812
Attn: Library 1
J. L. Sanders/PD13 1
R. Richmond/EP24 1
J. McCarty/EP21 1
L. Gross/EP23 1
O. K. Goetz/EP21 1
F. J. Dolan/EH14 1
S. Morea/EP01 1

National Aeronautics & Space Administration
Goddard Space Flight Center
Greenbelt, Maryland 20771
Attn: Library 1

National Aeronautics & Space Administration
John F. Kennedy Space Center
Cape Canaveral, Florida 32931
Attn: Library 1

National Aeronautics & Space Administration
Lyndon B. Johnson Space Center
Houston, Texas 77001
Attn: Library 1
R. J. Taeuber/EP4 1
L. R. Johnson/EP4 1

National Aeronautics & Space Administration
Langley Research Center
Langley Station
Hampton, Virginia 23365
Attn: Library 1

NASA Scientific & Technical Information Facility
P. O. Box 8757
Baltimore-Washington International Airport
Baltimore, Maryland 21240
Attn: Accessing Department 10

Jet Propulsion Laboratory
4800 Oak Grove Drive
Pasadena, CA 91103
Attn: Library 1

Defense Documentation Center
Cameron Station
Building 5
5010 Duke Street
Alexandria, Virginia 22314
Attn: TISIA 1

Advanced Research Projects Agency
1400 Wilson Blvd.
Washington, D. C. 20525
Attn: Library 1

Aeronautical System Division
Air Force Systems Command
Wright-Patterson Air Force Base
Dayton, Ohio
Attn: Library 1

Air Force Rocket Propulsion Laboratory
Edwards, CA 93523
Attn: Library 1
LKDB/D. Moon 1
LKDB/Lt. G. Jennings 1

Space Division
Los Angeles Air Force Station, CA 9009
Attn: Library 1

Bureau of Naval Weapons
Department of the Navy
Washington, D. C.
Attn: Library 1

Picatinny Arsenal
Dover, New Jersey 07801
Attn: Library 1

U. S. Naval Research Laboratory
Washington, D. C. 20390
Attn: Library 1

Marquardt Corporation
16555 Saticoy Street
Box 2013 South Annex
Van Nuys, CA 91409
Attn: Library 1

Martin-Marietta Corporation
P. O. Box 179
Denver, Colorado 80201
Attn: Library 1

McDonnell Douglas Astronautics
5301 Bosa Avenue
Huntington Beach, CA 92647
Attn: Library 1

Pratt & Whitney Aircraft Group
United Technologies Corporation
P. O. Box 2691
West Palm Beach, FL 33402
Attn: Library 1
J. Brown 1

Space Division
A Division of Rockwell International
12214 Lakewood Blvd.
Downey, CA 90241
Attn: Library 1

Rocket Research Corporation
Willow Road at 116th Street
Redmond, Washington 98052
Attn: Library 1

Boeing Aerospace Company
P. O. Box 3999
Seattle, Washington 98124
Attn: Library 1

John Hopkins University
Applied Physics Laboratory
John Hopkins Road
Laurel, Maryland 20810 1

Curtiss-Wright Corporation
One Passaic St.
Woodridge, New Jersey 07075
Attn: Library 1

General Dynamics/Convair
P. O. Box 80847
San Diego, CA 92138
Attn: Library 1

General Electric Company
Valley Forge Space Center
P. O. Box 8555
Philadelphia, PA 19101
Attn: Library 1

Grumman Aerospace Corporation
Bethpage, NY 11714
Attn: Library 1

Hughes Aircraft Company
Space & Communications Group
P. O. Box 92919
Los Angeles, CA 90009
Attn: Library 1

Walter Kidde & Company
675 Main St.
Belleville, New Jersey 07109
Attn: Library 1

Lockheed Missiles & Space Company
P. O. Box 504
Sunnyvale, CA 94087
Attn: Library 1

U. S. Army Missile Command
Redstone Scientific Information Center
Redstone Arsenal, Alabama 35808
Attn: Document Section 1

U. S. Naval Missile Center
Point Mugu, CA 93041
Attn: Technical Library 1

U. S. Naval Weapons Center
China Lake, CA 93557
Attn: Library 1

Aerospace Corporation
2350 E. El Segundo Blvd.
Los Angeles, CA 90045
Attn: Library 1

Garrett Turbine Engine Co.
A. Div. of the Garrett Corp.
402 South 36th Street
Phoenix, Arizona 85034
Attn: Library 1

Aerojet TechSystems Co.
P. O. Box 13222
Sacramento, CA 95813
Attn: Library 1
R. W. Michel 1
R. LaBotz 1
J. Pope 1
R. R. Davis 1

Avco Systems Division
201 Lowell St.
Wilmington, MA 01887
Attn: Library 1

Bell Aerospace Textron
Box 1
Buffalo, New York 14240
Attn: Library 1

1. Report No.	2. Government Accession No.	3. Recipient's Catalog No.
CR179455		

4. Title and Subtitle	5. Report Date
SSME Long-Life Bearings	July 1986
	6. Performing Organization Code 506-42-11
7. Author(s) Myles F. Butner, Brian T. Murphy	8. Performing Organization Report No. RI/RD86-168
	10. Work Unit No. YOS 1370
9. Performing Organization Name and Address Rockwell International Rocketdyne Division 6633 Canoga Avenue Canoga Park, CA 91304	11. Contract or Grant No. NAS3-23263
	13. Type of Report and Period Covered Final (1-82/7-86)
12. Sponsoring Agency Name and Address National Aeronautics and Space Administration NASA-Lewis Research Center 21000 Brookpark Road Cleveland, OH 44135	14. Sponsoring Agency Code

15. Supplementary Notes

Project Manager: Paul W. Spica
NASA-Lewis Research Center
Cleveland, Ohio 44135

16. Abstract

Hybrid hydrostatic/ball bearings for LH_2 and LO_2 service in turbopumps were studied as means of improving speed and life capabilities. Four hybrid bearing configurations were designed with emphasis on achieving maximum stiffness and damping. Parallel load bearings were tested at steady-state and transient conditions with LH_2 (externally fed) and LN_2 (internally fed). The hydrostatic elements were tested with Freon 113 for empirical determination of dynamic characteristics. Tests using an eccentric journal for loading showed the externally and internally fed hydrostatic bearings to have significant separated coefficients of direct stiffness and damping. For the internally fed bearing, the strongly speed-dependent cross-coupling stiffness arising from fluid swirl, along with significant cross-coupling damping, resulted in low net effective stiffness and damping. The test method used can produce separated coefficients with a sufficiently elliptic journal orbit; otherwise, only net effective coefficients combining direct and cross-coupling terms can be determined. Testing with nonsynchronous excitation is recommended to avoid this restriction. Investigation of hard materials, including ceramics, is recommended as a means of eliminating the need for the rolling bearing for startup and shutdown support. The testing was performed in 1984 (LH_2), 1985 (LN_2), and 1985-86 (Freon).

17. Key Words (Suggested by Author(s))	18. Distribution Statement
Hydrostatic Bearings Damping Turbopump Cryogenic	

19. Security Classif. (of this report)	20. Security Classif. (of this page)	21. No. of Pages	22. Price*
Unclassified	Unclassified	162	

* For sale by the National Technical Information Service, Springfield, Virginia 22161

NASA-C-168 (Rev. 10-75)